THEORETICAL CHARACTERIZATION OF COPLANAR WAVEGUIDE TRANSMISSION LINES AND DISCONTINUITIES

Nihad I. Dib and Linda P.B. Katehi

November 1992

THEORETICAL CHARACTERIZATION OF COPLANAR WAVEGUIDE TRANSMISSION LINES AND DISCONTINUITIES

Nihad I. Dib and Linda P. B. Katehi

Radiation Lab., University of Michigan, Ann Arbor, MI

1

TABLE OF CONTENTS

MISSING
PAGE

LIST OF APPENDICES

CHAPTER I

INTRODUCTION

1.1 Motivation and Background

The coplanar waveguide (CPW) was introduced for the first time in 1969 by C.P. Wen [1] as an appropriate transmission line for nonreciprocal gyromagnetic microwave device applications due to its ability to generate elliptically polarized magnetic fields in the slots. This new line, despite the fact that it exhibited many desirable properties, could not compete with the already established microstrip line in hybrid technology. As a result, coplanar lines attracted little attention in 1970's and early 80's. Recently, with the push to high frequencies and monolithic technology coplanar waveguides have experienced a growing demand due to their appealing properties [2]-[9].

With the increasing use of CPWs, the coplanar line technology cannot rely on the approximate quasi-TEM and semiempirical techniques which were developed a few years ago. It needs accurate high frequency modeling which can result only from rigorous analytical methods. Although coplanar waveguide has been well characterized as a transmission line [5], very little is available in literature on the analysis of coplanar waveguide discontinuities (relative to microstrip discontinuities). Nevertheless, despite this scarcity of reliable circuit models, CPW has provided an attractive alternative to conventional microstrip lines at high frequencies [8]-[20]. However, an

1

extensive study is needed in order to understand the electromagnetic behavior of CPW structures and be able to use them in high frequency applications.

As a response to this need, this dissertation presents a general method which can be implemented easily to theoretically characterize shielded coplanar waveguide discontinuities. This method is based on the Space Domain Integral Equation (SDIE) Approach and provides accuracy, computational efficiency and versatility in terms of the geometries it can solve. Briefly, the SDIE technique as applied to the CPW discontinuity problem proceeds as follows. A general magnetic field integral equation is derived for the CPW discontinuity problem. The method of moments is applied to solve this equation for the electric field or the equivalent magnetic current density in the slot aperture including the feed lines. The scattering parameters for the discontinuity can then be derived using transmission line theory.

Figure 1.1 shows the generic view of a coplanar waveguide which consists of a center conductor and two ground planes printed on the same surface of a dielectric slab. The coplanar line has basically two dominant modes of propagation. One is a quasi-TEM mode, often called the odd mode or coplanar mode, where the fields in the two slots are 180° out of phase as shown in Figure 1.2(a). The other is a non-TEM mode, called the even mode or the coupled slotline mode, where the fields are in phase as shown in Figure 1.2(b). In CPW microwave circuits, the coplanar mode is the most desired due to its low radiation properties. The excitation of the unwanted slotline mode can be avoided by either maintaining the symmetry of the structure or using air-bridges (or bond wires) to connect the ground planes of the CPW [9, 21]. It should be mentioned that the coplanar waveguide can be excited by either a coaxial line, a microstrip line or a slotline [22].

One of the main advantages of the CPW is that all the conductors lie on the
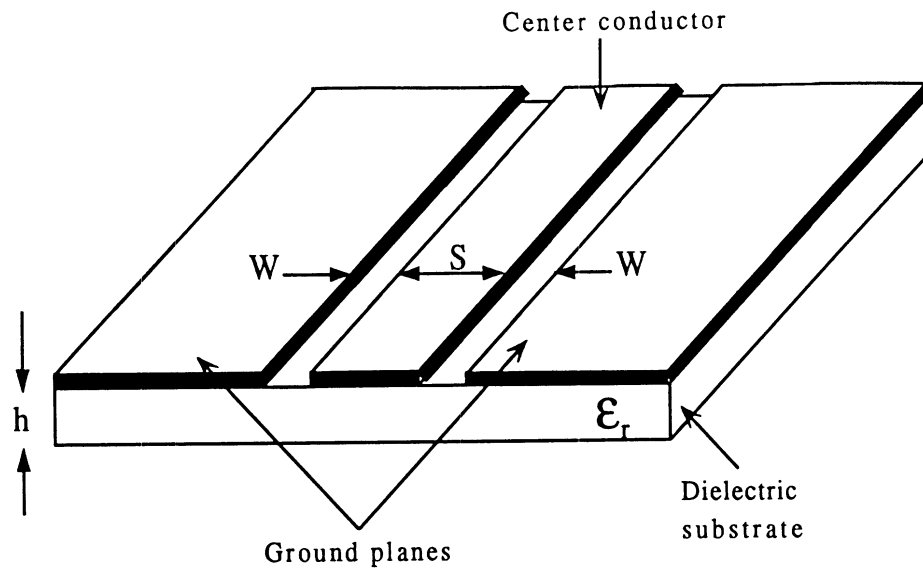
Figure 1.1: The generic view of a coplanar waveguide.

same plane, and therefore, there is no need for via holes which makes it easy to connect shunt or series lumped elements (active or passive). In addition, it makes it easier to wafer probe CPW microwave integrated circuits. Another important characteristic of coplanar waveguides is that the line impedance and phase velocity are less dependent on the substrate height than on the aspect ratio (slot width/center conductor width). Since the conducting surfaces of a CPW structure are all printed on the same interface, careful design could efficiently confine the fields to this interface. This characteristic is beneficial to both shielded and open CPW lines as it provides control over leakage and unwanted parasitic coupling. Printed lines which are not enclosed in a metallic package, such as the feed network of a monolithic antenna array, tend to radiate power in the form of space and surface waves. In microstrip lines, the level of parasitic radiation is strongly affected by the electric thickness of the substrate, which further complicates high frequency design due to little flexibility in choosing appropriate substrate structures. Since mechanical considerations put a

MAGNETIC WALL

(a) Coplanar mode

———— ELECTRIC FIELD LINES

————— MAGNETIC FIELD LINES

ELECTRIC WALL

(b) Coupled slotline mode

Figure 1.2: Coplanar and coupled slotline mode field configurations. (After Gupta [5])

lower limit on the physical thickness of integrated circuit substrates, it is difficult to avoid excessive loss in microstrip line, where the fields penetrate the whole substrate, when op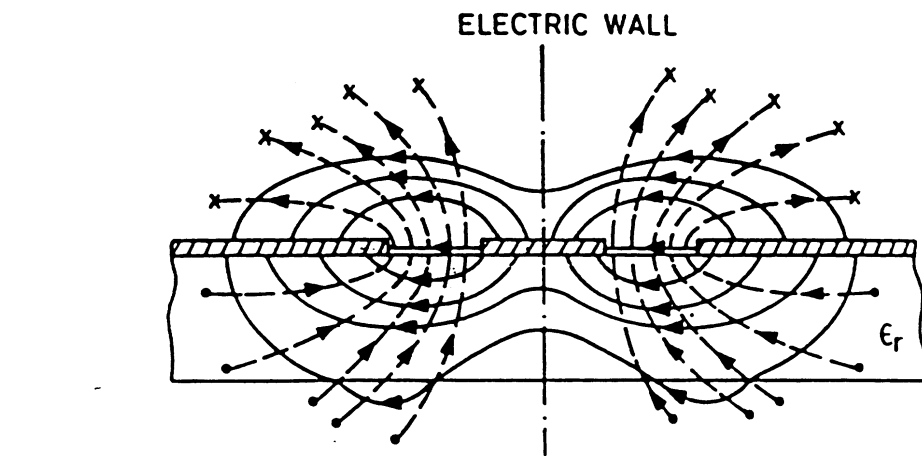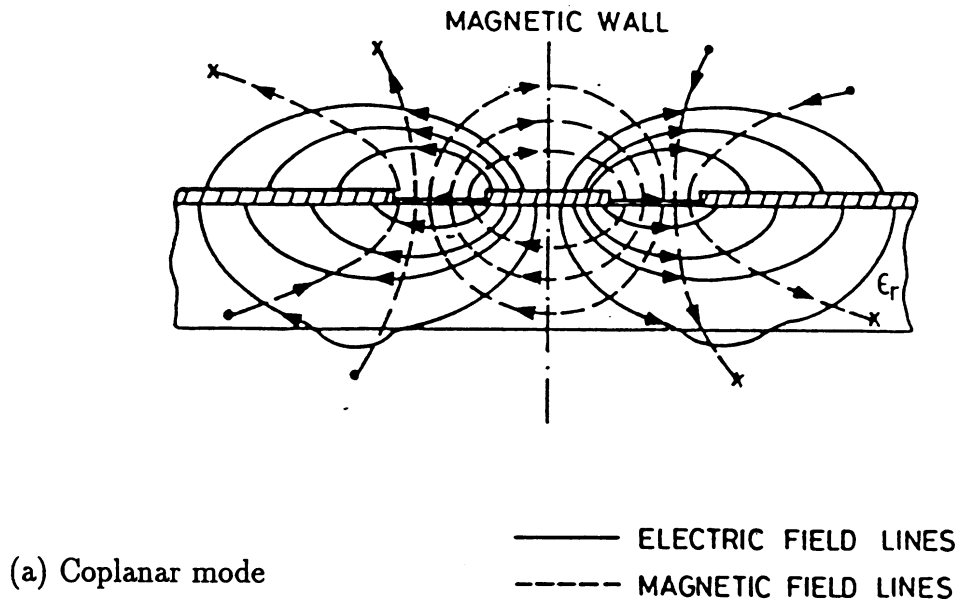erating above 100 GHz. In contrast, in coplanar waveguides the substrate thickness plays a less important role due to the fact that the fields are concentrated in the slots. Since the dimensions of the slots are limited only by photolithographic techniques, coplanar waveguides have more flexibility in design and therefore greater potential for low radiation loss and low dispersion at mm-wave frequencies.

However, even if coplanar waveguides radiate less than a microstrip operating at the same frequency, as this frequency enters the sub-mm-wave region the radiation loss increases complicating the design. As a result, further reduction of parasitic radiation is required. A way to achieve this and be able to extend the operation of a coplanar waveguide into the sub-mm-wave region is to generate a surface-wave-free environment. This is possible with the use of a matched dielectric lens which has been exploited effectively to excite aperture type radiating elements [12, 13]. One loss mechanism still pertaining in the CPW is conductor loss. Intuitively, conductor loss in CPW is expected to be higher than that found in microstrip line. However, it has been recently shown (using full-wave analyses) that CPW losses may be greater or less than microstrip losses depending on the choice of the slot and center conductor width [23, 24, 25].

1.2 Review

As mentioned earlier, the CPW was proposed in [1] to be used in gyromagnetic microwave device applications and conformal mapping was used to derive the quasi-TEM two dimensional parameters (ϵ_{eff} and Z_0) of a CPW printed on an infinite substrate. Since then, conformal mapping techniques have been used extensively

to obtain closed form expressions of these parameters which include the effects of finite substrate thickness, shielding walls and finite extent ground planes [26]-[35]. Alternatively, the quasi-TEM CPW properties were also obtained numerically using the point matching method [36, 37], the relaxation technique [38], the generalized transverse resonance method [39], and a hybrid approach that combines the finite-element method and the conformal mapping technique [40]. Since those quasi-TEM techniques cannot fully describe the CPW at high frequencies, full-wave analyses of CPW as a transmission medium have been developed throughout the years. A rigorous full-wave analysis of CPW (open and shielded) has been performed in [41]-[45] by using Galerkin's technique in the spectral domain. In addition, other techniques such as the singular integral equation approach [46], the network analytical method [47], the time domain finite difference method [48], and the method of lines [49] were employed to analyze coplanar lines.

Although the extent of applications of CPW circuits has been limited due to the unavailability of circuit elements and models, CPW has provided an attractive alternative to conventional microstrip lines since the early seventies [2, 3, 4, 5, 15, 22, 50]. One of the interesting early applications of CPW is its use as an energy coupler for medical applications [51]-[55]. Recently, driven by cost savings, process simplicity and the advantages it offers over other planar lines, the CPW has attracted a great deal of interest for RF circuit design [10, 11], [56]-[59]. In addition, it has been demonstrated that CPW is a very good candidate to be used in antennas and arrays [14], [60]-[63]. One problem in designing CPW circuits has been, and still is, the lack of CAD programs and reliable circuit models.

The first full-wave analysis of 3D CPW structures appeared in [64], where a Galerkin approach in conjunction with a spectral domain Green's function interpo-

lation technique was employed to characterize a shorted end CPW structure. Since then, the short and open-end CPW discontinuity problems have been studied extensively by others using the quasi-static finite difference (FD) approach [65], the integral equation technique (either in space or spectral domain) [23], [66]-[73], the TLM method [74], the transverse resonance technique [75, 76], and the full-wave finite difference frequency domain method [77]. A detailed description of the above techniques can be found in [78]. Other than these two simple discontinuities, the transverse resonance technique has been used to characterize the CPW step discontinuity problem [79, 80, 81] and the short-end-coupled CPW discontinuity [82]. Recently, more complex CPW discontinuities such as stubs, air-bridges, T-junction and bends have been analyzed using the integral equation approach [83]-[88], the finite difference time domain (FDTD) technique [89, 90, 91], the transmission line matrix method [92], and a hybrid approach [72], [93]-[97]. There have been also some attempts to characterize several CPW discontinuities experimentally [21, 59, 98, 99]. It can be seen from the above that there has been a great deal of interest in characterizing three dimensional (3D) CPW structures in the last five years. Methods used extend from the computationally intensive full wave FDTD method to quasi-static FD technique.

1.3 Overview

As indicated earlier, this dissertation presents a general method which can be implemented easily to theoretically characterize shielded coplanar waveguide discontinuities. This method is based on the Space Domain Integral Equation (SDIE) Approach and provides accuracy, computational efficiency and versatility in terms of the geometries it can solve. The SDIE approach as applied to the shielded CPW

discontinuity problem is presented in Chapter 2. In addition, the implementation of the method of moments to solve the magnetic field integral equation is described, and the dyadic Green's function appropriate to the CPW problem is derived.

One-port CPW discontinuities, namely: short and open-ends, are studied in Chapter 3. The technique to extract the reflection coefficient of such discontinuities is also described. In addition, the effect of mitering an open-end CPW on the reflection coefficient is investigated. The numerical results obtained using the SDIE technique are compared with published theoretical and/or experimental data.

Two-port CPW discontinuities which do not involve air-bridges are analyzed in Chapter 4. The discontinuities studied are coupled lines, series stubs and step discontinuities. The method to extract the scattering parameters of such two port structures is also presented. Extensive experiments were performed by Mr. G. Ponchak and Dr. R. Simons on some of these discontinuities and are included for comparison. The numerical results agree very well with experimental data.

Chapter 5 investigates two-port CPW discontinuities with air-bridges. A general technique to extract the scattering parameters of asymmetric structures is derived based on the Generalized Scattering Matrix (GSM) Approach. Again, extensive experiments were performed by Mr. G. Ponchak, the results of which are included for comparison. The GSM method is applied to CPW discontinuities in open environment where the radiation loss is also calculated.

In Chapter 6, a preliminary theoretical study of a new monolithic transmission line, the *microshield line*, is presented. The 2D parameters of the microshield line are obtained using two different methods, point matching and conformal mapping. Using the latter method, a closed form expression for the characteristic impedance of the line is derived. The results of the two methods are compared and found to

be in very close agreement. Several 3D microshield discontinuities are also studied and their response is compared to the corresponding ones in CPW. This has been done in cooperation with Dr. W. Harokopus. It is shown that the microshield line discontinuities tend to radiate much less than similar discontinuities in CPW lines. Moreover, the fabrication procedure of the microshield line is outlined in the chapter.

CHAPTER II

THEORETICAL METHODOLOGY

2.1 Introduction

This chapter presents a general method which can be implemented to theoretically characterize coplanar waveguide (CPW) discontinuities. This method is based on the Space Domain Integral Equation (SDIE) approach and provides accuracy, computational efficiency and versatility in terms of the geometries it can solve. Moreover, the SDIE technique is a full wave analysis that takes into account all the coupling mechanisms. In this approach, first, an integral equation for the unknown electric field distribution on the slot apertures is formulated in the space domain (section 2.3). Then, the dyadic Green's function pertinent to the problem under consideration is derived (section 2.4). Finally, the integral equation is solved numerically using the well known method of moments (MM) (section 2.5).

2.2 Assumptions

In the formulation, the following simplifying assumptions are made to reduce the complexity of the problem:

1. All metallized surfaces are of zero thickness and infinite conductivity.

2. Dielectric layers are isotropic, homogeneous and nonmagnetic.

3. The dielectric and conductor losses are zero. However, the analysis can be easily extended to take dielectric losses into consideration.

4. The time dependence is of the form $e^{j\omega t}$ which will be suppressed throughout the analysis.

2.3 Integral Equation

Figure 2.1 shows an open-end coplanar waveguide inside a rectangular cavity filled with several dielectric layers. Using transmission line theory, the original multilayer problem is reduced to a two layer one as shown in Figure 2.2. In this problem, the fields in the two regions (1) and (2), directly above and below the slots, are to be derived. The nature of the impedance boundary sides shown in Figure 2.2 will be discussed later in section 2.4. Then, using the equivalence principle [100], equivalent magnetic current densities $\vec{M}^{(1)}$ and $\vec{M}^{(2)}$ are introduced on the slot aperture, as shown in Figure 2.2, which are defined as:

$$\vec{M}^{(1)} = \vec{E}^{(1)} \times \hat{a}_x \tag{2.1}$$

$$\vec{M}^{(2)} = \vec{E}^{(2)} \times (-\hat{a}_x) \tag{2.2}$$

These surface magnetic currents radiate electromagnetic fields in the two waveguide regions (above and below the slots) so that the continuity of the tangential magnetic field on the surface of the slots is satisfied:

$$\hat{a}_x \times (\vec{H}^{(1)} - \vec{H}^{(2)}) = \vec{J}_s \tag{2.3}$$

where $\vec{J}_s$ vanishes everywhere on the plane of the slot apertures except at the position of the electric current sources exciting the CPW. The magnetic fields $\vec{H}^{(1)}$ and $\vec{H}^{(2)}$ can be expressed in terms of the equivalent magnetic current densities $\vec{M}^{(1)}$ and $\vec{M}^{(2)}$
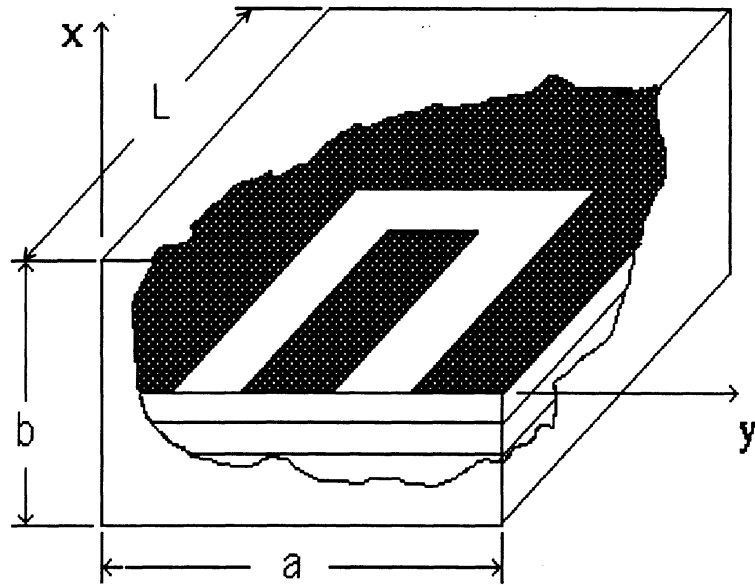
Figure 2.1: A typical one-port CPW discontinuity inside a cavity filled with several dielectric layers.
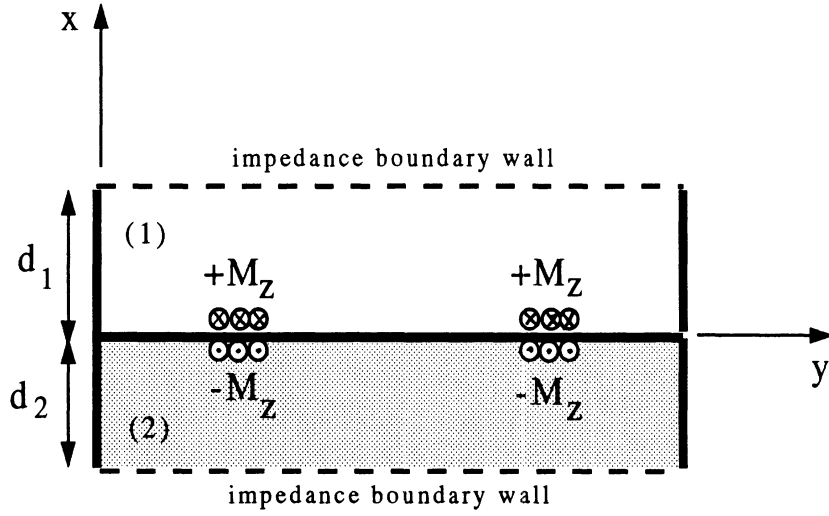
Figure 2.2: An equivalent two-layer problem is obtained after the application of transmission line theory and the equivalence principle. The z-component of the equivalent magnetic current is shown here only.

as follows [100]:

$$\vec{H}^{(1)} = \int_{S'} \int \bar{\bar{G}}_h^{(1)}(\vec{r}/\vec{r'}) \cdot \vec{M}^{(1)}(\vec{r'}) ds' \tag{2.4}$$

$$\vec{H}^{(2)} = \int_{S'} \int \bar{\bar{G}}_h^{(2)}(\vec{r}/\vec{r'}) \cdot \vec{M}^{(2)}(\vec{r'}) ds' \tag{2.5}$$

In the above equation, S' is the surface of the slot apertures, $\bar{\bar{G}}_h^{(1),(2)}$ are the dyadic Green's functions in the two waveguide regions which will be derived in the next section.

The remaining boundary condition to be applied is continuity of the tangential electric field on the surface of the slot apertures which leads to the following:

$$\vec{M}^{(1)} = -\vec{M}^{(2)} = \vec{M}_s \tag{2.6}$$

In view of (2.4), (2.5) and (2.6), equation (2.3) takes the form:

$$\hat{a}_x \times \int_{S'} \int [\bar{\bar{G}}_h^{(1)} + \bar{\bar{G}}_h^{(2)}] \cdot \vec{M}_s(\vec{r'}) \ ds' = \vec{J}_s \tag{2.7}$$

The above integral equation can be written as follows:

$$\int_{S'} \int M_y(G_{yy}^{(1)} + G_{yy}^{(2)}) + M_z(G_{yz}^{(1)} + G_{yz}^{(2)})ds' = J_z \qquad (2.8)$$

$$\int_{S'} \int M_y(G_{zy}^{(1)} + G_{zy}^{(2)}) + M_z(G_{zz}^{(1)} + G_{zz}^{(2)})ds' = J_y \qquad (2.9)$$

where the subscript h is suppressed for simplicity. In the above, $G_{ij}^{(k)}$ denotes the magnetic field $H_i^{(k)}$ at $x = 0$ due to an infinitesimal magnetic source M_j at $x' = 0$ with $i, j = y, z$ and $k = 1, 2$.

2.4 Derivation of the Green's Function

In this section, the dyadic Green's function pertinent to the CPW discontinuity problem will be derived. As pointed above, using the equivalence principle, the problem is divided into the four sub-problems shown in Figure 2.3. In these sub-problems, the fields due to infinitesimal magnetic dipoles inside rectangular cavities with one impedance boundary side should be derived. Only the main steps of the derivation of the fields in region (1) due to both y and z-directed magnetic dipoles (Figures 2.3(a) and 2.3(b)) will be presented here.

Figure 2.4 shows the sub-problem of Figure 2.3(a) with the z-directed magnetic dipole alleviated from the bottom wall of the cavity in order to simplify the application of the boundary conditions. The magnetic dipole can be expressed mathematically as:

$$\vec{M} = \hat{a}_z \delta(x - x')\delta(y - y')\delta(z - z') \qquad (2.10)$$

In Figure 2.4, regions I and II should not be confused with regions (1) and (2) shown in figure 2.2. In fact, both regions I and II constitute the dielectric layer directly above the slot aperture, i.e. region (1). Notice also that at the end of the analysis x' will be substituted by zero.
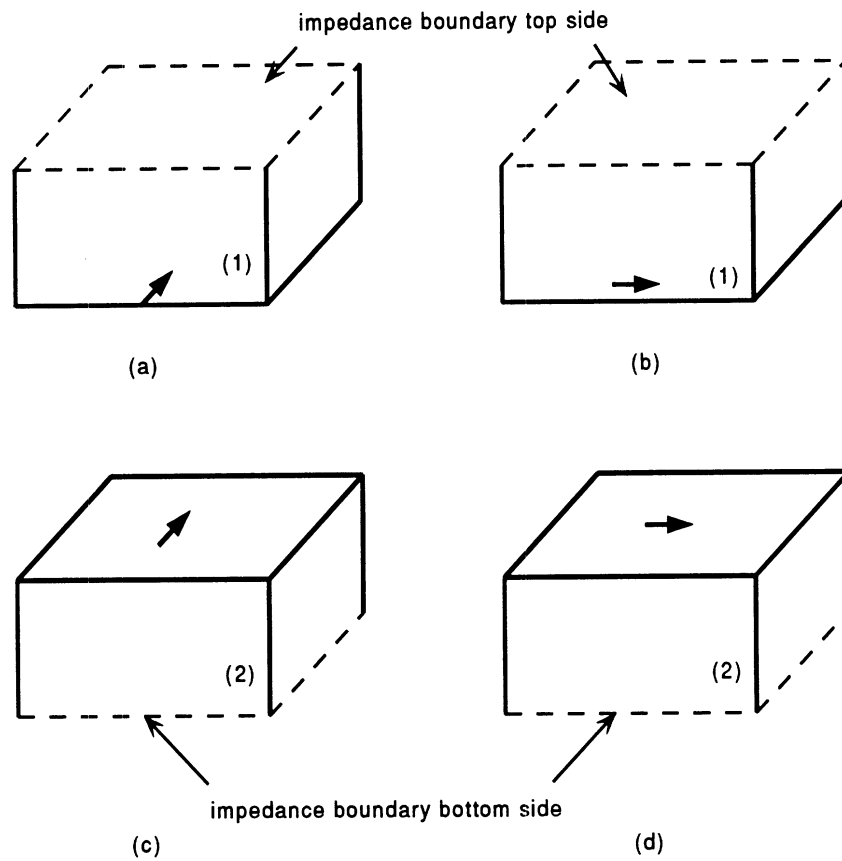
Figure 2.3: The structures used to derive the components of the dyadic Green's function. All the sides excluding the impedance boundaries are perfect conductors. The magnetic dipoles are placed at $(0,y',z')$.
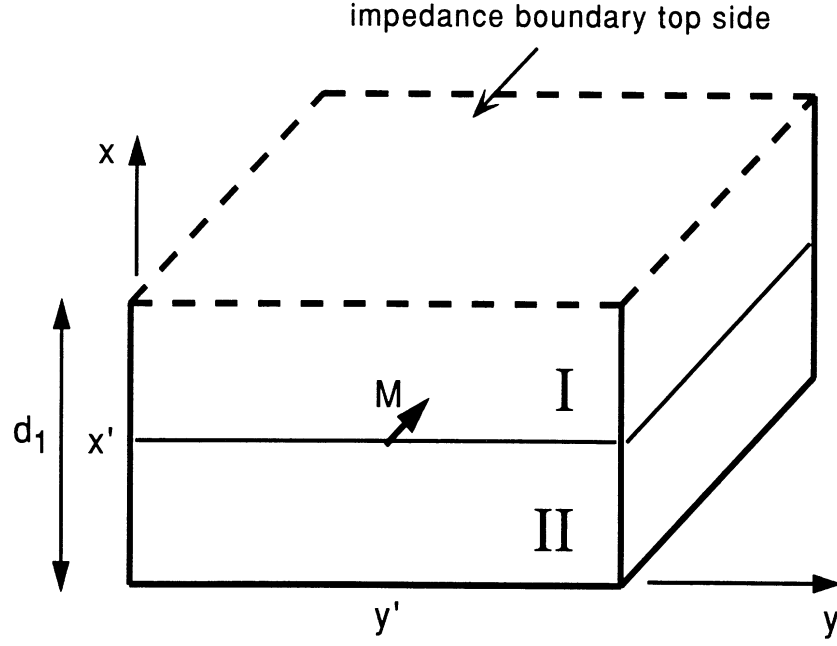
Figure 2.4: A z-directed magnetic dipole inside a cavity with an impedance boundary top side. The magnetic dipole is placed at (x',y',z').

The fields in regions I and II satisfy Maxwell's equations in the form:

$$\vec{\nabla} \times \vec{E} = -j\omega\mu\vec{H} \tag{2.11}$$

$$\vec{\nabla} \times \vec{H} = j\omega\epsilon\vec{E} \tag{2.12}$$

$$\vec{\nabla} \cdot \vec{H} = 0 \tag{2.13}$$

$$\vec{\nabla} \cdot \vec{E} = 0 \tag{2.14}$$

Due to the vanishing divergence of $\vec{E}$ and $\vec{H}$, the fields can be expressed in terms of a magnetic vector potential $\vec{A}$ and an electric vector potential $\vec{F}$ as follows [100, 101]:

$$\vec{E} = -\frac{1}{\epsilon}\vec{\nabla} \times \vec{F} + \frac{1}{j\omega\mu\epsilon}\vec{\nabla} \times \vec{\nabla} \times \vec{A} \tag{2.15}$$

$$\vec{H} = \frac{1}{\mu}\vec{\nabla} \times \vec{A} + \frac{1}{j\omega\mu\epsilon}\vec{\nabla} \times \vec{\nabla} \times \vec{F} \tag{2.16}$$

Since regions I and II are homogeneous source-free ones, the fields can be expressed

as the sum of LSE (TE$_x$) and LSM (TM$_x$) modes [100, 101]. Thus, choosing

$$\vec{A} = 0 \tag{2.17}$$

$$\vec{F} = \hat{a}_x \phi \tag{2.18}$$

and

$$\vec{F} = 0 \tag{2.19}$$

$$\vec{A} = \hat{a}_x \psi \tag{2.20}$$

uniquely characterize the LSE and LSM fields, respectively. In the above, ψ and ϕ are the scalar potentials which should satisfy the homogeneous wave equation (Helmholtz equation) in both regions I and II:

$$\nabla^2 \phi + k_1^2 \phi = 0 \tag{2.21}$$

$$\nabla^2 \psi + k_1^2 \psi = 0 \tag{2.22}$$

where $k_1^2 = \omega^2 \mu_0 \epsilon_0 \epsilon_{r1}$.

Using (2.15) and (2.16), the field components can be expressed in terms of the scalar potentials as follows [100]:

$$E_x = \frac{1}{j\omega\mu\epsilon} \left[-\frac{\partial^2 \psi}{\partial y^2} - \frac{\partial^2 \psi}{\partial z^2} \right] \tag{2.23}$$

$$E_y = \frac{1}{j\omega\mu\epsilon} \frac{\partial^2 \psi}{\partial x \partial y} - \frac{1}{\epsilon} \frac{\partial \phi}{\partial z} \tag{2.24}$$

$$E_z = \frac{1}{j\omega\mu\epsilon} \frac{\partial^2 \psi}{\partial x \partial z} + \frac{1}{\epsilon} \frac{\partial \phi}{\partial y} \tag{2.25}$$

$$H_x = \frac{1}{j\omega\mu\epsilon} \left[-\frac{\partial^2 \phi}{\partial y^2} - \frac{\partial^2 \phi}{\partial z^2} \right] \tag{2.26}$$

$$H_y = \frac{1}{\mu} \frac{\partial \psi}{\partial z} + \frac{1}{j\omega\mu\epsilon} \frac{\partial^2 \phi}{\partial x \partial y} \tag{2.27}$$

$$H_z = -\frac{1}{\mu} \frac{\partial \psi}{\partial y} + \frac{1}{j\omega\mu\epsilon} \frac{\partial^2 \phi}{\partial x \partial z} \tag{2.28}$$

Using the method of separation of variables [101] to solve (2.21) and (2.22), and enforcing the boundary conditions on the perfectly conducting walls of the cavity, the following expressions for the scalar potentials can be obtained:

$$
\begin{aligned}
\phi^I \;=\; & \sum_{m=0}^{\infty} \sum_{n=0}^{\infty} \{A_{mn} \sin(k_{x_1}(x - d_1)) \\
& + \; B_{mn} \cos(k_{x_1}(x - d_1))\} \cos(k_y y) \cos(k_z z)
\end{aligned}
\tag{2.29}
$$

$$
\phi^{II} \;=\; \sum_{m=0}^{\infty} \sum_{n=0}^{\infty} C_{mn} \sin(k_{x_1} x) \cos(k_y y) \cos(k_z z)
\tag{2.30}
$$

$$
\begin{aligned}
\psi^I \;=\; & \sum_{m=0}^{\infty} \sum_{n=0}^{\infty} \{K_{mn} \sin(k_{x_1}(x - d_1)) \\
& + \; N_{mn} \cos(k_{x_1}(x - d_1))\} \sin(k_y y) \sin(k_z z)
\end{aligned}
\tag{2.31}
$$

$$
\psi^{II} \;=\; \sum_{m=0}^{\infty} \sum_{n=0}^{\infty} D_{mn} \cos(k_{x_1} x) \sin(k_y y) \sin(k_z z)
\tag{2.32}
$$

In the above,

$$
k_y \;=\; \frac{m\pi}{a}
\tag{2.33}
$$

$$
k_z \;=\; \frac{n\pi}{L}
\tag{2.34}
$$

$$
k_1^2 \;=\; \omega^2 \mu_0 \epsilon_0 \epsilon_{r1} = k_{x_1}^2 + k_y^2 + k_z^2
\tag{2.35}
$$

where a and L are the width and length of the cavity, respectively.

The next step is to solve for the constants A_{mn}, B_{mn}, C_{mn}, D_{mn}, K_{mn} and N_{mn}. This can be accomplished by applying the following six boundary conditions at the interface between regions I and II:

$$
E_z^I \;=\; E_z^{II} \quad \text{at} \quad x = x'
\tag{2.36}
$$

$$
H_y^I \;=\; H_y^{II} \quad \text{at} \quad x = x'
\tag{2.37}
$$

$$
H_z^I \;=\; H_z^{II} \quad \text{at} \quad x = x'
\tag{2.38}
$$

$$
\left(\frac{E_y^I}{H_z^I}\right)^{LSE} \;=\; Z_1^{LSE} \quad \text{at} \quad x = d_1
\tag{2.39}
$$

$$
\left(\frac{E_y^I}{H_z^I}\right)^{LSM} \;=\; Z_1^{LSM} \quad \text{at} \quad x = d_1
\tag{2.40}
$$

$$E_y^{II} - E_y^I = \delta(x - x')\delta(y - y')\delta z - z') \tag{2.41}$$

In (2.39) and (2.40), Z_1^{LSE} and Z_1^{LSM} are the LSE and LSM input impedances seen at $x = d_1$ which can be computed using transmission line theory [102, 103]. That is, each dielectric layer is replaced by a section of an ideal transmission line with a characteristic impedance Z_0^{LSE} or Z_0^{LSM} and an eigenvalue k_{xi} where

$$k_{x_i}^2 + k_y^2 + k_z^2 = \omega^2 \mu_0 \epsilon_0 \epsilon_{r_i} \tag{2.42}$$

$$(Z_0^{LSE})^i = \frac{\omega \mu_0}{k_{x_i}} \tag{2.43}$$

$$(Z_0^{LSM})^i = \frac{k_{x_i}}{\omega \epsilon_0 \epsilon_{r_i}} \tag{2.44}$$

It should be noted that (2.39) and (2.40) should be satisfied for each LSE and LSM mode, respectively. In addition, (2.41) signifies the discontinuity in the y-component of the electric field due to the magnetic dipole. Finally, expressions for the six unknowns are derived from (2.36)-(2.41), and consequently the fields can be obtained using (2.23)-(2.28).

In the same manner, the fields in region (1) due to a y-directed magnetic dipole can be derived (see Figure 2.5). In this case, the magnetic current source can be expressed as:

$$\vec{M} = \hat{a}_y \delta(x - x')\delta(y - y')\delta(z - z') \tag{2.45}$$

Equations (2.29)-(2.40) are still applicable to the structure of Figure 2.5. Moreover, the following boundary condition holds:

$$E_z^I - E_z^{II} = \delta(x - x')\delta(y - y')\delta(z - z') \tag{2.46}$$

After lengthy straightforward manipulations, the components of the dyadic Green's function in (2.8) and (2.9) are found to be given by:

$$G_{yy}^{(1)}(\bar{r}/\bar{r'}) = \sum_{m=0}^{\infty} \sum_{n=0}^{\infty} \frac{2e_n}{aL} \frac{1}{k_{x_1}^2 - k_1^2} \left[k_y^2 P_1 + k_z^2 Q_1 \right]$$
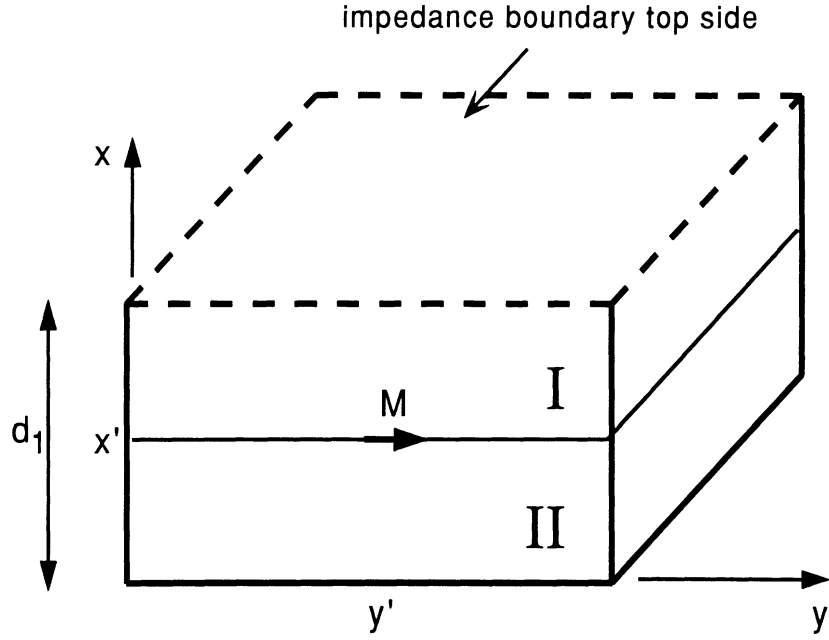
Figure 2.5: A y-directed magnetic dipole inside a cavity with an impedance boundary top side. The magnetic dipole is placed at (x',y',z').

$$\sin(k_y y') \cos(k_z z') \sin(k_y y) \cos(k_z z) \tag{2.47}$$

$$G_{zy}^{(1)}(\bar{r}/\bar{r}') = \sum_{m=0}^{\infty} \sum_{n=0}^{\infty} \frac{2e_n}{aL} \frac{k_y k_z}{k_{x_1}^2 - k_1^2} [P_1 - Q_1]$$

$$\sin(k_y y') \cos(k_z z') \cos(k_y y) \sin(k_z z) \tag{2.48}$$

$$G_{yz}^{(1)}(\bar{r}/\bar{r}') = \sum_{m=0}^{\infty} \sum_{n=0}^{\infty} \frac{2e_m}{aL} \frac{k_y k_z}{k_{x_1}^2 - k_1^2} [P_1 - Q_1]$$

$$\cos(k_y y') \sin(k_z z') \sin(k_y y) \cos(k_z z) \tag{2.49}$$

$$G_{zz}^{(1)}(\bar{r}/\bar{r}') = \sum_{m=0}^{\infty} \sum_{n=0}^{\infty} \frac{2e_m}{aL} \frac{1}{k_{x_1}^2 - k_1^2} \left[k_z^2 P_1 + k_y^2 Q_1 \right]$$

$$\cos(k_y y') \sin(k_z z') \cos(k_y y) \sin(k_z z) \tag{2.50}$$

where

$$P_1 = \left(\frac{k_{x_1}}{\omega \mu_0} \right) \frac{\omega \mu_0 + j k_{x_1} Z_1^{LSE} \tan(k_{x_1} d_1)}{k_{x_1} Z_1^{LSE} + j \omega \mu_0 \tan(k_{x_1} d_1)} \tag{2.51}$$

$$Q_1 = \left(\frac{\omega \epsilon_1}{k_{x_1}} \right) \frac{k_{x_1} + j \omega \epsilon_1 Z_1^{LSM} \tan(k_{x_1} d_1)}{\omega \epsilon_1 Z_1^{LSM} + j k_{x_1} \tan(k_{x_1} d_1)} \tag{2.52}$$

$$e_n = \begin{cases} 1 & n = 0 \\ 2 & n \neq 0 \end{cases} \tag{2.53}$$

$$e_m = \begin{cases} 1 & m = 0 \\ 2 & m \neq 0 \end{cases} \tag{2.54}$$

It should be noted that the frequencies at which the denominator of P_1 is zero correspond to the LSE resonating modes inside the upper cavity, while, those at which the denominator of Q_1 is zero correspond to the LSM resonating modes.

The components of $\bar{\bar{G}}_h^{(2)}$ are essentially the same as (2.47)-(2.54) with the following changes:

$$
\begin{aligned}
Z_1^{LSE} &\longrightarrow Z_2^{LSE} \\
Z_1^{LSM} &\longrightarrow Z_2^{LSM} \\
d_1 &\longrightarrow d_2 \\
k_{x1} &\longrightarrow k_{x2} \\
k_1 &\longrightarrow k_2 \\
\epsilon_{r_1} &\longrightarrow \epsilon_{r_2}
\end{aligned}
\tag{2.55}
$$

where d_2 is the thickness of the layer directly below the slot apertures, i.e. region (2), and Z_2^{LSE} and Z_2^{LSM} are the LSE and LSM input impedances seen at the interface $x = -d_2$.

In summary, the dyadic Green's function pertinent for the shielded CPW discontinuity problem has been derived in this section. This was accomplished by replacing the equivalent magnetic current density in the slot apertures by Dirac delta sources and deriving the fields due to these sources.

2.5 Application of the Method of Moments

The method of moments [104] is a numerical technique used for solving functional

equations for which closed form solutions cannot be obtained. By reducing the func-

tional relation to a matrix equation, known methods can be used to solve for the

unknown current distribution. The general steps involved in the moment method for

the computation of surface currents can be summarized as follows:

1. The integral equation for the electric or magnetic field in terms of the unknown

   surface electric and/or magnetic currents is formulated. The resulting functional

   equation can be put in the form

$$L_{op}\binom{\vec{J_s}}{\vec{M_s}} = \vec{g}\binom{\vec{E}}{\vec{H}} \qquad (2.56)$$

   where L_{op} is an integral operator on $\vec{J_s}$ and/or $\vec{M_s}$, and $\vec{g}$ is a vector function

   of either $\vec{E}$ and/or $\vec{H}$.

2. The unknown currents are expanded in terms of known basis functions as follows

$$\vec{J_s} = \sum_{i=1}^{N_1} a_i \vec{J_i} \qquad (2.57)$$

$$\vec{M_s} = \sum_{j=1}^{N_2} b_j \vec{M_j} \qquad (2.58)$$

   where the a_i's and b_j's are complex coefficients and N_1 and N_2 are the number

   of basis functions for $\vec{J_s}$ and $\vec{M_s}$ respectively.

3. A suitable inner product is defined and a set of test (or weighting) functions Ψ

   is chosen. If (2.57) and (2.58) are substituted in (2.56) and the inner products

   with the weighting functions are performed, the results may be expressed as

$$\sum_{i=1}^{N_1} a_i < \vec{\Psi}_q, L_{op}(\vec{J_i}) > + \sum_{j=1}^{N_2} b_j < \vec{\Psi}_q, L_{op}(\vec{M_j}) > = < \vec{W}_q, \vec{g} > \qquad (2.59)$$

where the inner product is defined as

$$< \vec{f_1}, \vec{f_2} > = \int_S \int \vec{f_1} \cdot \vec{f_2} \; ds \qquad (2.60)$$

In Galerkin's procedure, which will be adopted here, the test functions are chosen to be the same as the basis functions.

4. A matrix equation is formed after the integrals (2.60) are computed. This matrix equation can then be solved for the unknown current amplitudes a_i and b_j using standard mathematical techniques such as Gaussian elimination or LU decomposition and back substitution. One can notice that the method is computationally intensive, but with the advent of faster computers the moment method has become feasible.

In our problem, equation (2.7) represents a Fredholm integral equation of the first kind which maps the surface magnetic current (electric field) into a magnetic field on the interface. Applying the second step of the method of moments, the aperture of the CPW slots is divided into rectangles (Figure 2.6) and the unknown magnetic current density is expressed in the form of a finite double summation as follows [105]-[108]:

$$\vec{M_s}(\vec{r'}) = \hat{a}_y \sum_{i=1}^{N_y} \sum_{j=1}^{N_z+1} V_{y,ij} \, f_i(y') \, g_j(z') + \hat{a}_z \sum_{k=1}^{N_z} \sum_{l=1}^{N_y+1} V_{z,kl} \, f_k(z') \, g_l(y') \qquad (2.61)$$

where $V_{y,ij}$ and $V_{z,kl}$ are the unknown amplitudes of the y and z components of the magnetic current density.

The subdomain basis functions for each current component are assumed to have piecewise sinusoidal variation along the longitudinal direction and constant variation along the transverse direction as shown in Figure 2.6 [109, 110]. Note that there is an offset between the y and z directed magnetic currents in order to assure edge
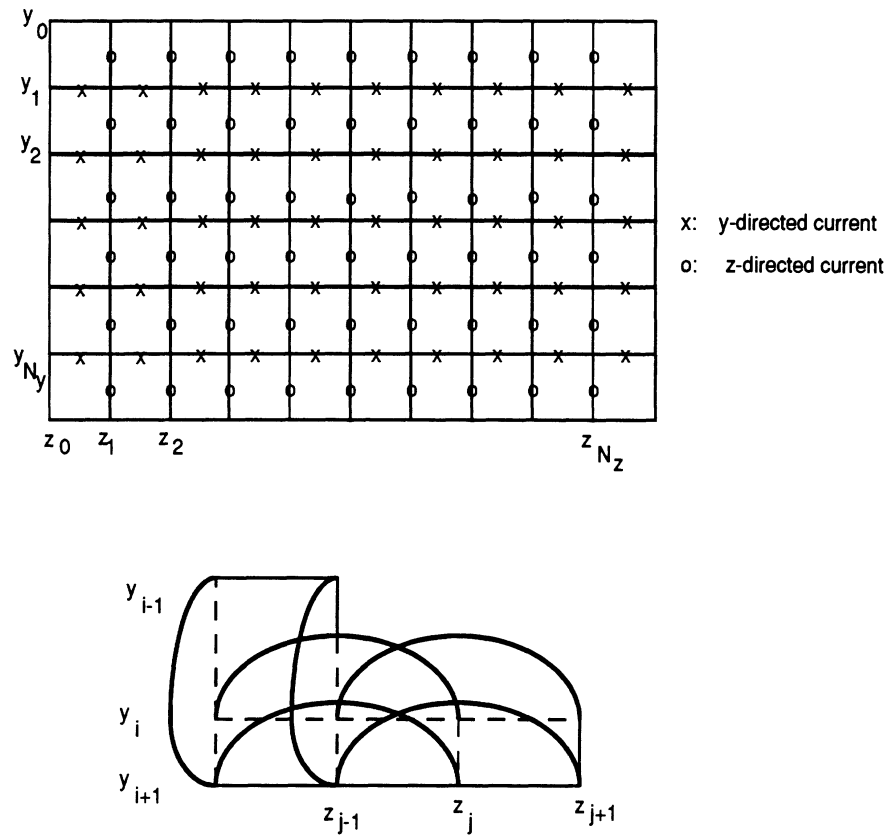
Figure 2.6: The discretization used in the expansion of the equivalent magnetic current in the slot aperture. Notice the overlapping piecewise sinusoidal basis functions for the y and z components of the magnetic surface current.

conditions [108]. In addition, it has been found numerically that such a scheme enhances the convergence behavior of the scattering parameters of the discontinuity under consideration with respect to the number of basis functions. The basis functions are given by the following expressions:

$$
f_i(y') = \begin{cases} \frac{\sin[k_s(y'-y_{i-1})]}{\sin(k_s\ell_{y_i})} & y_{i-1} \leq y' \leq y_i \\ \frac{\sin[k_s(y_{i+1}-y')]}{\sin(k_s\ell_{y_{i+1}})} & y_i \leq y' \leq y_{i+1} \\ 0 & elsewhere \end{cases} \tag{2.62}
$$

$$
g_j(z') = \begin{cases} 1 & z_{j-1} \leq z' \leq z_j \\ 0 & elsewhere \end{cases} \tag{2.63}
$$

where $\ell_{y_i} = y_i - y_{i-1}$ and k_s a scaling parameter chosen to be the wavenumber in the highest permittivity dielectric layer [111]. The functions $f_k(z')$ and $g_l(y')$ are given by equations similar to (2.62) and (2.63) with y, y', z and z' replaced by z, z', y and y' respectively.

Using (2.61), (2.7) can be written in the form:

$$
\begin{aligned}
\vec{J}_s + \Delta\vec{J}_s &= \hat{a}_x \times \left\{ \sum_{i=1}^{N_y} \sum_{j=1}^{N_z+1} V_{y,ij} \int_{S'} \int [\bar{\bar{G}}_h^{(1)} + \bar{\bar{G}}_h^{(2)}] \cdot \hat{a}_y\, f_i(y')\, g_j(z')\, ds' \right. \\
&\quad \left. + \sum_{k=1}^{N_z} \sum_{l=1}^{N_y+1} V_{z,kl} \int_{S'} \int [\bar{\bar{G}}_h^{(1)} + \bar{\bar{G}}_h^{(2)}] \cdot \hat{a}_z\, f_k(z')\, g_l(y')\, ds' \right\}
\end{aligned} \tag{2.64}
$$

where $\Delta\vec{J}_s$ represents the error introduced due to the approximations made in the magnetic current distribution.

Finally, Galerkin's procedure is used to minimize the error $\Delta\vec{J}_s$ resulting in the following inner products:

$$
\int \int (\hat{a}_x \times \Delta\vec{J}_s) \cdot \hat{a}_y\, f_o(y)\, g_p(z)\, ds = 0 \tag{2.65}
$$

$$
o = 1,\ldots,N_y \ ; \ p = 1,\ldots,N_z+1
$$

$$\int \int (\hat{a}_x \times \Delta \vec{J}_s) \cdot \hat{a}_z \, f_q(z) \, g_r(y) \, ds \; = \; 0 \qquad\qquad (2.66)$$

$$q = 1, \ldots, N_z \; ; \; r = 1, \ldots, N_y + 1$$

where $f_o(y)$, $g_p(z)$, $f_q(z)$ and $g_r(y)$ are weighting functions identical to the basis functions. In this manner, (2.64) reduces into the matrix equation of the form:

$$\begin{pmatrix} [Y_{yy}] & [Y_{yz}] \\ [Y_{zy}] & [Y_{zz}] \end{pmatrix} \begin{pmatrix} V_y \\ V_z \end{pmatrix} = \begin{pmatrix} I_z \\ I_y \end{pmatrix} \qquad\qquad (2.67)$$

In the above, V_y and V_z are the subvectors of the unknown coefficients for the y and z components of the magnetic current distribution respectively and I_y and I_z are the known excitation subvectors which are dependent on the impressed feed model. $[Y_{\zeta\xi}] \, (\zeta, \xi = y, z)$ represent blocks of the admittance matrix the elements of which are expressed in terms of multiple space integrals, involving trigonometric functions, as follows:

$$Y_{yy}(i,j/o,p) \; = \; \int \int \int \int \hat{a}_y \, f_o(y) \, g_p(z) \cdot \left[G_{yy}^{(1)} + G_{yy}^{(2)} \right] \cdot \hat{a}_y \, f_i(y') \, g_j(z') \, dy' \, dz' \, dy \, dz$$

$$(2.68)$$

$$Y_{yz}(k,l/o,p) \; = \; \int \int \int \int \hat{a}_y \, f_o(y) \, g_p(z) \cdot \left[G_{yz}^{(1)} + G_{yz}^{(2)} \right] \cdot \hat{a}_z \, f_k(z') \, g_l(y') \, dy' \, dz' \, dy \, dz$$

$$(2.69)$$

$$Y_{zy}(i,j/q,r) \; = \; \int \int \int \int \hat{a}_z \, f_q(z) \, g_r(y) \cdot \left[G_{zy}^{(1)} + G_{zy}^{(2)} \right] \cdot \hat{a}_y \, f_i(y') \, g_j(z') \, dy' \, dz' \, dy \, dz$$

$$(2.70)$$

$$Y_{zz}(k,l/q,r) \; = \; \int \int \int \int \hat{a}_z \, f_q(z) \, g_r(y) \cdot \left[G_{zz}^{(1)} + G_{zz}^{(2)} \right] \cdot \hat{a}_z \, f_k(z') \, g_l(y') \, dy' \, dz' \, dy \, dz$$

$$(2.71)$$

where i, j, k, l, o, p, q and r are as defined before.

2.5.1 Admittance Matrix

Equations (2.68)-(2.71) can be evaluated analytically resulting in the following expressions for the elements of the admittance matrix:

$$Y_{yy}(i,j/o,p) = \sum_{m=0}^{\infty} \sum_{n=0}^{\infty} \frac{2e_n}{aL} \left(\frac{k_y^2 P_1 + k_z^2 Q_1}{k_{x_1}^2 - k_1^2} + \frac{k_y^2 P_2 + k_z^2 Q_2}{k_{x_2}^2 - k_2^2} \right)$$
$$R_y(y_i) R_y(y_o) T_z(z_j) T_z(z_p) \tag{2.72}$$

$$Y_{yz}(k,l/o,p) = \sum_{m=1}^{\infty} \sum_{n=1}^{\infty} \frac{4}{aL} k_y k_z \left(\frac{P_1 - Q_1}{k_{x_1}^2 - k_1^2} + \frac{P_2 - Q_2}{k_{x_2}^2 - k_2^2} \right)$$
$$R_y(y_o) R_z(z_k) T_z(z_p) T_y(y_l) \tag{2.73}$$

$$Y_{zy}(i,j/q,r) = \sum_{m=1}^{\infty} \sum_{n=1}^{\infty} \frac{4}{aL} k_y k_z \left(\frac{P_1 - Q_1}{k_{x_1}^2 - k_1^2} + \frac{P_2 - Q_2}{k_{x_2}^2 - k_2^2} \right)$$
$$R_y(y_i) R_z(z_q) T_z(z_j) T_y(y_r) \tag{2.74}$$

$$Y_{zz}(k,l/q,r) = \sum_{m=0}^{\infty} \sum_{n=0}^{\infty} \frac{2e_m}{aL} \left(\frac{k_z^2 P_1 + k_y^2 Q_1}{k_{x_1}^2 - k_1^2} + \frac{k_z^2 P_2 + k_y^2 Q_2}{k_{x_2}^2 - k_2^2} \right)$$
$$R_z(z_k) R_z(z_q) T_y(y_l) T_y(y_r) \tag{2.75}$$

where

$$R_y(y_i) = \frac{k_s}{k_y^2 - k_s^2} \frac{1}{\sin(k_s l_{y_i}) \sin(k_s l_{y_{i+1}})} \left\{ \sin(k_y y_i) \sin\left(k_s (l_{y_i} + l_{y_{i+1}}) \right) \right.$$
$$\left. - \sin(k_y y_{i+1}) \sin(k_s l_{y_i}) - \sin(k_y y_{i-1}) \sin(k_s l_{y_{i+1}}) \right\} \tag{2.76}$$

$$R_z(z_i) = \frac{k_s}{k_z^2 - k_s^2} \frac{1}{\sin(k_s l_{z_i}) \sin(k_s l_{z_{i+1}})} \left\{ \sin(k_z z_i) \sin\left(k_s (l_{z_i} + l_{z_{i+1}}) \right) \right.$$
$$\left. - \sin(k_z z_{i+1}) \sin(k_s l_{z_i}) - \sin(k_z z_{i-1}) \sin(k_s l_{z_{i+1}}) \right\} \tag{2.77}$$

$$T_z(z_i) = \frac{1}{k_z} \left(\sin(k_z z_i) - \sin(k_z z_{i-1}) \right) \tag{2.78}$$

$$T_y(y_i) = \frac{1}{k_y} \left(\sin(k_y y_i) - \sin(k_y y_{i-1}) \right) \tag{2.79}$$

and P_i and Q_i (i=1, 2) are as in (2.51) and (2.52).

For a symmetric basis function (i.e. $l_{y_i} = l_{y_{i+1}} = l_y$ or $l_{z_i} = l_{z_{i+1}} = l_z$), (2.76) and (2.77) reduce to the following expressions:

$$R_y(y_i) = \frac{k_s}{k_y^2 - k_s^2} \frac{4 \sin(k_y y_i)}{\sin(k_s l_y)} \sin\left(\frac{(k_s + k_y) l_y}{2} \right) \sin\left(\frac{(k_y - k_s) l_y}{2} \right) \tag{2.80}$$

$$R_z(z_i) = \frac{k_s}{k_z^2 - k_s^2} \frac{4\sin(k_z z_i)}{\sin(k_s l_z)} \sin\left(\frac{(k_s + k_z)l_z}{2}\right) \sin\left(\frac{(k_z - k_s)l_z}{2}\right) \quad (2.81)$$

2.5.2 Excitation Vector

The elements of the excitation vector are given by

$$I_z(o,p) = \int\int J_z(y,z) f_o(y) g_p(z) \, dy \, dz \quad (2.82)$$

$$I_y(q,r) = -\int\int J_y(y,z) f_q(z) g_r(y) \, dy \, dz \quad (2.83)$$

In this research, the excitation is modeled by ideal current sources which are localized at specific node points [69, 84]. For example, the coaxial and slotline excitations shown in Figure 2.7 are modeled by two ideal current sources which are 180° out of phase and in phase, respectively. In this case, $\vec{J_s}$ can be written as:

$$\vec{J_s} = \hat{a}_y \, \delta(z - z_s) \left\{ J_1 \, p(y - y_{s1}) + J_2 \, p(y - y_{s2}) \right\} \quad (2.84)$$

with $y = y_{s1}$, $y = y_{s2}$ the center axes of the two slots and z_s the z-coordinate of the ideal current sources. In (2.84), $p(y - y_{si})$ is a pulse function that extends transversely over the ith slot, and J_1 and J_2 denote the amplitudes of the assumed current sources.

In general, the electric current source can be written as:

$$\vec{J} = \hat{a}_y \sum_{q=1}^{N_z} \sum_{r=1}^{N_y+1} J_y^{q,r} \, \delta(z - z_q) p(y - y_r) + \hat{a}_z \sum_{o=1}^{N_y} \sum_{p=1}^{N_z+1} J_z^{o,p} \, \delta(y - y_o) p(z - z_p) \quad (2.85)$$

where $J_z^{o,p}$ and J_y^{qr} are the amplitudes of the current sources and

$$p(y - y_r) = \begin{cases} 1 & y_{r-1} \le y \le y_r \\ 0 & otherwise \end{cases} \quad (2.86)$$

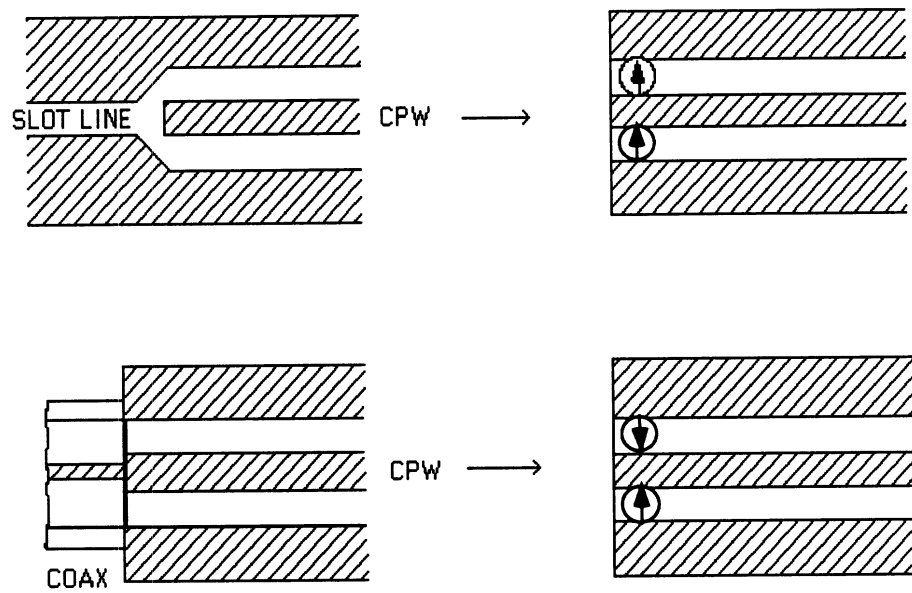$$p(z - z_p) = \begin{cases} 1 & z_{p-1} \le z \le z_p \\ 0 & otherwise \end{cases} \quad (2.87)$$

Figure 2.7: Two excitation mechanisms of a CPW and their corresponding numerical models.

Such a model results in an excitation vector which has zeros everywhere except at the positions of the ideal current sources (similar to the delta gap current generators model). Thus, the elements of the excitation vector are given by:

$$I_z(o, p) = \ell_{z_p} J_z^{o,p} \tag{2.88}$$

$$I_y(q, r) = \ell_{y_r} J_y^{q,r} \tag{2.89}$$

Although only a mathematical model, this feeding mechanism has proven to be efficient, accurate and reliable [69, 84, 112]. In addition, it does not introduce any unwanted numerical complications as it happens with other excitation techniques [23, 66]. As it will be presented in the coming chapters, the number, position and strength of these ideal current sources depend on the nature of the CPW discontinuity.

2.5.3 Computational Considerations

Up to this point, one can evaluate the matrix elements in (2.67) using the expressions given above. Then, the magnetic current vector in (2.67) can be obtained using LU-decomposition and back substitution (or by direct inversion). However, before proceeding in the calculation of the admittance matrix elements, these expressions may be written in a form suitable for faster and more efficient computation [102, 111]. Such forms can be facilitated if uniform discretization is used (i.e. $l_{y_i} = l_y$ and $l_{z_i} = l_z$ for all i). For example, using the identity

$$\sin(A)\sin(B) = \frac{1}{2}\left[\cos(A - B) - \cos(A + B)\right], \tag{2.90}$$

equation (2.75) can be written as follows:

$$Y_{zz}(k, l; q, r) = AR(k - q; l, r) - AR(k + q; l, r) \tag{2.91}$$

where $AR(i; l, r)$, i=0, ..., $2N_z$, is an array given by

$$AR(i; l, r) = \sum_{n=0}^{NSTOP} \sum_{m=0}^{MSTOP} \frac{4e_m}{aL} \frac{k_s^2}{(k_z^2 - k_s^2)^2} \left(\frac{k_z^2 P_1 + k_y^2 Q_1}{k_{x_1}^2 - k_1^2} + \frac{k_z^2 P_2 + k_y^2 Q_2}{k_{x_2}^2 - k_2^2} \right)$$
$$\frac{[-\cos(k_z l_z) + \cos(k_s l_z)]^2}{\sin^2(k_s l_z)} \cos(i k_z l_z) T_y(y_l) T_y(y_r) \qquad (2.92)$$

Thus, it can be seen that instead of performing the computations N^2 times to obtain the elements of $[Y_{zz}]$, where $N = N_z(N_y + 1)$ is the number of the z-directed basis functions, one has only to compute the $2N_z \times (N_y + 1)^2$ array AR from which the N^2 elements of $[Y_{zz}]$ can be obtained using (2.91). In addition, since the product $T_y(y_l) T_y(y_r)$ is independent of k_z, it is computed only once for each m and stored in a suitable array. It can be seen that the summations over m and n have been truncated to $MSTOP$ and $NSTOP$, the choice of which will be discussed in later chapters. In a similar manner, the other expressions may be rewritten in a more suitable form for computational purposes. Moreover, the symmetry of the admittance matrix is exploited to reduce the computational time appreciably.

In summary, a general full wave analysis of CPW discontinuities has been presented in this chapter. This analysis relies on solving an integral equation in the space domain using the method of moments which results in the electric field distribution in the slot apertures. In the rest of the thesis, techniques to extract the circuit parameters of a variety of CPW discontinuities will be discussed. In addition, convergence issues will be studied and numerical results will be presented.

CHAPTER III

ONE-PORT CPW DISCONTINUITIES

3.1 Introduction

In this chapter, the one-port CPW discontinuities shown in Figure 3.1, namely, a short-end and an open-end CPW, are analyzed. In addition, a CPW through line is shown which is used to compute the effective dielectric constant (or guided wavelength). Recently, these discontinuities have been of interest and have been extensively studied both theoretically and experimentally [64]-[77], [86, 98, 113]. It should be mentioned that these CPW discontinuities are essential for accurate S-parameter measurements using TRL and TSD calibration techniques.

3.2 Network Analysis

3.2.1 Guide Wavelength

In a lossless transmission line, the propagation constant γ_g is

$$\gamma_g = j\beta_g \tag{3.1}$$

where the phase constant β_g is given by

$$\beta_g = \frac{2\pi}{\lambda_g} \tag{3.2}$$
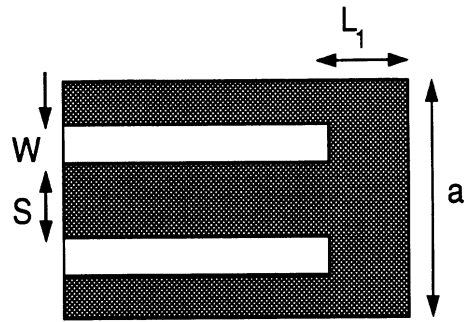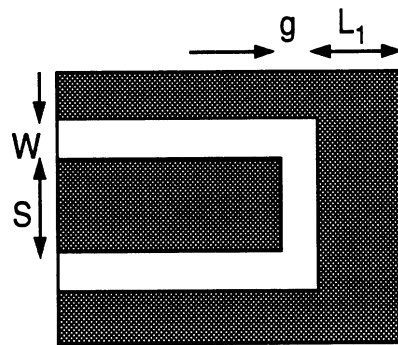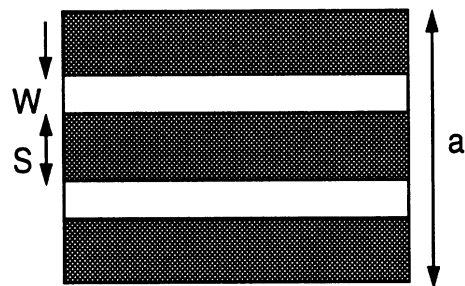
Figure 3.1: One-port CPW discontinuities. (a) Short-end CPW. (b) Open-end CPW. (c) CPW through line.

The guide wavelength, λ_g, can be obtained from the positions of the maximum and minimum absolute values of the electric field standing wave pattern derived from the method of moments solution [111, 114, 115, 116]. This method is based on the assumption that, away from the discontinuity and the feed point, the line supports only the quasi-TEM mode. In this technique, the magnetic current distribution is first smoothed by spline interpolation between the computed points [117]. For example, the spline between two consecutive points z_k and z_{k+1} is:

$$S_k(z) = A_k(z - z_k)^3 + B_k(z - z_k)^2 + C_k(z - z_k) + D_k \qquad (3.3)$$

where A_k, B_k, C_k, and D_k are the spline fit coefficients. Once these coefficients are obtained, the two points surrounding an extremum are found by searching for a sign change in the slope of the current ($S_k'(z_k) = C_k$) evaluated at each successive points [111]. Then, the position of the extremum is obtained by finding the root of $S_k'(z) = 0$ which lies within the interval $z_k \leq z \leq z_{k+1}$. Alternatively, Newton-Raphson search algorithm may be implemented to search for an extremum over a single spline [116]. It should be noted here that the voltage standing wave ratio (VSWR) for a lossless CPW structure is infinity since the absolute minimum value of the electric field standing wave is zero (see Figure 3.2). Recently, it has been shown that the higher the SWR, the smaller is the error contributed by using the cubic spline approximation to find the position of an extremum [116].

3.2.2 Short-End CPW

Figure 3.2 shows a typical electric field (or magnetic current) distribution along a short-end CPW, under either coplanar or slotline mode excitation, which is obtained from the method of moments solution. It can be observed that the electric field is discontinuous around the position of the ideal electric current exciting the CPW,
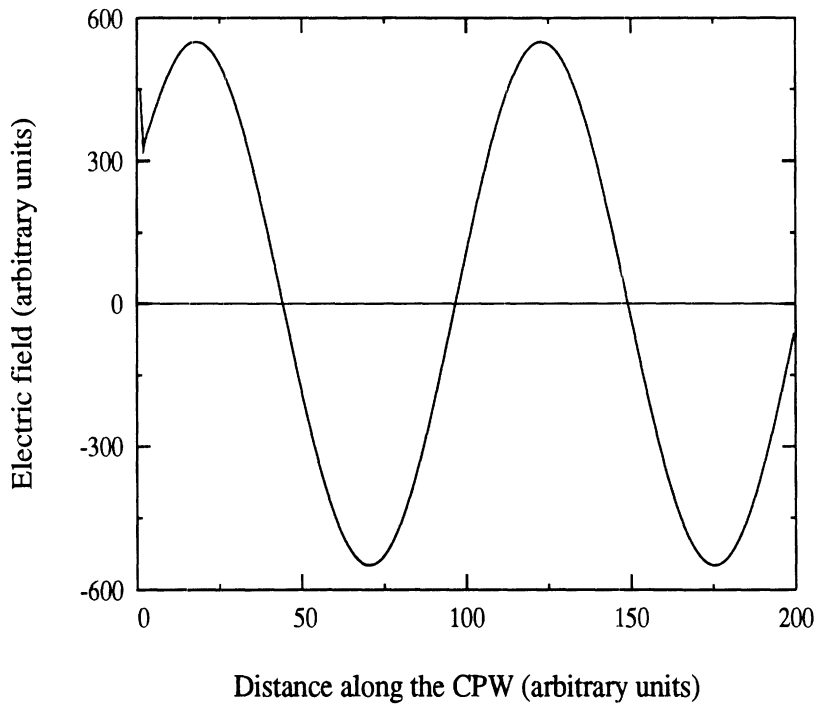
Figure 3.2: The imaginary part of the electric field (magnetic current) distribution for a short-end coplanar waveguide. The real part is zero since a lossless structure is considered.

however, it behaves well otherwise. In this case the ideal current source is located at the beginning of the line. The derived equivalent magnetic current may vary smoothly around the gap generator if the excitation is located at approximately $\lambda_g/4$ from the conducting wall [118]. It can be seen that the effect of the short-end is equivalent to an inductive load for both modes. This is expected since in a short-end CPW there is a storage of pure magnetic energy around the discontinuity [113]. In such a discontinuity, the parameter of interest is the effective length extension Δl_{sc} which represents the length of an ideal short circuited transmission line which, as a continuation of the slots, would present the same reflection coefficient, at the plane

of the discontinuity, as the short-end discontinuity [111]. It may be computed as

$$\Delta l_{sc} = \frac{\lambda_g}{4} - d_e \tag{3.4}$$

where d_e is the distance from the plane of the discontinuity (i.e. the end of the line) to the closest absolute maximum value of the electric field standing wave pattern. The error introduced by using (3.4) may be reduced by taking the average of the distances from the end of the line to the maxima along the line. The normalized inductive reactance, seen at the end of the line, may be calculated as

$$X_{sc} = \tan(\beta_g \Delta l_{sc}) = \frac{\omega L_{sc}}{Z_0} \tag{3.5}$$

where L_{sc} is the equivalent inductance and Z_0 is the characteristic impedance of the line.

3.2.3 Open-End CPW

Figure 3.3 shows typical magnetic current distribution along an open-end CPW, under coplanar mode excitation. As expected, this discontinuity behaves as an equivalent capacitance which may be computed from:

$$X_{oc} = \cot(\beta_g \Delta l_{oc}) = \frac{1}{\omega C_{oc} Z_0} \tag{3.6}$$

As before, Δl_{oc} represents the length of an ideal open circuited transmission line which, as a continuation of the slots, would present the same reflection coefficient, at the plane of the discontinuity, as the open-end discontinuity [111]. It may be computed as

$$\Delta l_{oc} = \frac{\lambda_g}{2} - d_e \tag{3.7}$$

On the other hand, it has been found that a CPW open-end behaves as an inductive load if excited with the slotline mode. This is due to the fact that a slotline mode
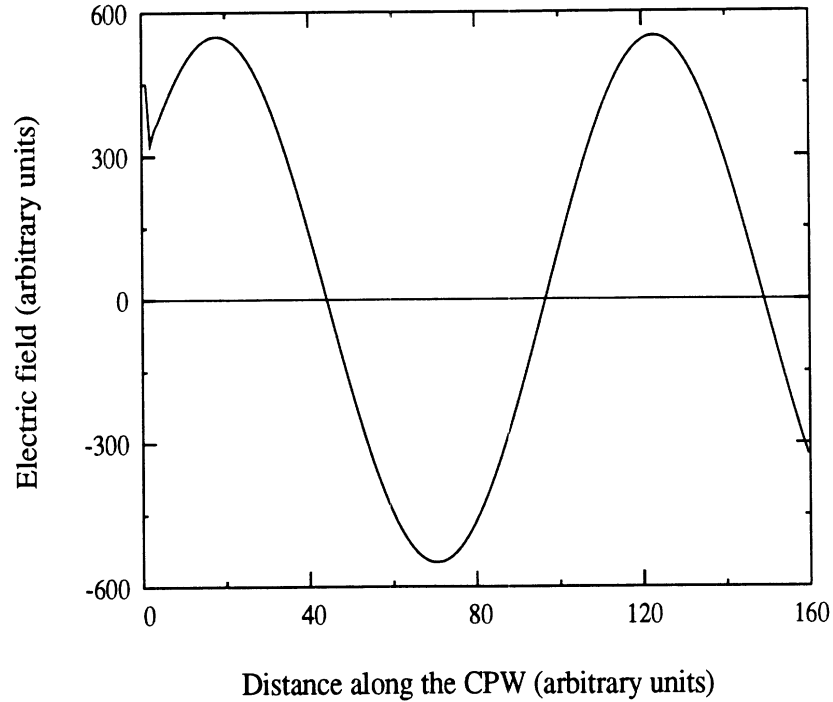
Figure 3.3: The imaginary part of the electric field (magnetic current) distribution for an open-end coplanar waveguide.

excitation in a CPW corresponds to an electric wall at the symmetry plane of the structure which makes the stored magnetic energy in the gap region higher than the stored electric energy. In a similar manner, one can define a corresponding effective length extension and an equivalent inductance at the end of the line.

3.3 Numerical Considerations

In the expressions for the elements of the admittance matrix as given by (2.72) - (2.73), the summations over m and n are theoretically infinite. However, for the numerical solution of (2.67), these summations are truncated and the number of terms kept depends on the convergence behavior of the admittance matrix. Due to the nature of the problem solved here, the above summations have a convergence behavior similar to the summations described in [102, 111]. As an illustration, Figure 3.4 shows the effective length extension (normalized to the substrate thickness h) at
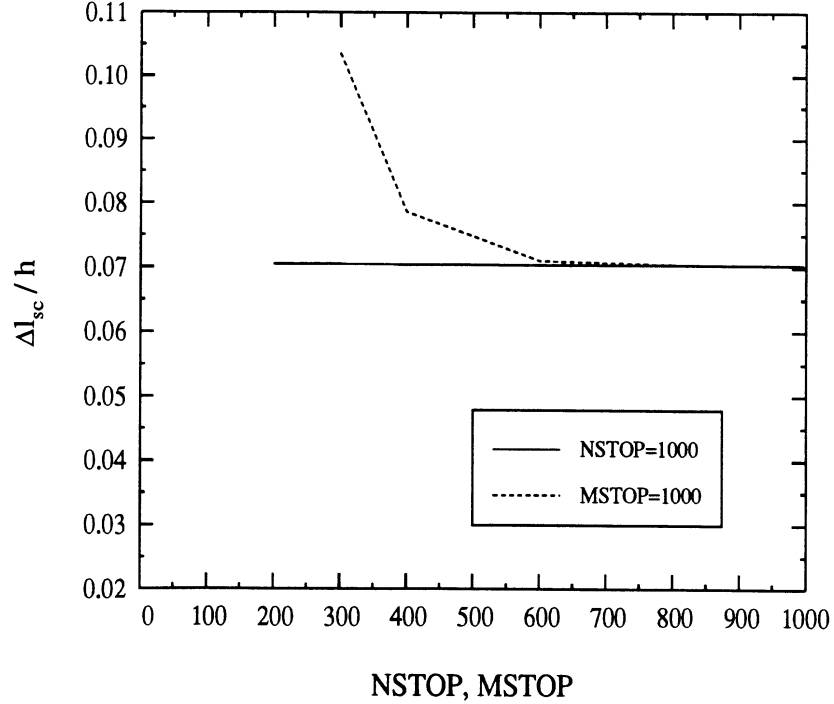
Figure 3.4: A typical convergence plot with respect to the number of modes.

the end of a shorted CPW as a function of the number of modes. The solid line

shows $\Delta l_{sc}/h$ as a function of $MSTOP$ with $NSTOP$=1000, while, the dashed line

shows $\Delta l_{sc}/h$ as a function of $NSTOP$ with $MSTOP$=1000. It should be noted

that $NSTOP$ and $MSTOP$ correspond to the maximum values of the k_z and k_y

eigenvalues considered in the summations. These eigenvalues are given by:

$$k_{z\,max} = \frac{(NSTOP)\,\pi}{L} \tag{3.8}$$

$$k_{y\,max} = \frac{(MSTOP)\,\pi}{a} \tag{3.9}$$

It can be seen from Figure 3.4 that Δl_{sc} is more sensitive to the choice of $NSTOP$

than $MSTOP$. This is due to the fact that the length of the cavity L is larger

than its width a, which makes the number of the required k_z eigenvalues larger than

the number of the k_y eigenvalues [64]. In the present work, far more terms than

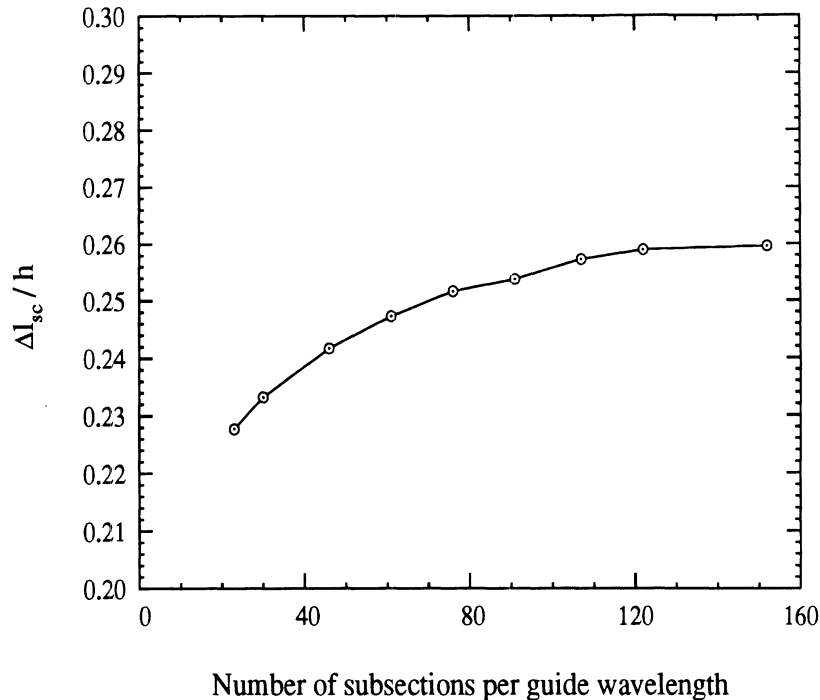necessary, typically 1000 modes in each direction, are usually used in order to avoid

Figure 3.5: Convergence behavior of the normalized effective length extension $\Delta\ell_{sc}/h$ for a shorted CPW (coplanar mode). (h=0.635 mm, h/λ_0=0.015, W/h=0.4, S/h=1, a/h=2(W/h)+S/h+20, L_1=5h, ϵ_{r1}=9.7, ϵ_{r2}=1, D_1=D_2=10h)

any convergence problems. This is facilitated by relatively optimizing the codes and the availability of very fast computers.

Another critical parameter for the convergence of the results is the number of basis functions used in the magnetic current expansion. Figure 3.5 shows the normalized effective length extension versus the number of subsections per guide wavelength for the case of a shorted CPW (coplanar mode) suspended inside a cavity as shown in Figure 3.6. In this example, only a longitudinal magnetic current is assumed to exist in the slots of the CPW. In addition, uniform discretization (i.e. constant subsection length) along the slots has been used. It can be seen that acceptable convergence is achieved when the partitioning of the line exceeds 60 subsections per guide wavelength. The percentage difference between $\Delta l_{sc}/h$ obtained with 60 subsections and
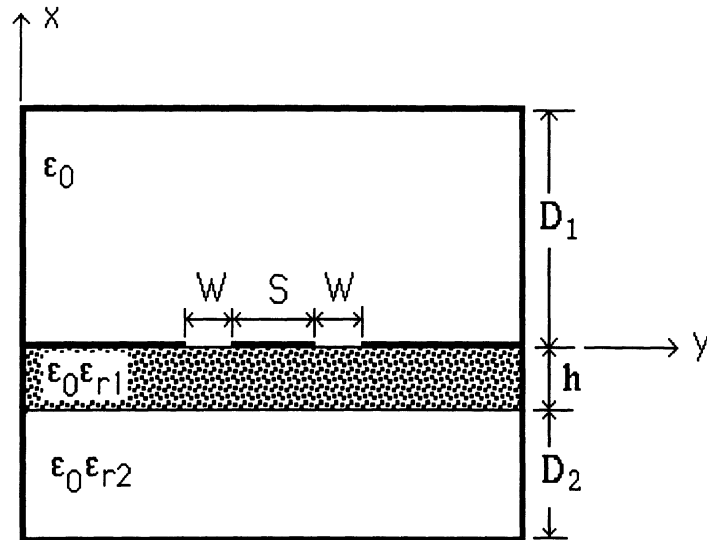
Figure 3.6: A suspended CPW structure inside a rectangular cavity.

150 subsections is only 5%. Typically, 120 subsections per wavelength are used to characterize a short-end CPW.

Figure 3.7 shows the normalized effective length extension of a shorted CPW (coplanar mode) versus the number of basis functions (n_y) used to represent the transverse component of the magnetic current in each slot. The percentage difference between $\Delta l_{sc}/h$ obtained with $n_y=0$ and $n_y=6$ is also shown in the same figure. It has been found that the number of basis functions n_y required to obtain accurate results is largely dependent on the aspect ratio S/W. For S/W greater than 1, only the longitudinal component of the magnetic current is required since the slot coupling effect is small. However, for S/W less than 1, the transverse component of the magnetic current is needed to represent the stronger coupling effect between the slots as can be clearly seen in Figure 3.7.

One can enhance the convergence and be able to accurately characterize the end effect without the need to have a high number of basis functions along the entire line
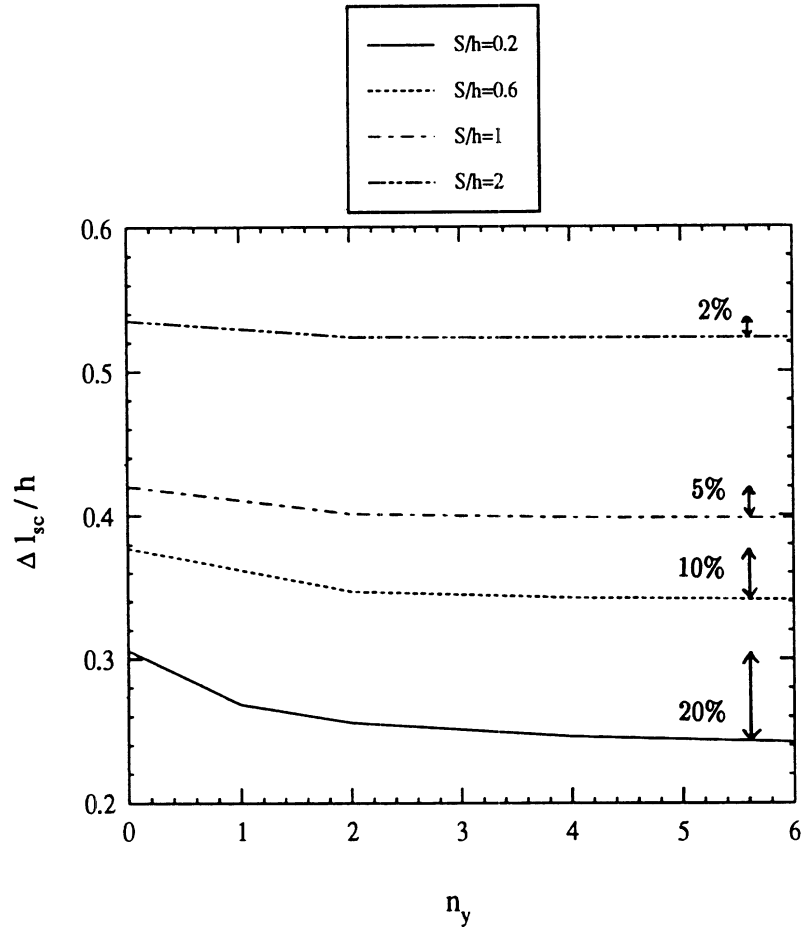
Figure 3.7: The normalized effective length extension $\Delta\ell_{sc}/h$ for a shorted CPW (coplanar mode) versus the number of basis functions n_y. (h=0.2 mm, f=20 GHz, W/h=1, a=4.24 mm, L_1=5h, ϵ_{r1}=13.1, ϵ_{r2}=1, D_1=D_2=5h)
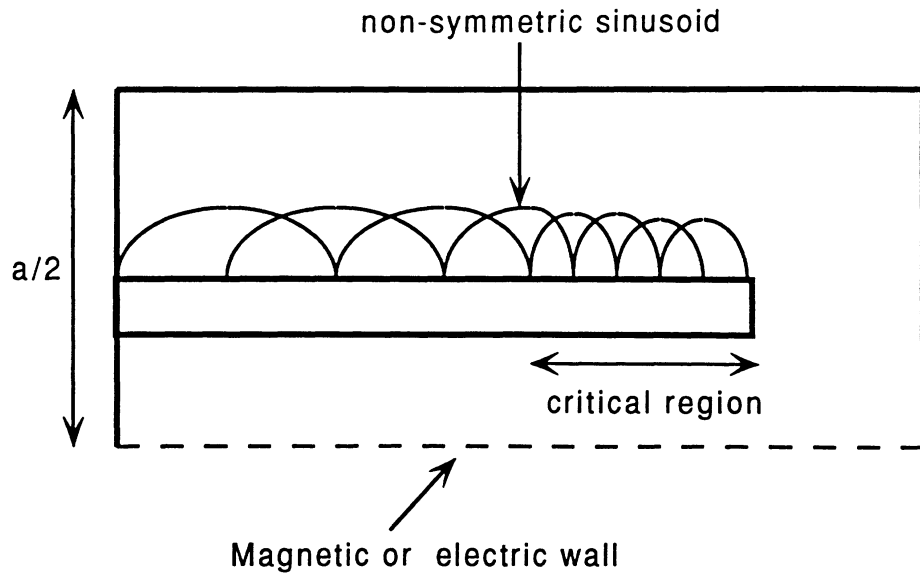
non-symmetric sinusoid

a/2

critical region

Magnetic or electric wall

Figure 3.8: Non-uniform discretization of a CPW short-end discontinuity. A magnetic
wall at the symmetry plane corresponds to the coplanar mode excitation,
while, an electric wall corresponds to the slotline mode.

by using non-uniform discretization as shown in Figure 3.8. In this case, the slots

are divided into two regions: a critical region within $\lambda_g/4$ from the short end and

a noncritical region which is the rest of the line. A non-symmetric basis function

connects the two regions in order to insure the continuity of the assumed magnetic

current density. After extensive numerical experiments, it has been found that around

40 basis functions are needed in the critical region and 30 basis functions per guide

wavelength in the rest of the line in order to insure convergence. Similarly, Figure 3.9

shows the discretization used in the expansion of the equivalent magnetic current in

the slot aperture of a CPW open-end. The slot aperture is divided into two regions:

the first is the uniform CPW feeding line where only a longitudinal magnetic current

is assumed, the second is the open-end region where both y- and z- directed currents

are considered (with n_{y_g} and n_{z_g} basis functions). The first region is further divided

into a critical region within $\lambda_g/4$ from the open end and a non-critical region which is
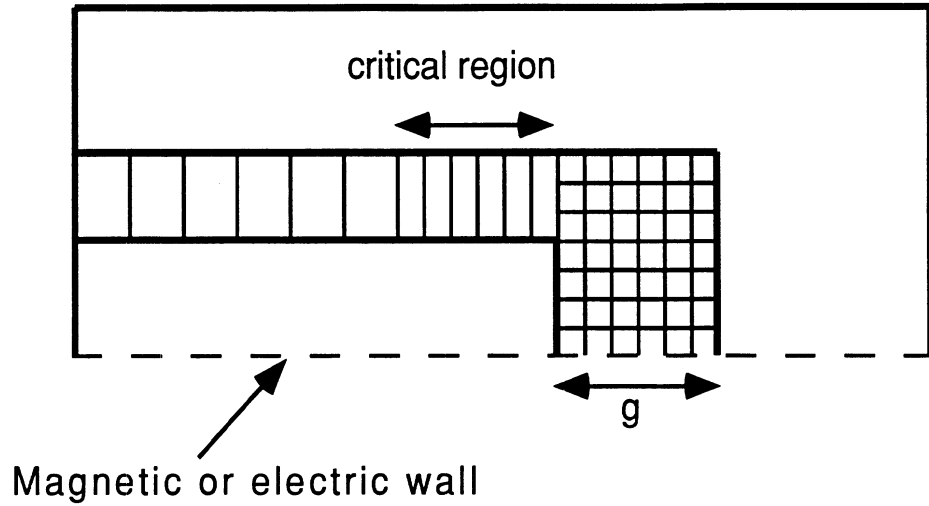
Figure 3.9: The discretization used in the expansion of the equivalent magnetic current for a CPW open-end.

the rest of the uniform line. It has been found that 50 basis functions are needed in the critical region and 30 basis functions per guide wavelength in the rest of the uniform line to ensure convergence of the results. On the other hand, n_{y_g} has to be chosen such that $\frac{S+2W}{n_{y_g}+1}$ is an integer fraction of W (i.e. $\frac{S+2W}{n_{y_g}+1} = \frac{W}{n}$, where n is an integer), or else erroneous results are obtained. For example, an inductive end reactance may be obtained if this condition is not satisfied. The choice of n_{z_g} depends mainly on S,W and the operating frequency. Figure 3.10 shows a sample convergence test with respect to n_{z_g}. The change in the reactance is only 1.7% when n_{z_g} is incremented form 9 to 12. The result starts to diverge if n_{z_g} is taken larger than 12 which is due to the inability of the moment method to converge when very small subsections are considered [111]. It is found that when $n_{z_g} = 15$, the admittance matrix becomes ill-conditioned (condition number $\approx 10^9$).

One can also take advantage of the transverse symmetry in CPW structures to reduce the computation time appreciably. This is due to the existence of either odd
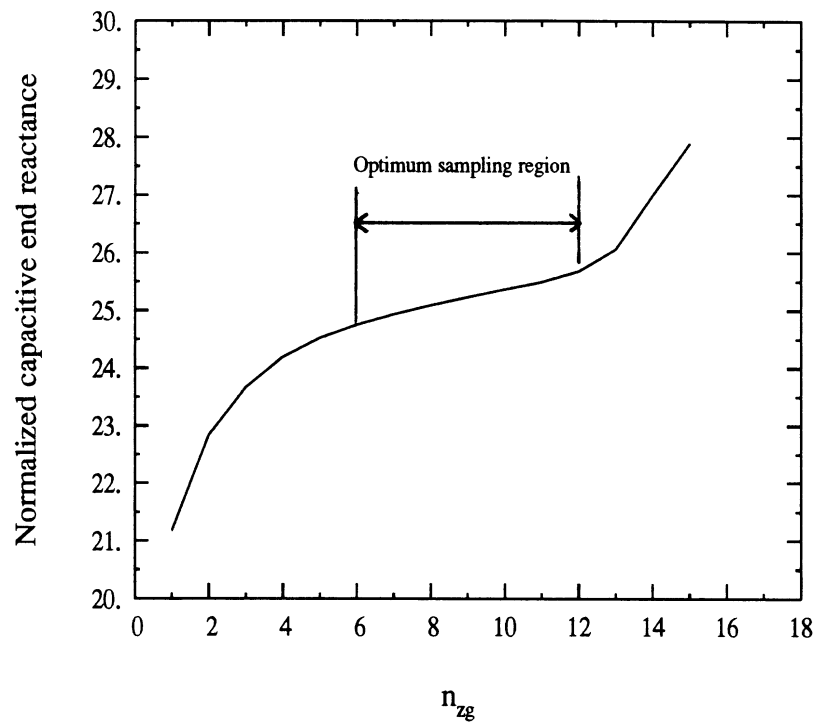
Figure 3.10: A sample convergence test for an open-end CPW. (W=20 μm, S=5W, g=100 μm, f=20 GHz, h=0.4064 mm, ϵ_{r1}=13.1, ϵ_{r2}=1, a=4 mm, L_1=5h, D_1=D_2=4h)

symmetry (coplanar mode) or even symmetry (coupled slotline mode) between the fields in the two slots of the CPW. Thus, a perfectly magnetic wall can be introduced in the symmetry plane of the structure (i.e. the y=$\frac{a}{2}$ plane) when the CPW is excited with a coplanar mode, while, a perfectly electric wall can be introduced when it is excited with a coupled slotline mode (see Figures 3.8 and 3.9). As a result, only half of the slot aperture is discretized which reduces the number of unknowns in (2.67) to half of that corresponding to the whole aperture. It should be noted that introducing a perfectly magnetic wall at the y=$\frac{a}{2}$ plane forces the z-component of the magnetic field to vanish at this plane. Using equations (2.48) and (2.50), it can be easily shown that such a boundary condition is satisfied if and only if m takes only odd values. Alternatively, the eigenvalue k_y can be written as:

$$k_y = \frac{(2m+1)\pi}{a}, \quad m = 0, 1, \ldots, MSTOP \qquad (3.10)$$

This, in effect, will further reduce the computation time since $MSTOP$ can now be taken as much as half of that used when symmetry is not exploited. Similarly, it can be shown that only even values of m have to be used if a perfectly electric wall is introduced at the symmetry plane $y = \frac{a}{2}$.

Taking the above numerical considerations into account, codes have been written to characterize CPW discontinuities shown in Figure 3.1. It should be mentioned that these codes (as well as other codes for other discontinuities) were written using Fortran. A typical condition number of the admittance matrix ranges from 10^2 to 10^5 since double precision was used. Numerical results are given below.

3.4   Numerical Results

All the considered CPW structures in this section are suspended inside a rectangular cavity, as shown in Figure 3.6, the dimensions of which are chosen such that the

interaction between the transmission line and the shielding box is weak. However, for illustration purposes, an example is included to show the effect of cavity resonances on the end effect of a shorted CPW. It has been found numerically that the top and bottom walls have negligible effect as long as D_1 and D_2 exceeds approximately three times the substrate thickness, h. Similarly, the distance L_1 between the end of the line and the rear cavity wall (see Figure 3.1) should be at least three times the substrate thickness.

3.4.1 Guide Wavelength

Before deriving the circuit parameters of any CPW discontinuity, one has to obtain the guide wavelength λ_g of the CPW under consideration. Figure 3.11 shows the CPW wavelength (for both coplanar and coupled slotline modes) obtained using the 3D theory applied to a CPW through line as compared to that obtained using electrooptic sampling [119]. In addition, values of λ_g obtained using 2D theory based on the spectral domain immitance approach [78, 120, 121] are shown in the same figure. This set of data is obtained from a 2D program written by the author which includes also the computation of the CPW characteristic impedance [121]. It can be noticed that the agreement between the three sets of data is very good which verifies both the used 2D and 3D theory. In addition, the derived results agree very well with those obtained using the closed form expression for λ_g reported in [45].

3.4.2 Coplanar Waveguide Short-End

Figure 3.12 shows $\Delta l_{sc}/h$ as a function of the normalized substrate thickness h/λ_0 of a CPW short-end excited with a coplanar mode. On the same figure, the theoretical results derived using a spectral domain cavity resonance method [64] are shown for
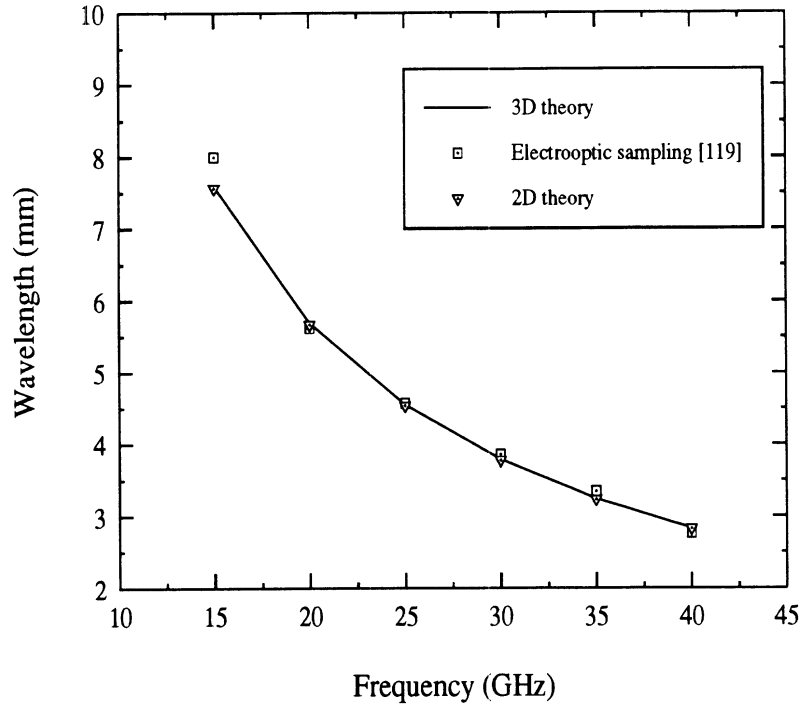
(a) Coplanar mode
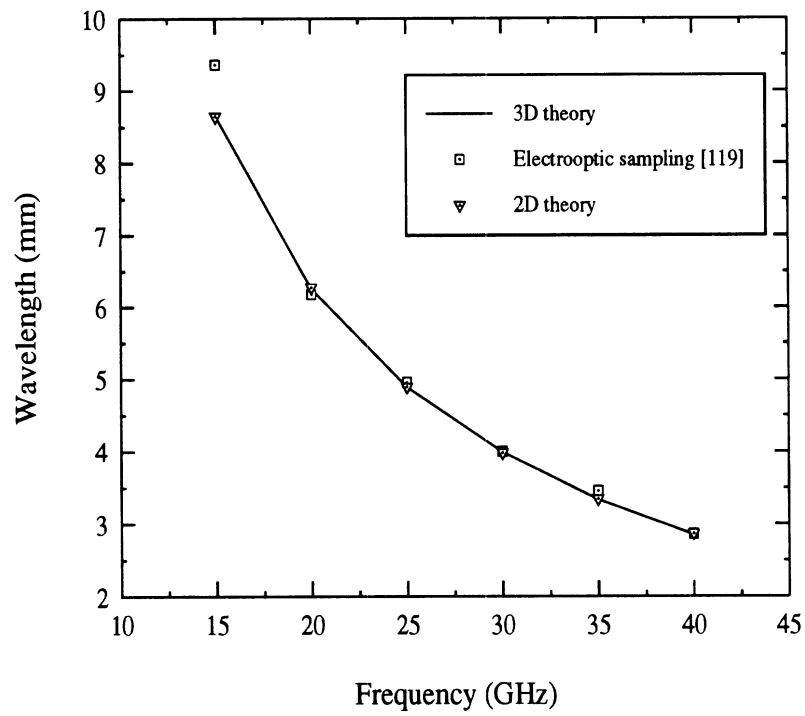
(b) Coupled slotline mode

Figure 3.11: CPW dispersion characteristics. (S=75 μm, W=50 μm, h=500 μm, ϵ_{r1}=13, ϵ_{r2}=1,)
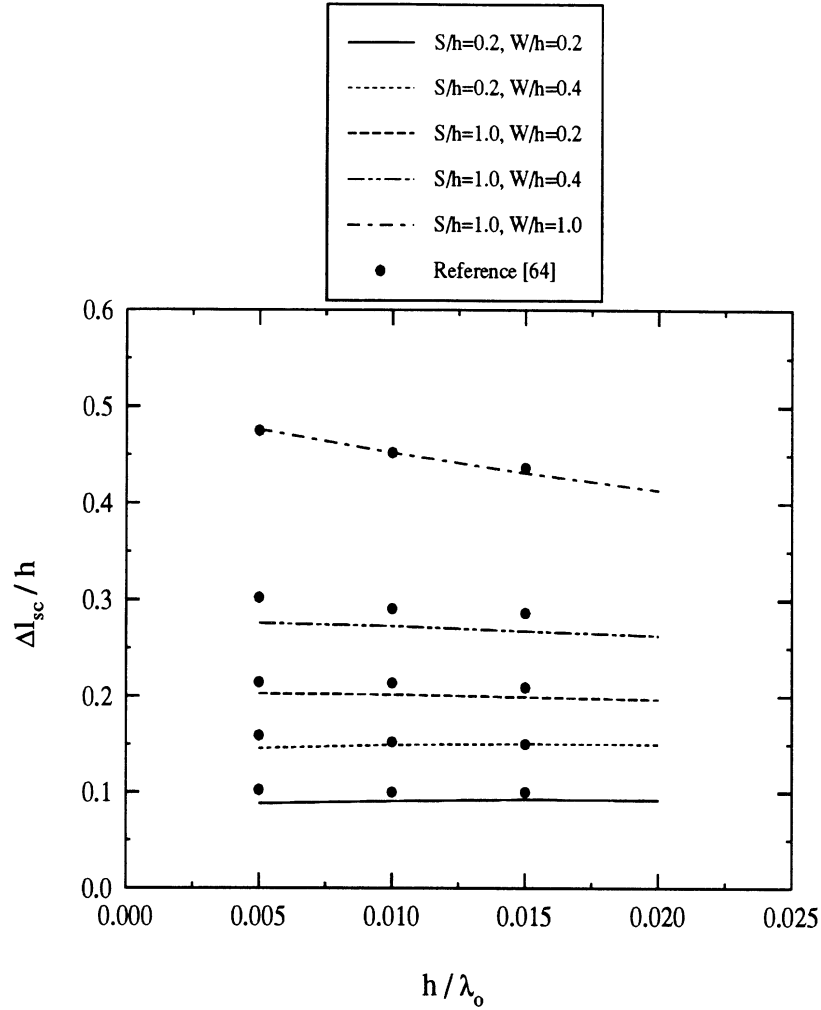
Figure 3.12: Effective length extension of a shorted CPW (coplanar mode) as compared to theoretical results from [64]. (h=0.635 mm, a/h=2(W/h)+S/h+20, L_1=5h, ϵ_{r1}=9.7, ϵ_{r2}=1, D_1=D_2=10h)

comparison. The agreement between the two theories is very good.

As another example and for validation purposes, Figure 3.13 shows a comparison between the normalized inductive reactance at the end of a shorted CPW obtained using the present theory and that reported in [67]. It should be noted that although an open structure is considered in [67], in contrast to a shielded one in the present theory, the agreement between both sets of data is very good. This is due to the fact that the amount of power radiated from a short-end CPW is very small [67].

The effects of the same discontinuity are also studied for the case of a coplanar line
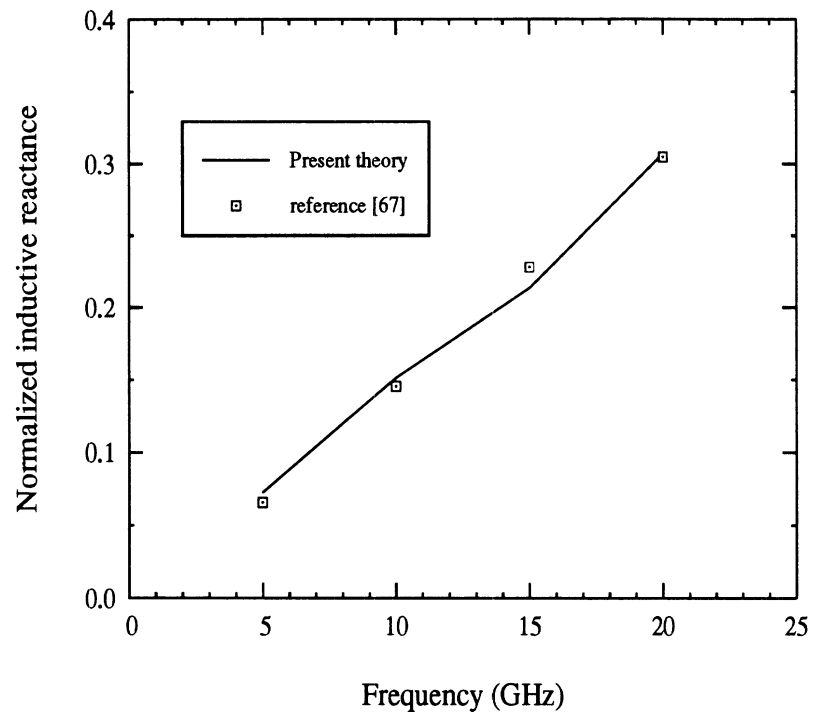
Figure 3.13: Normalized inductive reactance of a shorted CPW (coplanar mode)
as compared to theoretical results from [67]. (h=0.8 mm,
W=1.5 mm, S=0.789 mm, a=7 mm, L_1=10h, ϵ_{r1}=2.2, ϵ_{r2}=1,
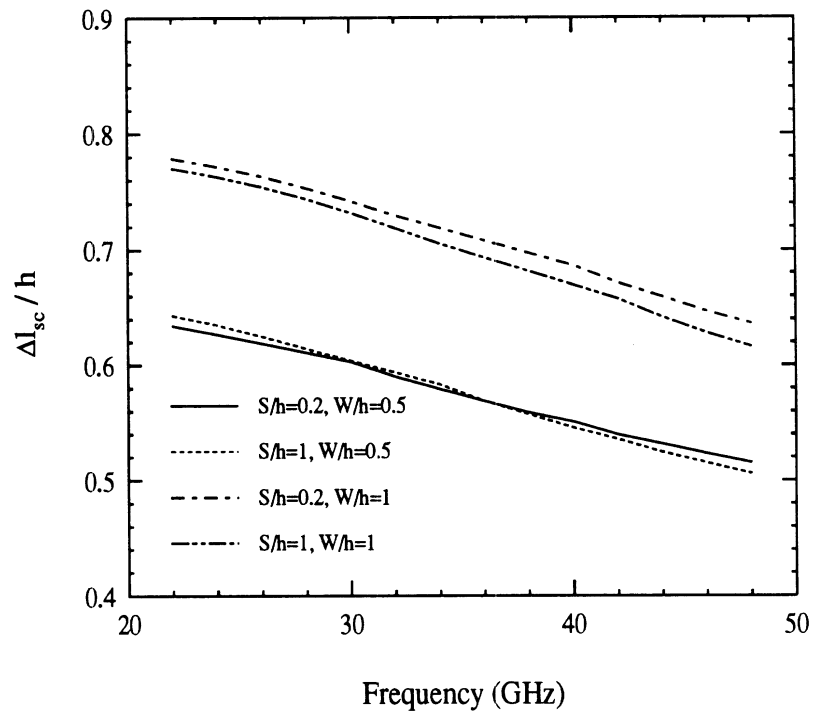D_1=D_2=5h)

printed on a 200 μm GaAs substrate. The effective extension length is evaluated and plotted for both the coplanar (Figure 3.14(a)) and coupled slotline excitations (Figure 3.14(b)) as a function of the width W/h and slot separation S/h. The effect of the normalized separation distance S/h on the magnetic field in the discontinuity region differs between the two excitations. For the coplanar excitation, the fields on the slot apertures are 180° out of phase resulting in small stored energy at the discontinuity. As the separation distance S becomes larger, more energy is stored at the discontinuity region. This explains why the effective extension length reduces considerably as S/h becomes smaller than one. In the case of coupled slotline excitation, where the fields on the slot apertures are in phase, the effective excess length is much less sensitive to the separation distance. This is due to the fact that only for very tight slot coupling the effect of S on Δl_{sc} becomes noticeable [64]. On the other hand, the effect of the slot width in both excitations is the same. As the slot width W increases the magnetic energy density stored around the discontinuity increases. As a result the discontinuity behaves as a larger inductor.

The effect of the center conductor width on Δl_{sc} of a shorted CPW can be more clearly seen in Figure 3.15. In this figure, the normalized effective length extension of a short-end CPW is plotted against the center conductor width for both the coplanar and slotline modes. For S/h=0, the end-effect corresponding to the coplanar and slotline modes is essentially equal to the end-effect of a slotline of width 2W excited with an odd and even mode, respectively [121]. On the other hand, for large center conductor widths, the end-effect due to both modes approaches that corresponding to a slotline of width W excited with an even mode. For the same configuration, Figure 3.16 shows the guide wavelength as a function of the center conductor width.

To illustrate the effect of cavity resonances on the end effect of a shorted CPW,
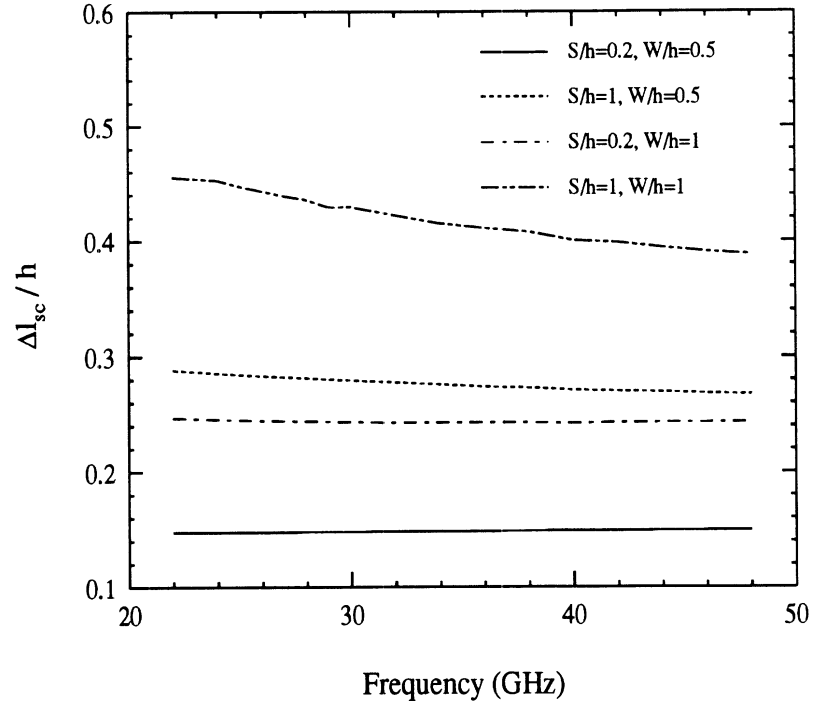
(a) Coplanar mode

(b) Coupled slotline mode

Figure 3.14: Effective length extension of a shorted CPW on GaAs substrate. (h=0.2 mm, a=2.6 mm, L_1=10h, ϵ_{r1}=13.1, ϵ_{r2}=1, D_1=D_2=5h)
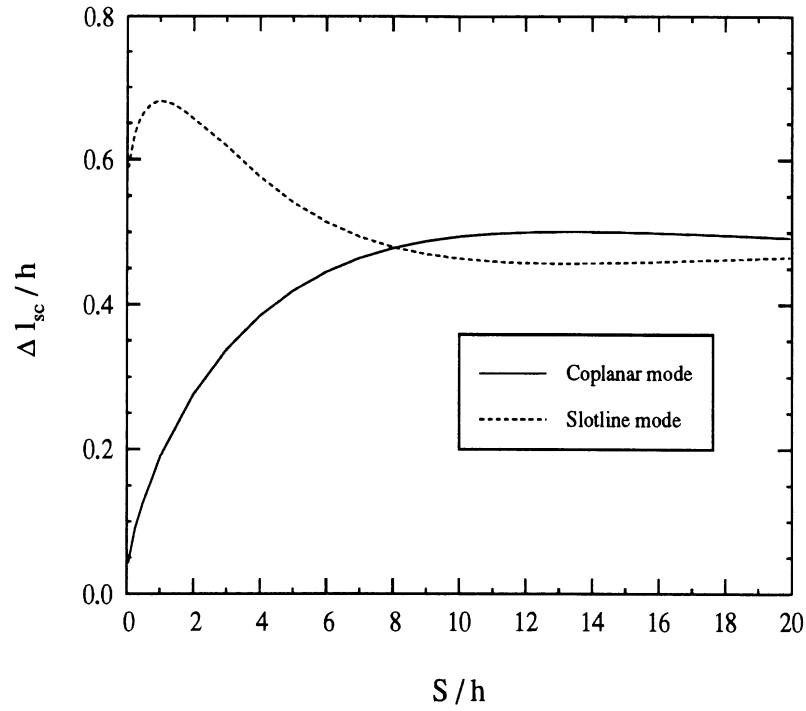
Figure 3.15: Normalized effective length extension vs. center conductor width. (h=0.635 mm, W/h=0.2, a/h=2(W/h)+S/h+20, L_1=5h, ϵ_{r1}=9.7, ϵ_{r2}=1, h/λ_0=0.015, D_1=D_2=10h)
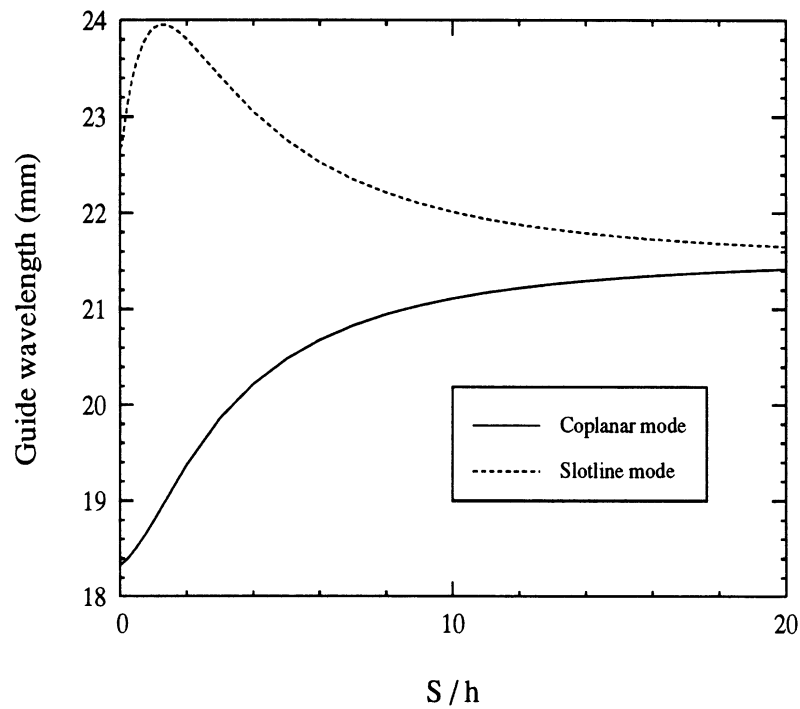

Figure 3.16: Guide wavelength vs. center conductor width. Dimensions are the same as in Figure 3.15.

Figure 3.17 shows the normalized effective length extension of a CPW excited with a coplanar mode in the frequency range 7-15 GHz. It can be seen that there is an anomalous behavior occurring around the following frequencies: 10.2, 11.3 and 15 GHz. In order to understand such a behavior, the suspended CPW structure shown in Figure 3.6 can be viewed as if it is composed of two cavities: an air filled upper one and a partially filled bottom one. The resonant frequencies of the upper cavity can be easily calculated using standard expressions [101]. For the partially filled cavity, the transverse resonance technique has been used to obtain the characteristic equations for the LSM and LSE modes, which were then solved numerically [101]. It has been found that the resonant frequencies corresponding to the LSM_{111}, LSM_{121} and LSM_{141} modes of the partially filled lower cavity are 10.17, 11.35 and 14.9 GHz, respectively. In addition, the resonant frequency f_{011} of the upper cavity is 11.2 GHz. The above observations clearly explain the anomalous behavior noticed around these frequencies in Figure 3.17. The reason behind such a behavior is that at the vicinity of a resonance, the cavity mode interacts with the fields in the CPW slots which results in a non-quasi-TEM distribution. As an example, Figure 3.18 shows the magnetic current distribution in the slots of the above shorted CPW at 11.4 GHz. It can be seen that the field distribution is totally distorted because of the cavity resonance. The same phenomenon was observed in the case of shielded open-end microstrip line [111]. On the other hand, Figure 3.19 shows the magnetic current distribution at 9 GHz for the same short-end CPW. It is interesting to note that although this frequency is only 1.2 GHz below the first cavity resonance, the magnetic current forms a uniform standing wave. In addition, a similar uniform standing wave has been found at 14 GHz in spite of the fact that there exists several resonances below this frequency.
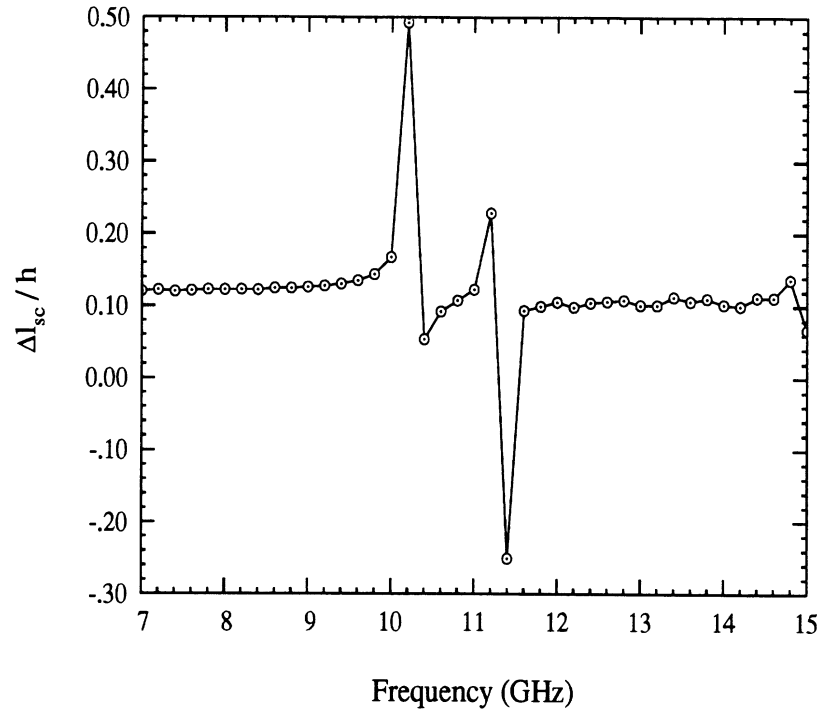
Figure 3.17: Effect of cavity resonances on the end effect of a shorted CPW. (h=3 mm, W=0.3 mm, S=2 mm, a=14 mm, ϵ_{r1}=2.2, ϵ_{r2}=1, D_1=D_2=3h)

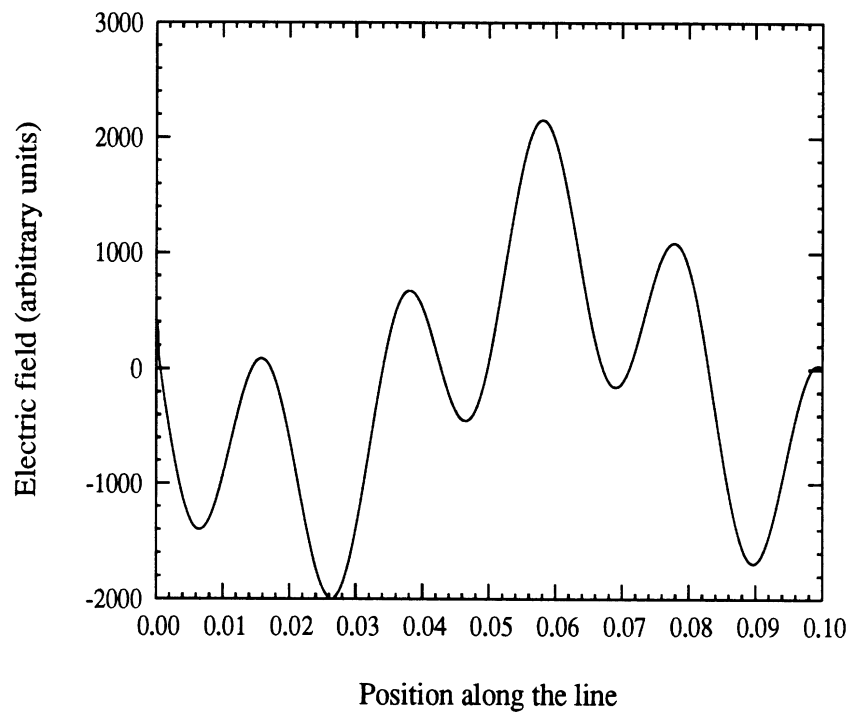
Figure 3.18: Imaginary part of the magnetic current distribution of a short-end CPW at a cavity resonance. Dimensions are as in Figure 3.17 and f=11.4 GHz.
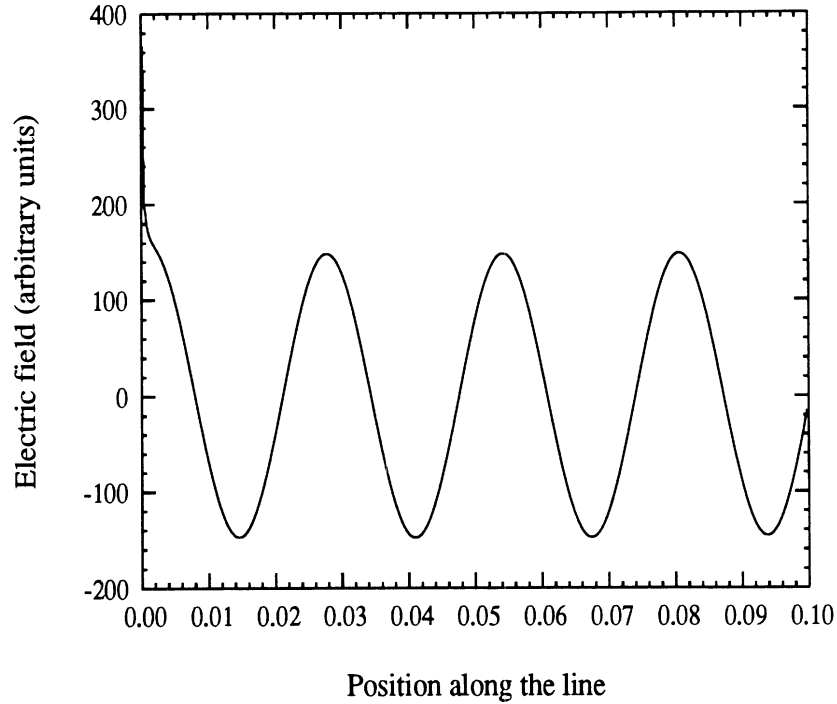
Figure 3.19: Imaginary part of the magnetic current distribution of a short-end CPW away from cavity resonances. Dimensions are as in Figure 3.17 and f=9 GHz.

3.4.3 Coplanar Waveguide Open-End

At first, for verification purposes, the effective length extension (as seen at the plane of the open end of the center conductor) of a coplanar waveguide open-end printed on Duroid is plotted as a function of frequency in Figure 3.20, and is compared to experimental data published in [158]. The agreement is satisfactory considering that the experimental values oscillate around the theoretical ones.

The effects of the same discontinuity printed on a 500 μm GaAs substrate in the form of an equivalent normalized reactance have been studied for both the coplanar and coupled slotline excitations and results are presented in Figure 3.21. As it was pointed above, the coupled slotline mode corresponds to an electric wall at the center of the gap. In this case, the discontinuity can be viewed as a parallel combination of two inductances L_y and L_z which depend on the y- and z-components of the
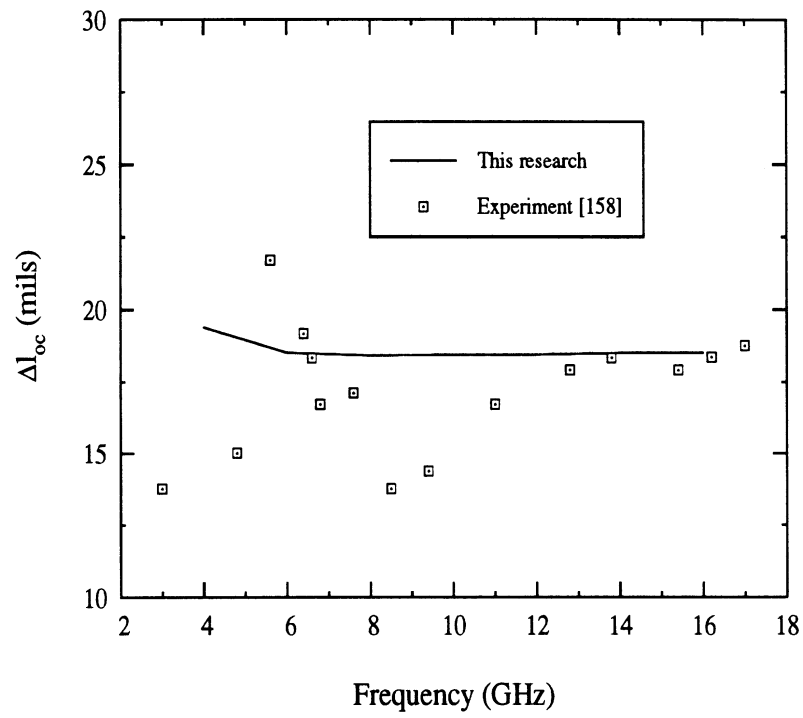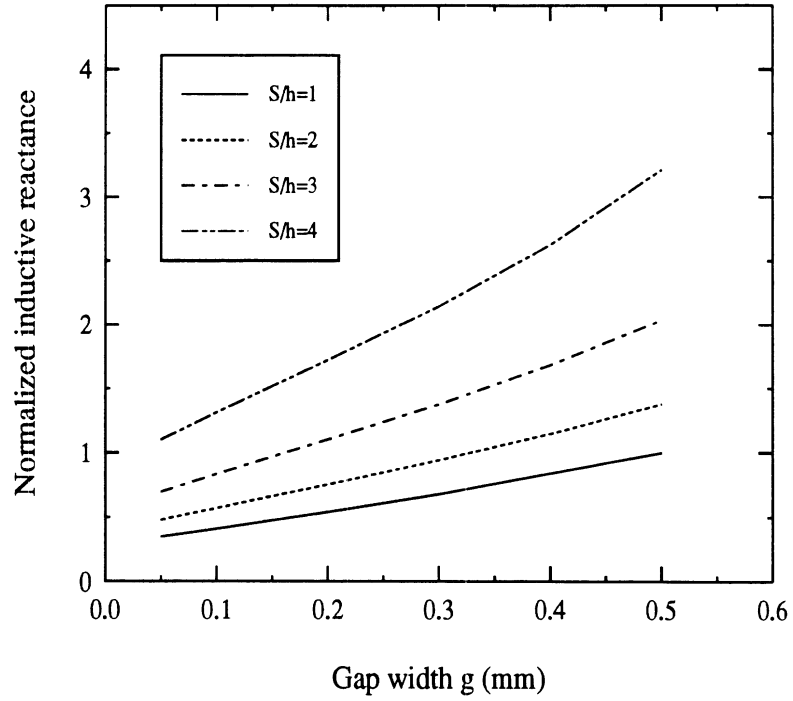
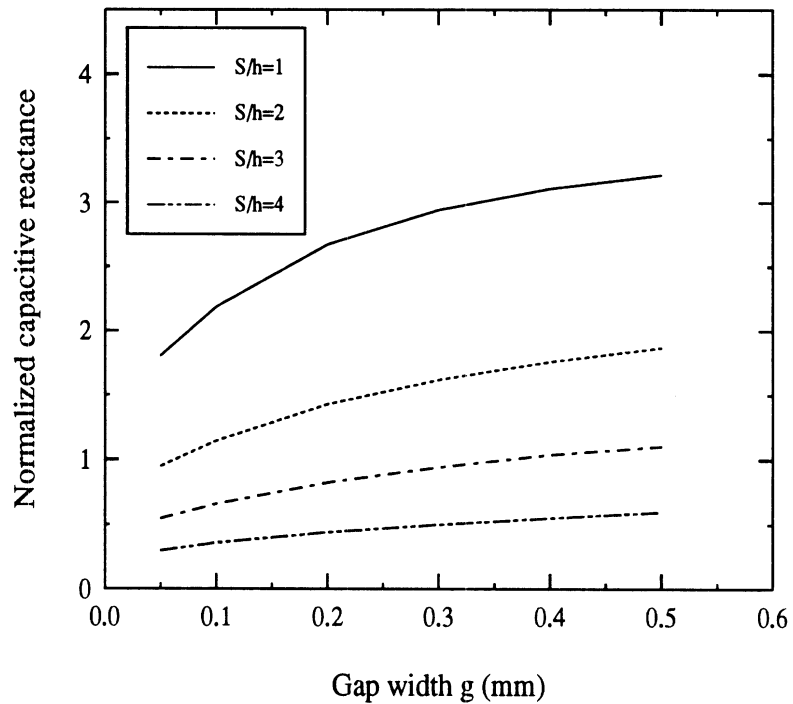Figure 3.20: Effective length extension of an open-end CPW (coplanar mode) as compared to experimental data from [158]. (h=3.175 mm, a=5.08 mm, g=0.381 mm, W=0.254 mm, S=1.14 mm, ϵ_{r1}=2.2, L_1=5h, ϵ_{r2}=1, D_1=4h, D_2=0)

(a) Coupled slotline mode

(b) Coplanar mode

Figure 3.21: Normalized reactance of an open-end CPW on GaAs substrate as a function of the gap width. (h=0.5 mm, a/h=2(W/h)+S/h+10, W=0.25 mm, L_1=5h, f=20 GHz, ϵ_{r1}=13.1, ϵ_{r2}=1, D_1=D_2=5h)

magnetic field distribution in the gap region. As a result, L_y varies as S/g while L_z is proportional to g/S. For large separation distance S, the combination of these two inductances results in an almost linear variation of the total inductance with respect to g (see Figure 3.21(a)). As S becomes much smaller than g, the total inductance is expected to vary as 1/g. On the other hand, a coplanar mode excitation corresponds to a magnetic wall at the center of the gap and, therefore, the discontinuity behaves as an equivalent capacitance. This capacitance can be viewed as a parallel combination of a capacitance due to fringing fields across the gap, and a capacitance due to the fields across the slot [98]. The former capacitance varies proportionally as 1/g, while, the latter one is independent of g. As a result, the equivalent reactance will increase with decreasing separation distance S/h and will increase with increasing gap size. In addition, it saturates to the slot dependent capacitive reactance for large gap widths as seen in Figure 3.21(b). It is worth mentioning that, recently, the CPW open-end discontinuity in open environment has been studied and the results obtained agrees very well with the ones derived here [85, 86].

Figures 3.22 and 3.23 show the effect of mitering the ground plane and the center conductor of an open-end CPW on the reflection coefficient angle with the reference plane taken at the end of the center conductor. In both mitering schemes, a stair-step approximation is used to model the mitered open-end as shown in Figure 3.24. Figure 3.22(a) shows that mitering the ground plane has a significant effect when the gap width g is small while it has little effect when g is large (compared to S). Figure 3.22(b) shows the effect of mitering the ground plane for different center conductor widths with constant g. On the other hand, Figure 3.23 shows the effect of mitering the center conductor on the reflection coefficient angle of the CPW open-end discontinuity with different center conductor widths. From the above results, it can be seen that mitering
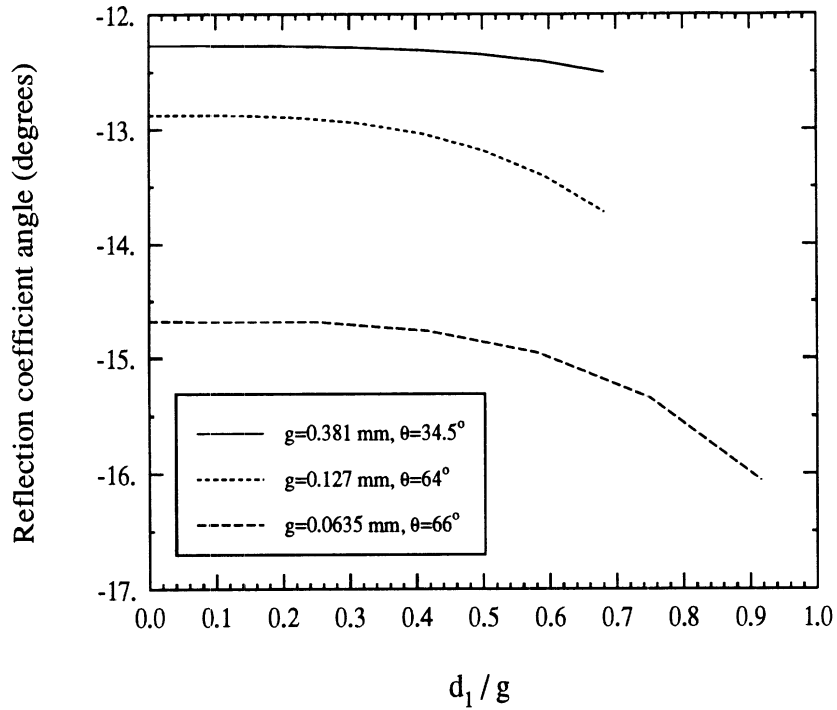
(a) S=6W
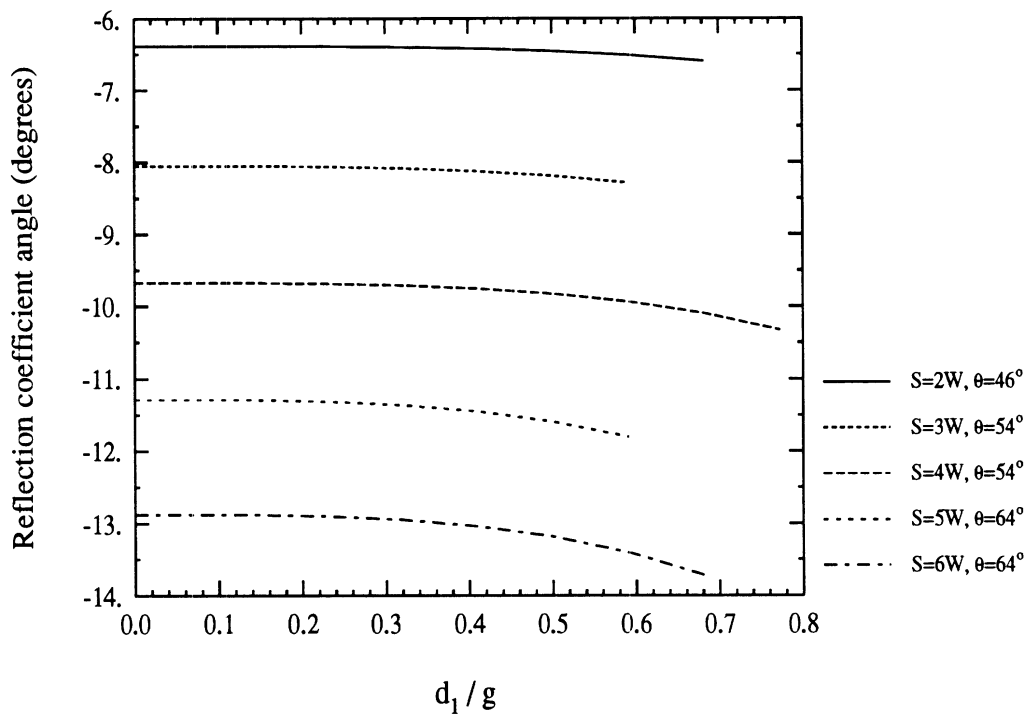
(b) g=0.127 mm

Figure 3.22: The effect of mitering the ground plane of an open-end CPW. (W=47.625 μm, h=0.635 mm, ϵ_{r1}=13, ϵ_{r2}=1, f=20 GHz, a=6 mm, L_1=3h, D_1=D_2=4h)
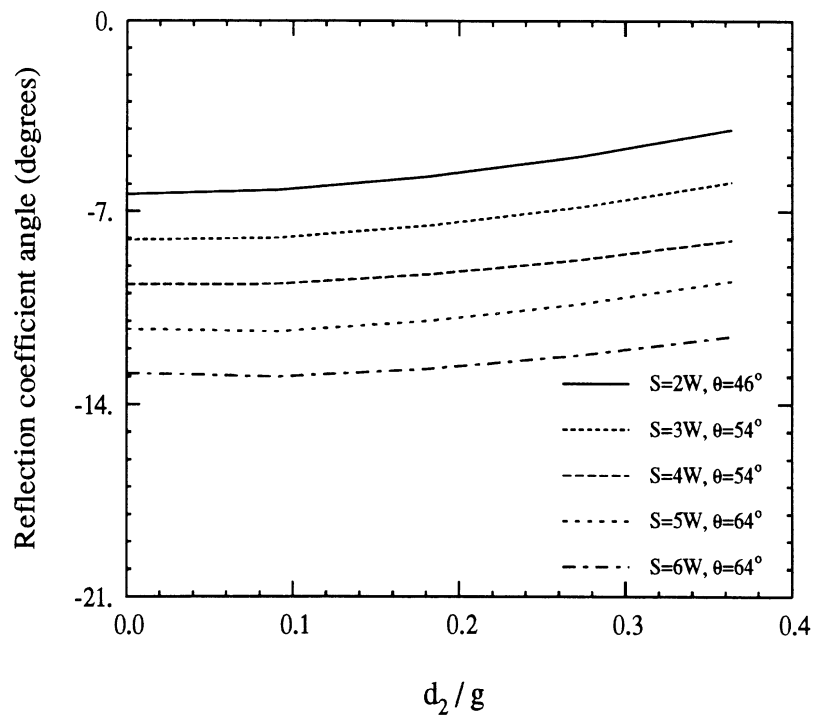
Figure 3.23: The effect of mitering the center conductor of an open-end CPW.
(W=47.625 μm, h=0.635 mm, ϵ_{r1}=13, ϵ_{r2}=1, f=20 GHz, g=0.127 mm,
a=6 mm, L_1=3h, D_1=D_2=4h)

the ground plane of an open-end CPW increases the capacitance seen at the end of

the line, while, mitering the center conductor decreases this capacitance.
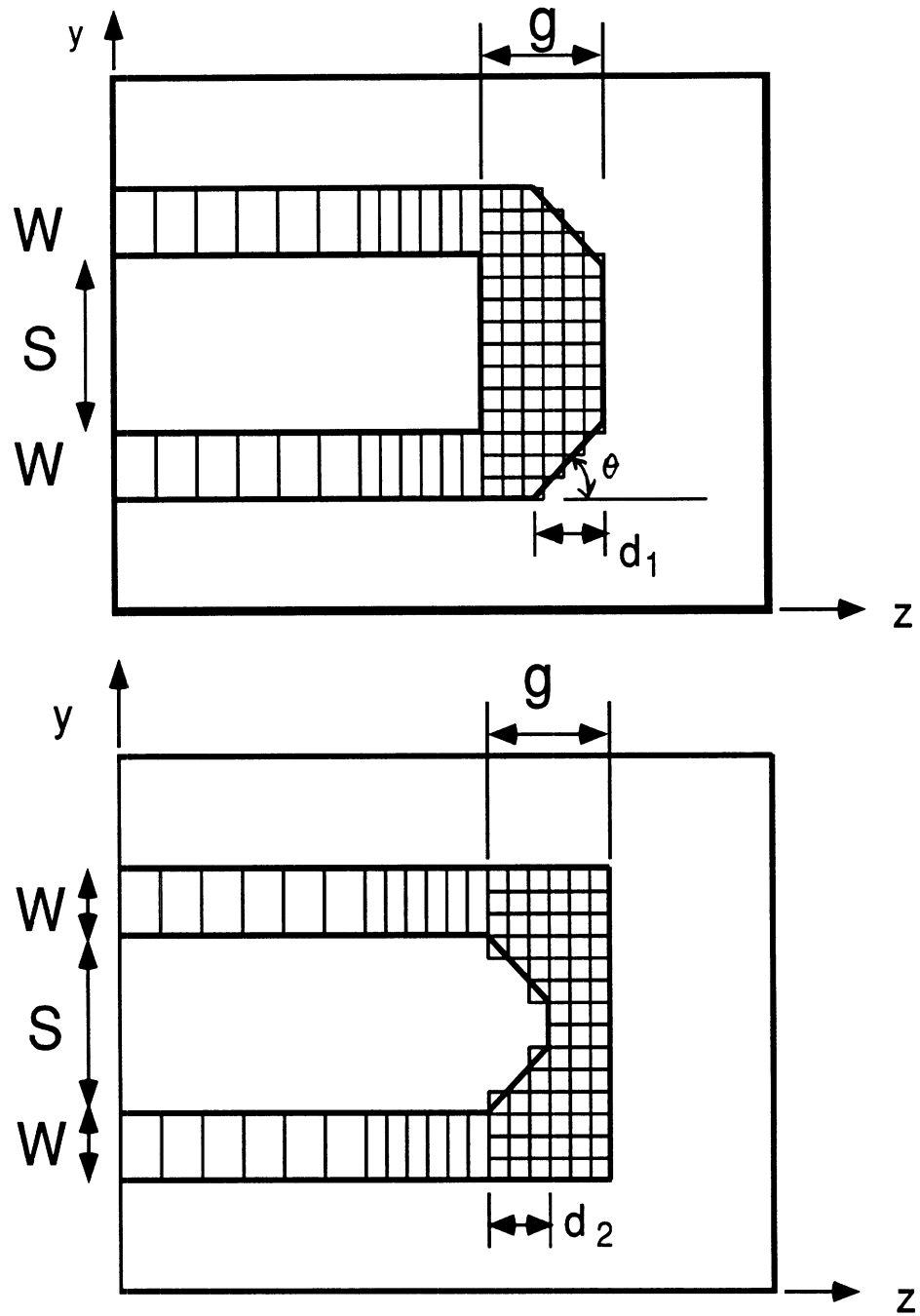
Figure 3.24: The discretization used to model mitered open end.

CHAPTER IV

TWO-PORT CPW DISCONTINUITIES WITHOUT AIR-BRIDGES

4.1   Introduction

In this chapter, the two-port CPW discontinuities shown in Figures 4.1-4.4 are analyzed. As can be clearly seen, all of these discontinuities exhibit transverse symmetry around the center conductor. Thus, theoretically, the coupled slotline is not excited in these lines, and consequently, no air-bridges (or bond wires) are needed.

Figure 4.1 shows three mechanisms of coupling between two CPWs, namely, coupling through short-ends, open-ends, or a gap in the center conductor. Very little is available in the literature about these discontinuities. The series gap in the center conductor of a CPW discontinuity has been studied experimentally in [98] where it was modeled as a Pi-network consisting of a coupling capacitance and two fringing capacitances. In addition, the same discontinuity has been analyzed using the quasi-TEM three dimensional finite difference method in [65]. On the other hand, the transverse resonance technique has been used to study the short-end-coupled CPW discontinuity where it was also modeled as a lumped element Pi-network [82].

Figure 4.2 shows the CPW step discontinuity with and without mitering. Recently, the un-mitered CPW step discontinuity has been studied using the transverse
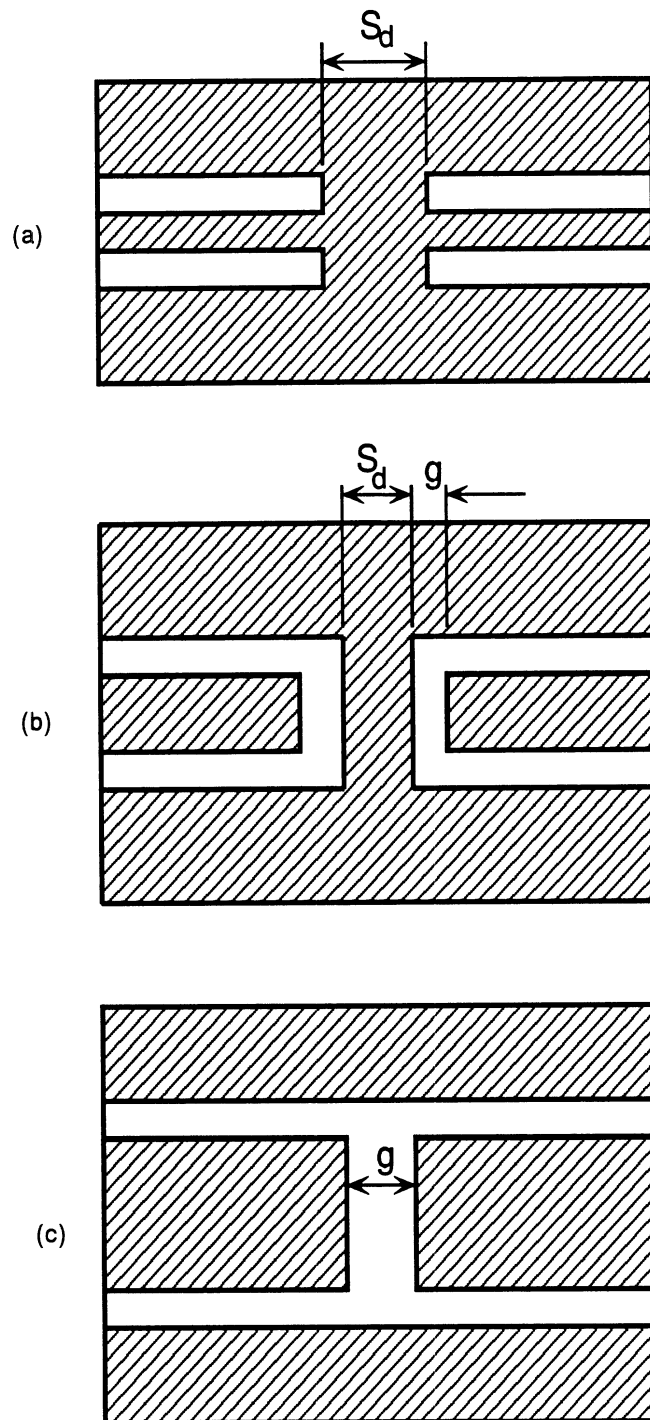
Figure 4.1: (a) Short-end-coupled CPW discontinuity . (b) Open-end-coupled CPW discontinuity. (c) A gap in the center conductor of a CPW.

resonance technique where it has been found that the finite conductor thickness has almost a negligible effect on the characteristics of the discontinuity [79, 80, 81]. Moreover, an approximate analytical model for the CPW step discontinuity has been presented in [123] which included a lumped shunt capacitance as the dominant effect. However, this model has been empirically adjusted so that it agrees with simulation data obtained using the em^{TM} simulator [124].

Filters are important blocks in microwave circuits and are among the first few circuit elements studied in any new technology. Microstrip or stripline filters have been extensively studied and very accurate design techniques have been presented in the literature. However, until recently, CPW filter elements have been investigated only experimentally and lack accurate characterization [2, 3, 4, 57, 99, 125, 126]. Figures 4.3 and 4.4 show four different CPW series stubs which can be used as building blocks for CPW filters. In these figures, PP' refers to the reference planes which are coincident with the input and output ports of the discontinuity. The short-end CPW series stubs shown in Figures 4.3 and 4.4(a) were modeled by Houdart [2] as series inductors. This model cannot predict the resonant nature of the stub as it approaches $\lambda_g/4$. In addition, it cannot predict the asymmetry of the bent stubs, therefore, it is valid only in the limit as the stub length approaches zero. The model used by Ponchak and Simons [59], an ideal short-end series stub, predicts the resonant nature of the stub but not the asymmetry. Similarly, the open-end CPW stub shown in Figure 4.4(b) was modeled by Houdart [2] as a series capacitor. However, such an equivalent circuit is too simple to predict the resonant nature of the stub or its asymmetry. Williams [57] expanded this model to a capacitive Pi-network and selected a reference plane which removed the element asymmetry. This improved model is difficult to incorporate into CAD programs since the reference planes are not at the plane of the
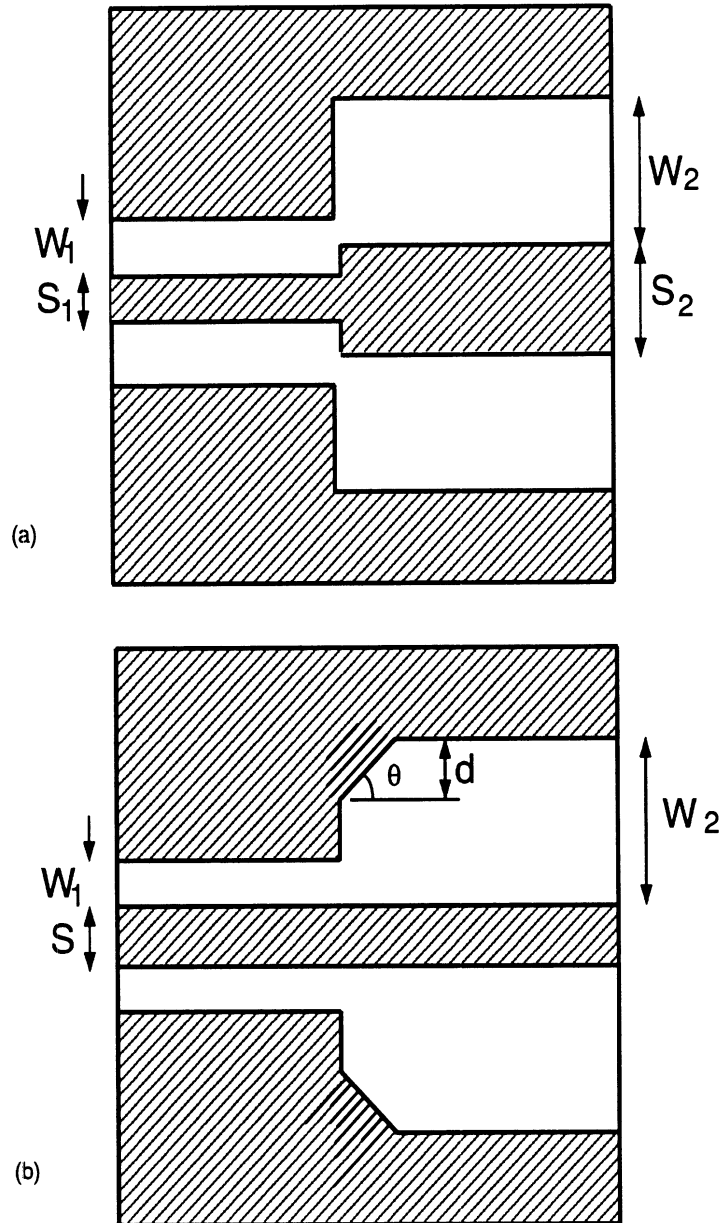
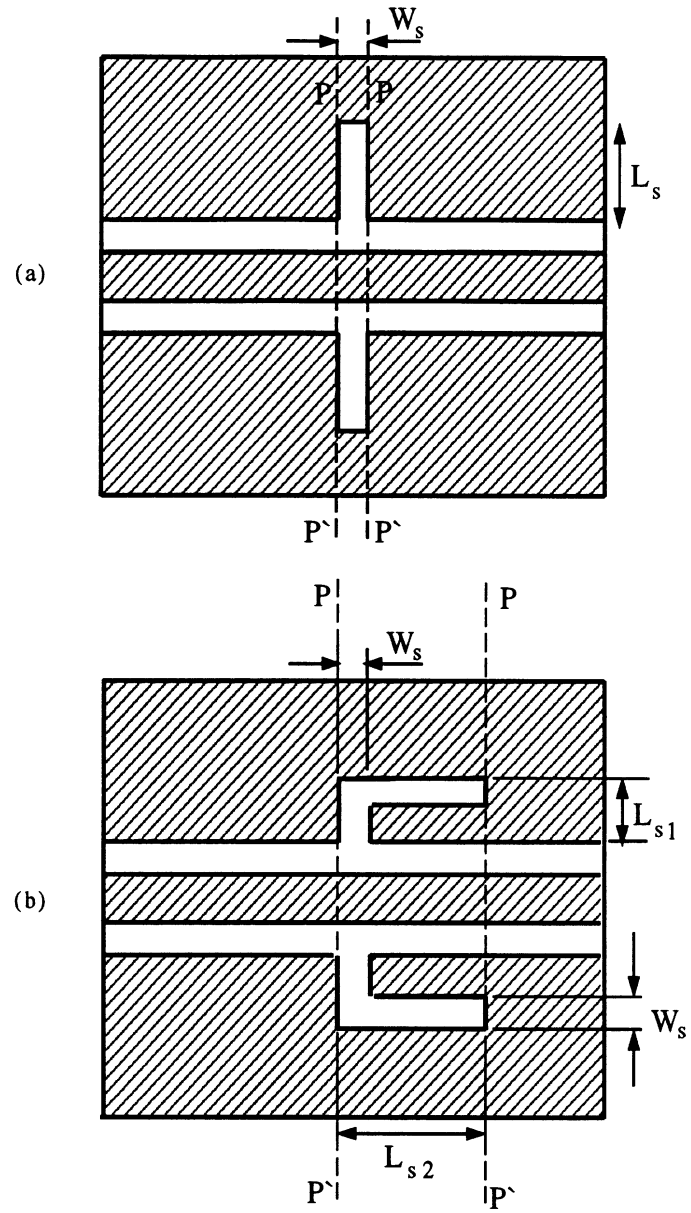Figure 4.2: (a) CPW step discontinuity. (b) Mitered CPW step discontinuity.

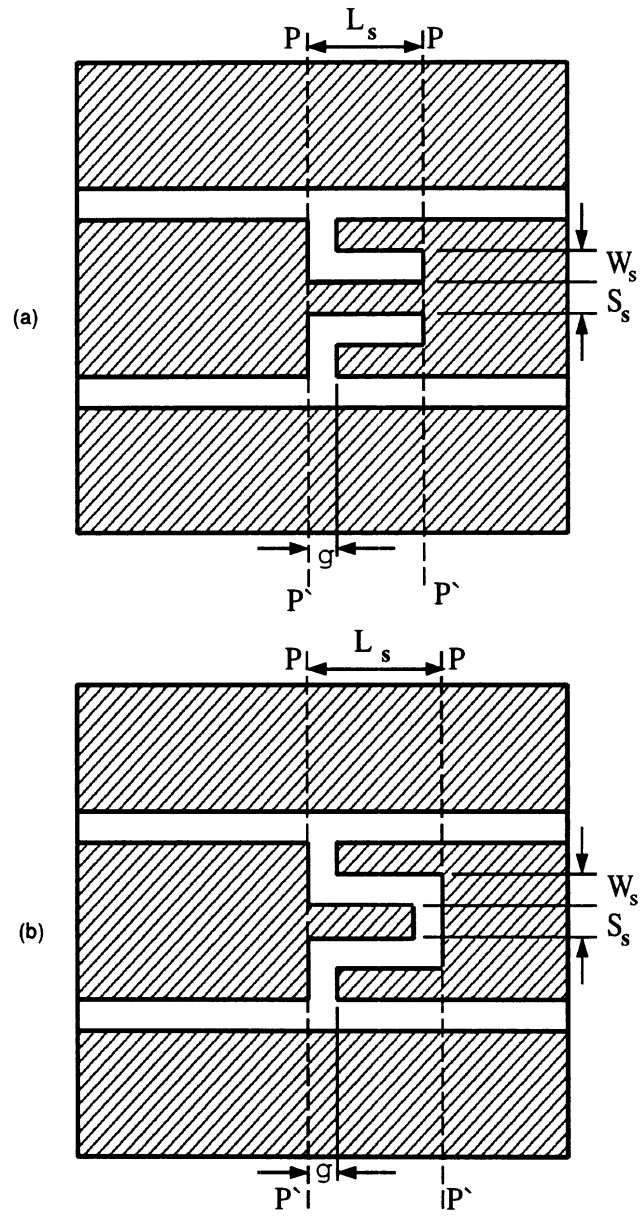Figure 4.3: Straight and bent CPW series stubs printed on the ground plane.

Figure 4.4: Short-end and open-end CPW series stubs printed on the center conductor.

discontinuity as shown in Figure 4.4(b). The model by Ponchak and Simons [59], an ideal open-end series stub, again cannot predict the element asymmetry. In section 4.4.6, lumped element equivalent circuits are proposed to model the discontinuities shown in Figure 4.4. The inductors and capacitors of these models are represented by closed-form expressions, as functions of the stub length, which have potential applications in the design of CPW circuits. It is worth mentioning that some of the two-port CPW discontinuities presented above have been recently used to transform electrical step-like excitations into picosecond pulses [127].

4.2   Network Analysis

In order to characterize a two-port CPW discontinuity, the two ports have to be excited simultaneously as shown in Figure 4.5(a). As it was discussed in the previous chapters, the excitation is modeled by ideal current sources located at specific node points. Hence, one should choose $I'_{g1} = -I_{g1}$ and $I'_{g2} = -I_{g2}$ in order to study the characteristics of the discontinuity under coplanar mode excitation. In contrast, the coupled slotline mode characteristics can be studied by choosing $I'_{g1} = I_{g1}$ and $I'_{g2} = I_{g2}$. However, only the coplanar mode will be considered here since it tends to concentrate the fields around the slot aperture (low radiation loss) and is therefore the commonly used mode in CPW circuits.

An equivalent lumped element T-network of the discontinuity and the corresponding equivalent Pi-network are shown in Figures 4.5(b) and (c). The elements of the equivalent Pi-network can be derived from those of the T-network using the following expressions [128]:

$$z_{f1} = \frac{z_{11}z_{22} - z_{12}^2}{z_{22} - z_{12}} \tag{4.1}$$

$$z_{f2} = \frac{z_{11}z_{22} - z_{12}^2}{z_{11} - z_{12}} \tag{4.2}$$
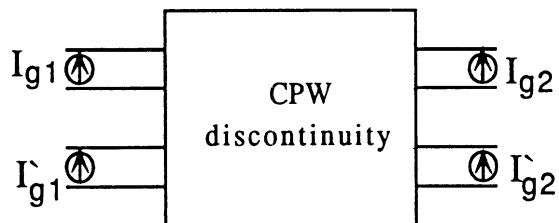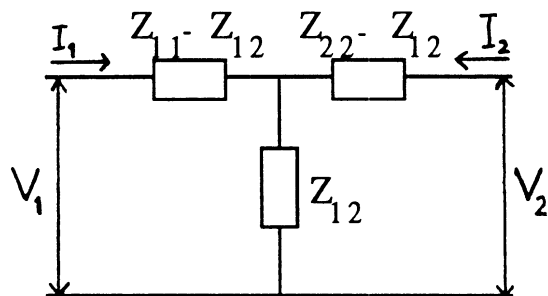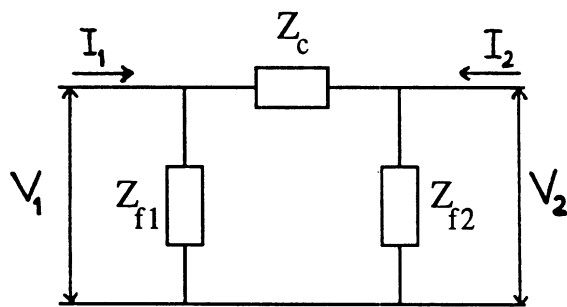
Figure 4.5: (a) A general two-port CPW discontinuity with ideal electric current sources. (b) Equivalent T-network representation. (c) Equivalent Pi-network representation.

$$z_c = \frac{z_{11}z_{22} - z_{12}^2}{z_{12}} \qquad (4.3)$$

It should be noted that the currents and voltages (I_1, I_2, V_1 and V_2) shown in Figures 4.5(b) and (c) are induced at the discontinuity ports as a consequence of the assumed ideal electric current sources. Thus, the discontinuity may be represented by a two-port network which is characterized by the following matrix equation:

$$\begin{bmatrix} V_1 \\ V_2 \end{bmatrix} = \begin{bmatrix} z_{11} & z_{12} \\ z_{12} & z_{22} \end{bmatrix} \begin{bmatrix} I_1 \\ I_2 \end{bmatrix} \qquad (4.4)$$

where $[z]$ is the normalized network impedance matrix (with respect to the line characteristic impedance). The scattering parameters matrix $[S]$ can be obtained from the equation:

$$[S] = ([z] - [U]) \, ([z] + [U])^{-1} \qquad (4.5)$$

where $[U]$ is the identity matrix.

For longitudinally symmetric discontinuities, such as the ones in Figures 4.1 and 4.3(a), the impedance parameters z_{11} and z_{22} are equal. Thus, in this case, there exists two unknowns to be determined; namely, z_{11} and z_{12}. These unknowns can be determined from the input impedances corresponding to the even ($I_{g1} = I_{g2} = I_e$) and odd ($I_{g1} = -I_{g2} = I_o$) excitation mechanisms of the two-port discontinuity. The even excitation mechanism corresponds to a perfectly magnetic wall placed at the center of the circuit (i.e. z=L/2 plane), while, the odd excitation mechanism corresponds to an electric wall. It should be noted that this is in contrast to symmetric microstrip discontinuities where an even (odd) excitation mechanism corresponds to an electric (magnetic) wall placed at the symmetry plane [111]. Thus, the normalized network impedance parameters can be evaluated as [111]:

$$z_{11} = \frac{z_{in}^e + z_{in}^o}{2} \qquad (4.6)$$

$$z_{12} = \frac{z_{in}^e - z_{in}^o}{2} \tag{4.7}$$

where z_{in}^e and z_{in}^o are the normalized input impedances at the reference plane PP′ (at either port) when the two-port discontinuity is under even and odd excitation mechanism, respectively. These input impedances may be obtained from the positions of the minima and the maxima of the electric field standing wave in the feeding lines as was discussed in Chapter 3.

In case of longitudinally asymmetric discontinuities, such as the ones in Figures 4.2, 4.3(b) and 4.4, three different excitation mechanisms are needed to evaluate the unknown impedance parameters z_{11}, z_{12} and z_{22}. One can use the above even and odd excitation mechanisms and any other third excitation that is linearly independent of them (e.g. $I_{g1}=1$ and $I_{g2}=2$). Then, the normalized network impedance parameters may be obtained from the following expressions [118]:

$$z_{11} = z_{in_1}^t + \left(z_{in_1}^t - z_{in_1}^o\right)\left(z_{in_1}^t - z_{in_1}^e\right)\frac{z_{in_2}^e - z_{in_2}^o}{Z} \tag{4.8}$$

$$z_{22} = z_{in_2}^t - \left(z_{in_2}^t - z_{in_2}^o\right)\left(z_{in_2}^t - z_{in_2}^e\right)\frac{z_{in_1}^e - z_{in_1}^o}{Z} \tag{4.9}$$

$$z_{12} = \pm\left(z_{in_1}^e - z_{11}\right)\sqrt{\frac{z_{in_2}^e - z_{22}}{z_{in_1}^e - z_{11}}} \tag{4.10}$$

where

$$Z = \left(z_{in_1}^t - z_{in_1}^o\right)\left(z_{in_2}^t - z_{in_2}^e\right) - \left(z_{in_1}^t - z_{in_1}^e\right)\left(z_{in_2}^t - z_{in_2}^o\right) \tag{4.11}$$

In the above, $z_{in_{1,2}}^{e,o,t}$ are the normalized input impedances at ports 1 and 2 for the even (e), odd (o) and the third (t) excitation mechanisms, respectively. The derivation of (4.8)-(4.11) is straight forward and may be found in [118]. The choice of the sign of z_{12}, as given in (4.10), can be decided by noting that z_{12} may be written as [118]:

$$z_{12} = \left(z_{in_1}^e - z_{11}\right)\left(\frac{V_1^e z_{in_2}^e}{V_2^e z_{in_1}^e}\right) \tag{4.12}$$

where V_1^e and V_2^e are the mode voltages at ports 1 and 2 for the even excitation mechanism. Comparing equations (4.10) and (4.12), it is clear that the sign of z_{12} in 4.10 should match the sign of the factor $\left(\frac{V_1^e z_{in_2}^e}{V_2^e z_{in_1}^e} \right)$.

4.3 Numerical Considerations

As was discussed in Chapter 3, the summations involved in computing the elements of the admittance matrix (2.72) - (2.73) are truncated to the values $MSTOP$ and $NSTOP$. The values of these two parameters should be chosen such that convergence of the scattering coefficients is assured. Figures 4.6 and 4.7 show the convergence behavior of the scattering parameters of a short-end series CPW stub printed on the center conductor with respect to each one of the above parameters. It can be seen that the results are more sensitive to the choice of $NSTOP$ than $MSTOP$. In Figure 4.6, results could not be derived with $NSTOP$ less than 400 because the admittance matrix was ill conditioned which resulted in an erroneous magnetic current distribution (i.e. without well defined peaks). For example, the condition number was of the order of 10^{13} for $NSTOP$=300. In addition, it can be noticed that $NSTOP$=600 is enough to insure convergence for the example shown in Figure 4.6. The percentage difference between Mag(S_{11}) at $NSTOP$=600 and that at $NSTOP$=1000 is only 0.13%. On the other hand, Figure 4.7 shows that small values of $MSTOP$ are adequate to generate a well conditioned admittance matrix. Specifically, in this example, the percentage difference between Mag(S_{11}) at $MSTOP$=100 and that at $MSTOP$=1000 is only 0.15%.

Another critical parameter for the convergence of the results is the number of the considered basis functions N_y and N_z. As shown in Figure 4.8 for the case of an open-end CPW series stub, only a longitudinal magnetic current is assumed to exist

Figure 4.6: Convergence behavior of the scattering parameters of a short-end CPW series stub printed on the center conductor with respect to the number of modes $NSTOP$ with $MSTOP=1000$. ($L_s=1500$ μm, W=225 μm, S=450 μm, $W_s=$g=75 μm, $S_s=150$ μm, h= 0.635 mm, $D_1=D_2=$ 3.175 mm, $\epsilon_{r1}=$ 9.9, $\epsilon_{r2}=$ 2.2, a=4.71 mm, f=15 GHz)
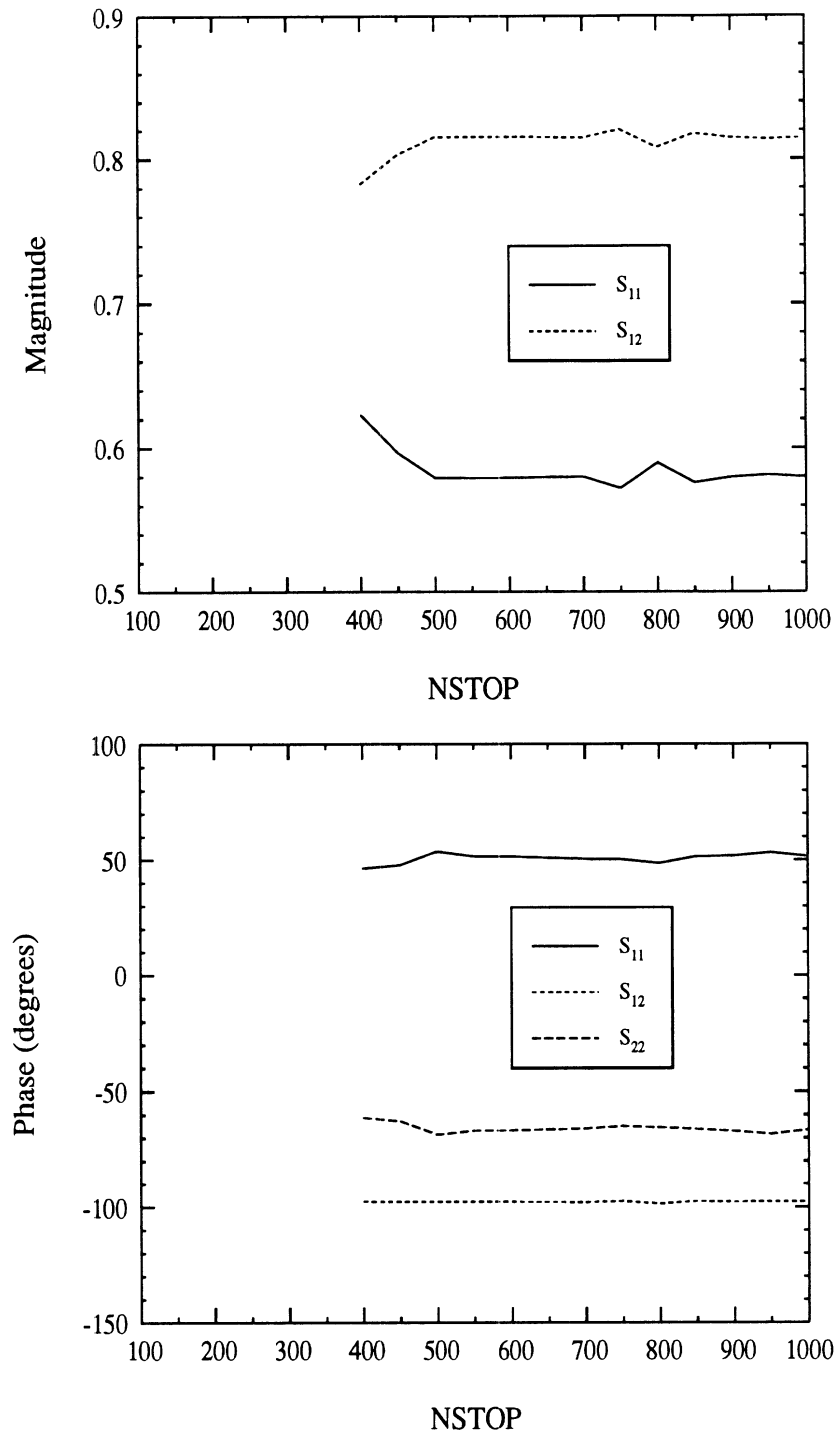
Figure 4.7: Convergence behavior of the scattering parameters of a short-end CPW series stub printed on the center conductor with respect to the number of modes *MSTOP* with *NSTOP*=1000. Dimensions are the same as in Figure 4.6
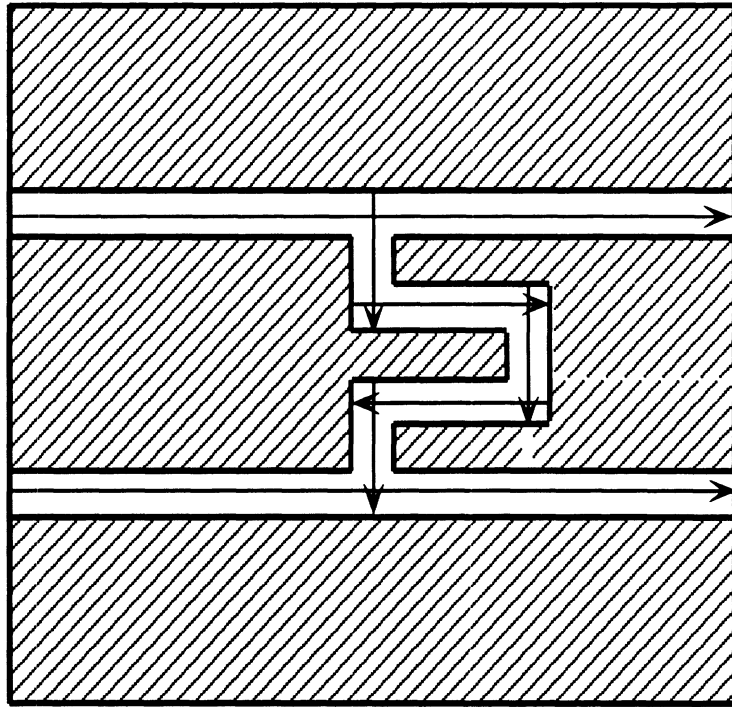
Figure 4.8: The assumed magnetic current distribution in the slot aperture of an open-end CPW series stub. A longitudinal magnetic current is assumed in the slots except in the transition regions where both components are considered.

in the slots, however, both longitudinal and transverse magnetic current components are considered in the transition regions. Figure 4.9 shows the scattering parameters of a short-end CPW series stub printed on the center conductor as a function of the number of basis functions per guide wavelength used to model the z-directed magnetic current in the feeding lines. The percentage difference between $Mag(S_{11})$ obtained with 35 basis functions per wavelength and that corresponding to 130 basis functions is only 0.3%.

The CPU time required for the evaluation of the scattering parameters depends mainly on the geometry and the electrical size of the structure. However, as it was mentioned in Chapter 3, the number of unknowns is reduced by placing a perfectly magnetic wall at the transverse symmetry plane of the discontinuity. A typical CPU
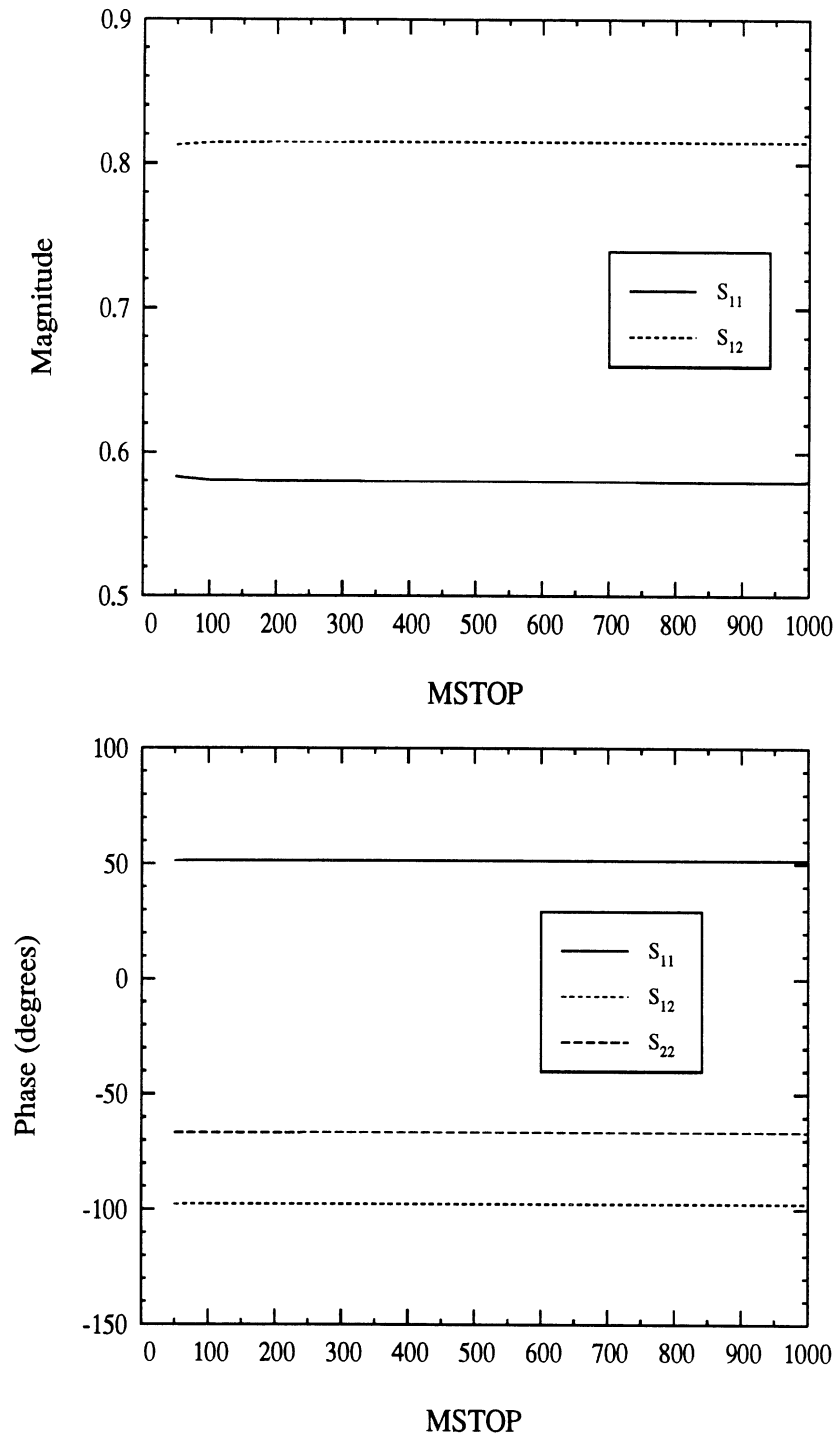
Figure 4.9: Convergence behavior of the scattering parameters of the short-end CPW series stub printed on the center conductor with respect to the number of basis functions per guide wavelength in the feeding lines. Dimensions are the same as in Figure 4.6 with $NSTOP=MSTOP=1000$.
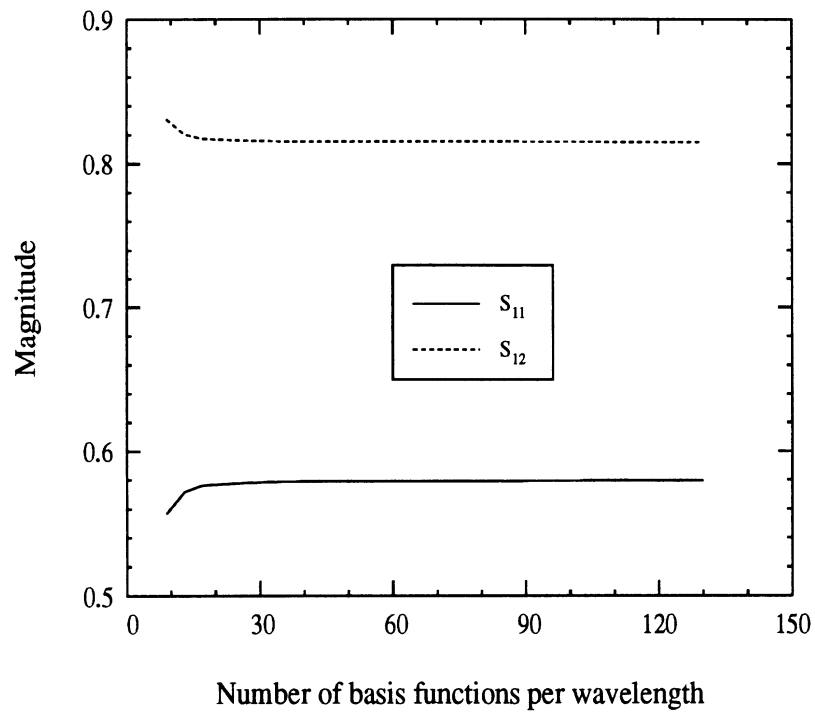
time ranges from 1 minute for the case of short-end-coupled CPWs discontinuity to 15 minutes for the case of a mitered CPW step discontinuity on an Apollo domain 10000.

4.4   Numerical Results

In all the results presented in this section, the CPW structure is suspended inside the rectangular cavity as shown in Figure 3.6. In almost all cases, the dimensions of the cavity are chosen such that cavity resonances are above the considered frequency range.

4.4.1   Short-End-Coupled CPW Discontinuity

The short-end-coupled CPW discontinuity shown in Figure 4.1(a) can be modeled as a lumped element T-network. Figure 4.10 shows the normalized reactances of this equivalent circuit for a short-end-coupled CPW discontinuity as a function of the separation distance between the two lines. In this figure, the reactances X_1 and X_2 denote the normalized series and shunt reactances in the T-network model, respectively, and are defined as follows (in accordance with Figure 4.5(b)):

$$X_1 = \frac{z_{11} - z_{12}}{j} \tag{4.13}$$

$$X_2 = \frac{z_{12}}{j} \tag{4.14}$$

It can be seen that both reactances are inductive and that X_2 approaches zero as the separation distance increases and the coupling between the two lines decreases. On the other hand, X_1 approaches the reactance corresponding to the end effect of a shorted CPW as the separation distance increases. Figure 4.10 shows that the coupling between the two lines is very small even for relatively small separation distances. Specifically, for the example shown in Figure 4.10, the insertion loss (i.e. S_{12})
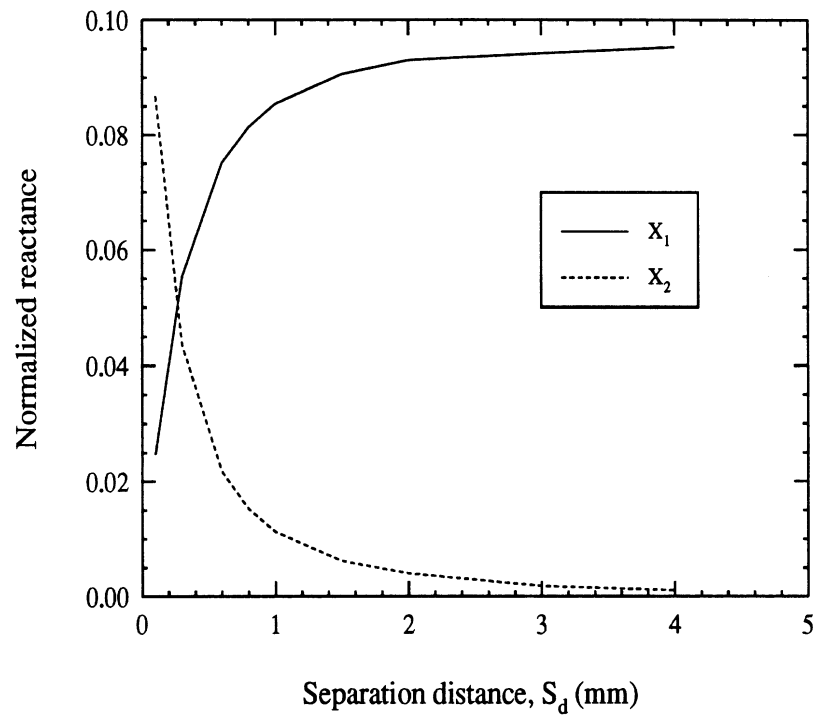
Figure 4.10: The normalized reactances of the T-network representing the short-end-coupled CPWs discontinuity as a function of the separation distance. (W=0.225 mm, S=0.45 mm, ϵ_{r1}=9.9, ϵ_{r2}=1, h=0.635 mm, f=15 GHz, a=4.71 mm, $D_1 = D_2$=3.175 mm)

is approximately -20 dB for a separation distance of just 0.3 mm.

4.4.2 CPW Gap Discontinuity

The CPW gap discontinuity shown in Figure 4.1(c) can be best modeled as a Pi-network (Figure 4.5(c)). In this case, one can define a fringing capacitance, C_f, due to the fringing field from the center conductor to the ground and a coupling capacitance, C_c, due to the fields between the two opposing center conductors [98]. These capacitances may be computed from the following expressions (in accordance with Figure 4.5(c)):

$$C_f = \frac{1}{j\omega z_f Z_0} \tag{4.15}$$

$$C_c = \frac{1}{j\omega z_c Z_0} \tag{4.16}$$

where Z_0 is the characteristic impedance of the CPW and $z_f = z_{f1} = z_{f2}$. Figure 4.11 shows the two equivalent capacitances in pF, obtained both theoretically and experimentally [98], as a function of gap width for a 50 Ω CPW. The maximum difference between the theoretical and experimental data for both capacitances is approximately 30%. This large discrepancy may be due to the fact that the experiments were performed on unshielded CPW structures [98]. Also, values of the coupling capacitance C_c obtained using the expression in [129] are shown in the same figure. This expression is derived by applying the principle of duality for electromagnetic fields on planar circuits and assuming a very narrow gap. Such an analysis is valid provided that the the circuits can be described reasonably as quasi-TEM structures. In addition, it assumes ideal discontinuities, thus, it can not predict values for the fringing capacitance. It can be noticed that this set of data agrees better with the results obtained using the theory developed here than the experimental ones. The
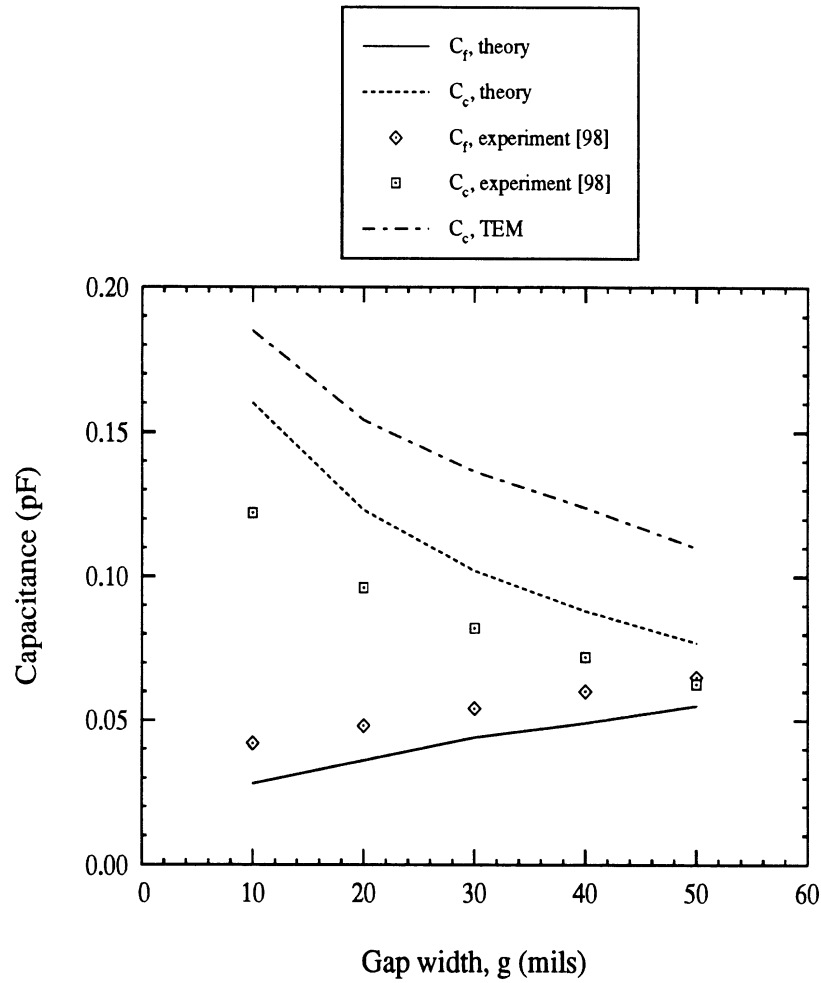
Figure 4.11: The equivalent capacitances due to a gap in the center conductor of a CPW. C_f is the fringing capacitance and C_c is the coupling one. (W=0.2794 mm, S=18W, ϵ_{r1}=2.2, ϵ_{r2}=1, h=3.175 mm, f=6 GHz, a=25 mm, $D_1 = D_2$=12.7 mm)

percentage difference increases from 13% at g=10 mils to 30% at g=50 mils. This is due to the fact that for relatively large gap widths, the fringing capacitance can no longer be neglected. Figure 4.11 shows that the coupling capacitance C_c decreases proportionally as $1/g$, while, the fringing capacitance C_f increases to the open-end saturation capacitance for large gap widths g [98].

Figure 4.12: Mag(S_{12}) for the open-end-coupled CPWs discontinuity for different separation distances. (h=300 μm, ϵ_{r1}=13, ϵ_{r2}=1, S=75 μm, W=50 μm, Z_0=50 Ω, g=25 μm, D_1=D_2=1.2 mm, a=2 mm)

4.4.3 Open-End-Coupled CPW Discontinuity

The open-end-coupled CPW discontinuity shown in Figure 4.1(b) is best modeled by a Pi-network (Figure 4.5(c)). In this case, z_c corresponds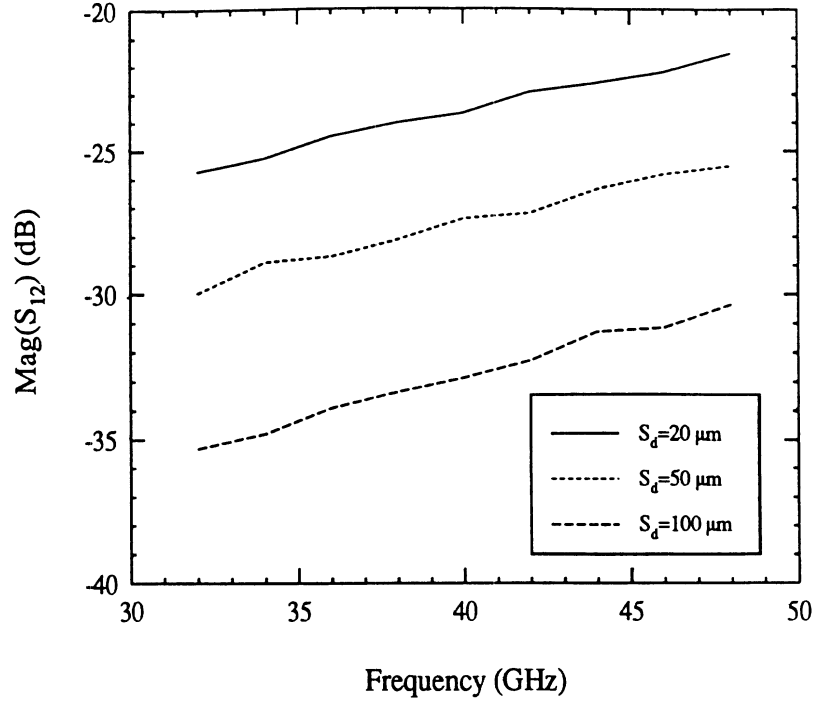 to the coupling between the two CPW lines, while, $z_f = z_{f1} = z_{f2}$ is due to the fringing fields at the end of the uniform lines. As a first example, Figure 4.12 shows Mag(S_{12}) for an open-end-coupled CPW discontinuity as a function of frequency for different separation distances. It can be seen that the coupling between the two lines is small even with a separation distance of 20 μm. Figure 4.13 shows the normalized fringing and coupling reactances (with respect to the characteristic impedance) of the equivalent Pi-model of the discontinuity with reference planes chosen to coincide with the end of the center conductors. It can be noticed that X_c increases as the separation distance increases, thus, reducing the coupling between the two lines. On the other hand, X_f decreases

Figure 4.13: Normalized coupling and fringing reactances for the open-end-coupled CPW discontinuity for different separation distances. Dimensions are as in Figure 4.12.

slightly as the separation distance increases.

As another example, Figure 4.14 shows $\text{Mag}(S_{12})$ for an open-end-coupled CPW discontinuity as a function of separation distance. It can be noticed that there is a resonance effect for a separation of 0.8 mm. In order to understand such a resonance, Figure 4.15 shows the normalized coupling and fringing reactances of the equivalent Pi-network for the same discontinuity. It is clearly seen that the coupling reactance X_c changes from capacitive to inductive at S_d=0.8 mm. On the other hand, the fringing reactance X_f converges to the value corresponding to the reactance seen at the end of an open-end CPW as the separation distance increases. It is worth mentioning here that the open-end-coupled CPW structure is widely used as a test fixture for making precise scattering parameters measurements of a wide variety of active and passive circuit elements [130, 131]. This is performed by mounting the element (or (M)MIC)
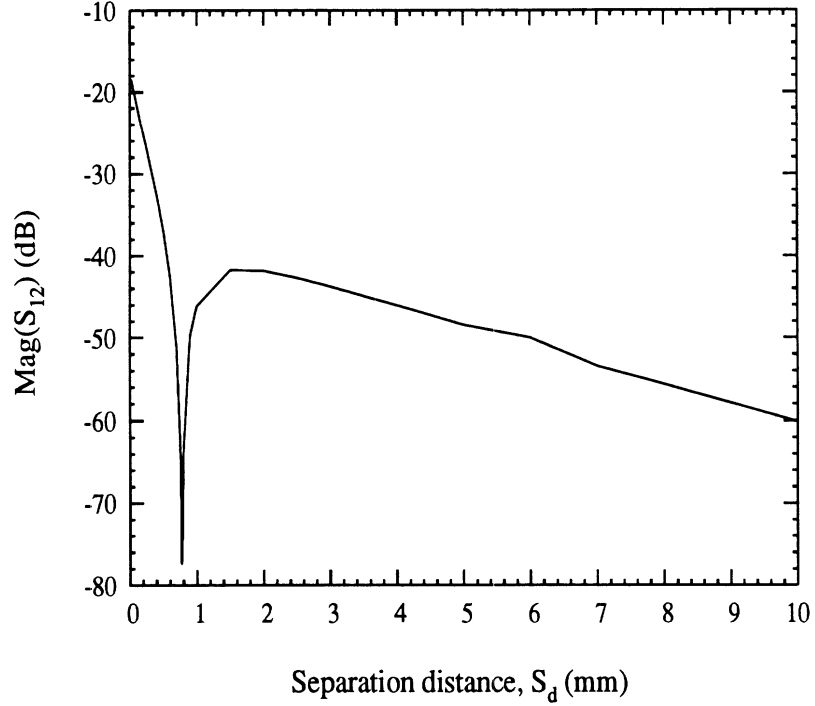
Figure 4.14: Mag(S_{12}) for the open-end-coupled CPW discontinuity as a function of separation distance. (h=500 μm, ϵ_{r1}=13.1, ϵ_{r2}=1, S=500μm, W=250 μm, g=300 μm, D_1=D_2=2.5 mm, a=6 mm, f=20 GHz)

on the central area (called ground plane mounting island) and connecting it to the CPW lines using bondwires. In the design of these fixtures, the isolation between the input and output ports must be high enough over an operating frequency range to insure the stability of the measurements.

4.4.4 CPW Step Discontinuity

Figure 4.16 shows Mag(S_{11}) for a CPW step discontinuity, shown in Figure 4.2(a), as compared to data derived using both mode matching technique [81] and ideal transmission line (TL) theory. The difference between the data obtained using the present theory and the mode matching technique is less than 1.5% in the whole frequency range. For this CPW step, the change in Mag(S_{11}) is only 7% as the operating frequency increases from 20 to 40 GHz. This suggests that the CPW step
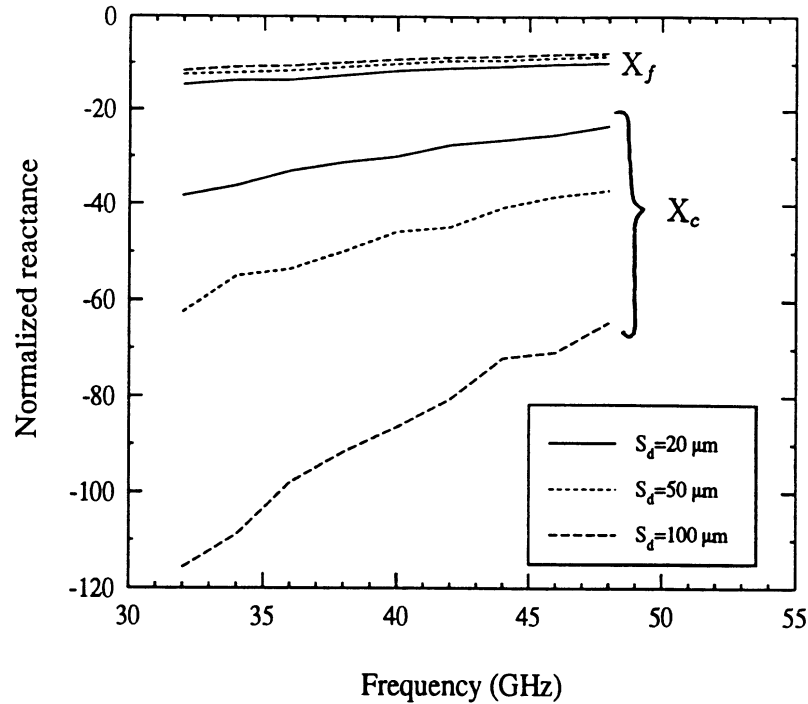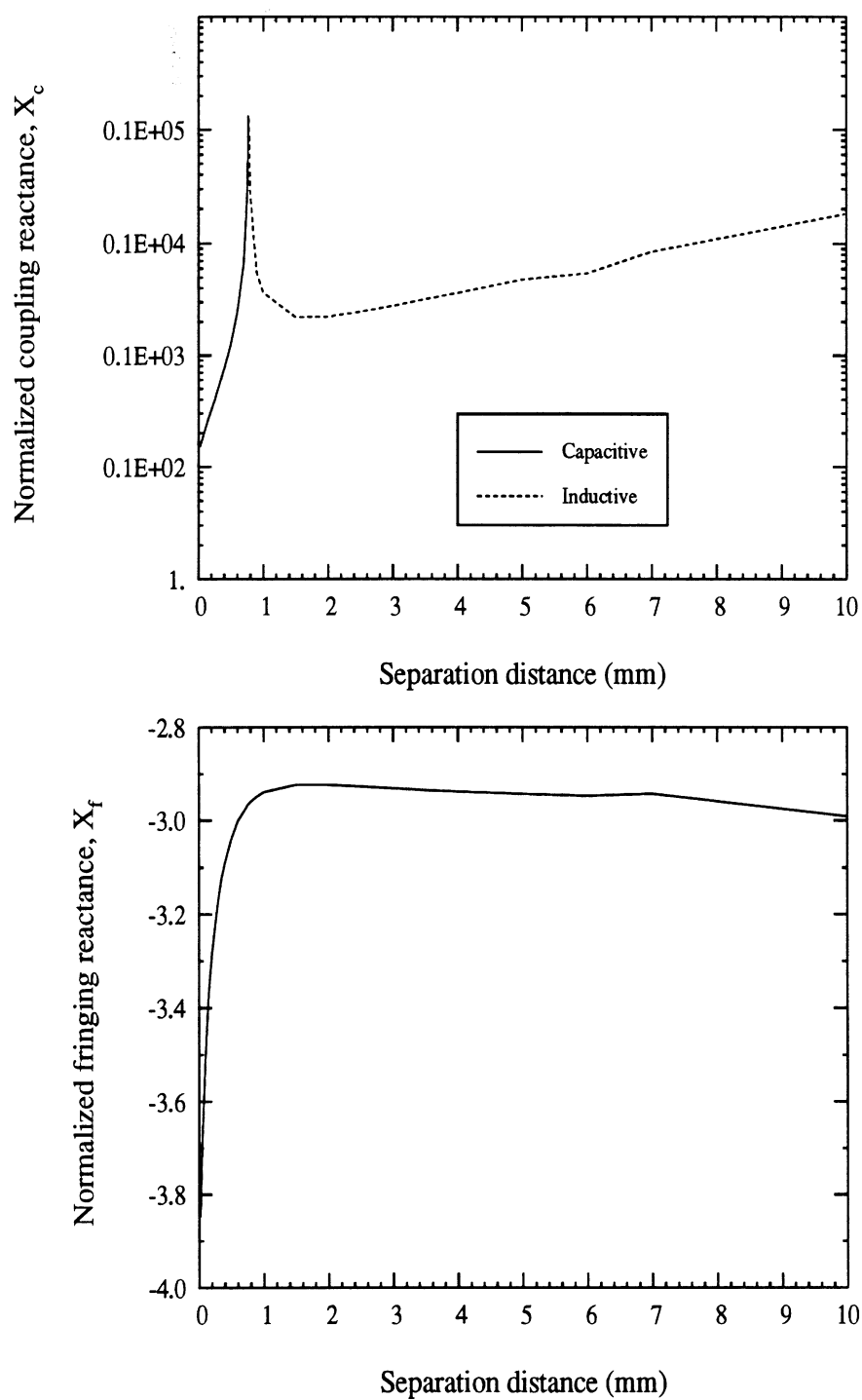
Figure 4.15: Normalized coupling and fringing reactances for the open-end-coupled CPW discontinuity as a function of separation distances, dimensions are as in Figure 4.14.
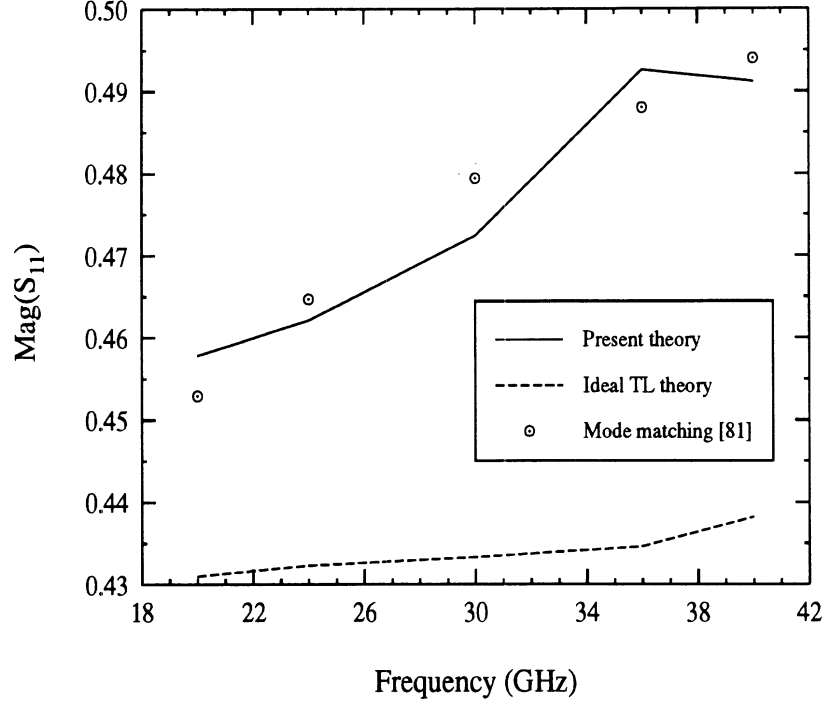
Figure 4.16: Mag(S_{11}) for the CPW step discontinuity as a function of frequency. (h=254 μm, ϵ_{r1}=9.6, ϵ_{r2}=1, S_1=800 μm, S_2=200 μm, W_1=100 μm, W_2=600 μm, D_1=3.555 mm, D_2=3.3 mm, a=3.56 mm)

discontinuity is not significantly dispersive. In the case of ideal TL theory, the return

loss is calculated using the formula

$$S_{11} = \frac{Z_{02} - Z_{01}}{Z_{02} + Z_{01}} \tag{4.17}$$

where the characteristic impedances are obtained using full wave analysis [121]. The

maximum difference between Mag(S_{11}) derived using the present theory and that

obtained using ideal TL theory is 12% occuring at 40 GHz. This is due to the fact

that the discontinuity effect of the step increases as the operating frequency increases.

Figure 4.17 shows the effect of mitering the CPW step discontinuity (Figure 4.2(b))

on the return loss for two different slot widths W_2. As expected, mitering reduces

the return loss since a smoother transition is obtained. It can also be noticed that
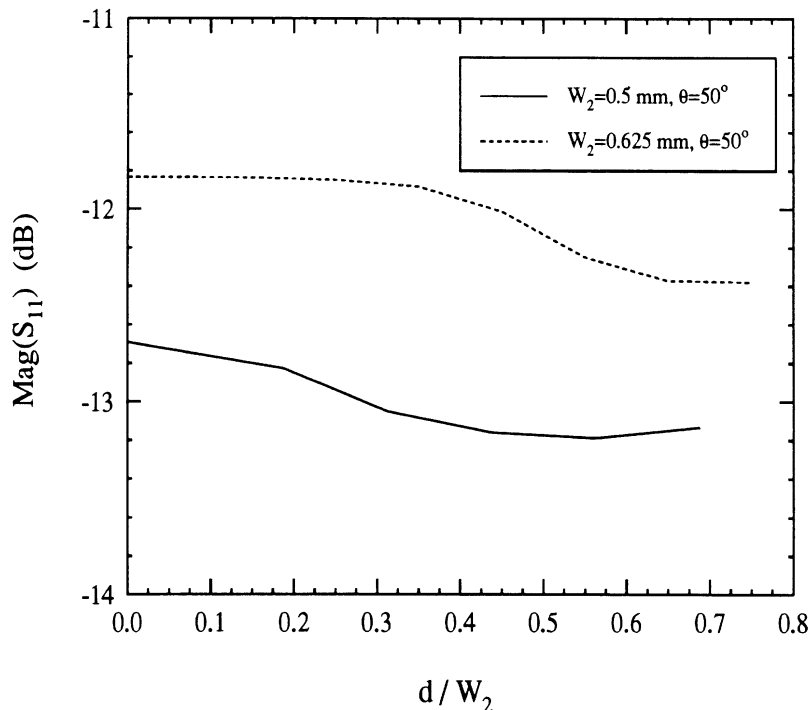
Figure 4.17: Effect of mitering on Mag(S_{11}) for the CPW step discontinuity. (h=254 μm, ϵ_{r1}=2.22, ϵ_{r2}=1, S=1 mm, W_1=125 μm, f=30 GHz, D_1=3.555 mm, D_2=3.3 mm, a=3.56 mm)

the return loss from the line with the larger slot width W_2 is higher than that from the line with the smaller W_2. In case ideal TL theory is used to compute the return loss (assuming un-mitered step), one gets -14.3 dB and -13.1 dB for the line with W_2=0.5 mm and W_2=0.625 mm, respectively.

4.4.5 CPW Series Stubs Printed on the Ground Plane

The structures under consideration in this section are shown in Figure 4.3, namely, the CPW straight and bent series stubs printed on the ground plane. Figure 4.18 shows the scattering parameters for the straight CPW stub discontinuity in the frequency range 5-30 GHz. From these results, one may observe that a resonant frequency exists at 22 GHz, at which the length of the stub is approximately a quarter of a wavelength. Experimental data, which were supplied by Ponchak [132], are also
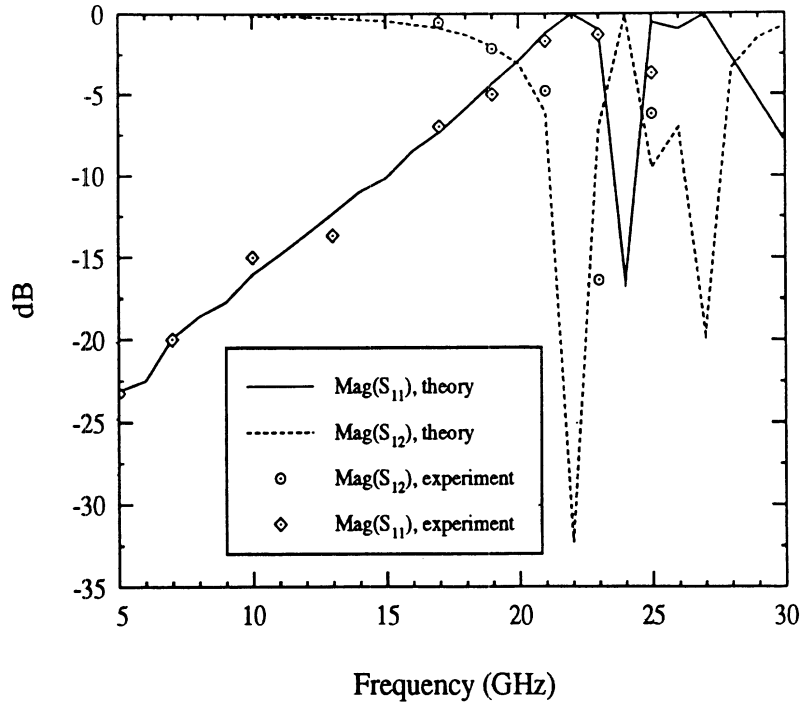
Figure 4.18: Scattering parameters for the CPW straight series stub printed on the ground plane. (W=0.225 mm, S=0.45 mm, h=0.635 mm, $D_1=D_2$=3.175 mm, L_s=1.25 mm, W_s=0.15 mm, ϵ_{r1}=9.9, ϵ_{r2}=2.2, a=4.71 mm)

shown in the same figure. It can be seen that the agreement is generally good. However, there is a discrepancy around resonance which is due to the fact that experiments were performed on an open CPW structure. Moreover, an anomalous behavior in the theoretical data can be noticed in Figure 4.18 around 24 GHz. This is due to the excitation of the LSM_{111} (f_{111}=24.1 GHz) cavity mode in the partially filled lower cavity. It should be noted that although the end of the stubs are just one substrate thickness away from the cavity walls, the theoretical results are in good agreement with experimental data which suggests that the fields are strongly confined to the slots.

As a second example, Figure 4.19 shows Mag(S_{12}) of both the straight and bent stub both with mean length of 1.35 mm. In addition, results for the same stubs in
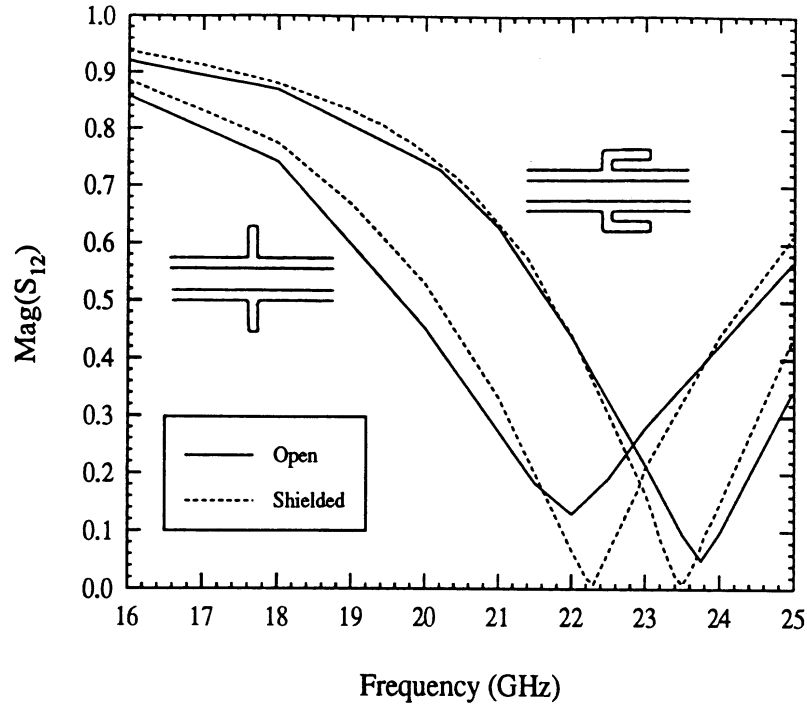
Figure 4.19: Mag(S_{12}) of the CPW series stub geometries (printed on the ground plane) with mean length of 1.35 mm. (W=0.225 mm, S=0.45 mm, h=0.635 mm, ϵ_{r1}=9.9, ϵ_{r2}=1, D_1=D_2=3.175 mm, L_s=1.35 mm, L_{s1}=0.45 mm, L_{s2}=1.125 mm, a=5 mm)

open environment, obtained by Harokopus [85, 86], are shown in the same figure. It can be seen that both simulations agree very well especially for the case of bent stub. This is due to the fact that the the electric fields in the two bent stubs are 180 degrees out of phase, while, they are in phase in the case of straight stubs. As a consequence, the bent stub radiates less than the straight stub. It is found that the loss factor $(1-|\ S_{11}\ |^2-|\ S_{12}\ |^2)$ of the straight stub has a maximum of 0.3 at the resonant frequency, while, it has a maximum of 0.16 for the case of the bent stub [85]. Moreover, Figure 4.19 indicates that the stub geometry may affect the resonant frequency by as much as 7%. Specifically, the straight stub has a resonance at about 22 GHz, while for the bent geometry the resonant frequency is 23.5 GHz.

Recently, there has been an attempt to model radiation loss from printed circuits
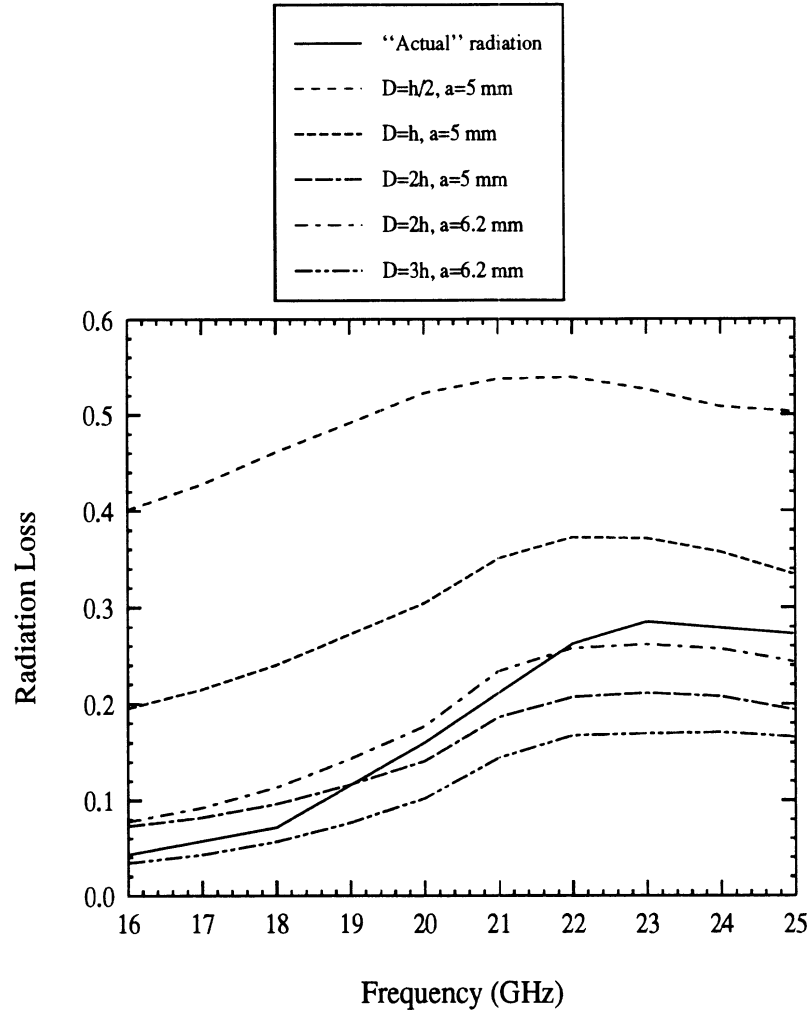
Figure 4.20: Forced radiation loss from a straight series stub as compared to *actual* loss. $D = D_1 = D_2$, other dimensions are the same as in Figure 4.19.

by setting the resistance of the top wall of the shielding box to 377 Ω (*forced radiation*) [133, 134]. However, such an attempt can lead to quite inaccurate and inconclusive results [85]. In fact, forced radiation simulations may predict a loss factor much larger than the *actual* one [134] which can only be obtained through a rigorous analysis of the open structure [86]. Figure 4.20 compares the radiation loss of a straight series stub, as predicted by setting the resistance of the top and bottom walls of the rectangular box to 377 Ω, to the *actual* radiation loss. This *actual* radiation loss has been obtained by Harokopus [85, 86] by analyzing the same stub in open environment. It can be noticed

that the distance at which the impedance walls are set (i.e. D_1 and D_2) undoubtedly affects the final result. Furthermore, there is no specific distance at which one can be sure that the predicted radiation loss is the closest to the actual one. Thus, such a simulation cannot provide any consistent results with respect to the radiation loss in printed circuits or radiation resistance in printed antennas. Nonetheless, such a simulation can still predict the resonant frequency of the circuit or antenna element.

4.4.6   CPW Series Stubs Printed on the Center Conductor

Using the space domain integral equation method, the scattering parameters for the two discontinuities shown in Figure 4.4 have been evaluated as a function of the stub length L_s and frequency. The theoretically derived data have been validated through extensive experiments performed by Ponchak and Simons [83, 84] in the 5 through 25 GHz frequency range. Figure 4.21 shows the scattering parameters for a short-end CPW stub of length 1500 μm. It can be seen that the agreement between the theoretical and experimental results is very good. The slight discrepancies are mainly due to radiation loss since an unshielded structure was used in the measurements. The difference in the resonant frequency may be due to conductor thickness whose effect is discussed below. From the characteristic behavior of the above stub, it can be concluded that a bandstop filter can be realized by cascading several of these stubs in series.

Figure 4.22 shows a comparison between theoretical and experimental values of the resonant frequency of a CPW short-end stub as a function of the stub length. Superimposed on these values are the resonant frequencies for the above CPW stub when operating under ideal conditions (i.e. no discontinuity effects and zero electromagnetic interactions). These values are calculated using the mean length of the
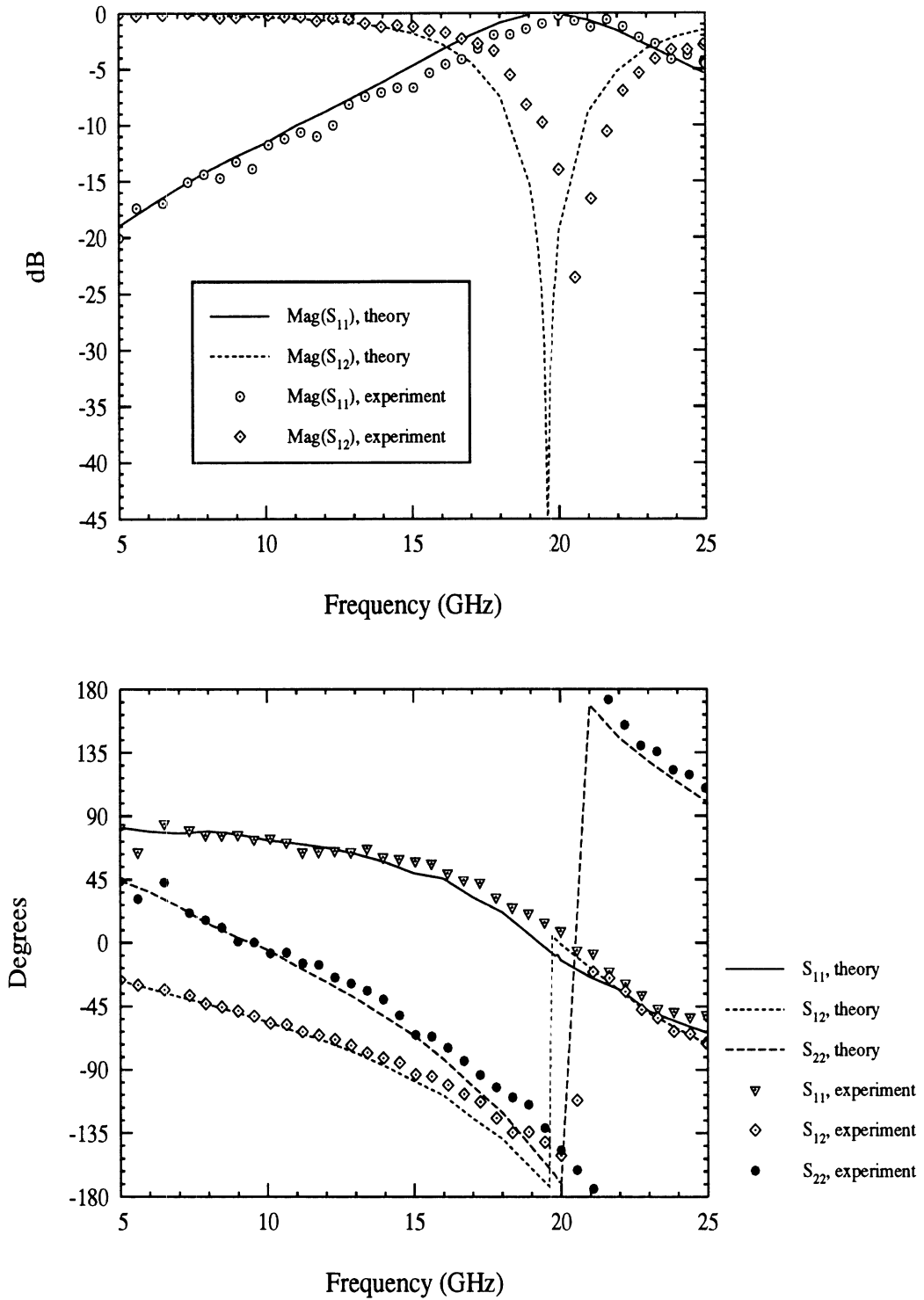
Figure 4.21: Scattering parameters for the short-end CPW stub printed on the center conductor. (L_s=1500 μm, W=225 μm, S=450 μm, W_s=g=75 μm, S_s=150 μm, h= 0.635 mm, D_1=D_2= 3.175 mm, ϵ_{r1}= 9.9, ϵ_{r2}= 2.2, a=3.44 mm)

stub, which can be obtained from $L_{mean}=L_s+67.5$ (both lengths in μm) for the specific dimensions in Figure 4.22. It is interesting to note that for all stub lengths, the measured resonant frequency is larger than the theoretically predicted one. This systematic deviation is due to the effect of finite metallization thickness which is neglected in the theoretical analysis. The finite metallization thickness reduces the phase constant [135], and thus, increases the stub resonant frequency [93]. It is also interesting to notice that both the theoretical and experimental resonant frequencies are less than that corresponding to an ideal stub. This is mainly due to the inductive effect at the end of the stub which makes the stub look longer than its physical length, and thus, resonating at lower frequency. In addition, it is found that the percentage difference between the theoretical resonant frequency and that corresponding to an ideal stub increases as the length of the stub decreases. Specifically, for the largest L_s shown in Figure 4.22 (L_s=2.475 mm), the percentage difference is approximately 3.2%, while, it is 6.5% for L_s=1.2 mm. This indicates that as the frequency increases, the parasitic effects become stronger resulting in a larger difference between the theoretically obtained resonant frequencies and the ones computed for the ideal stub.

Figure 4.23 shows a comparison between the short-end stub printed on the center conductor (Figure 4.4(a)) and the one printed on the ground plane (Figure 4.3(b)) with the same dimensions. It can be noticed that the stub printed on the ground conductor has a larger Q and both stubs have approximately the same resonant frequency. However, it is obvious that both stubs have different characteristics. Thus, it may be concluded that even though both stubs are of the same type and have the same dimensions, each produces a different discontinuity effect depending on the position of the stub.
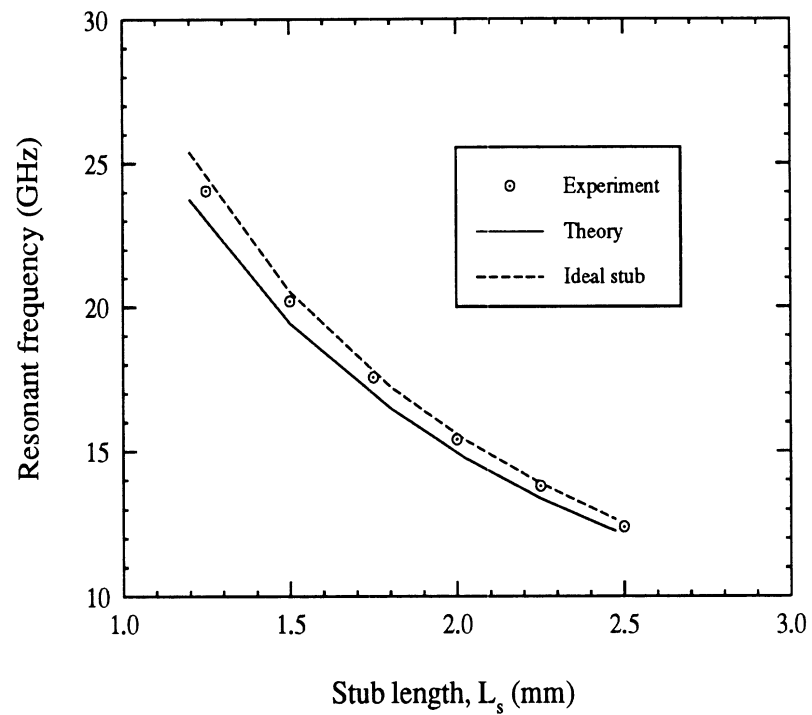
Figure 4.22: Resonant frequency of the short-end CPW stub as a function of stub
length. (W=240 μm, S=440 μm, W_s=90 μm, S_s=140 μm, g=75 μm,
h= 0.546 mm, D_1=D_2= 3.175 mm, ϵ_{r1}= 9.9, ϵ_{r2}= 2.2)
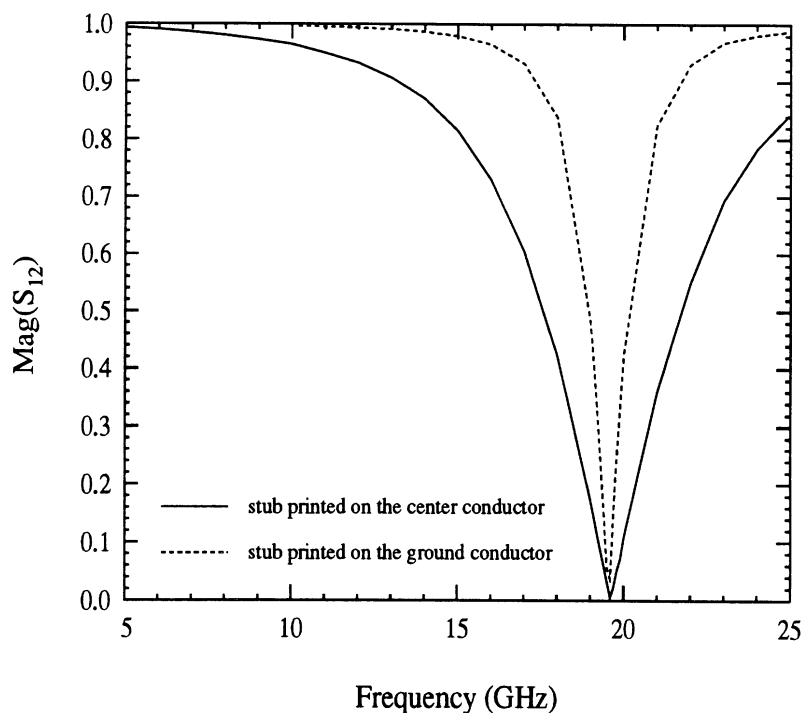
Figure 4.23: A comparison between the short-end stub printed on the center conductor and the one printed on the ground plane with the same dimensions. Dimensions are as in Figure 4.22.

Figure 4.24 shows the scattering parameters for the open-end CPW stub of length 1500 μm. As in the previous case, the agreement between the theoretical and experimental results is very good. Due to its performance, such structures can be used to build bandpass filters. As a last example, Figure 4.25 shows the magnitude of the scattering parameters of an open-end CPW stub obtained both theoretically and experimentally. The experimental data in this figure were supplied by Weller [136]. It can be seen that this stub with the dimensions shown in Figure 4.25 is a very broad band one. It should be noted that such a behavior will not be obtained if an ideal stub was assumed, which clearly shows the need for full-wave analysis of such structures.

In the theoretical analysis, the above CPW stubs were assumed to be inside a cavity while for the derivation of experimental data these structures were measured
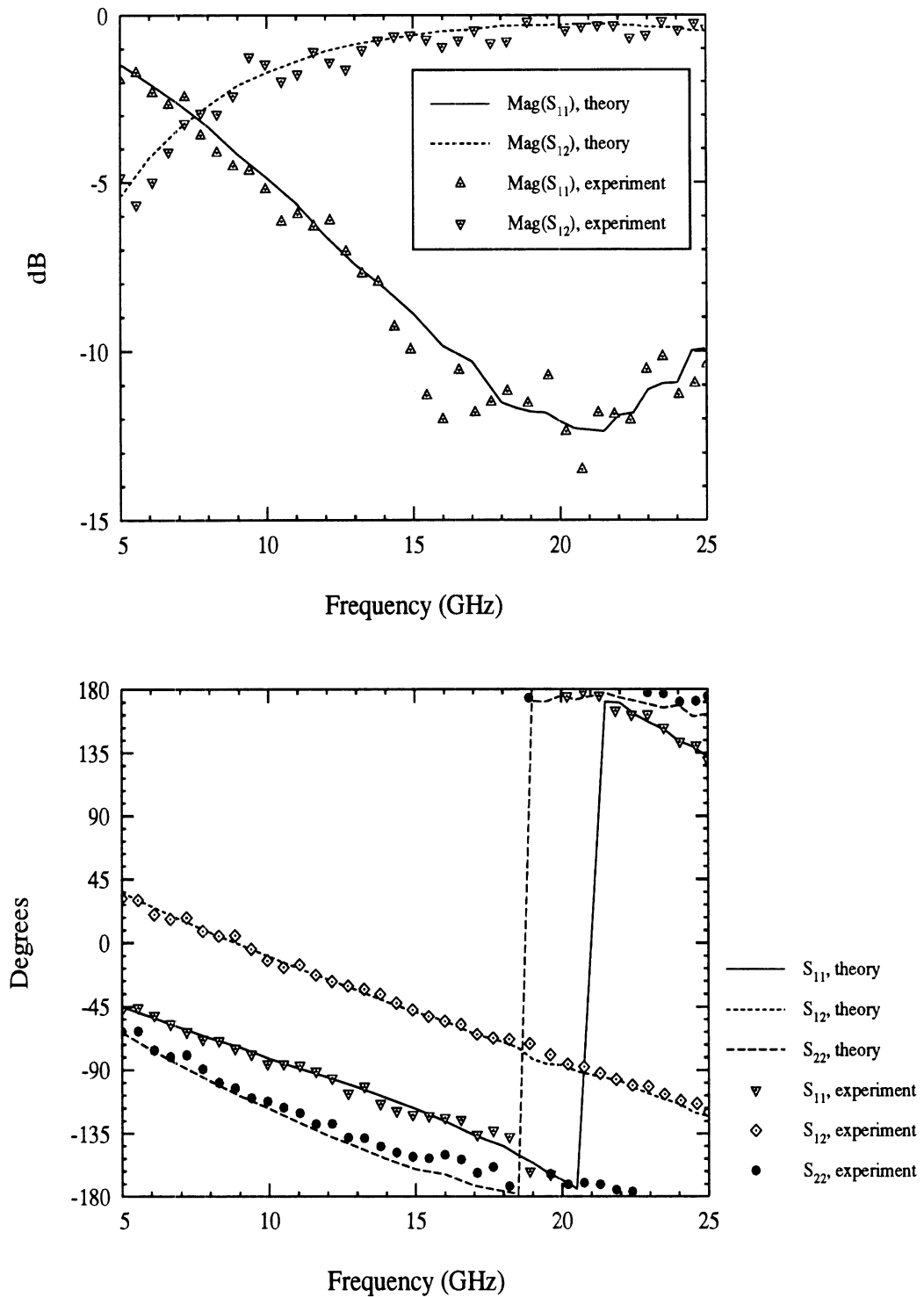
Figure 4.24: Scattering parameters for the open-end CPW stub printed on the center conductor. (L_s=1500 μm, W=225 μm, S=450 μm, W_s=g=75 μm, S_s=150 μm, h= 0.635 mm, D_1=D_2= 3.175 mm, ϵ_{r1}= 9.9, ϵ_{r2}= 2.2, a=4.71 mm)
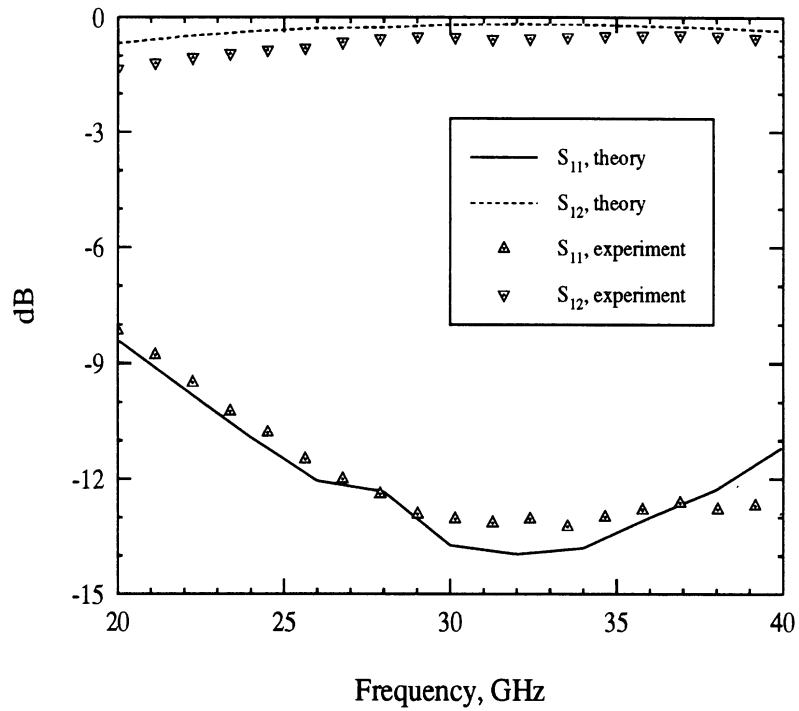
Figure 4.25: Scattering parameters for the open-end CPW stub printed on the center conductor. (L_s=900 μm, W=85 μm, S=100 μm, W_s=16.5 μm, g=45 μm, S_s=33 μm, h= 0.38 mm, D_1=3.8 mm, D_2= 1.9 mm, ϵ_{r1}=11.7, ϵ_{r2}=1, a=4 mm)

in open environment. The fact that there is a very good agreement between theory and experiment suggests that the encountered radiation loss is very low in such stubs. The loss factor of the measured stub discontinuities printed on the center conductor has been investigated and has shown a maximum value of -10 dB at the stub's resonant frequency. This indicates that it is possible to design CPW stub discontinuities with very low loss.

To accurately model the short-end CPW stub (printed on the center conductor) up to the first bandstop resonance, the model shown in Figure 4.26 is proposed [84]. Using the measured scattering parameters of the stub with the dimensions shown in Figure 4.22, Ponchak and Simons [84] evaluated the capacitances and inductances using commercial optimization software. The following relations have been found which give the values of the lumped elements in terms of the stub length L_s [84]:

$$C_s = 1.32 \times 10^{-4} L_s + 3.3515 \times 10^{-2} \tag{4.18}$$

$$C_{f1} = 1.5959 \times 10^{-2} \tag{4.19}$$

$$C_{f2} = 1.1249 \times 10^{-4} L_s + 7.522 \times 10^{-3} \tag{4.20}$$

$$L_1 = 2.6368 \times 10^{-4} L_s - 6.618 \times 10^{-3} \tag{4.21}$$

$$L_2 = 1.77 \times 10^{-4} L_s - 8.35 \times 10^{-4} \tag{4.22}$$

$$L_3 = 1.8656 \times 10^{-4} L_s - 8.34 \times 10^{-4} \tag{4.23}$$

where the stub length L_s is in μm, the inductances in nH, and the capacitances in pF. The above equations, which apply for the stub with the dimensions shown in Figure 4.22 only, have been verified for stub lengths L_s through 2500 μm. It should be noted that C_{f1} equals C_{f2} and L_1 equals L_3 when L_s=75 μm since a symmetric model is expected for a simple notch in the center conductor of a CPW.

Similarly, the equivalent circuit shown in Figure 4.27 is proposed to model the
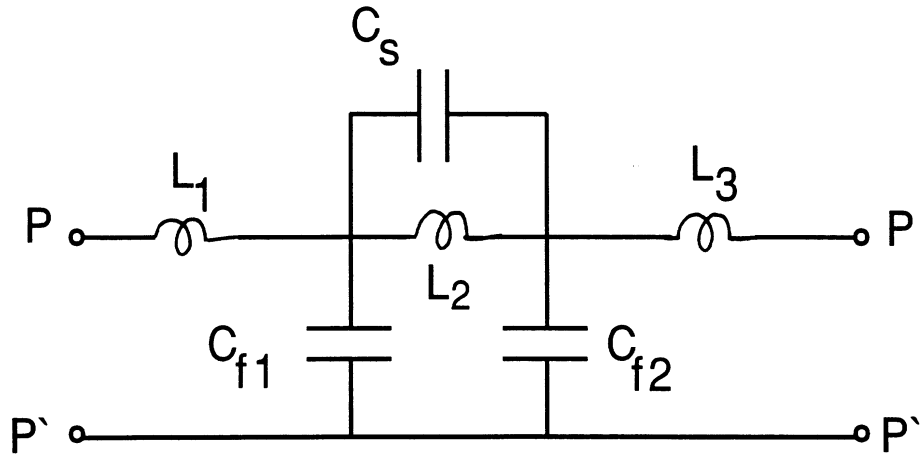
Figure 4.26: Equivalent circuit for the short-end CPW series stub printed on the center conductor.

open-end CPW stub up to the first bandpass resonance. The following relations have been found which give the values of the lumped elements in terms of the stub length L_s [84]:

$$C_s = 1.01 \times 10^{-4} \ L_s + 1.642 \times 10^{-2} \tag{4.24}$$

$$C_{f1} = 0.39 \times 10^{-4} \ L_s + 1.765 \times 10^{-2} \tag{4.25}$$

$$C_{f2} = 0.883 \times 10^{-4} \ L_s + 1.765 \times 10^{-2} \tag{4.26}$$

$$L_1 = 1.22 \times 10^{-4} \ L_s \tag{4.27}$$

$$L_2 = 1.43 \times 10^{-4} \ L_s \tag{4.28}$$

$$L_3 = 3.26 \times 10^{-4} \ L_s \tag{4.29}$$

As in the previous case, the above equations, have been verified for stublengths L_s through 2500 μm. In the limit as L_s approaches zero, the inductances reduce to zero and C_{f1} becomes equal to C_{f2} resulting in a capacitive Pi-network which is expected for a series gap. The above lumped element equivalent circuits predict the response up to the first resonant frequency with a 5% accuracy. It is expected that similar
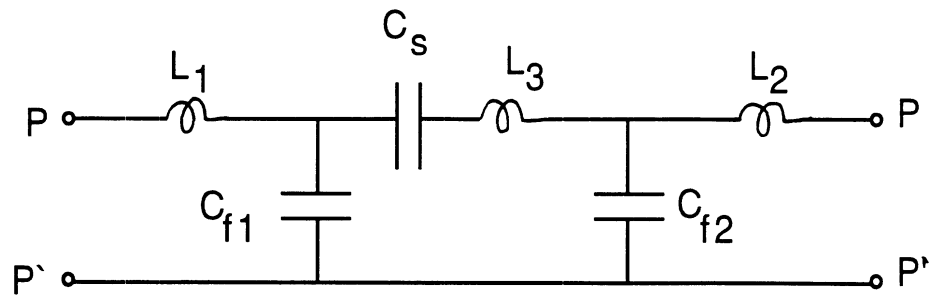
Figure 4.27: Equivalent circuit for the open-end CPW series stub printed on the center conductor.

linear relationships apply for a short or open-end CPW stub with any dimensions. Thus, it is enough to model two different stub lengths from which the characteristics of other lengths can be derived.

CHAPTER V

TWO-PORT CPW DISCONTINUITIES WITH AIR-BRIDGES

5.1 Introduction

While there is no need for via holes in CPW circuits, air-bridges are fundamental components required to connect the ground planes for suppression of the coupled slotline mode. In the past few years, there have been several attempts to characterize, theoretically and/or experimentally, CPW discontinuities with air-bridges or bond wires [21, 72, 137], [89]-[97]. The full wave computationally intensive Finite Difference Time Domain technique was used in [89, 90] to analyze a CPW shunt stub with bond wires and a modified CPW air-bridge T-junction. On the other hand, the Frequency Domain Finite Difference and TLM methods were used in [91] and [92], respectively, to treat two common types of CPW air-bridges where it was found that the reflection coefficient varies linearly with frequency. This fact suggests that a typical air-bridge (height of 3 μm and width of 10-20 μm) can be modeled as a frequency dependent lumped element [9, 21, 72, 94, 138]. With this in mind, a hybrid technique has been developed to analyze CPW discontinuities with air-bridges. In this technique, the frequency dependent equivalent circuit of the discontinuity, with the air-bridges removed, is derived using the Space Domain Integral Equation (SDIE) method. This

equivalent circuit is then modified by incorporating the air-bridge parasitic inductance and capacitance which are evaluated using a quasi-static model.

In this chapter, the above mentioned hybrid technique is used to study a variety of two-port CPW discontinuities with air-bridges (Figures 5.1-5.4), and the validity of the model is verified by comparisons with experimental results [93]-[97]. In Figure 5.1, the air-bridge connects the center conductors of two open-end-coupled coplanar waveguides. This discontinuity is used extensively in CPW MMIC's and has been recently studied by several authors [9, 21, 90, 91, 92, 94, 137]. Figures 5.2 and 5.3 show four different types of CPW shunt stubs that can be used as building blocks for the realization of CPW filters. In these stubs, air-bridges are used to connect the two ground planes of the CPW stub in order to prevent the coupled slotline mode from being excited in the stubs. These air-bridges will be called longitudinal air-bridges since they are parallel to the propagation direction of the feeding lines. In practice, transverse air-bridges may also be needed to connect the ground planes of the feeding CPWs. However, in theory, the coupled slotline mode should not be excited in the feeding lines of these discontinuities since they are transversely symmetric around the center conductor. On the other hand, in the case of asymmetric shunt stub (Figure 5.4(a)), two transverse air-bridges have to be used, besides the longitudinal air-bridge, so that the coupled slotline mode is not excited in the feeding lines. The scattering parameters of the stubs with and without air-bridges are presented and a very good agreement is found between theoretical and experimental data. In addition, numerical results for the asymmetric discontinuities in open environment are presented.
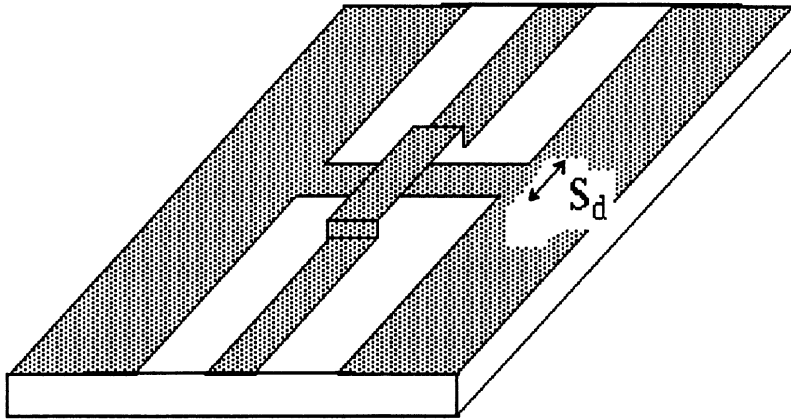
Figure 5.1: An air-bridge connecting the center conductors of two coplanar waveguides.
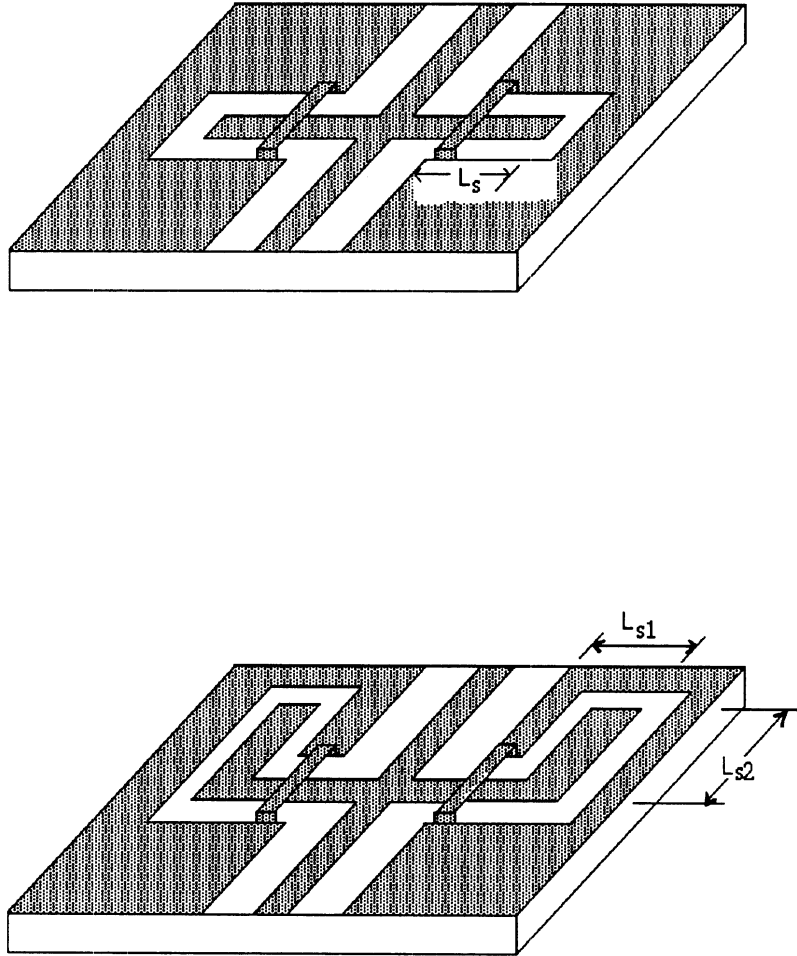
Figure 5.2: Straight and bent open-end CPW shunt stubs.
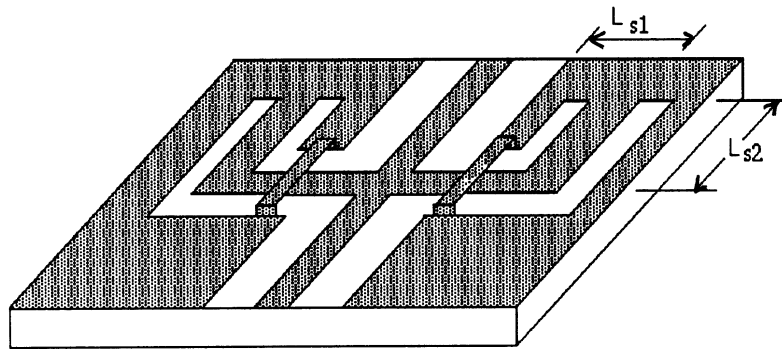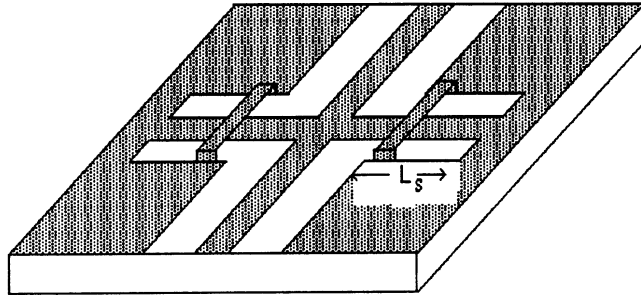
Figure 5.3: Straight and bent short-end CPW shunt stubs.
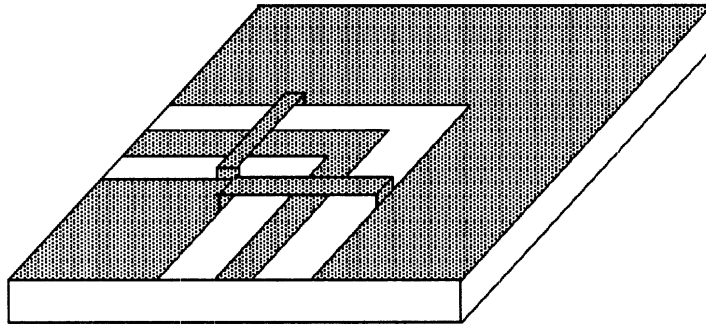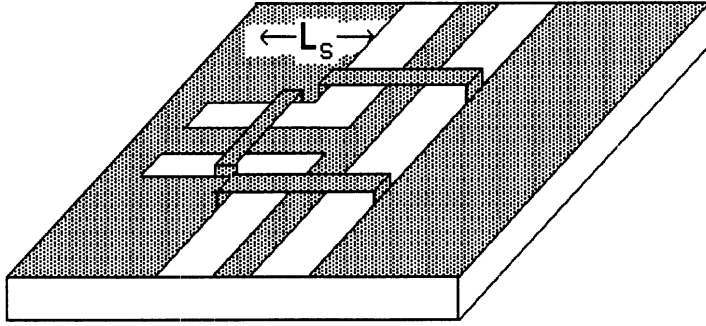
Figure 5.4: Asymmetric CPW discontinuities. (a) Asymmetric straight short-end CPW shunt stub. (b) CPW right angle bend.

5.2 Network Analysis

The first step in the developed hybrid technique is to remove the air-bridges and apply the SDIE method on the air-bridge-free discontinuity. The end result of this step is the knowledge of the surface magnetic current distribution in the slot aperture due to a specific excitation. In case of isolated CPW structures which are symmetric with respect to the center line (Figures 5.1-5.3), the coupled slotline mode is not excited in the feeding lines, and hence, the aperture fields in these lines form standing waves of the fundamental coplanar waveguide mode. Consequently, using the derived electric field, transmission line theory can be utilized to determine the scattering parameters of the discontinuity as was discussed in Chapter 4. In case of asymmetric CPW discontinuities (Figure 5.4), the derived field in the feeding lines is the sum of the fundamental coplanar and slotline modes each one having its own spatial parameters. Consequently, a special treatment is needed to separate the two modes and derive the scattering parameters of the discontinuity [96]. In this section, the approach to take the air-bridges into account for the cases of symmetric and asymmetric discontinuities is discussed separately [93]-[97].

5.2.1 Symmetric Discontinuities

As pointed above, in this case, the coupled slotline mode is not excited in the feeding lines if the discontinuity is fed by a coplanar mode, and thus, the aperture fields in these lines form standing waves of the fundamental coplanar waveguide mode [93, 94, 95]. Consequently, using the derived electric field distribution, transmission line theory can be utilized to determine the scattering parameters of the air-bridge-free discontinuity and derive a lumped element equivalent circuit. Figure 5.5(a) shows such an equivalent circuit (Pi-model) for a symmetric CPW discontinuity with the

air-bridges removed. For the case of the stubs shown in Figures 5.2 and 5.3, the removal of the air-bridges results in exciting both the coplanar and slotline modes in the stubs. The former mode presents the shunt reactances X_1 and X_2, while, the latter mode presents the series reactance X_3 [5]. The reference planes at which these reactances are evaluated are at the ends of the uniform feeding lines. It should be noted that in the case of straight stubs, the two reactances X_1 and X_2 are equal due to the symmetry of the circuit. Thus, only two independent excitations are needed to evaluate the elements of the equivalent circuit, as opposed to three required in the case of the bent stubs ($X_1 \neq X_2$) as was discussed in Chapter 4.

Figure 5.5(b) shows the new equivalent circuit after taking the air-bridges into consideration. The air-bridges can be modeled as sections of an air-filled microstrip line [9, 21, 92], and simple formulas can be used to evaluate the parasitic capacitance C_a and inductance L_a [5]. Alternatively, a parallel plate waveguide model can be employed to evaluate the same parasitic effects as follows:

$$L_a = \frac{\mu_o h_a}{W_a} S_s \qquad (5.1)$$

$$C_a = \frac{\epsilon_o W_a}{2h_a} S_s \qquad (5.2)$$

where h_a and W_a are the height and width of the air-bridge, respectively. It has been found that the difference in the values of the parasitic reactances as predicted by the two models (microstrip vs. parallel plate) has a negligible effect on the performance of the circuit. Finally, new scattering parameters are evaluated from the modified equivalent circuit. It should be emphasized that such a hybrid technique assumes that the air-bridges are positioned as close to the cross junction as possible, which is always the case in practice.
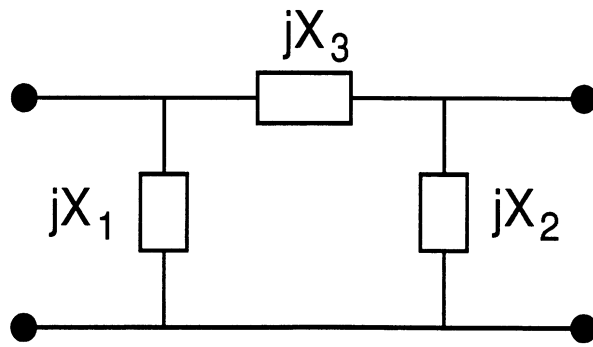
(a)
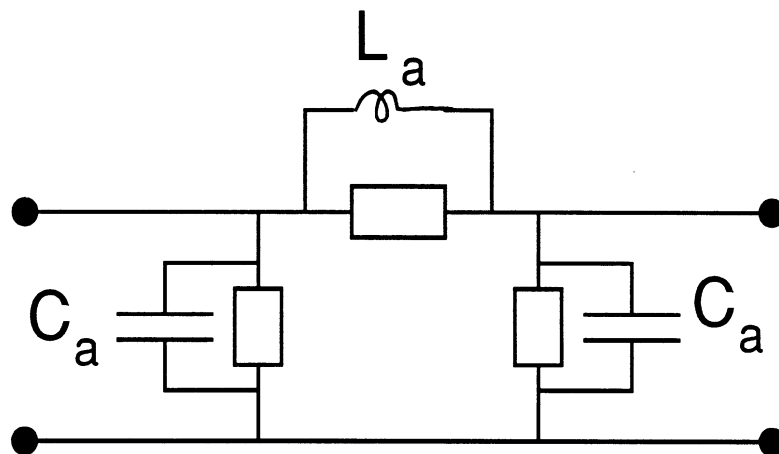
(b)

Figure 5.5: (a) Equivalent circuit of the air-bridge-free symmetric CPW discontinuities. (b) The modified equivalent circuit after taking the air-bridges into consideration.
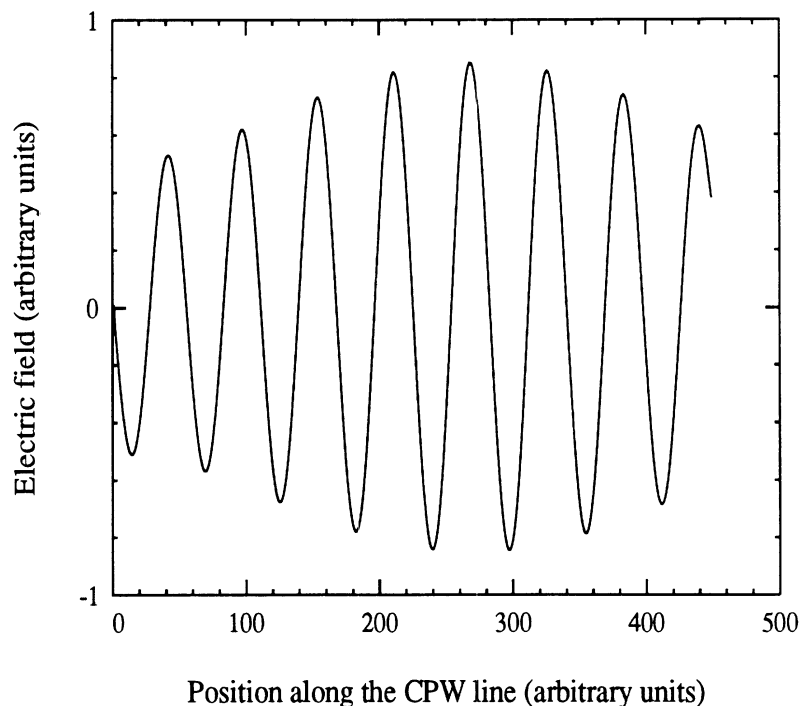
Figure 5.6: A sample amplitude modulated-like standing wave existing in one of the slots of the feeding CPW which results from the superposition of the fundamental coplanar and slotline modes.

5.2.2 Asymmetric Discontinuities

In this case, the derived electric field in each slot of the feeding lines (for any type of excitation) looks like an amplitude modulated signal (Figure 5.6) which results from the superposition of two fundamental modes (the coplanar and slotline modes). Thus, a special treatment is needed to separate the two modes and derive the scattering parameters of the discontinuity. Figure 5.7 shows an outline of the developed technique to analyze asymmetric CPW discontinuities with air-bridges [96, 97]. The steps involved in this technique are described below.

Separation of the Two Modes

As shown in Figure 5.6, the field in the feeding lines derived from the SDIE method is the superposition of the fundamental coplanar and slotline modes each one having
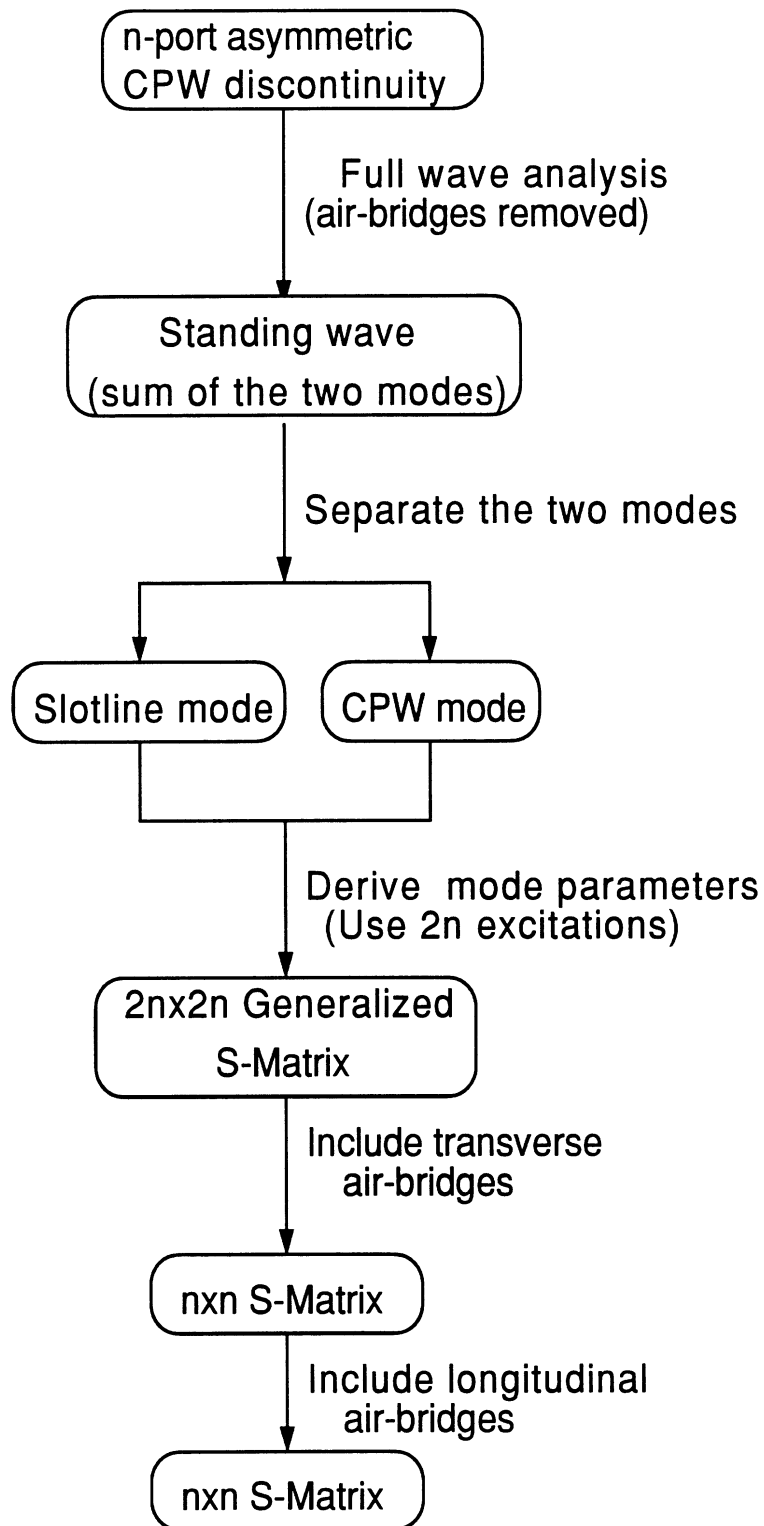
Figure 5.7: Outline of the hybrid technique used to analyze asymmetric CPW discontinuities with air-bridges.

its own spatial parameters (wavelength, amplitude and phase). This field is the sum of the two modes in one of the slots of the feeding CPW, and the difference between them in the other slot. To extract the parameters of each mode, one of the following methods may be used:

- **Prony's method.** The parameters of each mode can be obtained directly by applying Prony's method on the derived amplitude-modulated-like standing wave. Prony's method is a technique for modeling sampled data as a linear combination of exponential terms [139]. Assuming that one has N data samples of the electric field E(1), ..., E(N), Prony's method can be used to to estimate E(n) with a 4-term complex exponential model

$$\hat{E}(n) = \sum_{k=1}^{4} A_k \, exp[(\alpha_k + j2\pi f_k)(n-1)T + j\theta_k] \qquad (5.3)$$

for $1 \leq n \leq N$, where T is the sample interval, A_k is the amplitude of the complex exponential, α_k is the damping factor, f_k is the sinusoidal spatial frequency and θ_K is the sinusoidal initial phase. A detailed description of Prony's method and a computer program listing can be found in [139]. In case of real data (lossless coplanar structures), the exponential representation reduces to

$$\hat{E}(n) = \sum_{k=c,s} 2A_k \, cos[(2\pi f_k)(n-1)T + \theta_k] \qquad (5.4)$$

for 1≤n≤N, where c and s correspond to the fundamental coplanar and slotline modes, respectively. It is found that the frequencies obtained from Prony's method agree very well with the ones predicted by analyzing a CPW through line. In addition, the constructed signal is not distinguishable from the original one.

• **The Standing Wave method.** In this method, the standing waves of the fundamental coplanar and slotline modes can be derived as follows:

$$V_c = \frac{V_1 - V_2}{2} \qquad (5.5)$$

$$V_s = \frac{V_1 + V_2}{2} \qquad (5.6)$$

where V_1 and V_2 denote the voltages in the two slots of a CPW feeding an asymmetric discontinuity. Then, the parameters of each mode can be obtained from the position of the maxima and minima along its corresponding standing wave. Alternatively, Prony's method can be applied on each single mode standing wave to extract the parameters.

It is found that both methods give the same mode parameters with a difference of less than 0.5%. However, Prony's method has the advantage that it can be used to separate any number of modes in an overmoded structure, especially, if the number of these modes (and preferably their frequencies) is known. So, the end results of this step are the spatial parameters (wavelength, phase and amplitude) of the fundamental coplanar and slotline modes. Consequently, the reflection coefficient and the input impedance at any point along the feeding line can be obtained for each mode.

The Generalized Scattering Matrix

The next step is to derive the Generalized Scattering matrix which includes the interactions between the coplanar and slotline modes in the air-bridge-free asymmetric CPW discontinuity. Figure 5.8 shows a generalized 4-port equivalent representation of a 2-port asymmetric CPW discontinuity without air-bridges. This representation uses one port for each mode excited at each physical port. Thus, this 4-port equivalent network takes into account the occurring mode conversion at the discontinuity. The
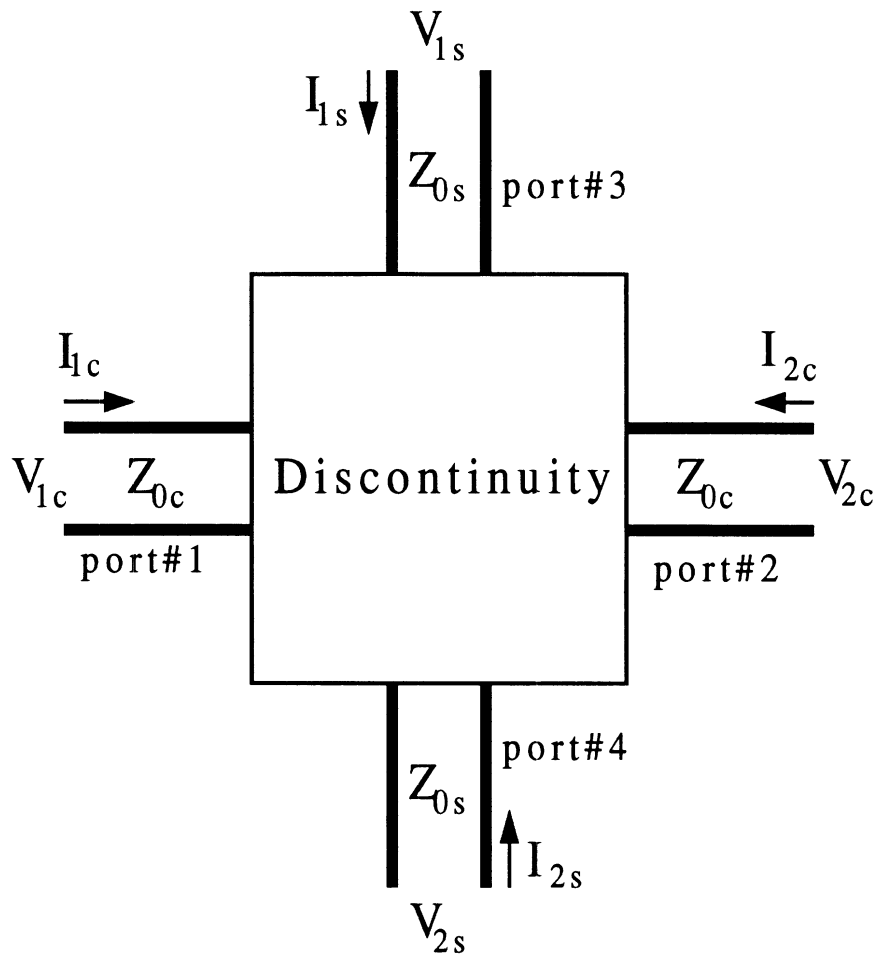
Figure 5.8: A generalized 4-port equivalent representation of a 2-port CPW asymmetric discontinuity without air-bridges where the fundamental coplanar and slotline modes are excited.

network relations between the ports in Figure 5.8 can be written as follows (see Appendix A for derivation):

$$\Gamma_{1c}(z) = S_{11} + S_{12}\frac{V_{2c}^+}{V_{1c}^+} + S_{13}\frac{V_{1s}^+}{V_{1c}^+} + S_{14}\frac{V_{2s}^+}{V_{1c}^+} \tag{5.7}$$

$$\Gamma_{2c}(z) = S_{21}\frac{V_{1c}^+}{V_{2c}^+} + S_{22} + S_{23}\frac{V_{1s}^+}{V_{2c}^+} + S_{24}\frac{V_{2s}^+}{V_{2c}^+} \tag{5.8}$$

$$\Gamma_{1s}(z) = S_{31}\frac{V_{1c}^+}{V_{1s}^+} + S_{32}\frac{V_{2c}^+}{V_{1s}^+} + S_{33} + S_{34}\frac{V_{2s}^+}{V_{1s}^+} \tag{5.9}$$

$$\Gamma_{2s}(z) = S_{41}\frac{V_{1c}^+}{V_{2s}^+} + S_{42}\frac{V_{2c}^+}{V_{2s}^+} + S_{43}\frac{V_{1s}^+}{V_{2s}^+} + S_{44} \tag{5.10}$$

where

$$V_k^+ = \frac{V_{k_{max}}e^{j\beta_k(z_{k_{max}}-z)}}{Z_{0_k}(1+|\Gamma_k|)} \tag{5.11}$$

In the above expressions, S_{ij} $(i,j = 1,\ldots,4)$ are the unknown components of the Generalized Scattering matrix, $V_{k_{max}}$ and $z_{k_{max}}$ are the value and position of a voltage maximum along the kth port, and β_k is the propagation constant at the kth port. In addition, Γ_k is the reflection coefficient at the reference plane z of port k, the magnitude of which ($|\Gamma_k|$) is equal to one for a shielded structure. Moreover, Z_{0_k} is the characteristic impedance of the transmission line connected to the kth port which is obtained using a 2D program. In general, 4 independent excitations are needed to evaluate the 16 unknown components of the Generalized Scattering matrix. For example, Figure 5.9 shows the four excitations used to derive the Generalized Scattering Matrix of an air-bridge-free asymmetric short-end CPW shunt stub.

The 2×2 Scattering Matrix

The 4×4 Generalized Scattering matrix derived above includes the interactions between the coplanar and slotline modes in the air-bridge-free CPW discontinuity. However, in practice, the slotline mode is always suppressed by connecting the two ground planes of the feeding lines with air-bridges. These transverse air-bridges can be
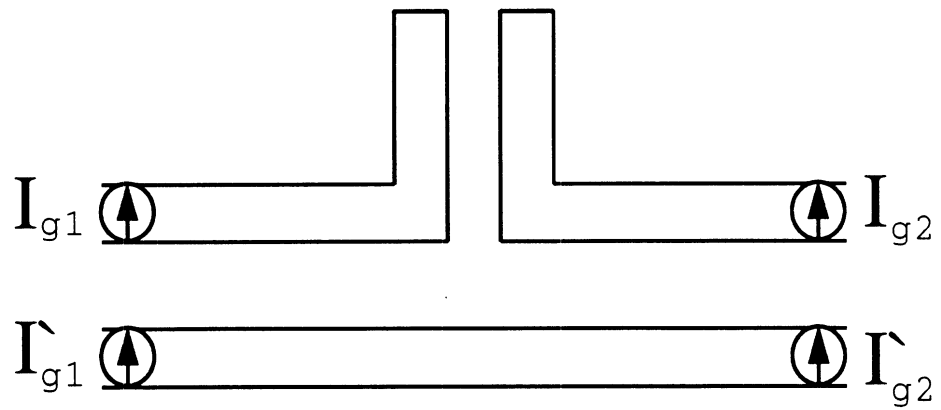
I_{g1}	Γ_{g1}	I_{g2}	Γ_{g2}
1	1	1	1
1	1	-1	-1
1	-1	1	-1
1	-1	-1	1

Figure 5.9: The four independent excitations used to derive the Generalized Scattering Matrix of an asymmetric short-end CPW shunt stub with the airbridges removed.

taken into account by connecting a parallel LC combination to the ports corresponding to the slotline mode, while connecting a series LC combination to those corresponding to the coplanar mode. These inductor and capacitor are due to the parasitic effects of the transverse air-bridges which can be evaluated quasi-statically as was discussed in section 5.2.1. However, for typical air-bridges, these connections effectively short the slotline mode ports and leaves the coplanar mode ports unaffected. Thus, the presence of the transverse air-bridges can be modeled numerically by imposing the following two conditions on the network shown in Figure 5.8:

$$V_{1s} = 0 \tag{5.12}$$

$$V_{2s} = 0 \tag{5.13}$$

It should be noted that such conditions apply to typical transverse air-bridges the parasitic effects of which have been found to be negligible [9, 21, 91, 92]. Hence, transverse air-bridges placed at the same reference planes at which the elements of the Generalized Scattering matrix are computed will reduce the 4-port network representation to a 2-port one. This, in effect, will give a 2×2 scattering matrix, describing the discontinuity under coplanar mode excitation only. It can be easily shown (see Appendix B) that the elements of this 2×2 scattering matrix are related to those of the 4×4 Generalized Scattering matrix as follows:

$$S'_{11} = S_{11} - S_{13}A - S_{14}B \tag{5.14}$$

$$S'_{12} = S'_{21} = S_{12} - S_{13}B - S_{14}A \tag{5.15}$$

$$S'_{22} = S_{22} - S_{23}B - S_{24}A \tag{5.16}$$

where

$$A = \frac{S_{31}(1 + S_{44}) - S_{41}S_{34}}{(1 + S_{33})(1 + S_{44}) - S_{34}S_{43}} \tag{5.17}$$

$$B = \frac{S_{41}(1 + S_{33}) - S_{43}S_{31}}{(1 + S_{33})(1 + S_{44}) - S_{34}S_{43}} \qquad (5.18)$$

and S_{ij}' are the components of the 2×2 scattering matrix. The final step is to take the longitudinal air-bridges (if any) into consideration. This can be done in exactly the same way as was described in section 5.2.1 for the case of symmetric discontinuities.

5.3   Numerical Considerations

As was the case in Chapter 4, the slots are assumed to be fairly thin compared to the center conductor width, and thus, only a longitudinal magnetic current is assumed to exist in the feeding lines. However, both longitudinal and transverse magnetic current components are considered in the transition regions. For the case of the symmetric shunt stubs shown in Figures 5.2 and 5.3, the convergence behavior of the scattering parameters has been found to be similar to that shown in Figures 4.6, 4.7 and 4.9 for the series stubs. However, it has been found that 90 subsections per coplanar mode wavelength are approximately needed to insure the convergence of the scattering parameters for the case of the asymmetric short-end shunt stub.

The CPU time required for the evaluation of the scattering parameters depends mainly on the geometry and the electrical size of the structure. However, as mentioned in Chapter 3, the number of unknowns is reduced by placing a perfectly magnetic wall at the transverse symmetry plane of the symmetric discontinuity. However, this can not be done for the case of asymmetric discontinuities, and thus, all of the slot aperture has to be discretized.

5.4 Numerical Results

5.4.1 Open-End-Coupled CPWs Connected with an Air-Bridge

Figure 5.10 shows the insertion loss of an air-bridge connecting the center conductors of two coplanar waveguides (Figure 5.1) as a function of frequency for different separation distances [94]. The dimensions are the same as those in Figure 4.12. The height of the air-bridge is assumed to be 3 μm. It can be noticed that the insertion loss in this case is very small compared to the case without the air-bridge shown in Figure 4.12. It is interesting to note that the variation of Mag(S_{12}) with respect to frequency as shown in figure 5.10 is analogous to the one found experimentally in [21] . Thus, it is indeed reasonable to model the air-bridge quasi-statically as long as it is adequately small.

5.4.2 Symmetric CPW Shunt Stubs

In this section, the symmetric CPW shunt stubs shown in Figures 5.2 and 5.3 are analyzed [93]. In the numerical results presented here, the considered CPW discontinuities are suspended inside a rectangular cavity, as shown in Figure 3.6, with h=400 μm, ϵ_{r1}=13, ϵ_{r2}=1, S=75 μm, W=50 μm, and D_1=D_2=1.2 mm. The characteristic impedance of such a line is approximately 50 Ω. On the other hand, the slots and center conductor of the CPW stubs have equal widths of 25 μm. In addition, in the case of the open-end stubs, the width of the open-end is 25 μm. In all examples presented here, the stubs are placed symmetrically at the center of the cavity.

The numerical results are compared to experimental data which were obtained by Ponchak [93]. The experiments were performed in an open environment with the
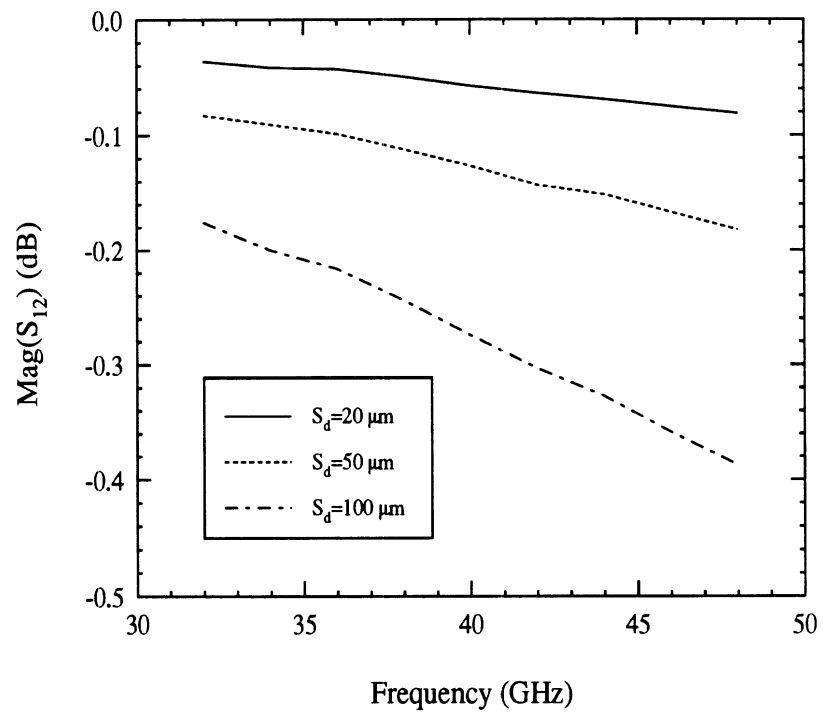
Figure 5.10: Mag(S_{12}) for the open-end coupled CPWs discontinuity connected with an air-bridge for different separation distances. (h=300 μm, ϵ_{r1}=13, ϵ_{r2}=1, S=75 μm, W=50 μm, Z_0=50 Ω, g=25 μm, D_1=D_2=1.2 mm, a=2 mm)

CPW circuits fabricated on 400 μm thick GaAs using lift-off processing. The CPW center strip and ground planes consist of 200 $\mathring{A}$ of Cr and 1.5 μm of Au. The air-bridge thickness, height and width are 1.0 μm, 3.0 μm and 14 μm, respectively. The GaAs circuit rests on a piece of 3.175 mm 5880 RT/duroid which has a dielectric constant of 2.2.

It will be shown that the theoretical and experimental data agree despite the difference in ϵ_{r2} of the substrate ($\epsilon_{r2}=1$ versus 2.2). This is due to the relatively large thickness of the GaAs substrate layer as compared to S+2W. The choice of $\epsilon_{r2}=1$ in the theoretical calculations is intended in order to avoid some of the unwanted cavity resonances.

Open-End Shunt Stubs

Figure 5.11 shows the magnitude of the scattering parameters of the straight open-end stub of length $L_s=1100$ μm with the air-bridges removed as a function of frequency. It can be seen that the theoretical and experimental results agree very well up to the first resonance, after which, discrepancy is noticeable. This is attributed to the fact that no loss is assumed in the theoretical formulation, while, experiments were performed on CPW structures in an open environment. The loss encountered in the measurements is mainly due to radiation by the slotline mode excited in the CPW stubs in the absence of the air-bridges. To understand the unexpected behavior seen between 42 and 45 GHz, the reactances X_1 and X_3 of the equivalent circuit are plotted in Figure 5.12. It can be seen that X_1, which corresponds to the coplanar mode in the CPW stub, behaves as a real open-end shunt stub. On the other hand, the series reactance X_3 behaves somewhat anomalously between 42 and 45 GHz. It is found that this behavior is due to a cavity resonance at 43 GHz which corresponds
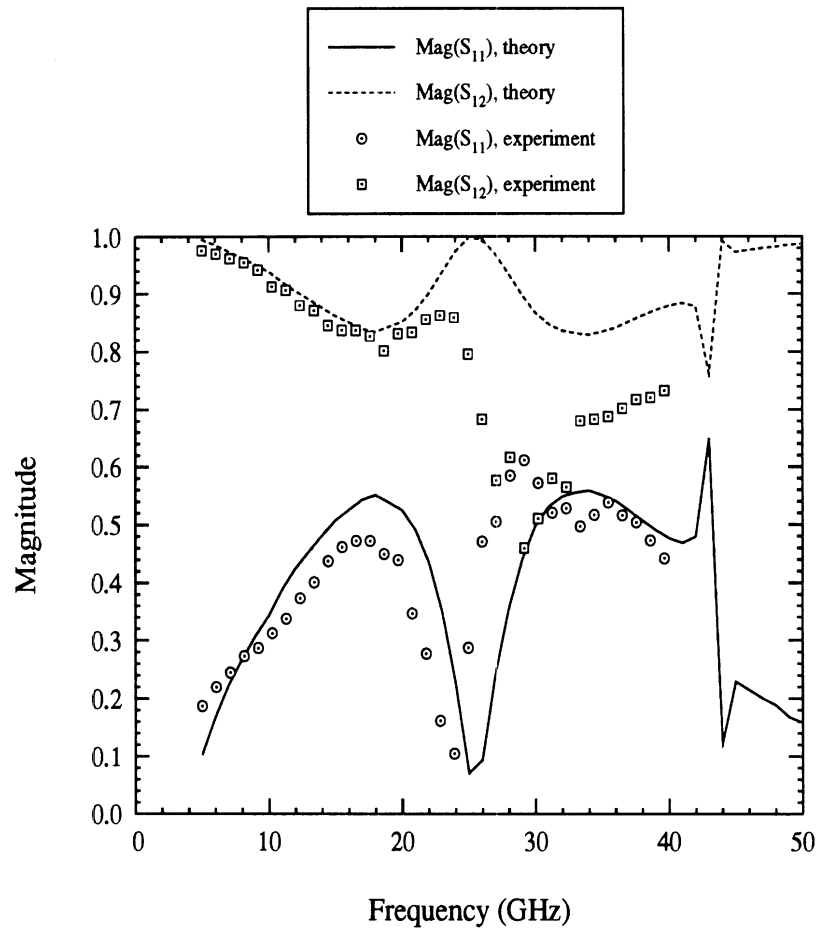
Figure 5.11: Scattering parameters of the straight open-end stub without air-bridges. (L_s=1100 μm)
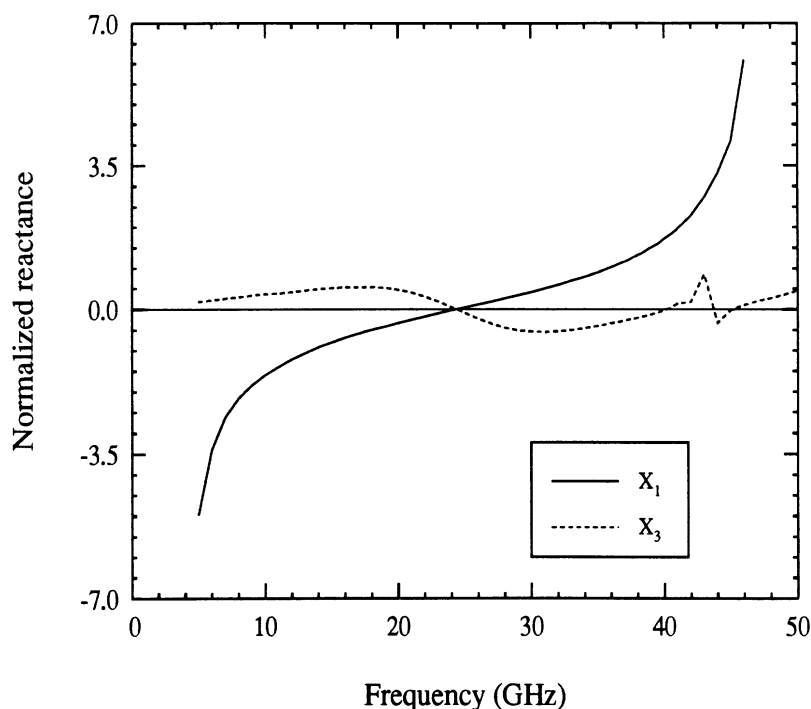
Figure 5.12: The normalized reactances of the equivalent circuit for the straight open-end stub of length L_s=1100 μm.

to the LSM_{121} mode excited in the partially filled lower cavity (the cavity width was chosen to be 3.425 mm). It is interesting to note that the LSM_{111} cavity mode, which has a resonant frequency of 38 GHz, do not show an observable effect on the stub under consideration. Also, the shunt reactances seem to be not affected by the LSM_{121} cavity mode.

Figure 5.13 shows the scattering parameters (magnitude and phase) of the same straight open-end stub with air-bridges. The good agreement between the theoretical and experimental results validates the developed hybrid technique. As it can be seen, the stub resonates at nearly 24.5 GHz where the length of the stub is approximately quarter of a coplanar mode wavelength. It can be noticed that the agreement between the theoretical and experimental data in Figure 5.13 is much better than the one seen in Figure 5.11. This is due to the fact that the air-bridges tend to prevent the slotline
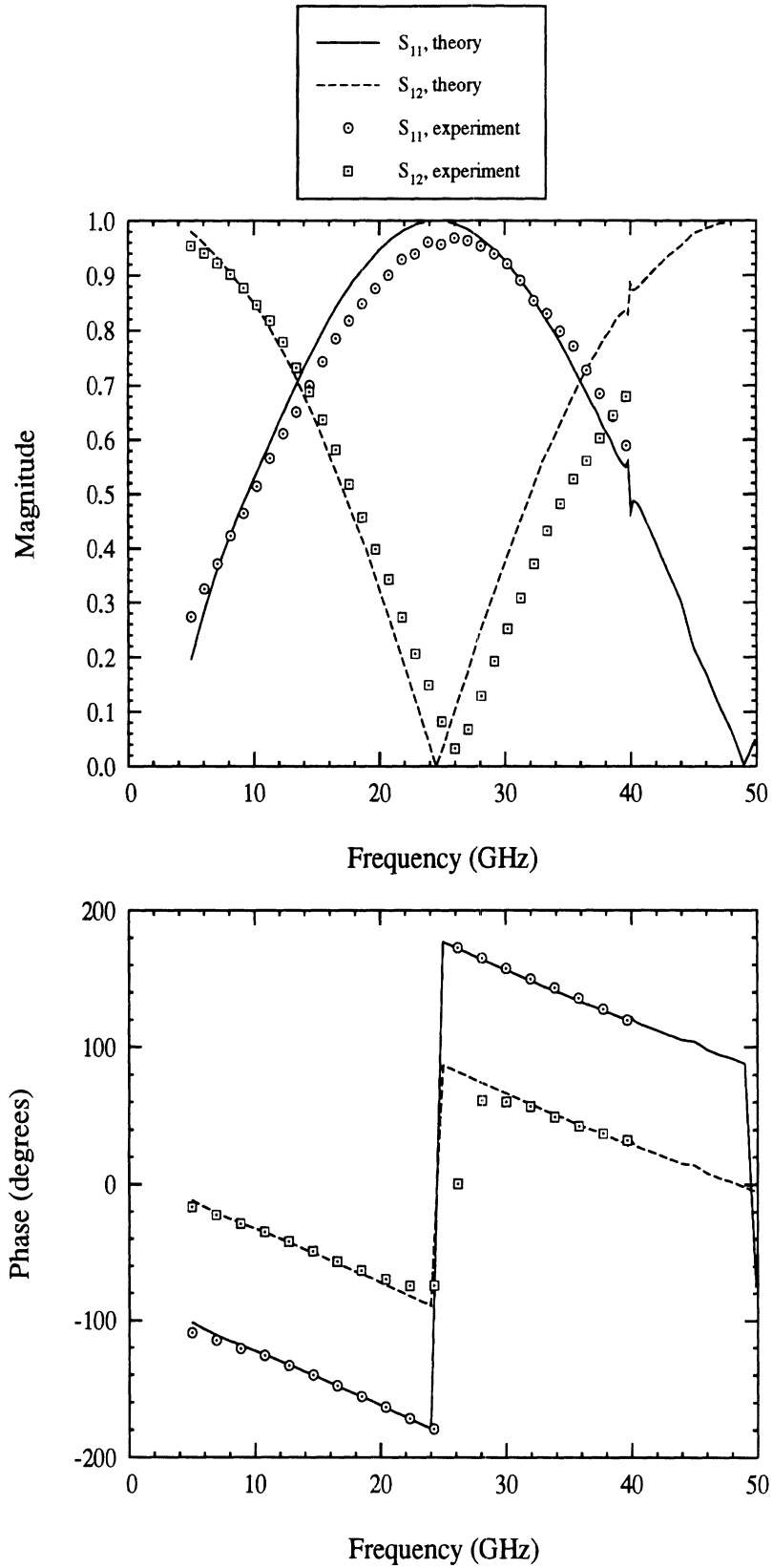
Figure 5.13: Scattering parameters of the straight open-end stub with air-bridges. (L_s=1100 μm)

mode from being excited in the CPW stubs which effectively reduces radiation losses encountered in the measurements. In addition, it can be seen that the resonance effect noticed in Figure 5.11 has disappeared since X_3 is shorted by the relatively small air-bridge inductance L_a. As a result, with the presence of air-bridges, cavity resonances have no effect on the characteristics of a straight stub as long as it is placed symmetrically inside the cavity. One can also notice an anomalous effect at 40 GHz existing in Figure 5.13. A similar effect has been reported in [89] for the case of a bent open-end stub. This effect may be due to a resonating slotline mode excited in the stubs beyond the air-bridge.

Figure 5.14 shows the magnitude of the scattering parameters for the bent open-end CPW stub of mean length 1100 μm without air-bridges. In this case, the width of the cavity is taken to be 2 mm. It can be seen that the agreement between theory and experiment is better than that seen in Figure 5.11 for the straight stub without air-bridges. Moreover, it has been found that the parallel combination of X_1 and X_2 behaves as expected for a real shunt open-end stub (i.e. similar to the variation of X_1 in Figure 5.12). Figure 5.15 shows the magnitude of the scattering parameters of the same bent open-end stub with air-bridges. It can be seen that the anomalous effect at 40 GHz is more pronounced in this case than that in Figure 5.13. In addition, the resonant frequency of this bent stub with air-bridges is approximately the same as the one for the straight stub of the same mean length.

Short-End Shunt Stubs

Figures 5.16 and 5.17 show Mag(S_{11}) for the straight and bent short-end CPW stubs, respectively, of mean length equal to 1100 μm with and without air-bridges. It can be noticed that both stubs resonate at approximately 25.5 GHz. The same
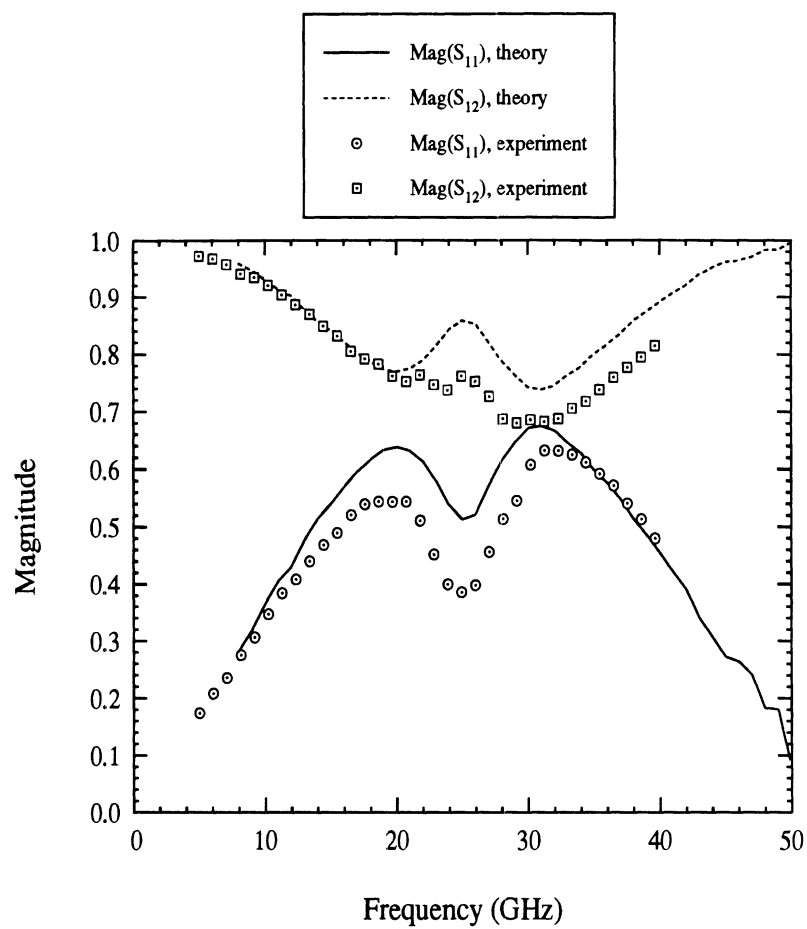
Figure 5.14: Scattering parameters of the bent open-end stub without air-bridges. (L_{s1}=100 μm, L_{s2}=1025 μm)
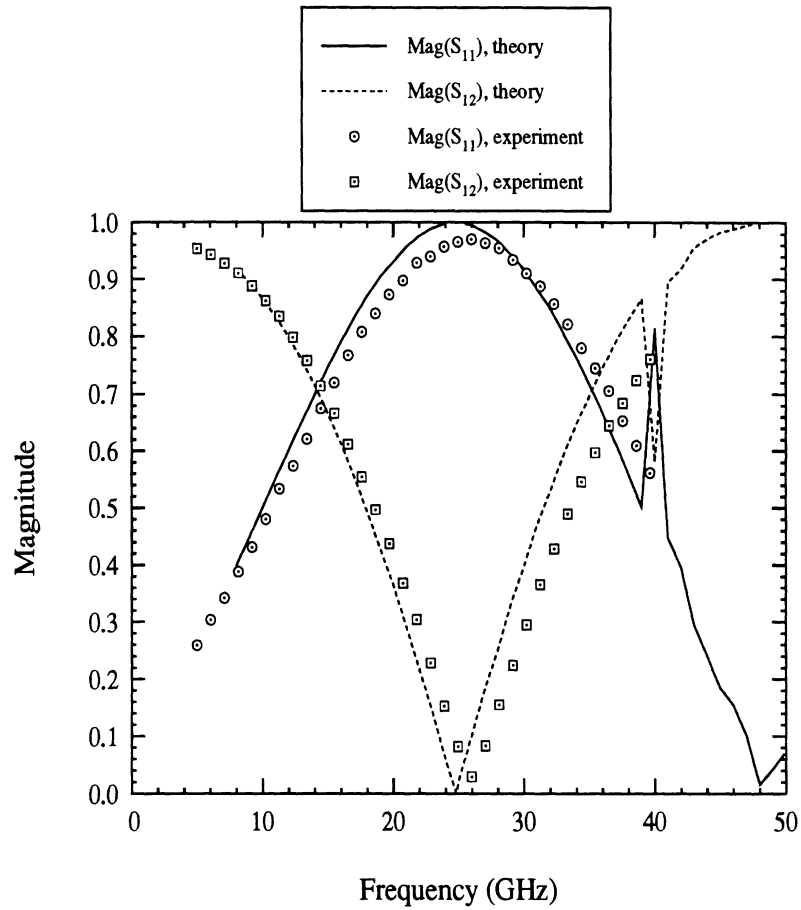
Figure 5.15: Scattering parameters of the bent open-end stub with air-bridges. (L_{s1}=100 μm, L_{s2}=1025 μm)
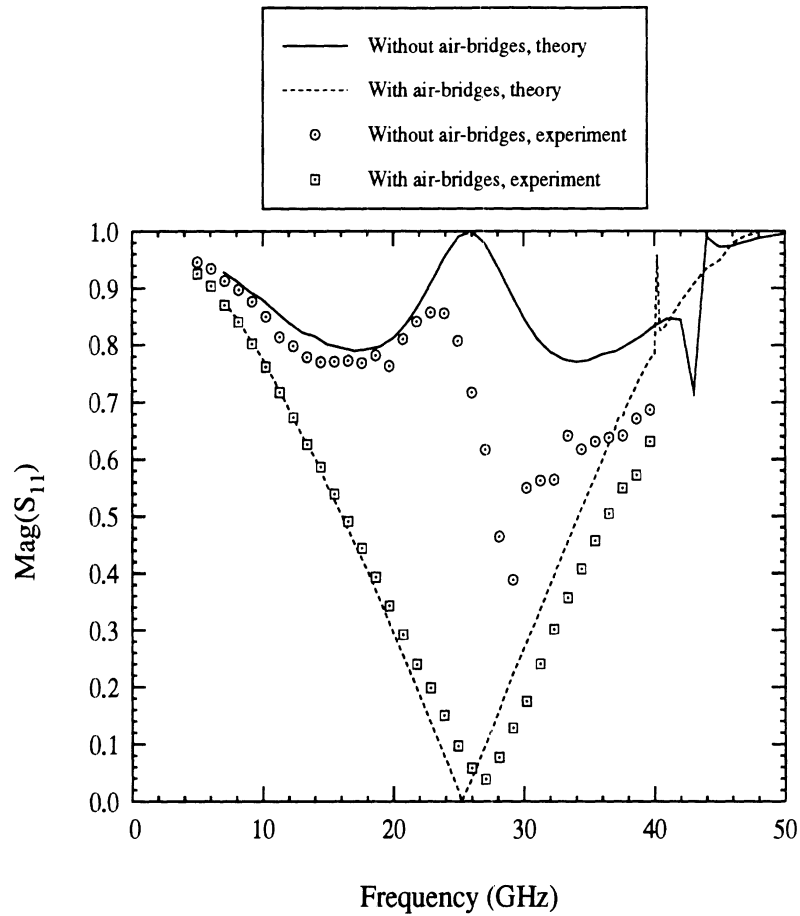
Figure 5.16: Mag(S_{11}) of the straight short-end stub with and without air-bridges. (L_s=1100 μm)

arguments presented above for the open-end stub hold here too.

It is interesting to note that for all structures containing air-bridges, the measured resonant frequency is larger than the theoretically predicted one. This systematic deviation may be due to the effect of finite metallization thickness (1.5 μm) which is neglected in the theoretical analysis. The finite metallization thickness reduces the phase constant [135] and thus increases the stub resonant frequency.

Since the experiments were performed on open CPW discontinuities, the measured scattering parameters can provide the loss factor. This loss factor includes radiation, conductor and dielectric losses. However, since the stubs are all of the same length
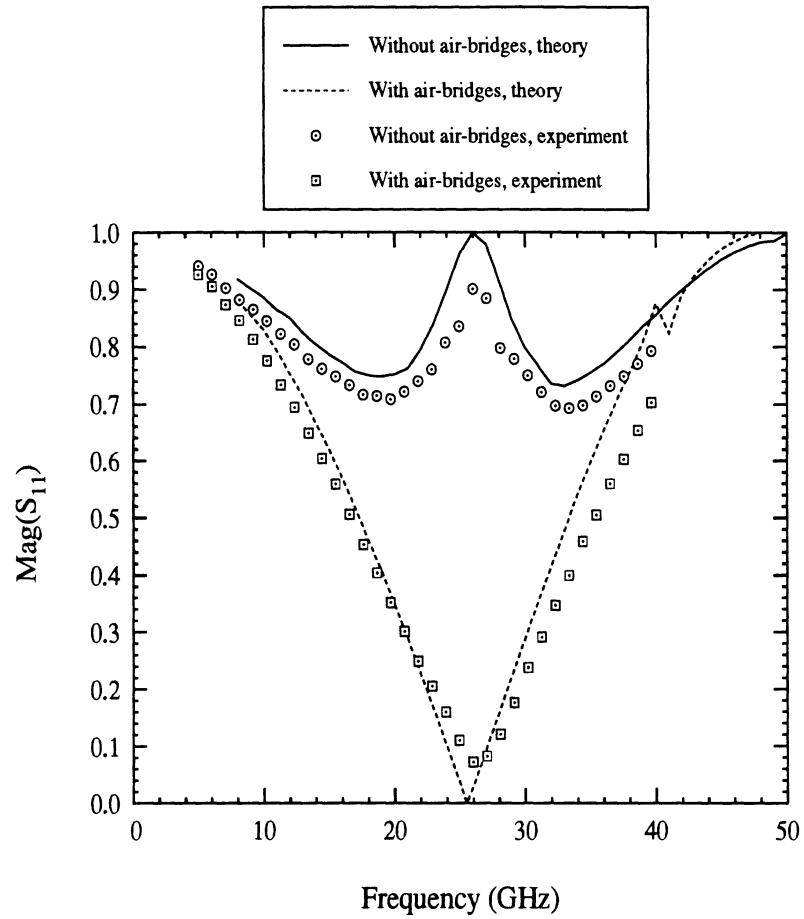
Figure 5.17: Mag(S_{11}) of the bent short-end stub with and without air-bridges. (L_{s1}=100 μm, L_{s2}=1025 μm)

and printed on the same substrate, a comparison of the loss factor can provide a measure of the radiation loss. Figures 5.18(a) and 5.19(a) show the measured loss factor of the short-end and open-end stubs without air-bridges, respectively. It is noticed that loss is maximum at the resonant frequency for all stubs, which is similar to what has been found in microstrip stubs [112]. Furthermore, the loss factor for straight stubs is larger than that for bent stubs especially after resonance. This behavior is due to the fact that in the case of bent stubs, the fields radiated by the coupled slotline mode in the two opposing stubs partially cancel. This explains why the agreement between the theoretical and experimental results for the bent stubs without air-bridges (Figure 5.14 and Figure 5.17) is better than that for the straight stubs without air-bridges (Figure 5.11 and Figure 5.16). The loss factor for the stubs with air-bridges is shown in Figures 5.18(b) and 5.19(b). It can be seen that the presence of air-bridges reduces the loss factor appreciably since they short out the radiating coupled slotline mode. However, it is still noted that the straight stubs have increasing radiation loss after the first resonant frequency. Finally, it can be seen that the difference between the loss factor of the straight and bent stubs (with or without air-bridges) below the resonant frequency is within the experimental error. Thus, no concluding remarks can be made concerning the loss from the two stubs in this region. It should be mentioned that the above loss factor plots were supplied by Ponchak [85, 93] and are included here for the sake of completeness.

As a last example, Figure 5.20 shows the scattering parameters of a shorted-end shunt CPW stub discontinuity without air-bridges with a stub length of 550 μm [94]. The dimensions are as in the above examples except that h=300μm, S_s=20 μm and the width of the cavity is 2 mm. It can be noticed that such a structure behaves as a series stub (instead of a shunt stub) with a resonant frequency 46.5 GHz. Figure
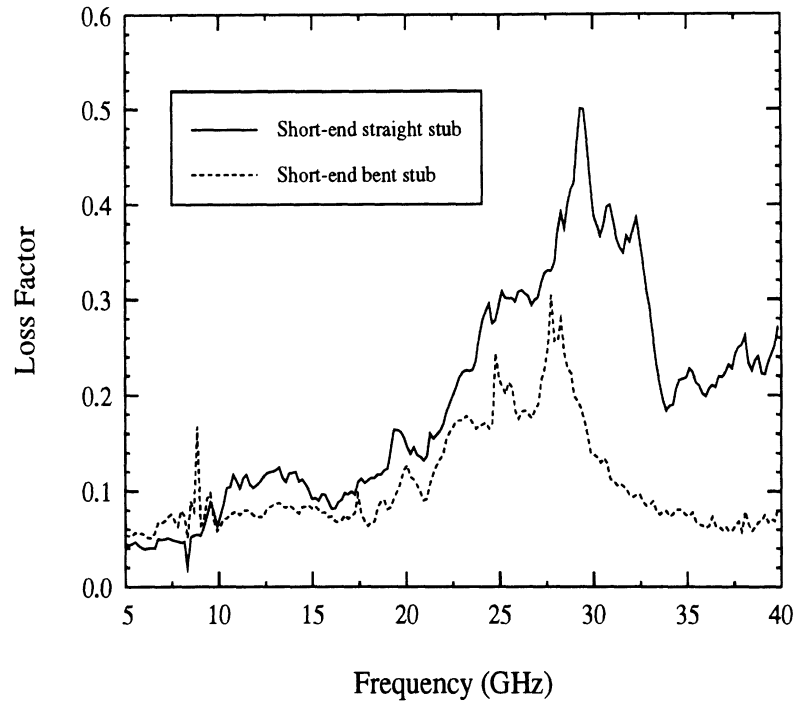
(a) Without air-bridges.
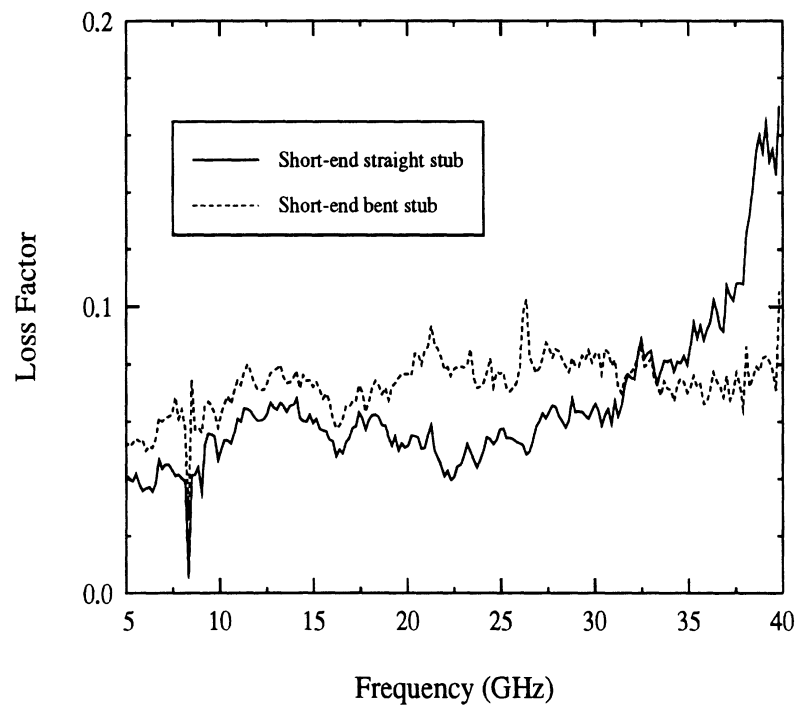
(b) With air-bridges.

Figure 5.18: The measured loss factor $(1- \mid S_{11} \mid^2 - \mid S_{12} \mid^2)$ of the short-end CPW stubs.
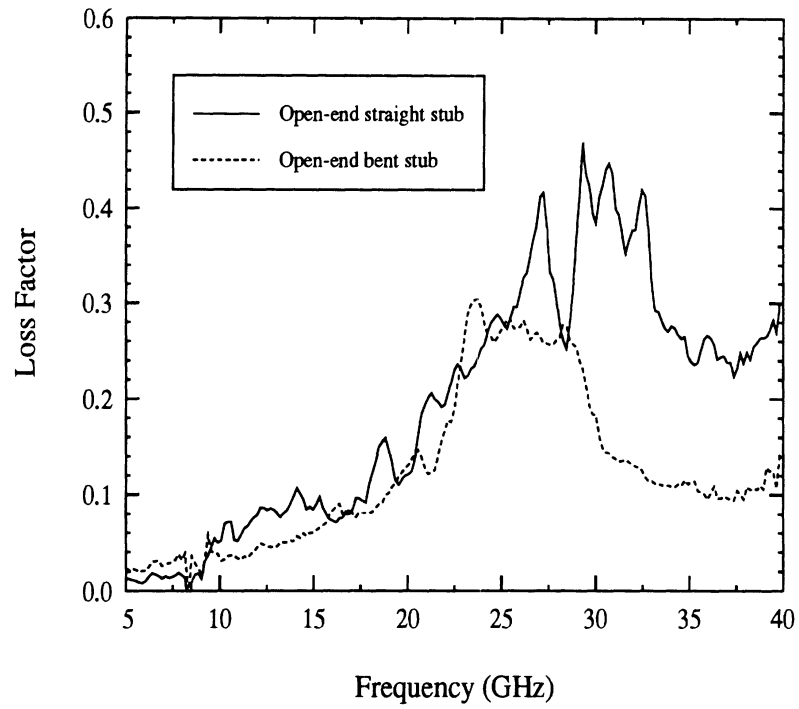
(a) Without air-bridges.
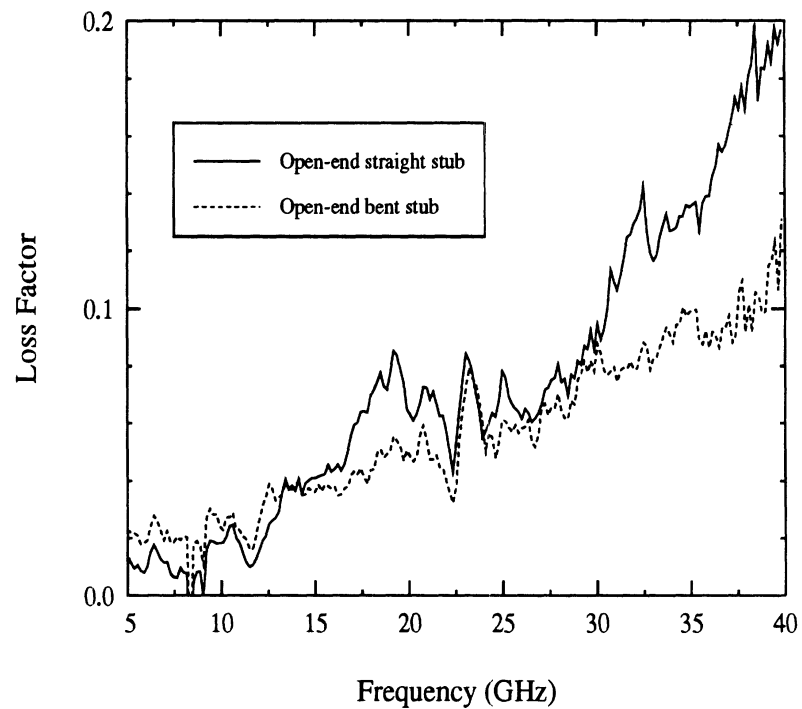
(b) With air-bridges.

Figure 5.19: The measured loss factor of the open-end CPW stubs.
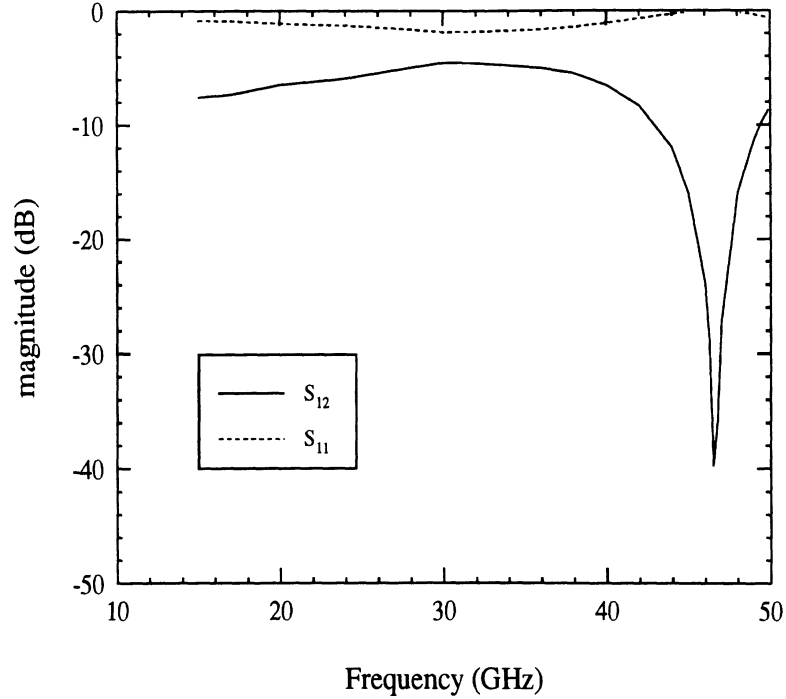
Figure 5.20: Scattering parameters of the straight short-end stub without air-bridges. (L_s=550 μm)

5.21 clarifies this by showing that the series reactance X_3 resonates at this frequency while the shunt reactance X_1 resonates at 49.5 GHz (at which the length of the stub is approximately a quarter of a coplanar mode wavelength). However, the effect of this latter resonance does not appear in Figure 5.20 because of the existence of the series reactance X_3. It has been found that these two resonant frequencies are approximately independent of the separation distance between the two coplanar lines (ranging from 20-80 μm) depending mainly on the stub length.

Figure 5.22 shows the scattering parameters of the same stub with air-bridges connecting the ground planes of the CPW stubs. The air-bridges are chosen with width of 10 μm and height of 3 μm. These air-bridges ensure that the two ground planes of the CPW stub are at the same potential and suppress the coupled slotline mode. This results in shorting the series reactance, and thus reducing the equivalent
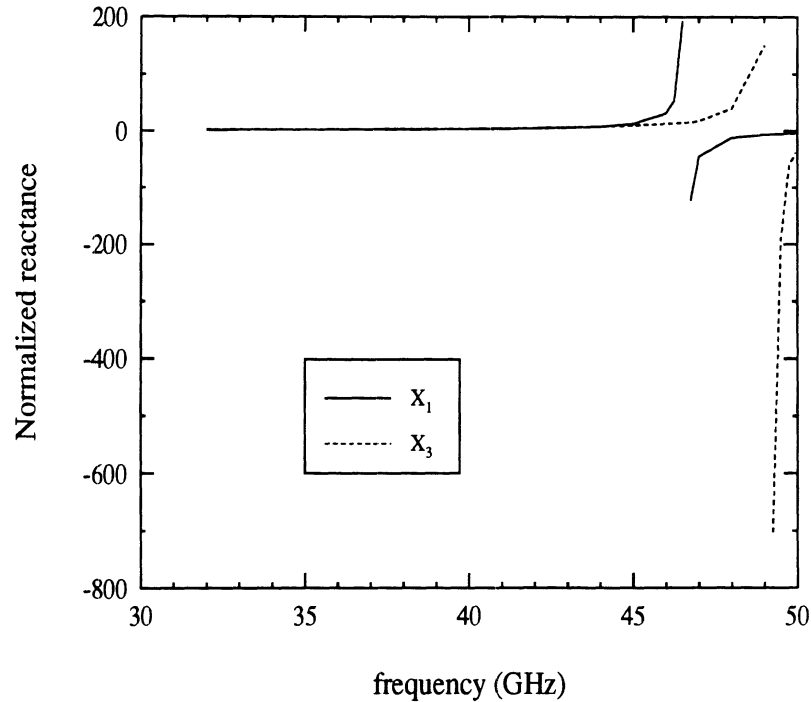
Figure 5.21: Series and shunt reactances for the short-end shunt CPW stub without air-bridges. (L_s=550 μm)

circuit to a shunt reactance (with air-bridge parasitic effects).

5.4.3 Asymmetric Discontinuities

The technique described in section 5.2.2 is quite general so that it can be applied to any n-port asymmetric CPW discontinuity. The method is employed here to analyze the asymmetric short-end CPW shunt stub and the CPW right angle bend shown in Figure 5.4. Five examples are presented in this section. In the first example, an asymmetric stub is analyzed theoretically and is compared to a symmetric stub with the same dimensions. In the second example, theoretical data for an asymmetric stub are compared to experimental results obtained from CPW circuits with bond-wires. In the third example, theoretical data for an asymmetric stub are compared to experimental results obtained from CPW circuits with air-bridges. In the fourth
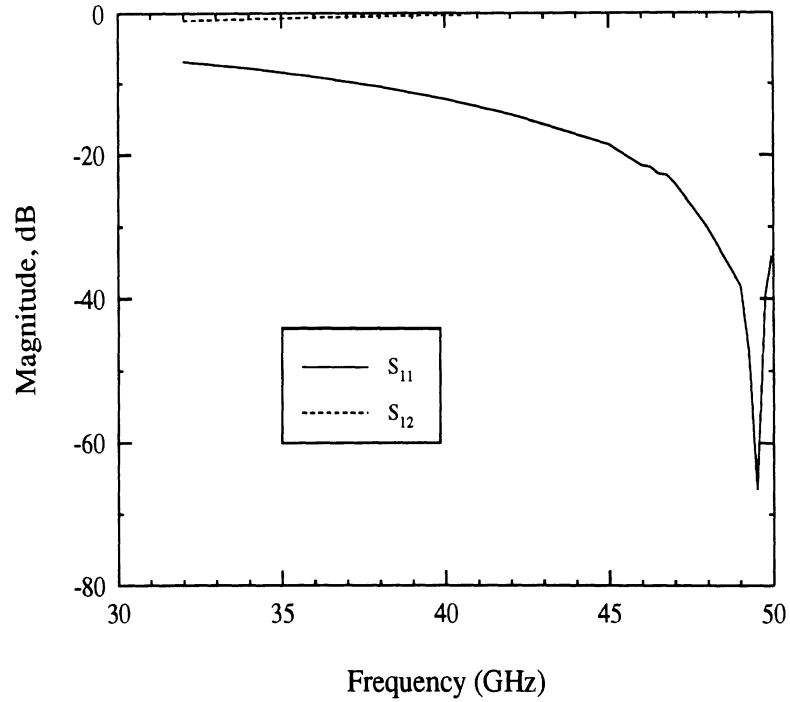
Figure 5.22: Scattering parameters of the straight short-end stub with air-bridges. (L_s=550 μm)

and fifth examples, an asymmetric stub and a right angle bend in open invironment are analyzed, respectively.

Example 1

In the numerical results shown in Figures 5.23 through 5.27, the considered CPW discontinuities are suspended inside a rectangular cavity, as shown in Figure 3.6, with h=400 μm, ϵ_{r1}=13, ϵ_{r2}=1, S=75 μm, W=50 μm, a=3.425 mm, and D_1=D_2=1.2 mm. On the other hand, the CPW stubs are placed at the center of the cavity with a slot width of 25 μm and a center conductor of 25 μm.

Figures 5.23 and 5.24 show the elements of the first and third rows of the 4×4 Generalized Scattering Matrix of an air-bridge-free asymmetric short-end stub. Other elements can be obtained using symmetry considerations, e.g. S_{21}=S_{12}, S_{22}=S_{11},
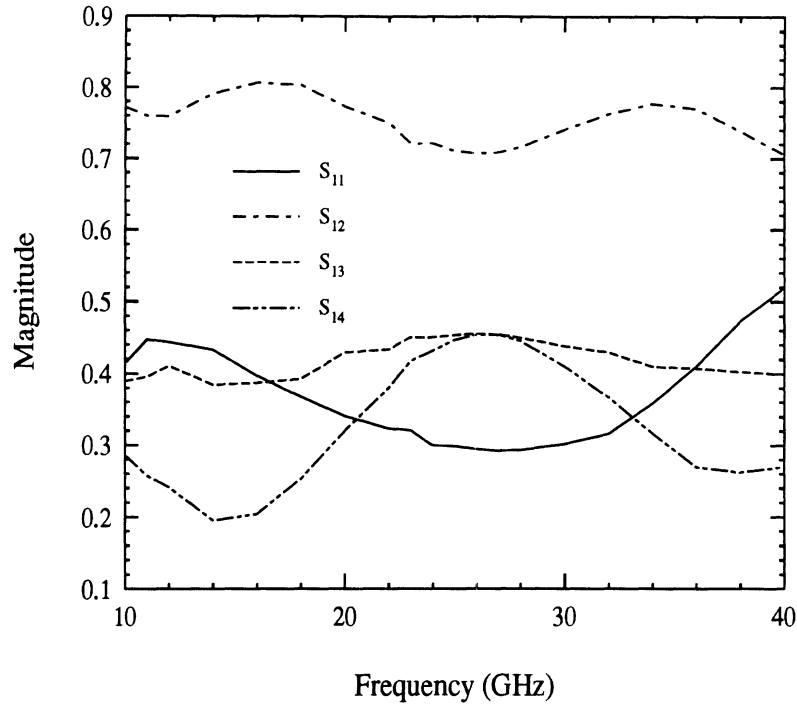
Figure 5.23: Elements of the first row of the Generalized Scattering Matrix of an air-bridge-free asymmetric short-end CPW shunt stub. (L_s=1100 μm)

S_{23}=S_{14}, ... etc. It should be noted here that ports #1 and #2 correspond to the coplanar mode at the first and second physical ports, respectively, while, ports #3 and #4 correspond to the slotline mode (see Figure 5.8). Thus, it can be noticed from the values of S_{12} in Figure 5.23 that if one of the physical ports is excited by a coplanar mode, 50-65% of the power is transmitted to the coplanar mode appearing on the other physical port in the whole frequency range. On the other hand, S_{13} shows that 15-20% of the input power is transferred to the slotline mode appearing on the same physical port. It is interesting to note that at 27 GHz, the amount of power in the slotline mode appearing at both ports is the same and that the return loss (S_{11}) reaches its minimum value. In addition, it can be noticed from the values of S_{34} in Figure 5.24 that if one of the physical ports is excited by a slotline mode, the power transmitted to the slotline mode on the other port decreases as the frequency
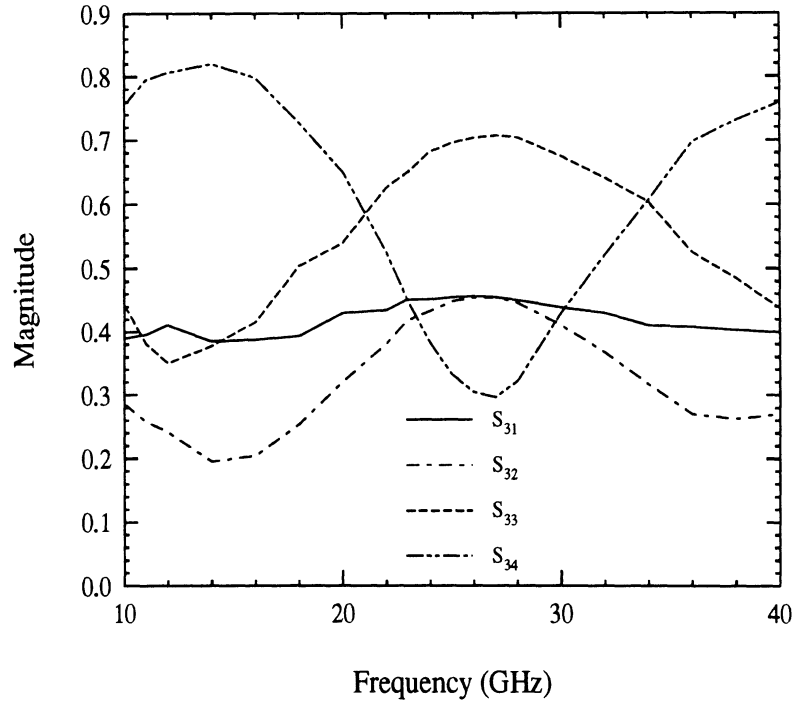
Figure 5.24: Elements of the third row of the Generalized Scattering Matrix of an air-bridge-free asymmetric short-end CPW shunt stub. (L_s=1100 μm)

increases until it reaches a minimum value at 27 GHz after which it increases with frequency. The opposite happens for the amount of power carried by the reflected slotline mode on the same input port as depicted from S_{33}. From the above, it can be deduced that the stub excites a series slotline mode resonance at 27 GHz.

Figure 5.25 shows the scattering parameters of the same asymmetric stub discontinuity after taking the transverse air-bridges into consideration. In addition, the scattering parameters of a symmetric stub discontinuity (with the same dimensions) without air-bridges are plotted in the same figure. It can be noticed that both structures exhibit totally different characteristics when the longitudinal air-bridges are removed. It is interesting to observe that the asymmetric stub without the longitudinal air-bridges still behaves as a shunt stub resonating at approximately 27 GHz. However, this frequency is not the expected resonant frequency of the coplanar mode
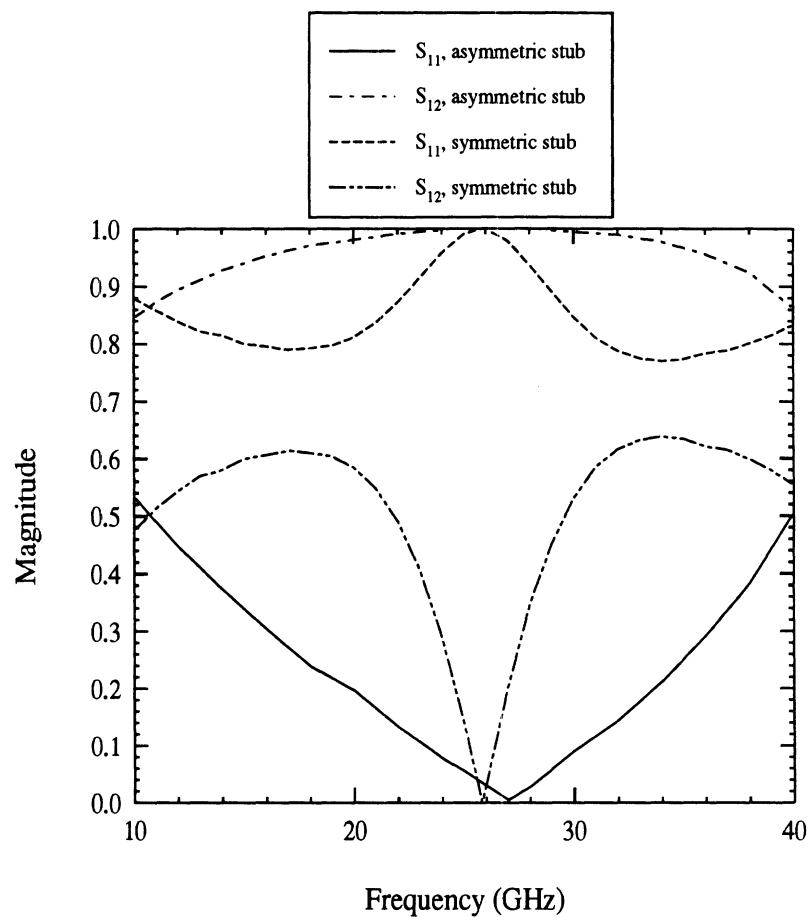
Figure 5.25: Scattering parameters of both the symmetric and asymmetric short-
end shunt CPW stub discontinuities without longitudinal air-bridges.
(L_s=1100 μm)

in the stub (see Figure 5.26). On the other hand, the behavior of the symmetric stub without the longitudinal air-bridges is far from being a shunt stub [69, 95, 93].

Figure 5.26 shows the scattering parameters of both discontinuities with all air-bridges taken into consideration. The width and height of the longitudinal air-bridge are assumed to be 15μm and 3μm, respectively. It is seen now that indeed both the asymmetric and symmetric structures behave as short-end shunt stubs with resonant frequencies of approximately 24.5 GHz and 25.2 GHz, respectively. The difference in the resonant frequencies can be attributed to the asymmetry in one of the discontinuities. It is also interesting to note that the symmetric stub has a higher Q than the asymmetric stub. The difference between the resonant frequencies of an asymmetric stub with and without the longitudinal air-bridge (as seen in Figures 5.25 and 5.26) decreases if a substrate with higher dielectric constant and/or smaller stub dimensions (slot and center conductor widths) were chosen as will be shown in Example 3. This is due to the fact that for a CPW with very small S and W and/or large ϵ_r, the propagation constants of the slotline mode and the coplanar mode become approximately equal as the frequency increases [140].

Figure 5.27 shows the phase of the scattering parameters of both discontinuities with all air-bridges taken into consideration. The similarity between the two types of shunt CPW stubs when all air-bridges are present is clearly seen.

Example 2

A comparison between theoretical and experimental results for an asymmetric stub discontinuity without longitudinal air-bridge is shown in Figure 5.28. For this structure, h=353 μm, ϵ_{r1}=11.7, ϵ_{r2}=1, S=140 μm, W=100 μm, a=4.56 mm, D_1=3.5 mm and D_2=1.8 mm. In addition, the CPW stub has a slot width of 100 μm and
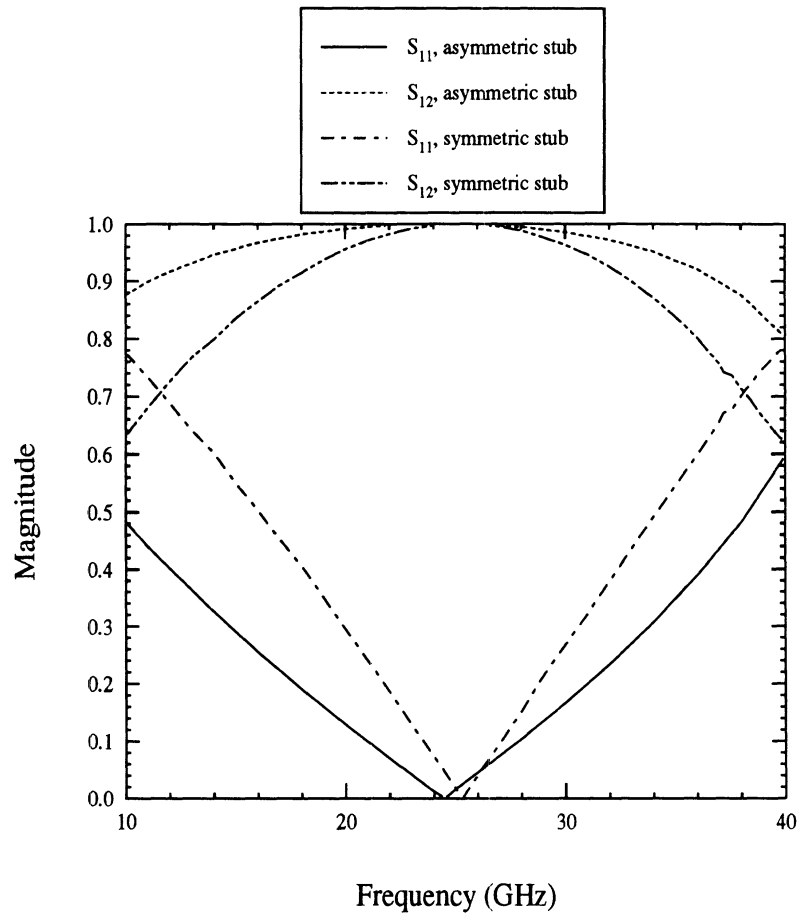
Figure 5.26: Scattering parameters of both the symmetric and asymmetric short-end shunt CPW stub discontinuities with all air-bridges taken into consideration. (L_s=1100 μm)
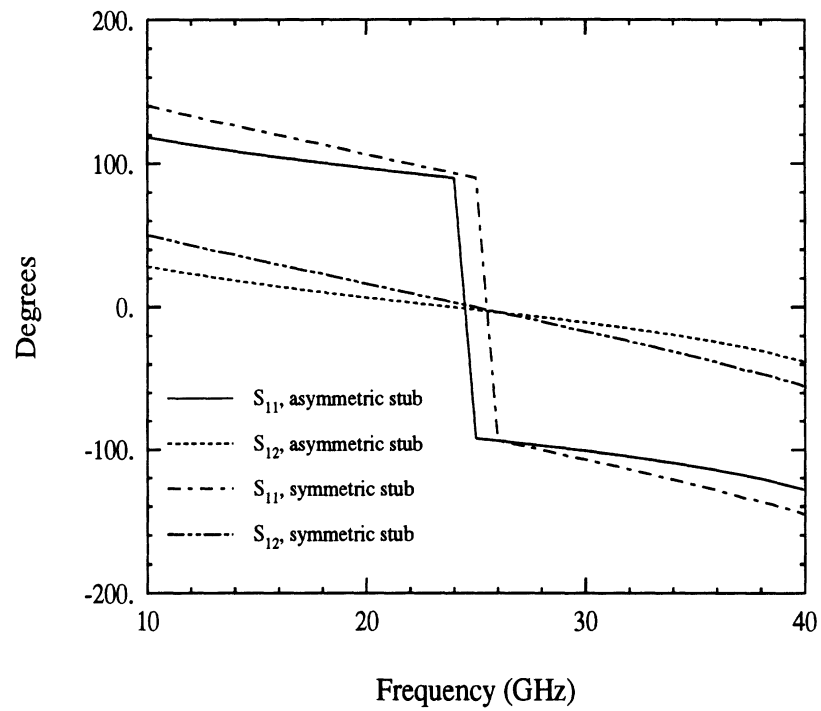
Figure 5.27: The phase of the scattering parameters of the symmetric and asymmetric short-end shunt CPW stub discontinuities with all air-bridges taken into consideration. The reference planes are taken at the end of the uniform coplanar lines. (L_s=1100 μm)
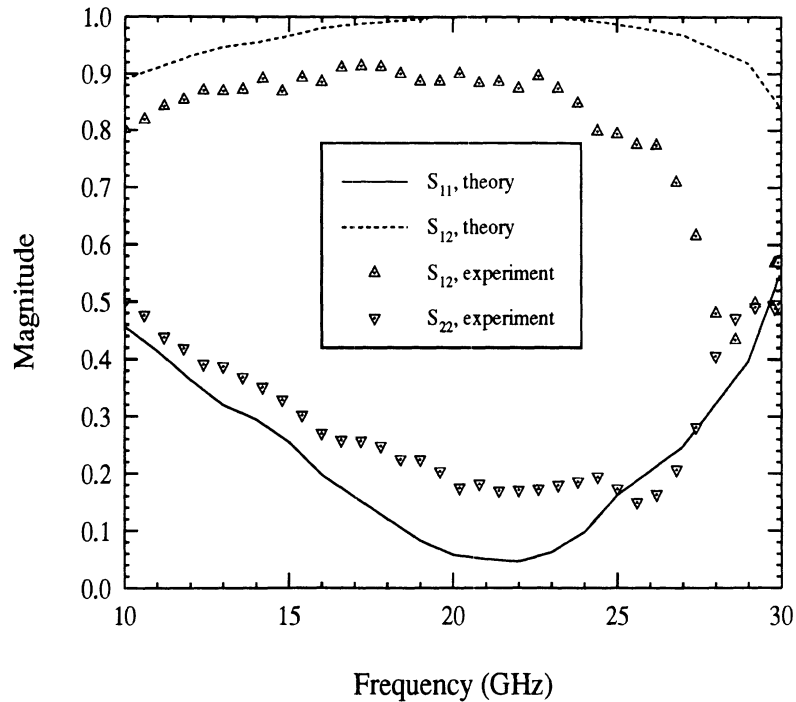
Figure 5.28: Scattering parameters of an asymmetric short-end shunt CPW stub without longitudinal air-bridge. (L_s=1600 μm)

a center conductor of 140 μm. The experiments were performed by M. Gupta [97] using a probe station and a network analyzer. It should be mentioned that the measurements were done on unshielded structures and that bond wires were used to connect the ground planes (instead of air-bridges). In Figure 5.28, the discrepancy between theory and experiment is due to radiation loss from the measured stub and the fact that bond-wires are not very effective in suppressing the slotline mode. It should be mentioned here that in the measured stub, the transverse bond-wires, which connect the ground planes of the feeding lines, were placed at a distance of 90 μm from the junction. However, the theoretical methodology assumes that ideal transverse air-bridges exist exactly at the junction.

Figure 5.29 shows the scattering parameters (theoretical and experimental) of the same asymmetric stub after including the longitudinal bond-wire in the experiments
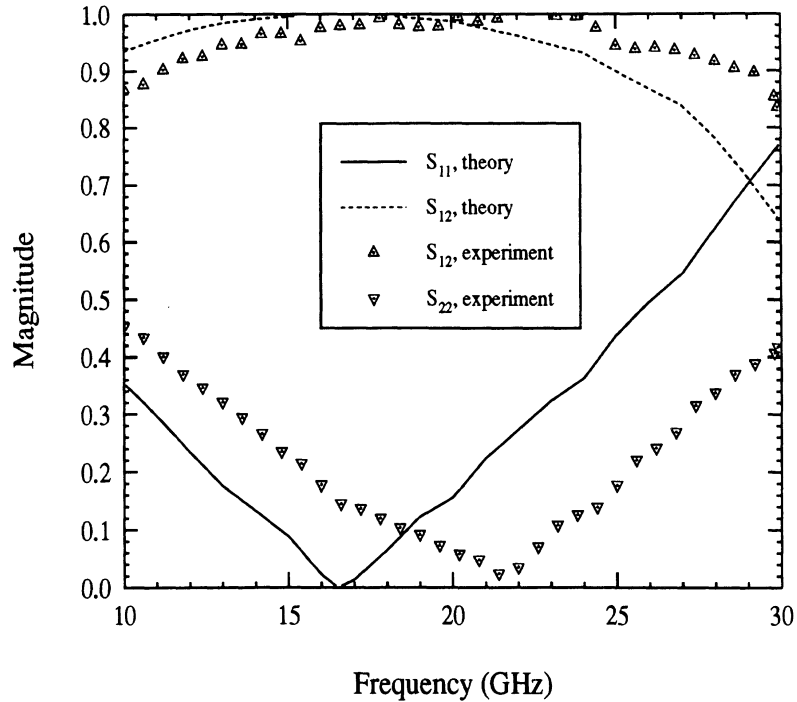
Figure 5.29: Scattering parameters of an asymmetric short-end shunt CPW stub with longitudinal air-bridge. (L_s=1600 μm)

and taking the longitudinal air-bridge into consideration in the theory. The air-bridge is assumed to be of height 3 μm and width of 10 μm. In this figure, the agreement between theory and experiment is better than that in Figure 5.28. This is due to the fact that the longitudinal bond-wire tends to suppress the radiating slotline mode in the measured stub. The difference in the resonant frequency can be attributed to the fact that the longitudinal bond-wire, which connects the stub ground planes, was placed at a distance of 190 μm from the junction. This reduces the effective length of the stub, and thus, increases the measured resonant frequency. On the other hand, the derived theoretical data for this discontinuity are based on the assumption that a longitudinal air-bridge is placed exactly at the junction. Another reason for the discrepancy in the resonant frequency is the relatively thick metallization used in the measured circuits (3 μm) which is neglected in the theoretical analysis.

Example 3

Figures 5.30 and 5.31 show the scattering parameters (theoretical and experimental) of an asymmetric stub with and without air-bridges. For this structure, h=483 μm, ϵ_{r1}=13, ϵ_{r2}=1, S=32 μm, W=20 μm, a=4.318 mm, D_1=3.0 mm and D_2=3.175 mm. In addition, the CPW stub has a slot width of 15 μm and a center conductor of 20 μm. The measurements were performed by Ponchak [97] on unshielded structures and air-bridges were used to connect the ground planes. As opposed to bond-wires, the air-bridges were placed at the junction exactly. The agreement between theory and experiment is very good which validates both sets of data. The discrepancy seen around the second resonance is mainly due to radiation losses. It is interesting to note that the behavior of the stub with and without the longitudinal air-bridge is almost the same. The resonant frequencies shown in Figures 5.30 and 5.31 differ by almost 0.8 GHz only. The reason is that the dimensions of the stub (slot and center conductor widths) are very small, and thus, the transverse air-bridges tend to equalize the potential of the two ground planes of the stub as well as the ground planes of the feeding lines. In addition, as mentioned earlier, the propagation constants of the slotline and coplanar modes are approximately the same for the CPW under consideration. Specifically, β_c/β_0 equals 2.64 and β_s/β_0 equals 2.4 at 18 GHz, where β_c, β_s and β_0 are the coplanar mode, slotline mode and free space propagation constants, respectively. A symmetric CPW stub with the same dimensions has also been measured and found to have a higher Q-factor and a somewhat larger resonant frequency than the asymmetric stub which conforms with what was found theoretically in Example 1. It has been found that this is due to the fact that the amount of energy stored in the symmetric stub is larger than that stored in the asymmetric one [97].
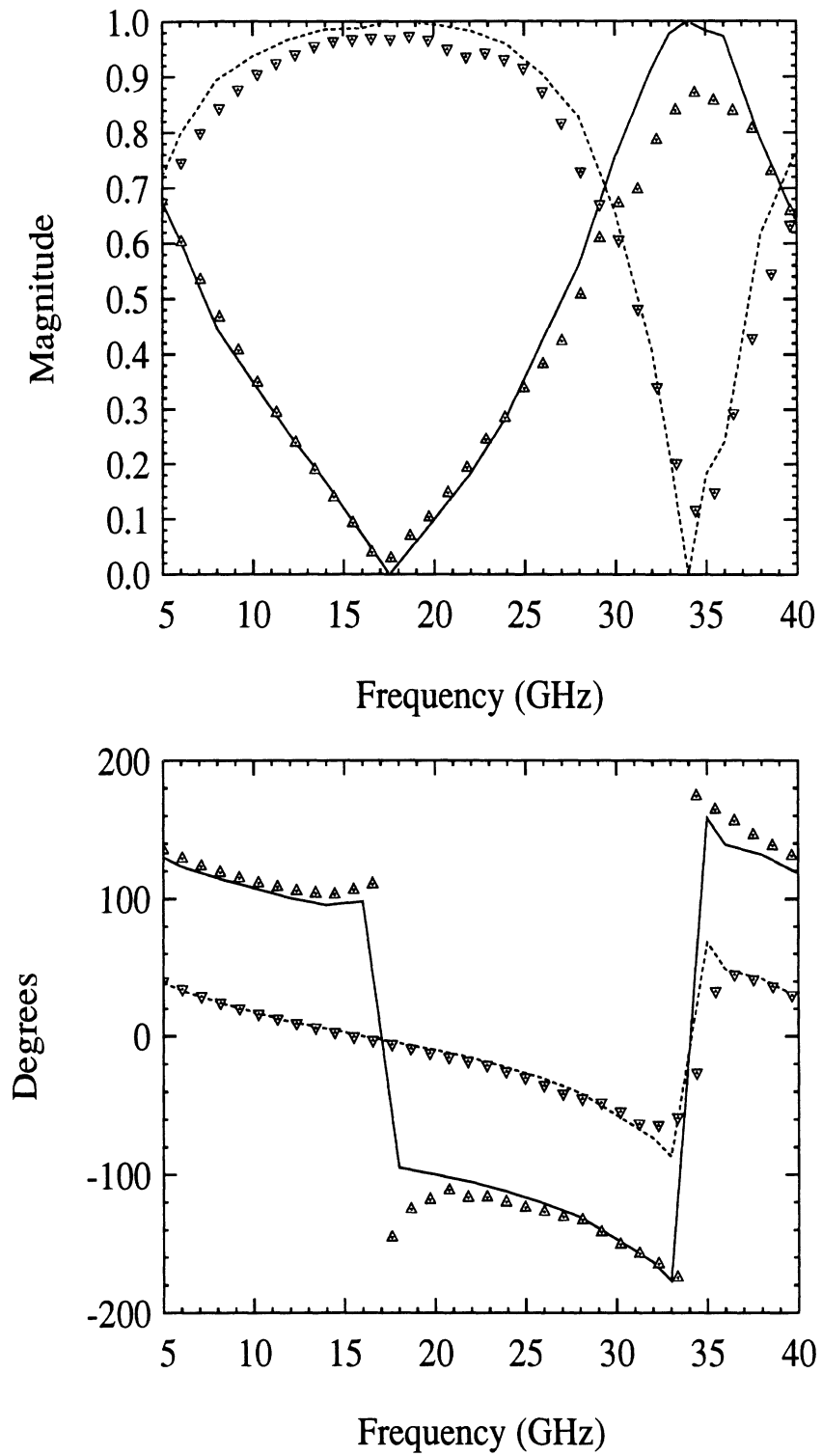
Figure 5.30: Scattering parameters of an asymmetric CPW shunt stub without longitudinal air-bridge. (L_s=1650μm).
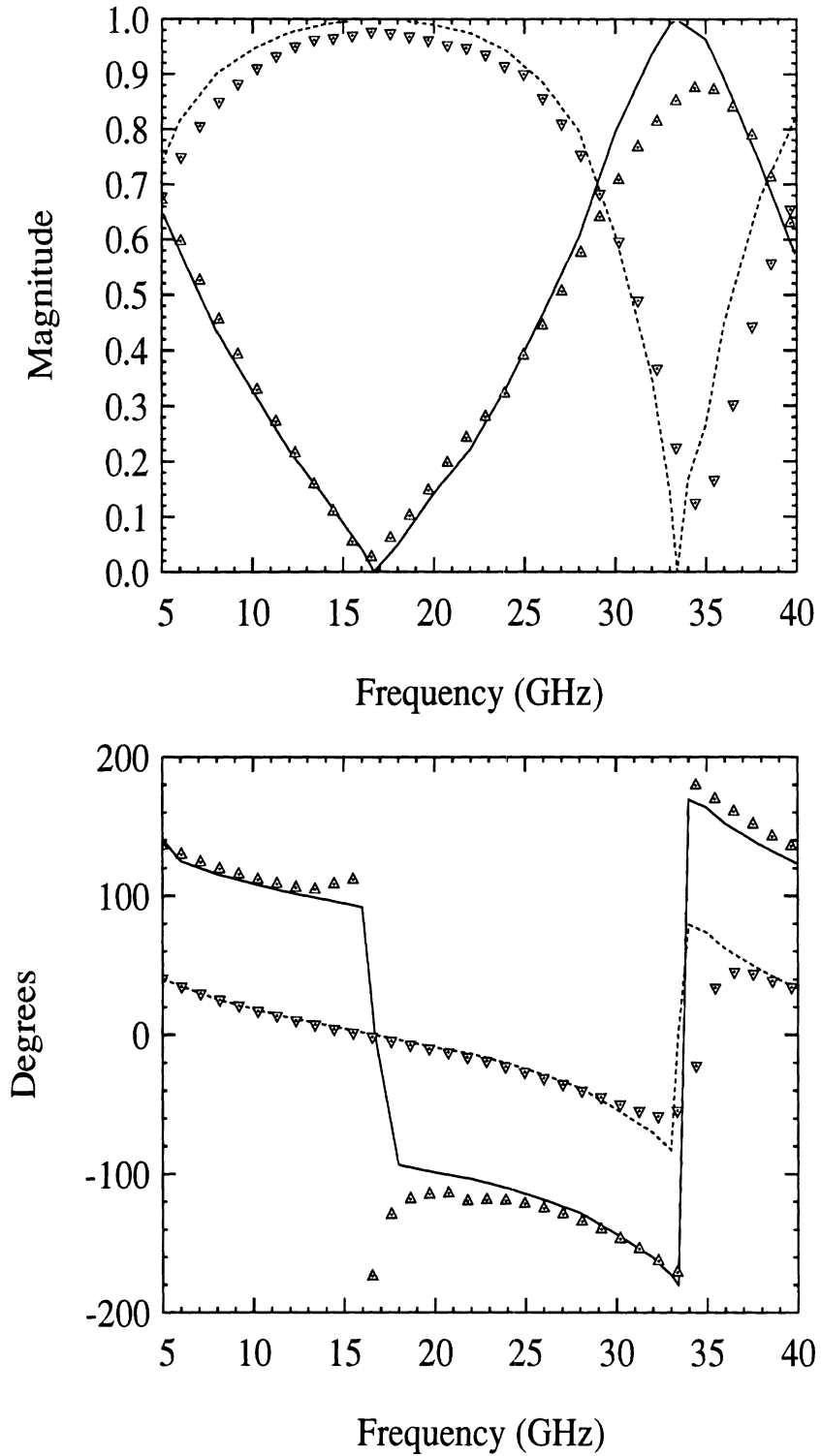
Figure 5.31: Scattering parameters of an asymmetric CPW shunt stub with longitudinal air-bridge. (L_s=1650μm).
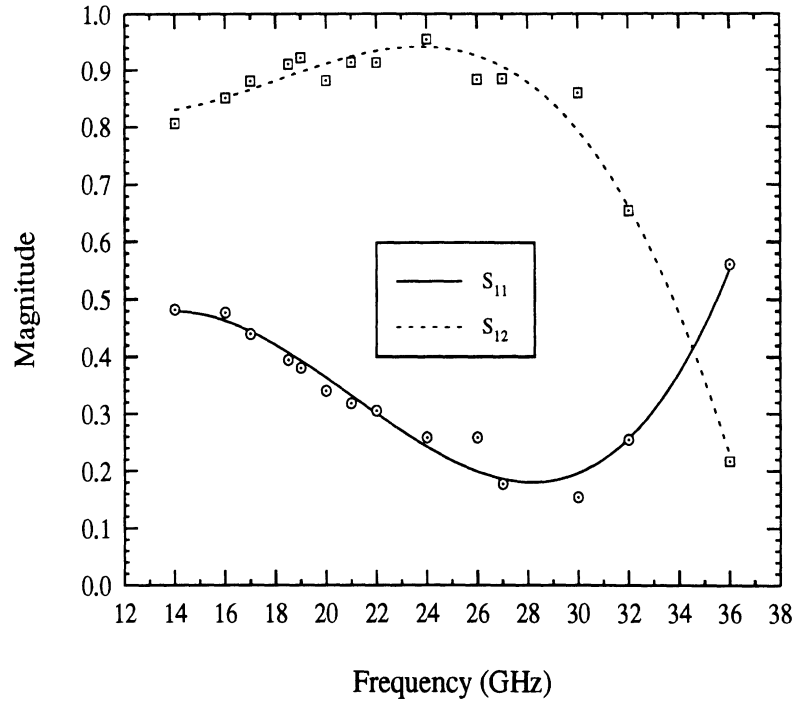
Figure 5.32: Scattering parameters of an asymmetric short-end CPW shunt stub without the longitudinal air-bridges in open environment. (S=450 μm, W=225 μm, h=635 μm, ϵ_r=9.9, W$_s$=112.5 μm, S$_s$=450 μm, L$_s$=1350 μm)

Example 4

As mentioned above, the developed numerical technique is employed to analyze asymmetric CPW discontinuities in open environment. This is performed by utilizing programs written by Harokopus [85, 86] for the CPW discontinuity problem in open environment. Figure 5.32 shows the scattering parameters of an asymmetric short-end CPW shunt stub without longitudinal air-bridges in open environment. The symbols are the numerically obtained data and the lines are the best least square error fit connecting the points. The non-smoothness of the numerical results is due to the fact that the same physical subsection length is used in the whole frequency range which creates a non-systematic error from one frequency to another. Figure 5.33 shows the scattering parameters of the same stub after taking the longitudinal air-bridge into
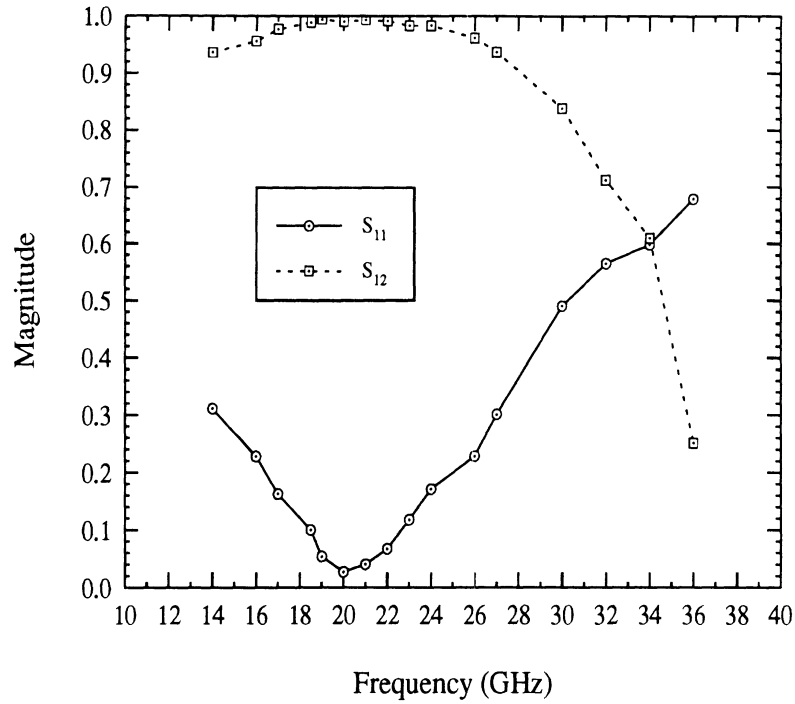
Figure 5.33: Scattering parameters of an asymmetric short-end CPW shunt stub with longitudinal air-bridges in open environment.

consideration (no fitting is used here). The height and width of the air-bridge are assumed to be 3 μm and 14 μm, respectively. It is clear that the stub resonates at 20 GHz which has been found to be approximately 2 GHz less than the frequency at which the stub is a quarter of a wavelength. Figure 5.34 shows how much power is radiated from this asymmetric stub with and without longitudinal air bridges. As expected, the presence of the longitudinal air-bridges reduces the amount of radiated power since it prevents the slotline mode from being excited in the stubs. It is clear that both stubs have negligible radiation below the resonant frequency as the case with microstrip stubs [114].
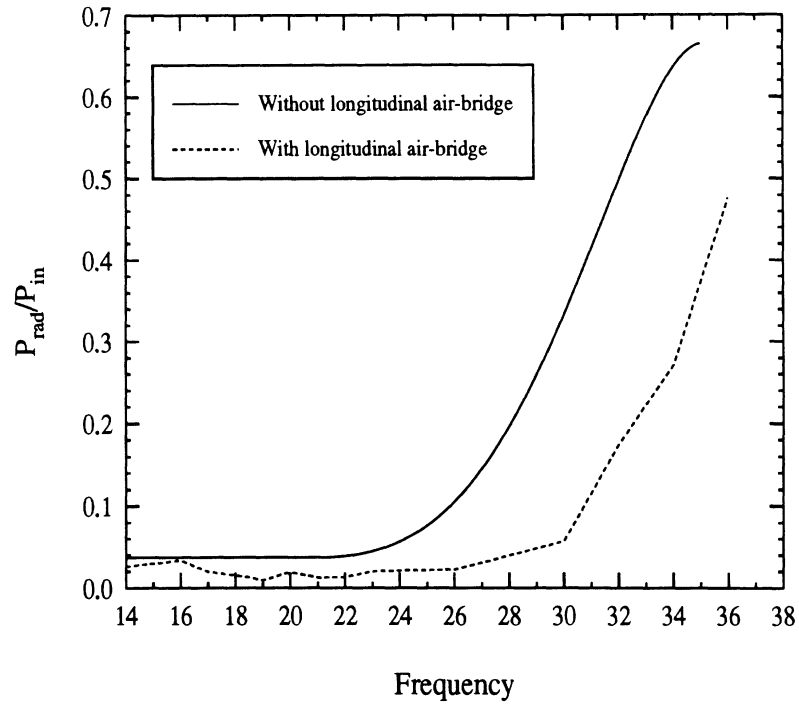
Figure 5.34: Radiation loss of the asymmetric CPW stub.

Example 5

Figure 5.35 shows the scattering parameters of a CPW right angle-bend in open environment. In this figure, the symbols are the numerically derived data and the lines are the best least square error fit. The same behavior has been reported in [72] for a shielded CPW right angle bend. Figure 5.36 shows the radiation loss of the same CPW bend. As expected, the radiated power increases as the frequency of operation increases. It is worth mentioning that a microstrip right angle bend has a similar behavior to the CPW bend [114].
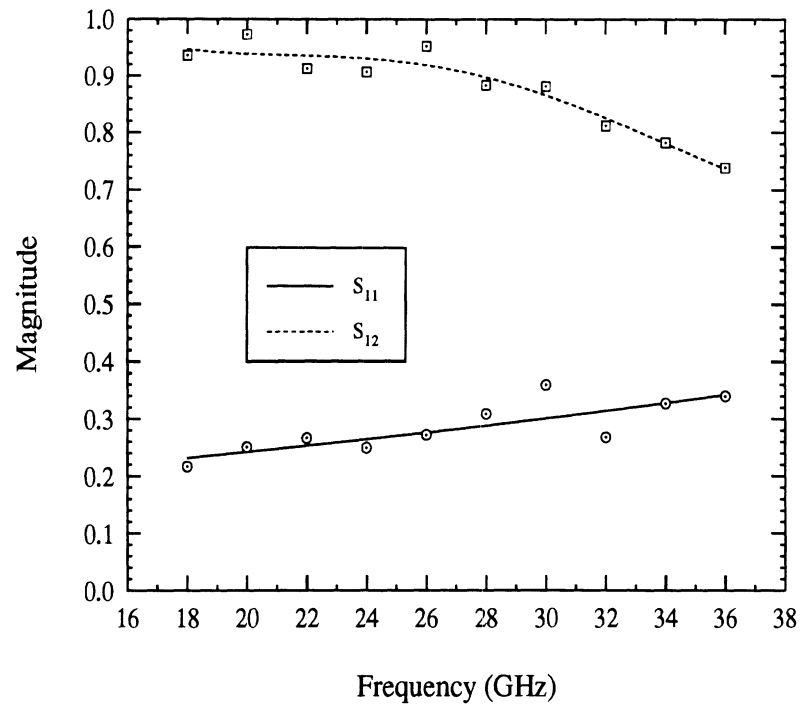
Figure 5.35: Scattering parameters of a CPW right angle bend. (S=450 μm, W=112.5 μm, h=635 μm, ϵ_r=9.9)
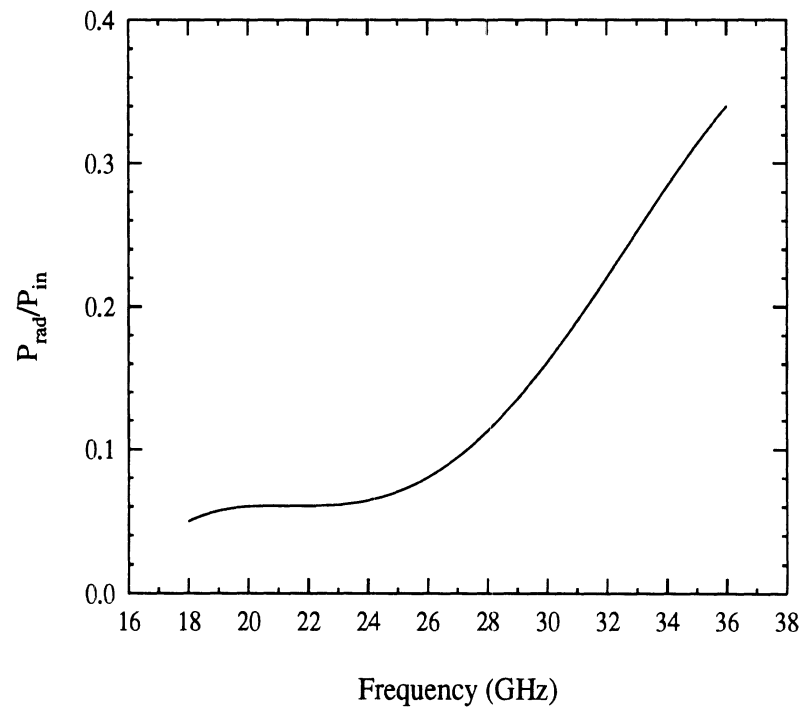
Figure 5.36: Radiation loss of the CPW right angle bend.

CHAPTER VI

MICROSHIELD LINE

6.1 Introduction

The first planar transmission line, the stripline, was introduced almost forty years ago and created the basis of a new and revolutionary hybrid technology. Since then, the hybrid technology has evolved into a monolithic one drastically increasing operating frequencies and consequently reducing weight and volume. In conventional planar transmission lines, the power propagates by creating an RF voltage difference between two planar conductors printed on the same (coplanar waveguides, coplanar strips) or opposite surfaces (stripline, microstrip, coupled strips) of a dielectric slab structure. In most cases, the geometry of the conventional lines permitted great design flexibility, tremendous reduction of the space occupied by the circuit, and realization of very large scale, very high frequency applications.

The planarization of the conductors in the above transmission lines provided the capability of integration but also generated fringing in the electromagnetic fields, led to unwanted mechanisms such as radiation and dispersion, and enhanced ohmic losses and electromagnetic coupling. These mechanisms are frequency dependent and impose serious limitations as we approach the submillimeter frequency range. The ability to find new geometries [141]-[147] which reduce or eliminate the above loss

or coupling mechanisms but do not affect the monolithic character of the line will extend the operating frequencies long into the Terahertz region and will improve circuit performance in existing applications.

As a common practice, elimination of radiation losses and reduction of electromagnetic coupling has been achieved by enclosing the planar circuits in shielding cavities. In most cases, the cavities have to be placed away from the circuit to avoid proximity effects, thus introducing cavity resonances which interfere with the circuit's electrical performance. While shielding is possible in many circuit applications, in monolithic arrays where the enviroment has to remain open, radiation from the feeding structure and parasitic coupling to the radiating elements has been a major issue.

This chapter presents a preliminary theoretical analysis of the **microshield line**, a new type of monolithic line appropriate for circuit or array applications, which was proposed by Katehi and Rebeiz in 1990 [148]-[152]. This geometry may be considered as an evolution of the conventional microstrip line or coplanar waveguide and is characterized by low radiation loss, reduced electromagnetic interference and compatibility to antennas of microstrip or aperture type. In addition, the microshield geometry can create the basis of a new technology and can lead to novel ideas in antenna and array design [152]. In this new line, the ground plane has been deformed from its original planar form to totally or partially surround the inner strip conductor as a shielding microcavity (see Figure 6.1). Such a structure can be made monolithically using etching and metal deposition techniques. Furthermore, the inner conductor can be suspended in air (Figures 6.1(a) and (b)) by using membrane technology [153]. This eliminates dielectric losses which could be high at millimeter-wave frequencies. Membranes have been effectively employed to provide high-efficiency monolithic antennas and arrays operating at frequencies as high as 2.5 THz [154].
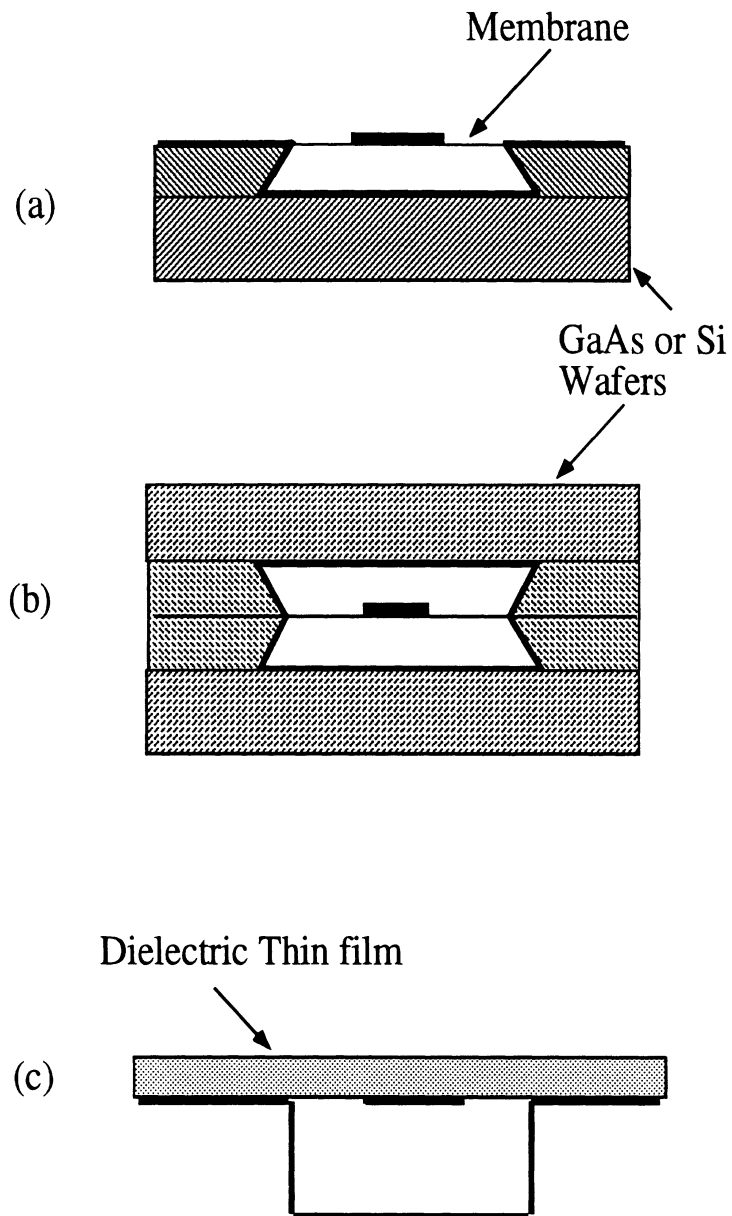
Figure 6.1: Cross sectional views of (a) microshield line, (b) shielded microshield line, and (c) dielectric microshield line suitable for scaled measurements.

One of the advantages of the microshield line, in comparison with the more conventional ones such as the microstrip or the coplanar waveguide, is the ability to operate without the need for via-holes or the use of air-bridges for ground equalization. Furthermore, due to the many available parameters in design, a wide range of impedances may be achieved. Specifically, by varying the size of the shielding microcavity (see Figure 6.1), the per unit length capacitance of the line can increase or decrease from the value of the corresponding microstrip or coplanar waveguide resulting in lower or higher values of the characteristic impedance. One loss mechanism still pertaining in this novel structure is conductor loss. Due to the geometry of the ground plane, conductor loss is expected to be slightly higher than microstrip and lower than conventional CPW. The presence of conductor losses limits the use of microshield lines and circuits to the lower end of the sub-mm wave spectrum (up to 500 GHz).

In this chapter, for the sake of completeness, the process for the fabrication of the microshield line is described in section 2 although the author of this dissertation has not fabricated a microshield line himself. Then, the microshield line 2D parameters (propagation constant and characteristic impedance) are derived in section 3 where two techniques are used to obtain these parameters: a computational technique based on the point matching method (PMM) and an analytical one based on the conformal mapping method (CMM). Furthermore, to provide an indication of the tendency of the microshield line to radiate less, several three-dimensional discontinuities are analyzed and their response is compared to the same discontinuity geometries in conventional coplanar waveguide form (section 4). In all cases, the microshield discontinuities show much lower radiation than the conventional CPW ones.

6.2 Fabrication

The fabrication of microshield circuits is dependent on the thin dielectric membrane technology and the anisotropic etching of the supporting wafers. A Si membrane is a 3-layer $SiO_2/Si_3N_4/SiO_2$ structure which must be slightly in tension to yield flat and rigid self-supporting characteristics. The bottom SiO_2 layer is made by high temperature thermal oxidation (1100°), while the other layers are made by chemical vapor deposition at 800° [153]. After the development of the three-layer structure, the membranes are fabricated in two steps. First, an opening in the silicon-nitride layers is defined on the back of the wafer, and then the silicon is etched until a transparent membrane appears. The etching solution is anisotropic and yields pyramidal cavities which can be exploited for microshield transmission-lines. Figure 6.2 gives the most important steps of the procedure in a simplified way. Once the membranes are fabricated, it is easy to lithographically define several different microshield geometries for impedance and propagation constant measurements. It should be noted that the capacitance between the upper ground and lower ground metallizations is very high, which essentially presents an RF short at high frequencies.

The microshield geometry can create the basis of a new technology and can lead to novel ideas in antenna and array design. Figure 6.3 shows a bottom view of a microshield line filter with the shielding ground plane removed. This circuit has been made as a proof of fabrication feasibility and it does not present an optimized design. It was fabricated by Prof. G. Rebeiz's group. In fact, in order to successfully design this antenna configuration many important issues associated with the microshield geometry have to be studied and understood. Some of these issues are (i) dispersion (ii) parasitic radiation, (iii) transitions from conventional planar lines to microshield structures and (iv) electromagnetic coupling to neighboring circuit elements.

Step 1

Si or GaAs Waffer

Step 2

1 μ Membrane

Etch

Step 3

Metallize

Metallize

Step 4

Shield the back of the Cavity
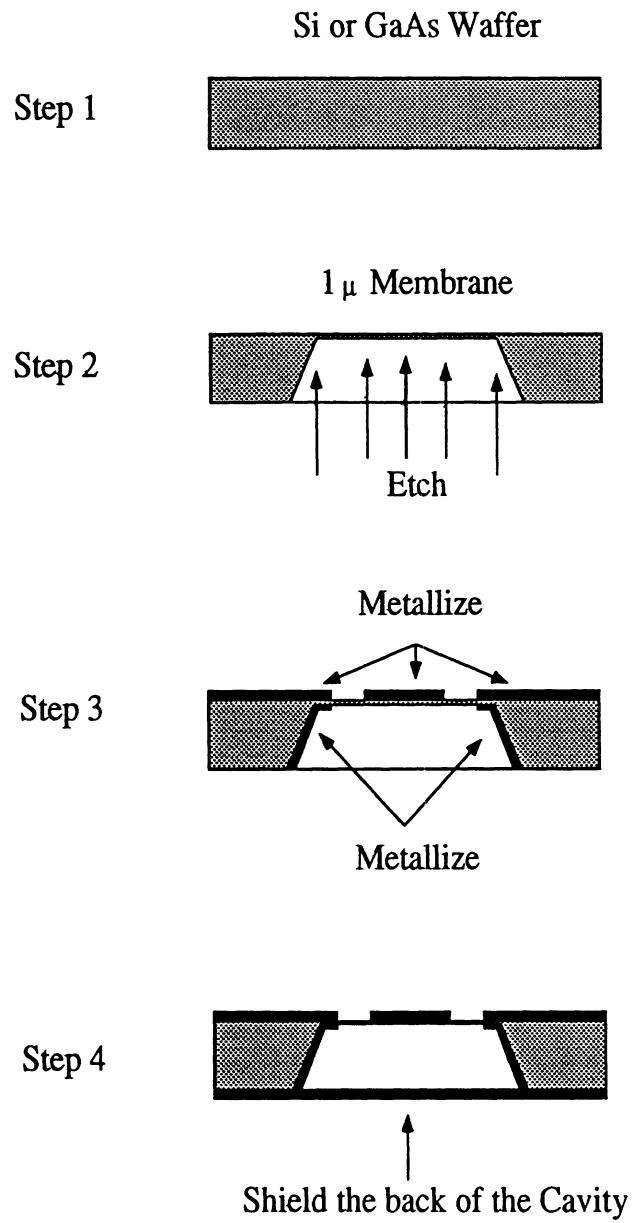
Figure 6.2: Fabrication process for the microshield line.
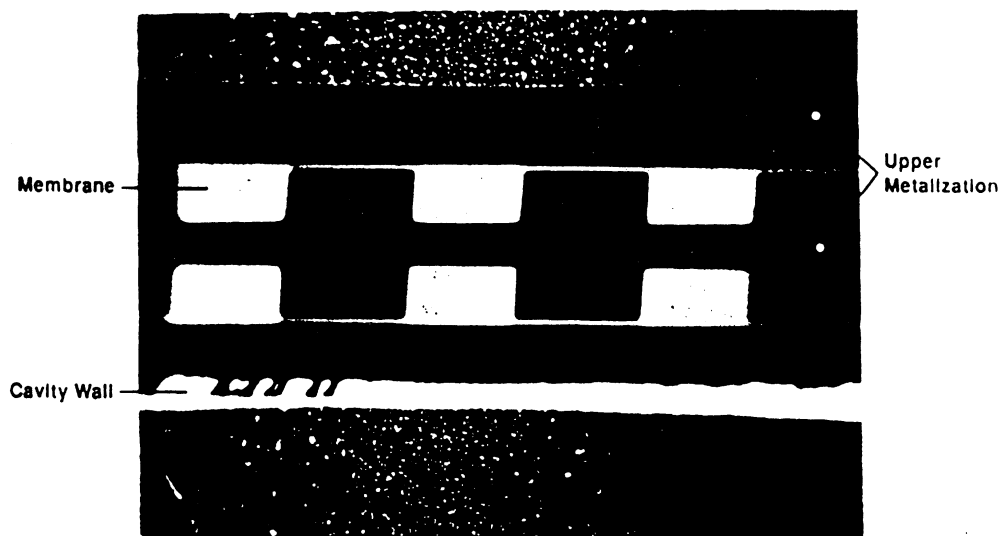
Figure 6.3: A microshield line low-pass filter.

6.3   2D Characterization

In this section, two techniques are used to obtain the 2D parameters (effective dielectric constant and characteristic impedance) of the microshield line: a computational technique based on the point matching method (PMM) [36, 37] and an analytical one based on the conformal mapping method (CMM). A CAD-oriented closed form expression, that can be easily evaluated, is derived using the CMM. This expression gives values of the characteristic impedance which are in very good agreement with those obtained using the PMM. In addition, the effect of finite-extent ground planes on the characteristic impedance is demonstrated.

For the numerical analysis, the cross section of the microshield line is simplified as shown in Figure 6.4. In this figure, the effect of the membrane is neglected since its thickness ($\simeq 1.4$ μm) is very small compared to the waveguide height. Also, the
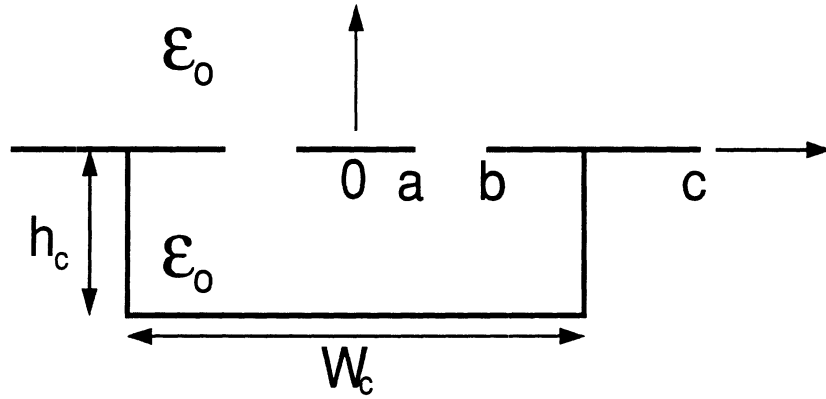
Figure 6.4: Simplified cross sectional view of the microshield line suitable for 2D theoretical formulation.

ground planes are assumed to be of finite extent in order to be able to investigate their effect on the characteristics of the line, and the pyramidal shielding cavity is replaced by a rectangular one.

In the PMM [36, 37], first, Laplace's equation is solved in the air and the waveguide regions (and the dielectric region in case of dielectric microshield). Then, the boundary conditions in the plane of the slot aperture are enforced which result in a matrix equation that can be solved to give the unknown potential distribution. Finally, the capacitance per unit length and consequently ϵ_{eff} and Z_0 can be computed from the derived potential. The details of the PMM as applied to the microshield line geometry can be found in Appendix C. One disadvantage of the PMM is that it is computationally intensive. Thus, it will be helpful to derive an analytical formula for the evaluation of Z_0 of the microshield line. Such a formula can be easily obtained using the CMM as discussed below.

The CMM has been widely used to obtain analytical formulas for the quasi-TEM parameters of the coplanar waveguide (CPW) structures [1], [27]-[35]. For the microshield line (Figure 6.4), the overall capacitance per unit length is the sum of the

capacitance of the upper half plane (open air region) and the lower half plane (the waveguide region). The former capacitance, C_a, can be easily obtained using the following formula [27]:

$$C_a = 2\,\epsilon_0 \frac{K(k)}{K(k')} \tag{6.1}$$

where

$$k = \frac{a}{b}\sqrt{\frac{1 - b^2/c^2}{1 - a^2/c^2}}$$

$$k' = \sqrt{1 - k^2}$$

and K(k) is the complete elliptic integral of the first kind [155]. The capacitance due to the waveguide region, C_w, can be evaluated through a suitable sequence of conformal mappings from which the following formula can be obtained (see Appendix D for details):

$$C_w = 2\,\epsilon_0 \frac{K(\zeta)}{K(\zeta')} \tag{6.2}$$

where

$$\zeta = \frac{sn(a/\beta)}{sn(b/\beta)}$$

$$\zeta' = \sqrt{1 - \zeta^2}$$

$$\beta = \frac{W_c}{2K(\gamma)}$$

$$\gamma = \left[\frac{e^{\pi W_c/2h_c} - 2}{e^{\pi W_c/2h_c} + 2}\right]^2 .$$

In the above, $sn(\theta)$ is the Jacobian elliptic function which can be evaluated using the routine in [156]. After evaluating (6.1) and (6.2), the total capacitance per unit length of the line may be obtained as

$$C_{total} = C_a + C_w \tag{6.3}$$
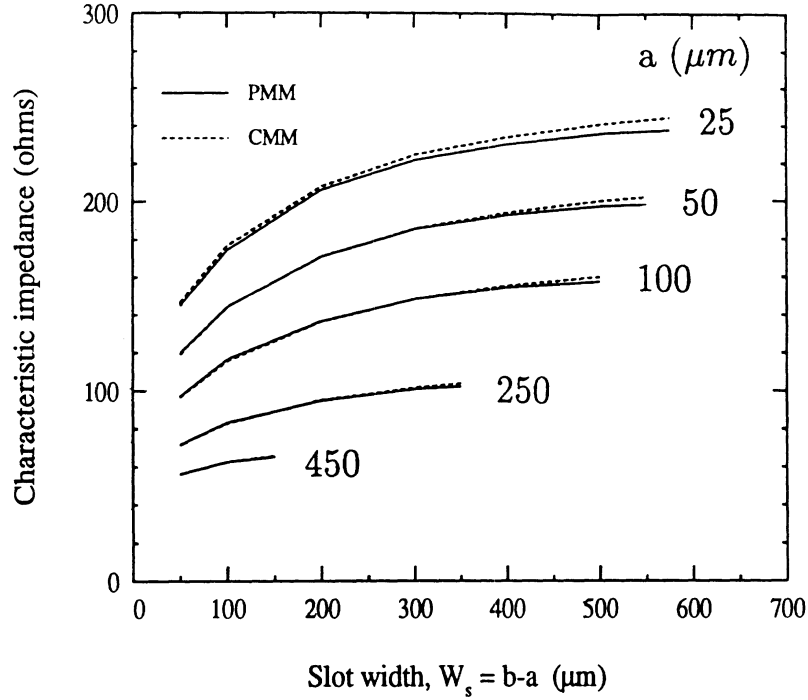
Figure 6.5: Characteristic impedance of a microshield line with $W_c=1200$ μm, $h_c=400$ μm and $c=1800$ μm.

from which the characteristic impedance Z_0 can be derived as

$$Z_0 = \frac{1}{v_0 C_{total}} \tag{6.4}$$

where v_0 is the speed of light in free space. The above TEM analysis, using either PMM or CMM, should provide the exact characteristic impedance of the microshield line as long as the line operates in the single mode frequency range.

Figure 6.5 shows Z_0 of a microshield line, evaluated using PMM and CMM, as a function of slot width, W_s, and with the center conductor width as a variable. As shown, the results obtained by the two methods differ by less than 3%, which validates the derived closed form analytical expression. It should be mentioned that for small slot and/or center conductor width (≤ 100 μm), the size of the matrix involved in the PMM becomes very large in order to insure convergence.

Figure 6.6 shows the characteristic impedance of a microshield line as a function
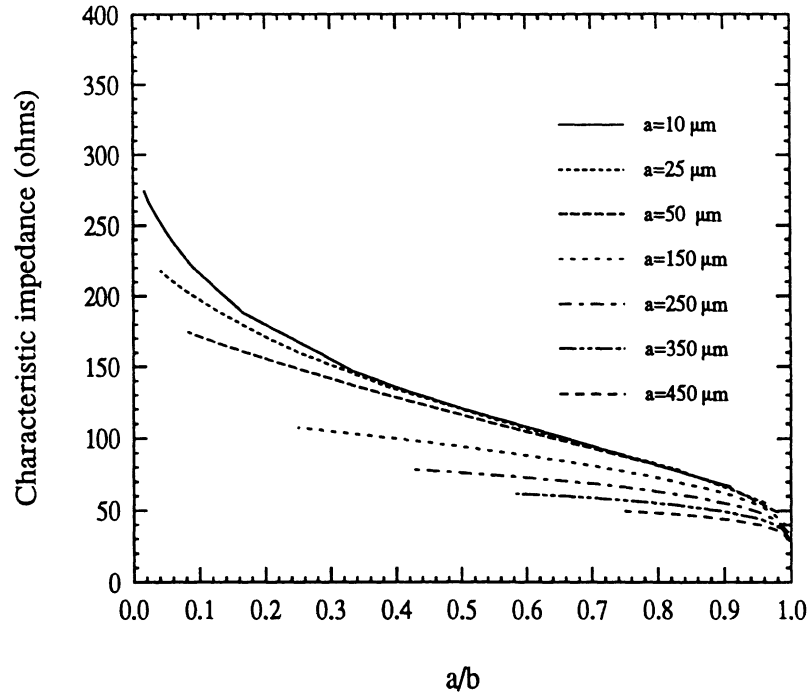
Figure 6.6: Characteristic impedance of a microshield line with W_c=1200 μm, h_c=200 μm and c→ ∞.

of the aspect ratio a/b for different center conductor widths. In this figure, the cavity height is half of that in Figure 6.5 which results in a smaller Z_0 (for the same a and b) due to the increase in the capacitance of the line. It is worth mentioning here that Z_0 of the microshield line approaches the microstrip limit as a/b →0 [36]. For example, Z_0 of an air-filled microstrip with a conductor width to substrate height ratio of 0.5 is approximately 167 Ω which is 4% different from the upper limit of Z_0 of the microshield line shown in Figure 6.6 with a=50 μm. On the other hand, the coplanar limit is approached as h_c/a → ∞ [36] or a/b → 1. This can be clearly seen in Figure 6.7 where Z_0 of a free-space CPW is compared to that of a microshield line with different cavity heights.

Figure 6.8 shows the effect of finite extent ground planes on the characteristic impedance of a microshield line. It can be seen that finite extent ground planes have
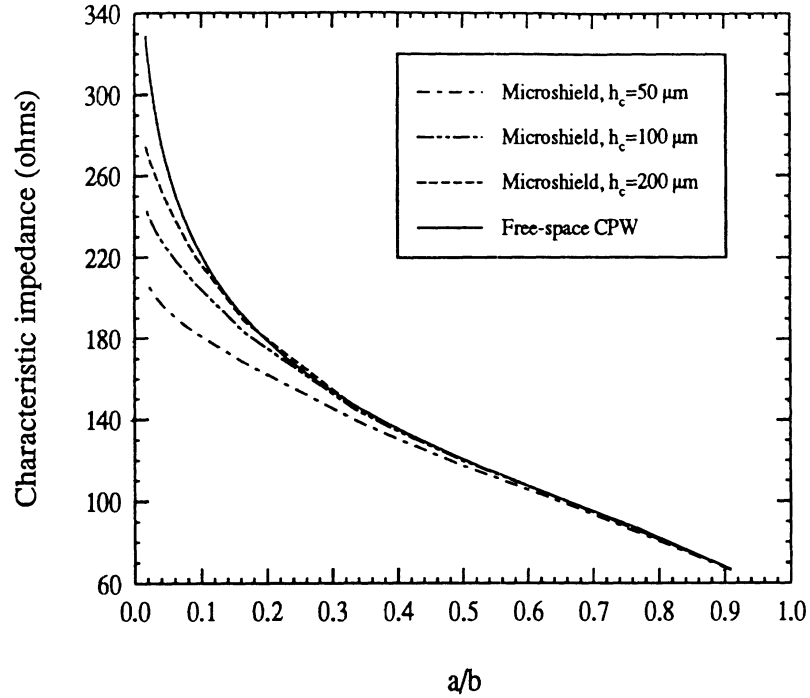
Figure 6.7: Comparison of the characteristic impedance of a microshield line (W_c=1200 μm) and a free-space CPW. Center conductor width=20 μm for both lines.

negligible effect on Z_0 as long as $c/b > 2$. This is an advantage of the microshield line over the conventional CPW where c/b should be larger than 4 to insure that the variation is negligible [27]. This is due to the fact that the fields are more confined in the shielding microcavity of the microshield line.

Figure 6.9 shows ϵ_{eff} and Z_0 of the microshield and dielectric microshield lines as functions of the aspect ratio a/b (a closed form expression for the characteristic impedance of a dielectric microshield line is derived in Appendix D). In this figure, the center conductor width ($2a$) varies while b stays equal to $W_c/2$. As expected, the characteristic impedance of the dielectric microshield is lower than that of the microshield since the dielectric layer tends to increase the capacitance of the line. In addition, it can be seen that ϵ_{eff} of the dielectric microshield is relatively insensitive to the center conductor width.
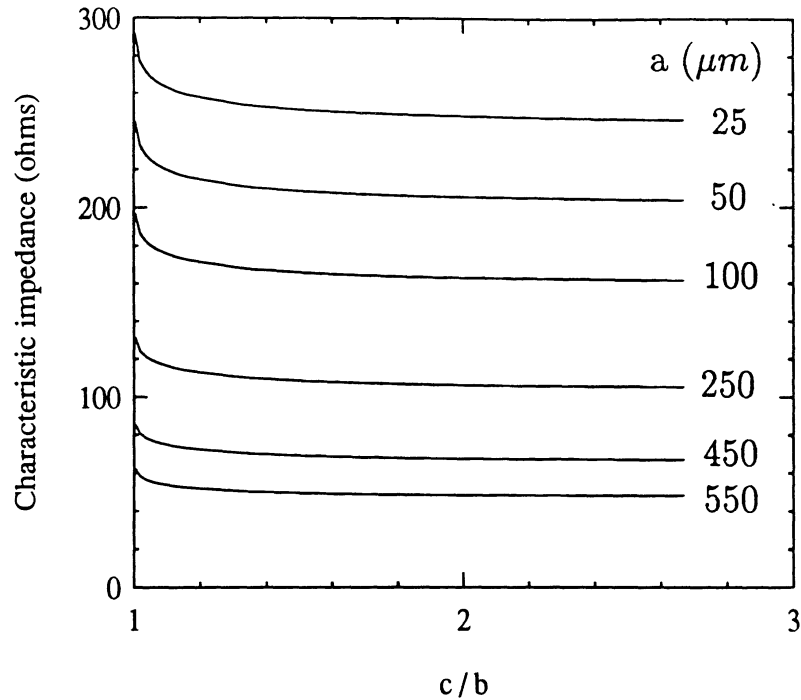
Figure 6.8: The effect of finite ground plane extent on the characteristic impedance of a microshield line with W_c=1200 μm, h_c=400 μm and b=600 μm.

6.4 3D Characterization

In this section, several 3D microshield discontinuities are analyzed and their response is compared to the same discontinuity geometries in conventional CPW. The theoretical method, used to analyze microshield line discontinuities, is based on the Space Domain Integral Equation (SDIE) method described in Chapter 2. The only difference here is that the components of the dyadic Green's function $\overline{\overline{G}}_1^h$ are Sommerfeld type integrals. Thus, the theoretical analysis of 3D microshield structures has been performed in cooperation with Harokopus [148].

In the numerical results shown in Figures 6.10 through 6.13, the microshield lines and the conventional coplanar waveguides have a center conductor width of 500 μm and slot widths of 250 μm. The substrate used in the dielectric microshield and in
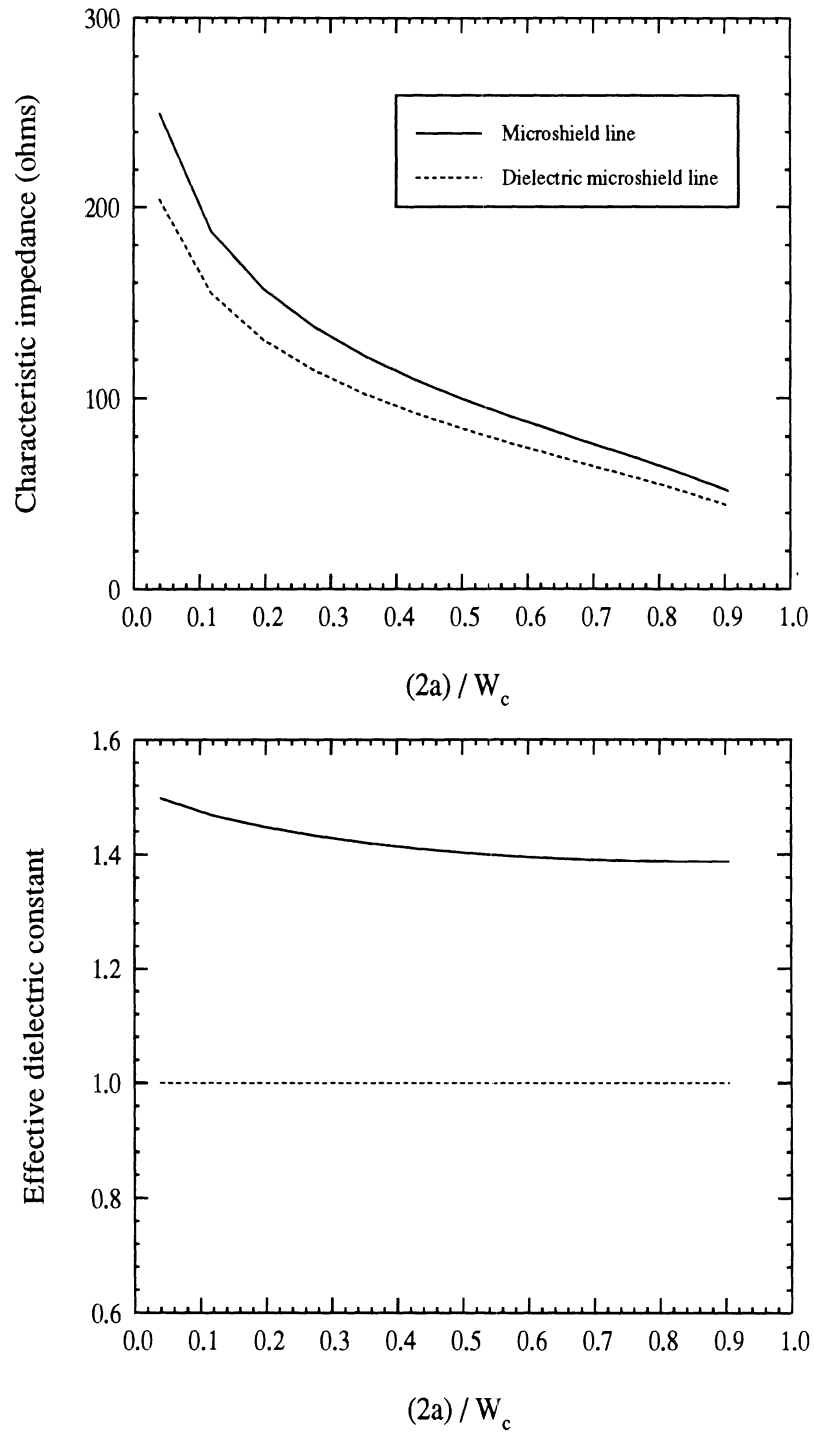
Figure 6.9: Characteristic impedance and effective dielectric constant of microshield and dielectric microshield lines. (W_c=2.54 mm, b=1.27 mm, dielectric thickness=0.7874 mm, ϵ_r=2.2, h_c=1.27 mm)

the coplanar waveguide is 635 μm thick and has a dielectric constant ϵ_r=2.1. The waveguide size (height and width) is specified in the figures' captions. The chosen waveguide size does not present an optimum design and the results presented here, by no means, provide a complete study of the electrical performance of the microshield line. These specific dimensions were merely used as examples to demonstrate the capability of the proposed microshield line to radiate considerably less than the corresponding coplanar waveguides.

Four different microshield discontinuities are treated in this section: a short-end (Figure 3.1(b)), an open-end (Figure 3.1(c)), coupled short-ends (Figure 4.1(a)), and coupled open-ends (Figure 4.1(b)). Even if there are other discontinuities which radiate more, the above geometries can give a very good indication of what should be expected from other more complex planar structures.

6.4.1 Short-End

As shown in Figure 6.10, the microshield line short-end tends to give lower normalized inductive reactance than the conventional coplanar waveguide and the dielectric microshield. This tendency is consistent over the whole frequency range.

6.4.2 Open-End

Figure 6.11(a) shows the normalized capacitive reactance of an open-end as a function of the gap width for the three types of the proposed microshield line and is compared to the CPW open end. In addition, the radiation loss factor, 10 log(1-| Γ |^2), for the same discontinuity is shown in Figure 6.11(b). It can be noticed that the microshield line has an open-end reactance which is almost 40% higher than the dielectric microshield line and the conventional CPW. At the same time, the dielectric
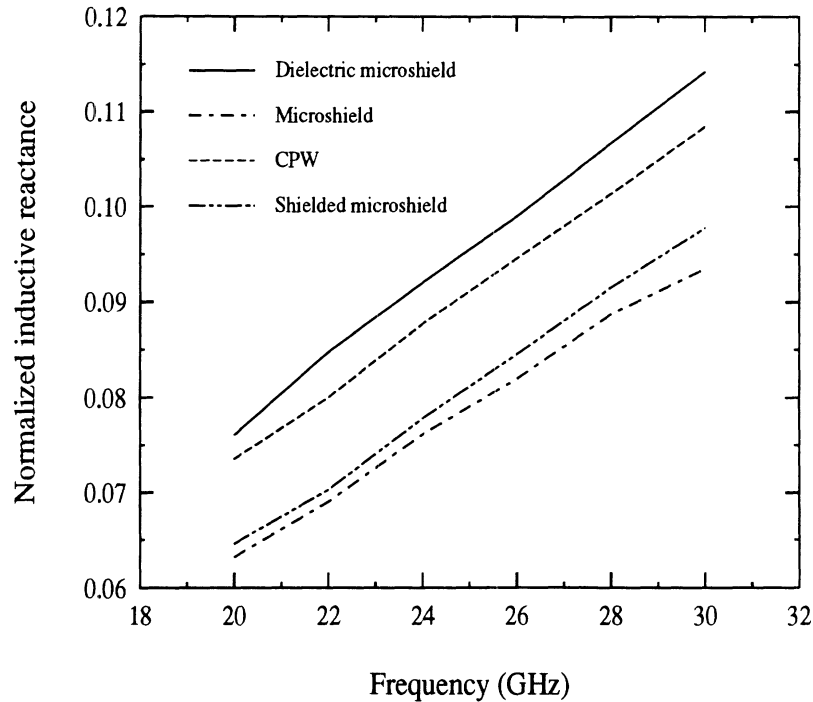
Figure 6.10: Normalized inductive end reactance of a short-end discontinuity. (h_c=3 mm, W_c=1.5 mm)

microshield open-end has the lowest radiation loss which is approximately half of that encountered in the conventional CPW open-end. Low radiation results from the good confinement of the fields in the slots which is due to the presence of the dielectric substrate and the shielding cavity.

6.4.3 Coupled Short-Ends

Figure 6.12 shows the loss factor, $10 \log(1-|S_{11}|^2-|S_{12}|^2)$, for the coupled short-ends discontinuity as a function of frequency. Again, the dielectric microshield has smaller radiation loss factor than the microshield and the conventional CPW. Despite these differences, the radiation loss is very small in all cases due to the type of the planar discontinuity.
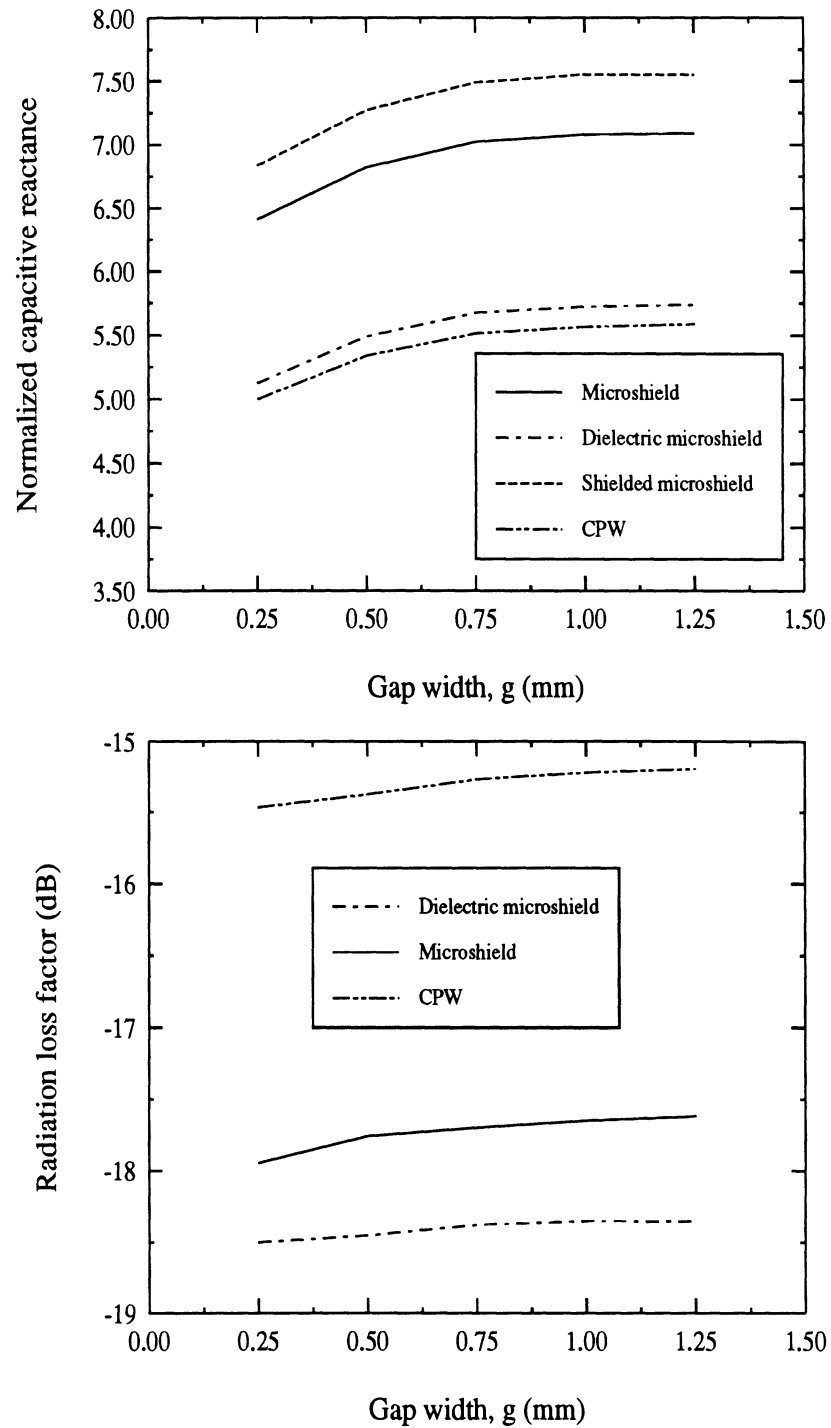
Figure 6.11: Normalized capacitive end reactance and the radiation loss due to an open-end discontinuity. (h_c=3 mm, W_c=3 mm, f=24 GHz)
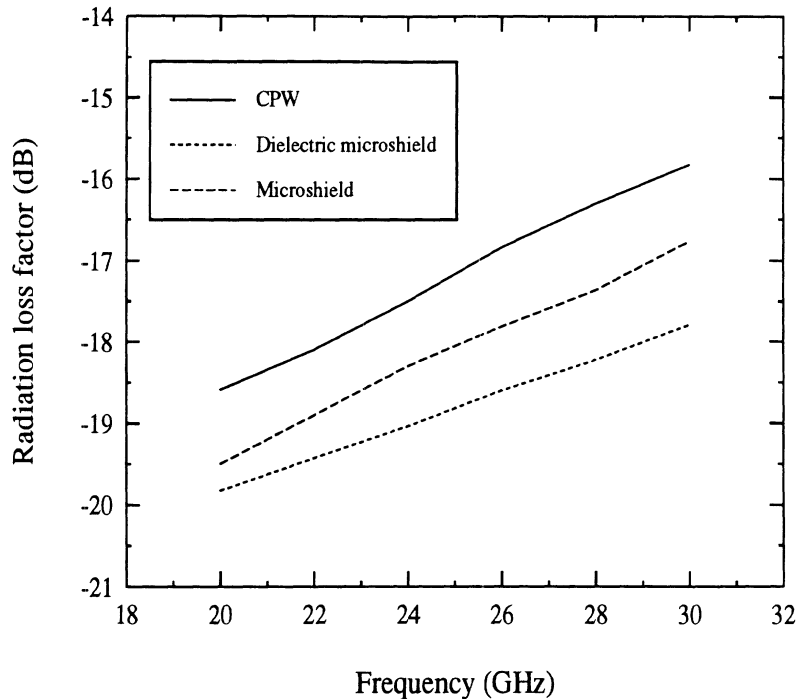
Figure 6.12: Radiation loss factor of two coupled short-ends. (h_c=3 mm, W_c=3 mm, separation between the two lines=0.25 mm)

6.4.4 Coupled Open-Ends

Figure 6.13 shows the magnitude of S_{12} and the loss factor for this discontinuity as a function of frequency. Here the cavity size is chosen such that the sidewalls touch the slot edges and with height equal to one slot width. It can be seen that the amount of radiated power from the coupled microshield open-ends is approximately one third that from coupled open-ends made of conventional CPW. In addition, the dielectric microshield coupled open-ends radiate more than the microshield in contrast to the coupled short-end discontinuity (Figure 6.12). This is due to the excitation of the surface waves from the open ends along the direction of propagation.

As a second example, Figure 6.14 shows the loss factor for the coupled open-ends discontinuity configuration with an inner conductor width of 1.5 mm, slot-width of 0.5 mm and microcavity width and height given by 2.54 mm and 1.27 mm, respectively.
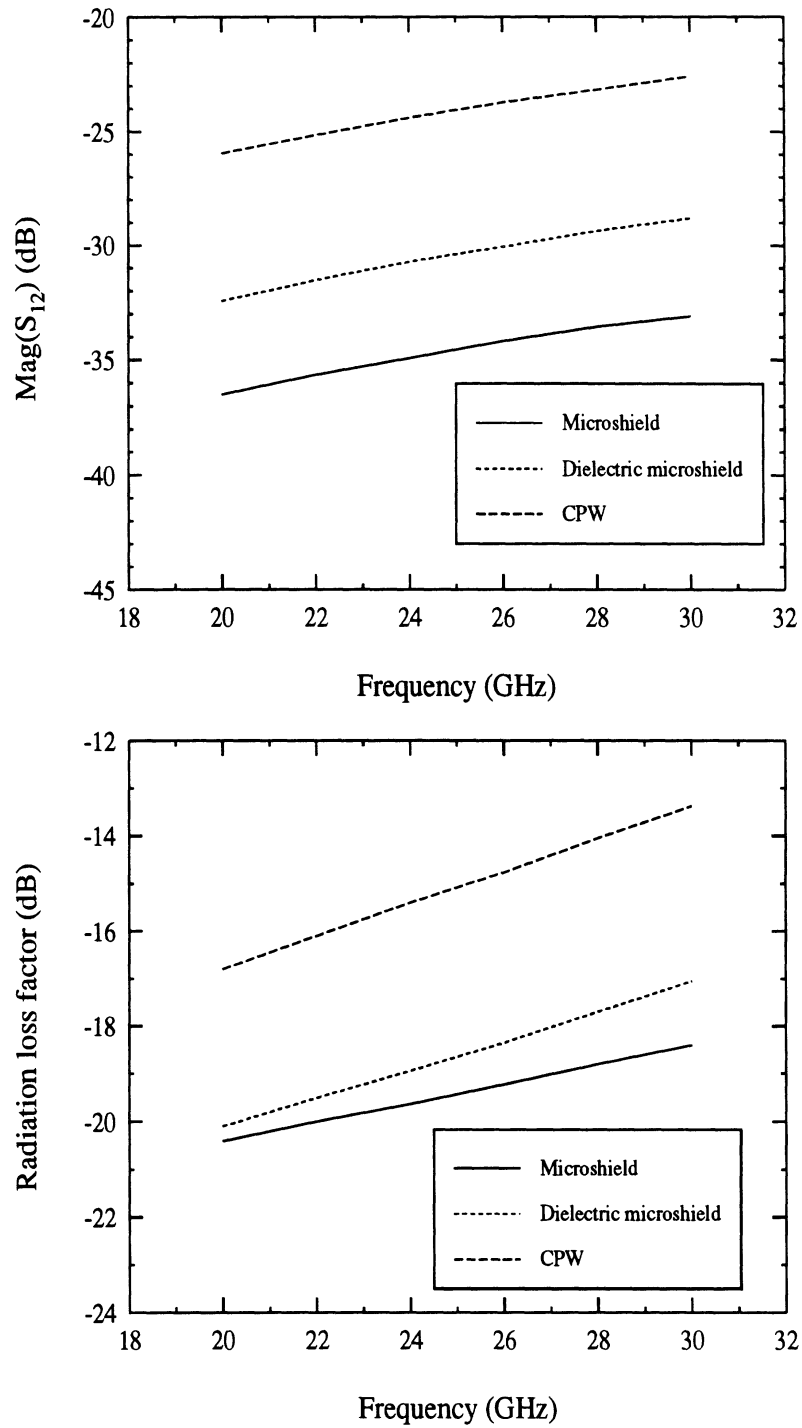
Figure 6.13: Insertion loss and the radiation loss factor of coupled open-ends discontinuity. (h_c=0.25 mm, W_c=1 mm, S_d=0.5 mm, g=0.25 mm)

-5

-8

Loss factor (dB)

-11

-14

-17

-20

Dielectric Microshield

Membrane Microshield

CPW

10 11 12 13 14 15 16 17 18

Frequency (GHz)
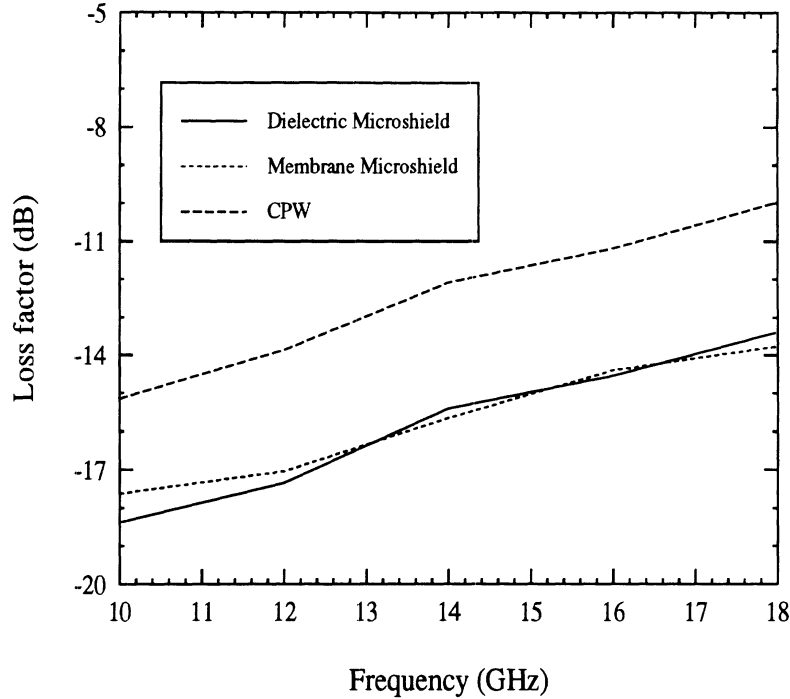
Figure 6.14: Radiation Loss factor of coupled open-ends discontinuity. (S_d=3 mm, g=0.5 mm)

The substrate used in the dielectric microshield and in the coplanar waveguide is 0.762 mm thick and has a dielectric constant ϵ_r=2.2. It can be seen that, in this case, radiation from the coupled microshield open-ends is approximately one half the radiation from coupled open-ends made of conventional CPW. In addition, for this specific discontinuity with the above dimensions, the dielectric microshield line and the membrane microshield line have almost the same radiation loss factor.

For the same configuration, Figure 6.15 shows the scattering parameters and the loss factor of the dielectric microshield as were evaluated theoretically and measured experimentally. The measurements were performed by R. Franklin using an HP 8510 network analyzer [149, 151]. The ripple seen in the measured data is mainly due to the very small coupling between the two lines which intensifies the effect of connector repeatability. As a last example, Figure 6.16 shows the scattering parameters (mag-
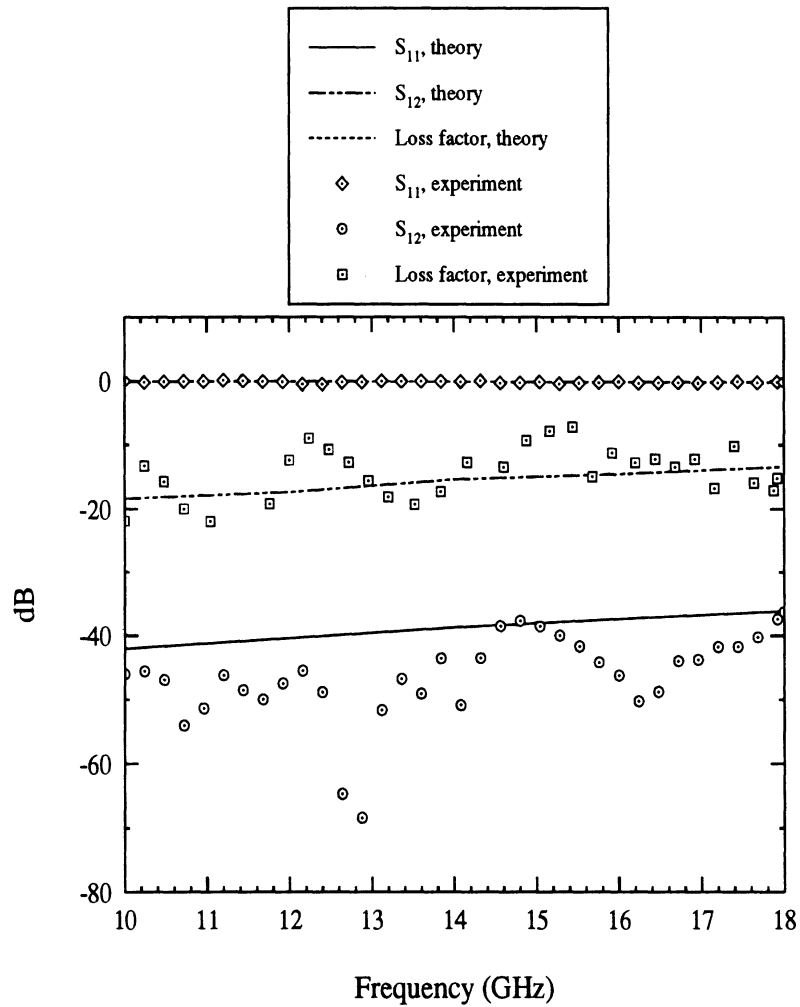
Figure 6.15: Scattering parameters and loss factor of coupled open-end dielectric microshield lines discontinuity. Dimensions are as in Figure 6.14.

nitude and phase) of a dielectric microshield line as were evaluated theoretically and measured experimentally. The agreement between the two sets of data is very clear which validates more the derived numerical method.
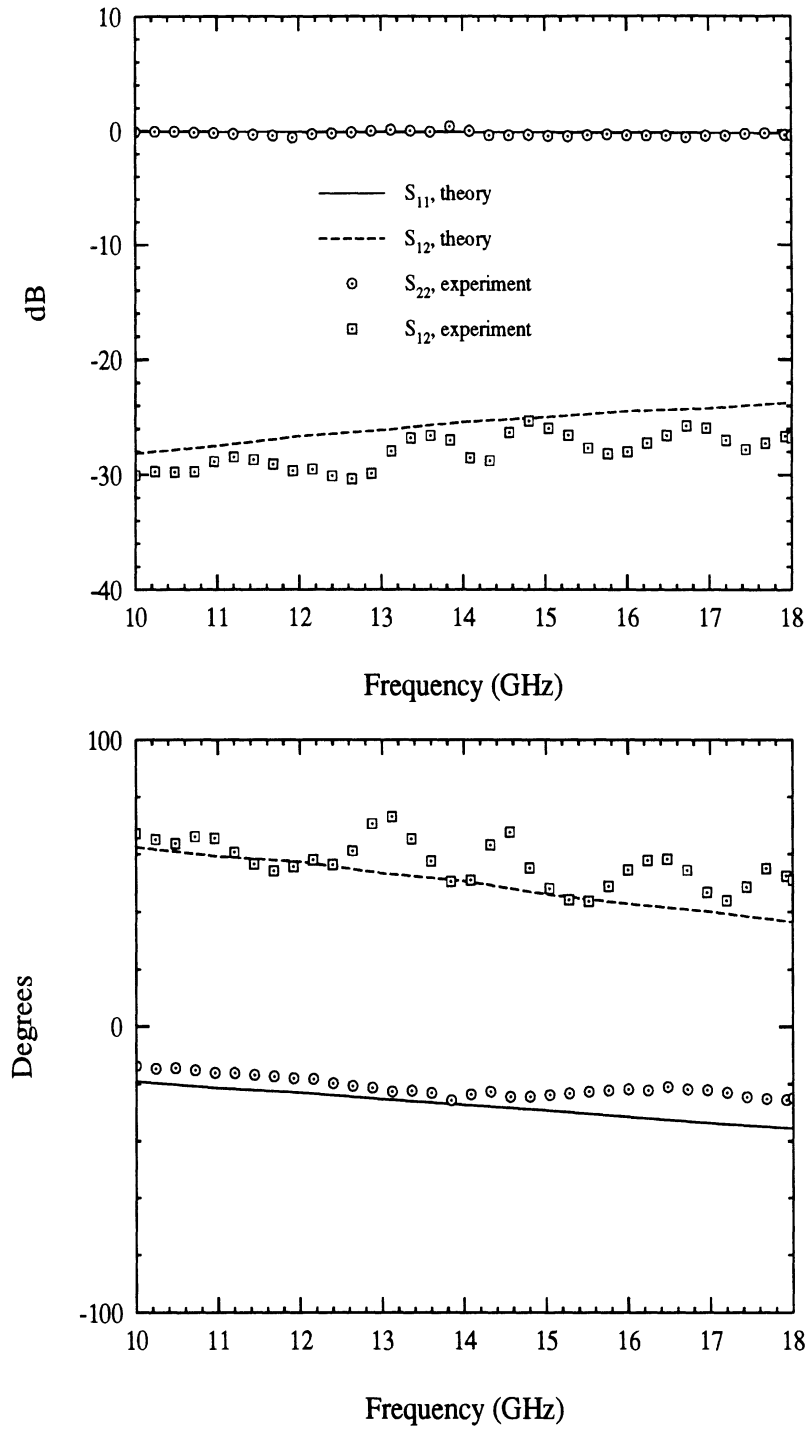
Figure 6.16: Scattering parameters (magnitude and phase) of an open-end coupled dielectric microshield discontinuity, Solid lines: theory, Dots: experiment. (S_d=0.5 mm and other dimensions are similar to those in Figure 6.14)

CHAPTER VII

CONCLUSIONS

A rigorous three dimensional simulation of shielded coplanar waveguide (CPW) circuit structures has been performed using the full-wave Space Domain Integral Equation (SDIE) Approach. The integral equation approach has proven to be accurate, computationally efficient and versatile in terms of the geometries it can solve. In this approach, first, the equivalence principle is used to replace the slot aperture of the CPW structure with an equivalent surface magnetic current density. Then, a magnetic field integral equation is derived by applying the appropriate boundary conditions at the slot aperture interface. This integral equation contains the Green's functions, pertinent to the shielded CPW discontinuity problem, which is formulated such that the effect of any number of dielectric substrates and/or superstrates can be taken into account. Finally, the space domain integral equation is solved numerically using the method of moments in conjunction with Galerkin's technique which results in the electric field distribution in the slot apertures. Using this distribution, and with the assumption that only the quasi-TEM mode propagates in the uniform lines away from the discontinuity and the feed point, transmission line theory is utilized to derive the scattering parameters. The feeding mechanism is modeled by ideal electric current sources which are localized at specific nodes. This rather simple, mathematical,

and non-physical model has proven to be efficient, accurate and reliable. In addition, it does not introduce any unwanted numerical complications as it happens with other excitation techniques. The presented theoretical technique allows the analysis of distributed CPW passive structures taking into account proximity and shielding effects such as cavity resonances. The originality of the SDIE approach as applied in this research lies in the fact that the integral equation is formulated in terms of equivalent magnetic currents flowing on the slot apertures, as opposed to an integral equation in terms of the electric current on the conducting surface. The former technique is more appropriate for CPW problems where the ground planes approach the boundary surfaces, while the latter better fits CPW problems having finite size conductors and microstrip problems.

A variety of CPW discontinuities have been analyzed which were divided into three categories: one-port discontinuities, two-port discontinuities without air-bridges, and two-port discontinuities with air-bridges. The convergence behavior of the derived results and the numerical stability of the method were studied extensively by performing several computer experiments. Non-uniform discretization of the slot aperture has been used to be able to model the magnetic current accurately and to enhance convergence. It has been shown that the number of basis functions has to be carefully chosen to insure the convergence of the scattering parameters. Extensive numerical results were presented which illustrated important aspects concerning the high frequency behavior of CPW structures. In almost all cases, numerical results were validated by comparisons with experimental data and/or already published results. The results of this research have led to several conclusions which are summarized in the following sections.

7.1 One-Port CPW Discontinuities

The short-end and open-end CPW discontinuities have been analyzed when the CPW is excited with a coplanar mode and a slotline mode. Equivalent circuits for these discontinuities were evaluated numerically over a wide frequency range for various slot widths and separations. It has been found that the properties of both terminations depend significantly on the center conductor and the slot widths of the CPW. An exception to this is the inductive effect seen at the end of a shorted CPW supporting the slotline mode. In this case, the effect of the center conductor width on the short-end characteristics becomes noticeable only for very tight slot coupling. In addition, it has been found that the number of basis functions n_y required to obtain accurate results is largely dependent on the aspect ratio S/W. For S/W greater than 1, only the longitudinal component of the magnetic current is required since the slot coupling effect is small. However, for S/W less than 1, the transverse component of the magnetic current is needed to represent the stronger coupling effect between the slots. Also, it has been demonstrated that the parasitic effects of an open-end CPW can be reduced by mitering the center conductor. On the other hand, mitering the ground plane of the open-end tends to increase the capacitance seen at the end of the line.

The effect of cavity resonances on the magnetic current distribution was investigated. It has been shown that at the vicinity of a cavity resonance, the magnetic current distribution becomes distorted which affects the circuit parameters of the discontinuity. However, as long as the operating frequency is not within approximately 1 GHz from a cavity resonance, the magnetic current is uniform and undistorted.

7.2 Two-Port CPW Discontinuities Without Air-Bridges

In these discontinuities, air-bridges are not needed to connect the ground planes of the CPW, and thus, standard techniques have been used to derive the scattering parameters. Coupled CPWs through open-ends, short-ends and a gap in the center conductor have been studied. It has been found that the coupling through open or short ends is very small even for relatively small separation distances which is due to the fact that the fields are strongly confined to the slots. In addition, it has been demonstrated that the open-end-coupled CPW discontinuity may exhibit a resonance effect depending on the separation distance and the CPW dimensions. Such an observation may help in realizing efficient test fixtures where the isolation between the input and output ports is very high. In case of CPW step junction, the numerical results showed that this discontinuity is not significantly dispersive. In addition, it has been shown that mitering can reduce the parasitic effects of the step discontinuity, and thus, reduce the return loss.

Two different realizations of CPW series stubs, namely, stubs printed on the ground conductor and those printed on the center conductor, have been analyzed. It has been found that the bent stub printed on the ground plane has a higher Q than a similar one printed on the center conductor and both stubs have approximately the same resonant frequency. However, both stubs have different characteristics which shows that even though both stubs are of the same type and have the same dimensions, each produces a different discontinuity effect depending on the stub position. Moreover, it has been found that a bent series stub printed on the ground plane has a higher resonant frequency than a straight stub with the same mean length. It has also been demonstrated that as the frequency increases, the parasitic effects of the stub becomes more noticeable. In addition, the series stubs printed on the center

conductor have shown the tendency to radiate less than those printed on the ground conductor. It has been indicated that it is possible to design CPW stub discontinuities with very low loss (as low as -10 dB). Lumped element equivalent circuits were proposed to model the CPW series stubs printed on the center conductor, and closed form expressions to compute the values of the capacitances and inductances were given as functions of stub length (for a specific configuration). These models take into account the asymmetry of the structure and the discontinuity effects and predict the response up to the first resonant frequency with a 5% accuracy.

The notion of *forced radiation* simulation has been presented in which an open structure is simulated by setting the resistances of the top and bottom walls of the shielding box to 377 Ω. The results of such a simulation as applied to a straight series CPW stub printed on the ground plane have been compared to the *actual* radiation loss obtained rigorously. It has been found that these results are not reliable since they are considerably affected by the size of the cavity. Thus, such a simulation cannot provide any consistent results with respect to the radiation loss in printed circuits or radiation resistance in printed antennas. Nonetheless, such a simulation can still predict the resonant frequency of the circuit or antenna element.

7.3   Two-Port CPW Discontinuities With Air-Bridges

In Chapter 5, a hybrid technique has been developed to analyze CPW discontinuities with air-bridges. In this technique, the air-bridge-free CPW discontinuity is analyzed, first, using the SDIE approach which results in the surface magnetic current distribution in the slot aperture. In case of transversely symmetric discontinuities where the slotline mode is not excited in the feeding lines, a frequency dependent equivalent circuit of the discontinuity is derived using ideal transmission

line theory. Then, this equivalent circuit is modified by incorporating the air-bridge parasitic inductance and capacitance which are evaluated using a quasi-static model. On the other hand, in case of transversely asymmetric discontinuities, the magnetic current distribution derived from the SDIE method is a superposition of both the coplanar and slotline modes. Thus, the Generalized Scattering Matrix technique is used to derive the scattering parameters. In this technique, a 4×4 generalized scattering matrix is derived, first, which includes the interactions between the coplanar and slotline modes in the air-bridge-free discontinuity. Then, the voltages at the ports corresponding to the slotline mode are forced to be zero which in turn reduces the 4×4 scattering matrix into a 2×2 one. The developed hybrid technique has been validated by comparisons with experimental data where a very good agreement has been obtained.

The hybrid technique has been used to analyze different types of shielded CPW symmetric and asymmetric shunt stubs. In addition, it has been applied to analyze two CPW discontinuities in open environment, namely, the asymmetric short-end shunt stub and the right angle bend. It has been found that CPW shunt stubs do not behave as expected if the two ground planes of the CPW stubs are not connected together due to the presence of the slotline mode in the stub itself. It is the air-bridge, the parasitic effects of which are typically negligible, that makes these structures behave as required. It has been shown that bent CPW stubs should be used whenever the circuit layout permits to reduce the radiation loss caused by the parasitic coupled slotline mode. The effect of the cavity resonances on the behavior of the stubs has been studied. It was found that cavity resonances interact with the fields in the stub, and thus, affect the characteristics of the stub. From the analysis of open structures, it has been found that the radiation loss increases as the operating frequency increases.

In addition, for the examples studied, the CPW right angle bend experienced lower radiation loss than the stub discontinuity.

7.4 Microshield Line

A new type of monolithic planar transmission line, the microshield line, has been proposed. This line has the following advantages:

- There is no need for via-holes or air-bridges for ground equalization.

- A wide range of impedances can be obtained.

- Wavelength is equal to the free space wavelength which results in larger circuit dimensions.

- Radiates much less than the conventional CPW.

The radiation loss factor of several discontinuities has been evaluated and compared with similar discontinuities in conventional CPW. It has been found that the microshield line has lower radiation which is approximately half of that encountered in the conventional CPW. Comparisons with results obtained from experiments on scaled models have shown very good agreement.

The microshield line characteristic impedance has been obtained using two techniques: the point matching method (PMM) and the conformal mapping method (CMM). The analytical closed form expression derived using CMM is shown to agree very well with data obtained by PMM. The effect of finite extent ground planes on the characteristic impedance has been demonstrated. It has been found that small ground planes suffice to insure negligible effect on the line characteristics. In addition, it has been shown that the microshield line has the ability to achieve a wide range of characteristic impedances.

7.5 Possible Future Work

The Generalized Scattering Matrix Approach described in Chapter 5 to analyze asymmetric CPW discontinuities is quite general so that it can be applied to any n-port asymmetric CPW discontinuity. The method has been employed to analyze the asymmetric short-end CPW shunt stub and the CPW right angle bend. The Generalized Scattering Matrix Approach could be extended to analyze other asymmetric CPW discontinuities (e.g. T-junction). Another possible future development of the theoretical methodology presented here could be the use of triangular subdomain basis functions instead of the piecewise sinusoidal ones. This will allow for more complicated CPW discontinuities to be considered.

APPENDICES

APPENDIX A

Derivation of Network Relations of the Generalized Representation of an Asymmetric Discontinuity

In this appendix, equations (5.7)-(5.11) are derived. The voltage at any point along a transmission line (connected to port k) can be expressed in terms of forward and backward traveling waves as follows:

$$V_k(z) = V_k^+ e^{-j\beta_k z} + V_k^- e^{j\beta_k z} \tag{A.1}$$

The above equation may be written as:

$$V_k(z) = V_k^+ e^{-j\beta_k z} \left(1 + \Gamma(z)\right) \tag{A.2}$$

where $\Gamma(z)$ is the reflection coefficient at the point z along the line. Using the fact that the angle of this reflection coefficient is zero at a voltage maximum, V_k^+ may be written as:

$$V_k^+ = \frac{V_{max} e^{j\beta_k z_{max}}}{1 + \mid \Gamma \mid} \tag{A.3}$$

where V_{max} is the complex value of the voltage maximum, z_{max} is its position along the line and β_k is the propagation constant.

Now, the network relations between the four ports of the generalized representation shown in Figure 5.8 may be written as follows:

$$
\begin{bmatrix} b_{1c} \\ b_{2c} \\ b_{1s} \\ b_{2s} \end{bmatrix} = \begin{bmatrix} S_{11} & S_{12} & S_{13} & S_{14} \\ S_{21} & S_{22} & S_{23} & S_{24} \\ S_{31} & S_{32} & S_{33} & S_{34} \\ S_{41} & S_{42} & S_{43} & S_{44} \end{bmatrix} \begin{bmatrix} a_{1c} \\ a_{2c} \\ a_{1s} \\ a_{2s} \end{bmatrix}
$$

(A.4)

In the above, a_k and b_k are defined as:

$$
a_k = \frac{V_k^+ e^{-j\beta_k z}}{\sqrt{Z_{0_k}}}
$$

(A.5)

$$
b_k = \frac{V_k^- e^{j\beta_k z}}{\sqrt{Z_{0_k}}}
$$

(A.6)

where Z_{0_k} is the characteristic impedance of the connecting line at port k. Substituting (A.5) and (A.6) in (A.4) and using (A.3), it is straight forward to derive (5.7)-(5.11).

APPENDIX B

Derivation of the 2×2 Scattering Matrix

In this appendix, the derivation of equations (5.14)-(5.18) is outlined. First, the following conditions are enforced on the generalized network shown in Figure 5.8:

$$V_{1s} = 0 \tag{B.1}$$

$$V_{2s} = 0 \tag{B.2}$$

The above conditions lead to the following relations between the incident and reflected waves on the ports corresponding to the slotline mode:

$$a_{1s} = -b_{1s} \tag{B.3}$$

$$a_{2s} = -b_{2s} \tag{B.4}$$

Using (B.3) and (B.4), (A.4) may be written as:

$$
\begin{bmatrix} b_{1c} \\ b_{2c} \\ b_{1s} \\ b_{2s} \end{bmatrix}
=
\begin{bmatrix} S_{11} & S_{12} & S_{13} & S_{14} \\ S_{21} & S_{22} & S_{23} & S_{24} \\ S_{31} & S_{32} & S_{33} & S_{34} \\ S_{41} & S_{42} & S_{43} & S_{44} \end{bmatrix}
\begin{bmatrix} a_{1c} \\ a_{2c} \\ -b_{1s} \\ -b_{2s} \end{bmatrix}
\tag{B.5}
$$

Using the third and fourth equations of the above system, one can derive expressions for b_{1s} and b_{2s} in terms of a_{1c} and a_{2c}. Finally, substituting these expressions in the first and second equations of (B.5), equations (5.14)-(5.18) can be obtained.

APPENDIX C

2D Characterization of Microshield Line Using Point Matching Method (PMM)

In this appendix, a numerical method, based on the point matching technique, is presented to calculate the effective dielectric constant and the characteristic impedance of microshield lines. The structure under consideration is shown in Figure C.1. The dielectric microshield line may be simulated by taking the width and height of the upper waveguide relatively large compared to the dimensions of the lower guide. On the other hand, the microshield line may be simulated by setting $\epsilon_{r2}=1$ in addition to the above condition. The analysis presented here is similar to that presented in [36, 37], and thus, only the main steps will be given here.

The first step in this quasi-TEM analysis is to solve the following Laplace's equation in the three regions shown in Figure C.1:

$$\vec{\nabla}_t^2 \phi = 0 \tag{C.1}$$

where ϕ is the scalar potential function related to the electric field as follows:

$$\vec{E} = -\vec{\nabla}\phi \tag{C.2}$$

Accounting for the fact that the tangential electric field on the waveguide walls vanishes, the following expressions may be written for the potential in the three regions:

$$\phi^{(1)} = \sum_{i=0}^{\infty} a_i \cos\left(k_i^{(1)} x\right) \sinh\left(k_i^{(1)}(y - h)\right) \tag{C.3}$$
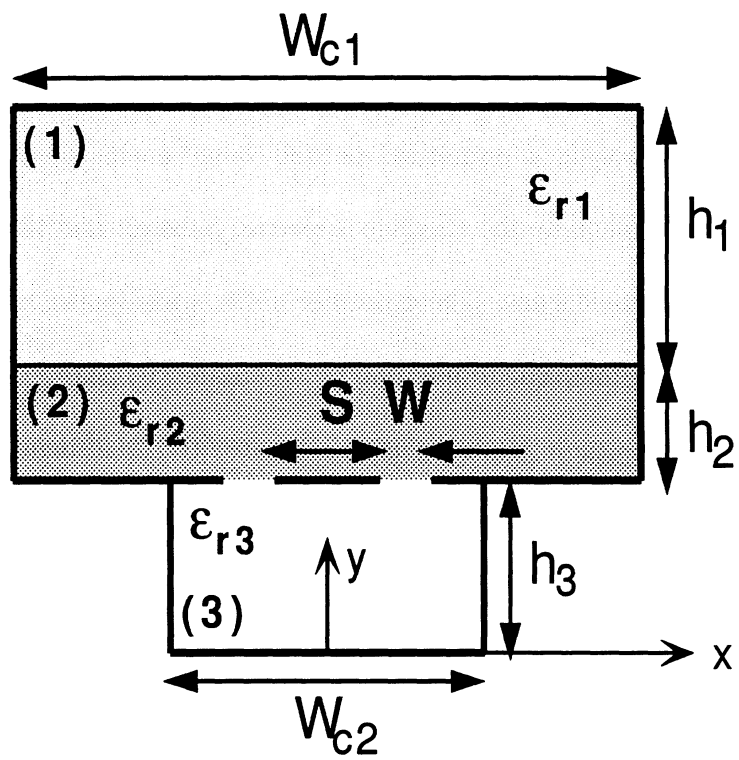
Figure C.1: A cross sectional view of the structure under consideration

$$\phi^{(2)} = \sum_{i=0}^{\infty} \cos\left(k_i^{(1)}x\right) \left[c_i \sinh\left(k_i^{(1)}y\right) + d_i \cosh\left(k_i^{(1)}y\right)\right] \qquad \text{(C.4)}$$

$$\phi^{(3)} = \sum_{i=0}^{\infty} b_i \cos\left(k_i^{(2)}x\right) \sinh\left(k_i^{(2)}y\right) \qquad \text{(C.5)}$$

where

$$k_i^{(1)} = \frac{(2i+1)\pi}{W_{c1}} \qquad \text{(C.6)}$$

$$k_i^{(2)} = \frac{(2i+1)\pi}{W_{c2}} \qquad \text{(C.7)}$$

$$h = h_1 + h_2 + h_3. \qquad \text{(C.8)}$$

Applying the following boundary conditions at the dielectric interface between regions (1) and (2):

$$\phi^{(1)} = \phi^{(2)} \qquad \text{(C.9)}$$

$$\epsilon_{r1}\frac{\partial \phi^{(1)}}{\partial y} = \epsilon_{r2}\frac{\partial \phi^{(2)}}{\partial y} \qquad \text{(C.10)}$$

one can express the unknowns c_i and d_i in terms of a_i as follows:

$$c_m = A_m a_m \qquad \text{(C.11)}$$

$$d_m = B_m a_m \qquad \text{(C.12)}$$

where

$$A_m = \frac{\cosh\left(k_m^{(1)}h_1\right)\left[\epsilon_{r1} + \epsilon_{r2}\tanh\left(k_m^{(1)}h_1\right)\tanh\left(k_m^{(1)}(h_2+h_3)\right)\right]}{\epsilon_{r2}\cosh\left(k_m^{(1)}(h_2+h_3)\right)\left[1 - \tanh^2\left(k_m^{(1)}(h_2+h_3)\right)\right]} \qquad \text{(C.13)}$$

$$B_m = \frac{\cosh\left(k_m^{(1)}h_1\right)}{\cosh\left(k_m^{(1)}(h_2+h_3)\right)}\left\{-\tanh\left(k_m^{(1)}h_1\right) - \tanh\left(k_m^{(1)}(h_2+h_3)\right)\right.$$

$$\left.\frac{\epsilon_{r1} + \epsilon_{r2}\tanh\left(k_m^{(1)}h_1\right)\tanh\left(k_m^{(1)}(h_2+h_3)\right)}{\epsilon_{r2}\left[1 - \tanh^2\left(k_m^{(1)}(h_2+h_3)\right)\right]}\right\} \qquad \text{(C.14)}$$

Applying the boundary condition (C.9) at the interface between regions (2) and (3) leads to the following:

$$\sum_{i=0}^{\infty} b_i \cos(k_i^{(2)}x)\sinh(k_i^{(2)}h_3) = \sum_{i=0}^{\infty} a_i \cos(k_i^{(1)}x)O_i \qquad \text{(C.15)}$$

where

$$O_i = A_i \sinh(k_i^{(1)} h_3) + B_i \cosh(k_i^{(1)} h_3) \qquad \text{(C.16)}$$

Multiplying both sides of (C.15) by $\cos(k_m^{(2)} x)$, integrating from $-\frac{W_{c2}}{2}$ to $\frac{W_{c2}}{2}$, and

using the orthogonality properties of the cosine functions, give:

$$b_m = \frac{2}{W_{c2} \sinh(k_m^{(2)} h_3)} \sum_{i=0}^{\infty} a_i O_i S_{im} \qquad \text{(C.17)}$$

$$m = 0, 1, 2, \ldots$$

where

$$S_{im} = \frac{\sin\left((k_i^{(1)} + k_m^{(2)}) \frac{W_{c2}}{2}\right)}{k_i^{(1)} + k_m^{(2)}} + \frac{\sin\left((k_i^{(1)} - k_m^{(2)}) \frac{W_{c2}}{2}\right)}{k_i^{(1)} - k_m^{(2)}}$$

Applying the boundary condition (C.10) in the gaps (i.e. $S/2 <| x |< S/2 + W$)

between regions (2) and (3) and using (C.17), the following expression is obtained:

$$\sum_{i=0}^{\infty} a_i \left\{ \epsilon_{r2} \cos(k_i^{(1)} x) k_i^{(1)} M_i - \frac{2\epsilon_{r3}}{W_{c2}} O_i \sum_{j=0}^{\infty} k_j^{(2)} \cos(k_j^{(2)} x) \frac{S_{ij}}{\tanh(k_j^{(2)} h_3)} \right\} = 0 \quad \text{(C.18)}$$

where

$$M_i = A_i \cosh(k_i^{(1)} h_3) + B_i \sinh(k_i^{(1)} h_3) \qquad \text{(C.19)}$$

Now, setting the potential on the center conductor to unity, and that on the

ground to zero leads to the following expression (using C.4):

$$\sum_{i=0}^{\infty} a_i \cos(k_i^{(1)} x) O_i = \begin{cases} 1 & | x | \le S/2 \\ 0 & | x | \ge S/2 + W \end{cases} \qquad \text{(C.20)}$$

Thus, the problem is reduced to finding the unknown coefficients a_i from which the

potential in each layer can be derived. In order to solve (C.18) and (C.20) numerically,

the above sums are truncated at $i = N$ and $j = P$ which reduces the problem to

finding the $N + 1$ unknowns a_i's. In order to accomplish this, the two equations are

forced to apply at discrete values of x along the interface between regions (2) and (3). In other words, the above two equations are point matched at $x = x_m$, where

$$x_m = m\frac{W_{c1}/2}{N+1}, \quad m = 0, 1, ..., N \tag{C.21}$$

Due to the symmetry of the structure and the potential function, one needs only to point match at half of the interface as seen in (C.21). With this point matching, (C.18) and (C.20) reduce to a linear system of equations to be solved for the a_i's. as follows:

$$\sum_{i=0}^{N} K_{mi}a_i = d_m \tag{C.22}$$

where

$$d_m = \begin{cases} 0 & x_m > S/2 \\ 1 & x_m \leq S/2 \end{cases} \tag{C.23}$$

and

$$\begin{aligned} K_{mi} &= \epsilon_{r2}\cos(k_i^{(1)}x_m)k_i^{(1)}M_i - \frac{2\epsilon_{r3}}{W_{c2}}O_i \\ &\quad \sum_{j=0}^{P} k_j^{(2)}\cos(k_j^{(2)}x_m)S_{ij}\coth(k_j^{(2)}h_3) \quad S/2 < x_m < S/2 + W \quad \text{(C.24)} \\ &= O_i\cos(k_i^{(1)}x_m) \quad\quad\quad x_m \leq S/2 \ \text{or} \ x_m \geq S/2 + W \quad \text{(C.25)} \end{aligned}$$

In order to obtain the characteristic impedance of the line, the capacitance per unit length should be computed first. This can be accomplished using the following expression:

$$C = \int_S \vec{D} \cdot d\vec{s} = -\epsilon_0 \int_S \epsilon_r \vec{\nabla}\phi \cdot d\vec{s} \tag{C.26}$$

where S is a Gaussian surface surrounding the inner conductor which can be chosen as shown in Figure C.2. In this Gaussian surface, the path of integration is contracted to touch the infinitely thin center conductor [37] which reduces (C.26) to the following
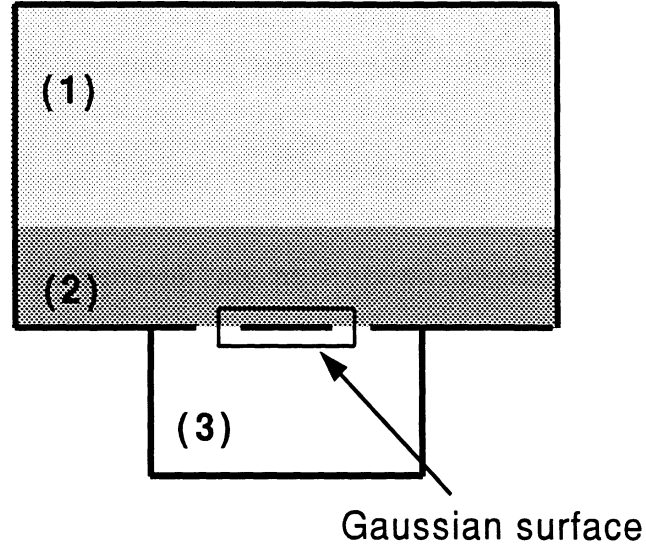
Figure C.2: Gaussian surface used to compute the capacitance of the line.

expression for the evaluation of the capacitance:

$$
C = 2\epsilon_0 \sum_{i=0}^{N} a_i \left\{ -\epsilon_{r2} M_i \sin \left(k_i^{(1)} \left(\frac{S+W}{2} \right) \right) \right.
$$

$$
\left. + \frac{2\epsilon_{r3}}{W_{c2}} O_i \sum_j \sin \left(k_j^{(2)} \left(\frac{S+W}{2} \right) \right) \coth(k_j^{(2)} h_3) S_{ij} \right\} \qquad \text{(C.27)}
$$

Finally, the characteristic impedance and the effective dielectric constant of the dielectric microshield line can be evaluated as:

$$
Z_0 = \frac{1}{v_0 \sqrt{C C_0}} \qquad \text{(C.28)}
$$

$$
\epsilon_{eff} = \frac{C}{C_0} \qquad \text{(C.29)}
$$

where v_0 is the velocity of light in free space and C_0 is the capacitance of the line with $\epsilon_{r2}=1$ (i.e. the microshield line).

APPENDIX D

2D Characterization of Microshield Line Using Conformal Mapping Method (CMM)

In this appendix, an analytical approach, based on the conformal mapping technique, is presented to calculate the effective dielectric constant and the characteristic impedance of microshield lines. The structure under consideration is shown in Figure D.1. In this figure, the microshield line may be simulated by setting $\epsilon_r=1$. In addition, the ground planes are assumed to have finite extent.

The use of conformal mapping technique to derive analytical expressions for the quasi-TEM 2D parameters of CPW resides on the assumption that the two slots are modeled as magnetic walls. Thus, the overall capacitance per unit length of the microshield line is the sum of the capacitance of the upper half plane (dielectric and air region) and the lower half plane (the waveguide region). The former capacitance, C_a, can be obtained using the following formula (see [27, 29, 35] for details):

$$C_a = 2\,\epsilon_0 \frac{K(k)}{K(k')} + 2\,\epsilon_0(\epsilon_r - 1)\frac{K(k_1)}{K(k_1')} \tag{D.1}$$

where

$$k = \frac{a}{b}\sqrt{\frac{1 - b^2/c^2}{1 - a^2/c^2}} \tag{D.2}$$

$$k' = \sqrt{1 - k^2} \tag{D.3}$$
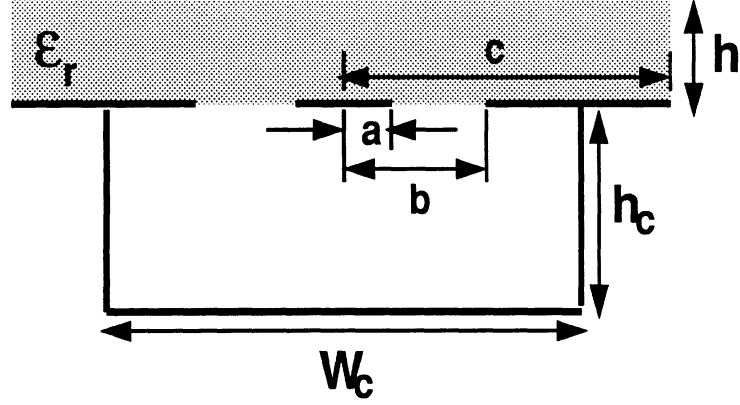
Figure D.1: A cross sectional view of the dielectric microshield line with finite extent ground planes.

$$k_1 = \frac{\sinh(\pi a/2h)}{\sinh(\pi b/2h)} \sqrt{\frac{1 - \sinh^2(\pi b/2h)/\sinh^2(\pi c/2h)}{1 - \sinh^2(\pi a/2h)/\sinh^2(\pi c/2h)}} \tag{D.4}$$

$$k_1' = \sqrt{1 - k_1^2} \tag{D.5}$$

In the above expression, $K(k)$ is the complete elliptic integral of the first kind [155].

The capacitance due to the waveguide region, C_w, can be evaluated through a suitable sequence of conformal mappings. First, the interior of the rectangle shown in Figure D.2(a) is mapped into the upper ω half-plane of Figure D.2(b) through the inverse of the following Schwarz-Christoffel mapping [157]

$$z = f(\omega) = A \int_0^\omega \frac{d\theta}{\sqrt{(\theta^2 - 1)(\theta^2 - 1/\gamma^2)}} \tag{D.6}$$

where A and γ are constants to be determined and $\gamma < 1$. Alternatively, the above expression can be viewed as a transformation that maps the half plane $Im(\omega) > 0$ to the interior of the rectangle shown in Figure D.2(a). It should be noted that the above transformation is arbitrarily chosen such that the following holds [157]:

$$f(1) = W_c/2 \tag{D.7}$$

$$f(-1) = -W_c/2 \tag{D.8}$$

(a)

(b)

(c)
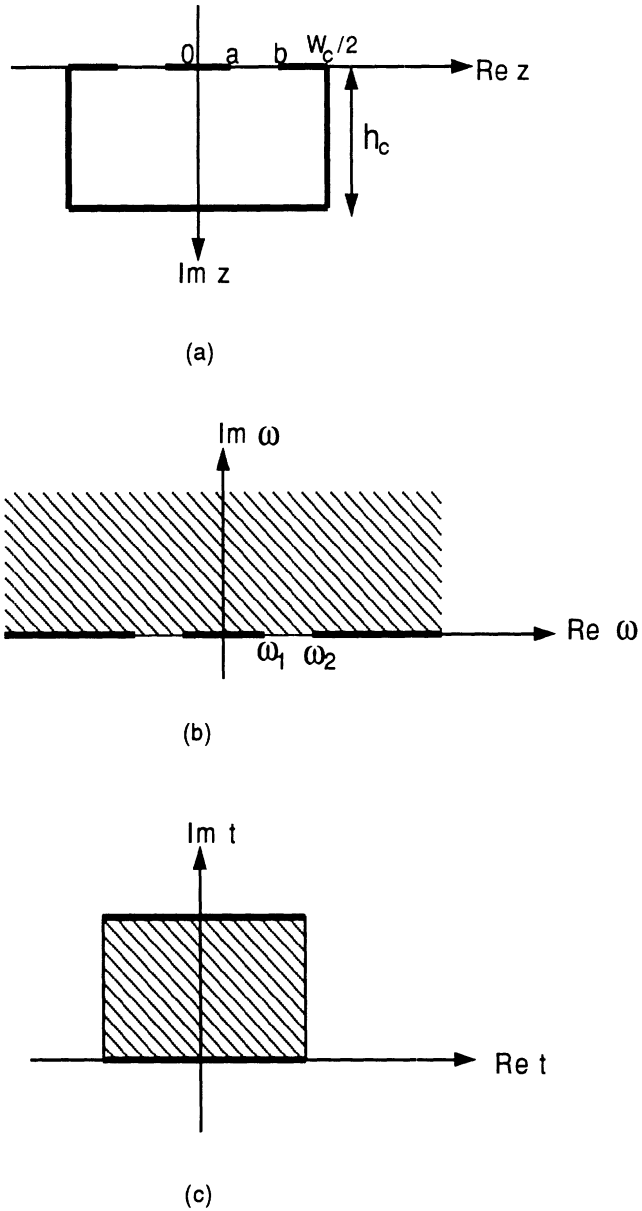
Figure D.2: Conformal mapping for the shielding waveguide of a microshield line: (a) original structure, (b) intermediate ω plane, (c) final mapping into a plane-parallel capacitor.

$$f(1/\gamma) = \frac{W_c}{2} + jh_c \tag{D.9}$$

$$f(-1/\gamma) = -\frac{W_c}{2} + jh_c \tag{D.10}$$

This transformation can be written in terms of the elliptic integral of the first kind as follows:

$$z = f(\omega) = B \int_0^\omega \frac{d\theta}{\sqrt{(1 - \theta^2)(1 - \theta^2\gamma^2)}} = B\,E(\gamma, \omega) \tag{D.11}$$

where $B = \gamma A$. The inverse of the above mapping can be written as [157]:

$$\omega = sn\left(\frac{z}{B}\right) \tag{D.12}$$

where sn is the Jacobian elliptic function. The next step is to evaluate the unknown constants B and γ. Using (D.7) and (D.9), the following two equations can be obtained:

$$\frac{W_c}{2} = BK(\gamma) \tag{D.13}$$

$$h_c = BK_1(\gamma) \tag{D.14}$$

where $K(\gamma)$, the complete elliptic integral of the first kind, and $K_1(\gamma)$ are defined as

$$K(\gamma) = \int_0^1 \frac{d\theta}{\sqrt{(1 - \theta^2)(1 - \theta^2\gamma^2)}} \tag{D.15}$$

$$K_1(\gamma) = \int_1^{1/\gamma} \frac{d\theta}{\sqrt{(\theta^2 - 1)(1 - \theta^2\gamma^2)}} \tag{D.16}$$

It can be shown that $K_1(\gamma) = K(\gamma')$ where $\gamma'^2 = 1 - \gamma^2$ [155]. Thus, the following equation can be obtained from (D.13) and (D.14) with γ as an unknown:

$$\frac{W_c}{2h_c} = \frac{K(\gamma)}{K(\gamma')} \tag{D.17}$$

The above equation can be solved for γ using either of the following expressions [5]:

$$\frac{K(\gamma)}{K(\gamma')} = \frac{1}{\pi} \ln\left[2\frac{1 + \sqrt{\gamma}}{1 - \sqrt{\gamma}}\right] \quad for \quad 0.707 \leq \gamma \leq 1 \tag{D.18}$$

$$\frac{K(\gamma)}{K(\gamma')} = \frac{\pi}{\ln\left[2\frac{1+\sqrt{\gamma'}}{1-\sqrt{\gamma'}}\right]} \quad for \quad 0 \leq \gamma \leq 0.707 \tag{D.19}$$

It has been found that both expression give the same final result. Using (D.18), the following expression for γ may be obtained:

$$\gamma = \left[\frac{e^{\pi W_c/2h_c} - 2}{e^{\pi W_c/2h_c} + 2}\right]^2 \tag{D.20}$$

With the knowledge of γ, B can be obtained using (D.13) where $K(\gamma)$ may be evaluated using the polynomial approximations in [155]. Up to this point, the mapping ω in (D.12) is completely identified, and thus the points ω_1 and ω_2 which are the mappings of $z = a$ and $z = b$, respectively, are defined as:

$$\omega_1 = sn(a/B) \tag{D.21}$$

$$\omega_2 = sn(b/B) \tag{D.22}$$

Thus, the problem of finding C_w has been reduced to obtaining half of the capacitance of a free-space CPW with center conductor and slot widths of $2\omega_1$ and $\omega_2 - \omega_1$, respectively, as shown in Figure D.2(b). This capacitance can be easily obtained by transforming the upper ω half-plane back into the rectangular region of Figure D.2(c) through the mapping [1]

$$t = \int_0^\omega \frac{d\theta}{\sqrt{(\theta^2 - \omega_1^2)(\theta^2 - \omega_2^2)}} \tag{D.23}$$

from which the capacitance can be obtained as [1, 27]:

$$C_w = 2\,\epsilon_0 \frac{K(\zeta)}{K(\zeta')} \tag{D.24}$$

where

$$\zeta = \frac{\omega_1}{\omega_2} = \frac{sn(a/B)}{sn(b/B)} \tag{D.25}$$

$$\zeta' = \sqrt{1 - \zeta^2} \tag{D.26}$$

In the above, $sn(\theta)$, the Jacobian elliptic function, may be evaluated using the routine in [156]. After evaluating (D.1) and (D.24), the total capacitance per unit length of

the line may be obtained as

$$C_{total} = C_a + C_w \hspace{4cm} \text{(D.27)}$$

Finally, the characteristic impedance and the effective dielectric constant may be obtained using (C.28) and (C.29).

BIBLIOGRAPHY

BIBLIOGRAPHY

[1] C. P. Wen, " Coplanar Waveguide: A Surface Strip Transmission Line Suitable for Nonreciprocal Gyromagnetic Device Applications, " *IEEE Trans. on Microwave Theory and Techniques*, Vol. 17, 1087-1090, December 1969.

[2] M. Houdart, " Coplanar Lines: Application to Broadband Microwave Integrated Circuits, " *Proc. of 6th European Microwave Conference*, Rome, pp. 49-53, 1976.

[3] M. Houdart, C. Aury and A. Jean-Frederic, "Coplanar Lines: Application to Lumped and Semi-Lumped Microwave Integrated Circuits, " *Proc. of 7th European Microwave Conference*, pp. 450-454, 1977.

[4] P. A. Holder, " X-Band Microwave Integrated Circuits Using Slotlines and Coplanar Waveguide, " *Radio Electronics Engineering*, Vol. 48, pp. 38-42, January/February 1978.

[5] K. C. Gupta, R. Garg and I. J. Bahl, *Microstrip Lines and Slotlines*, Dedham, MA : Artech House, 1979.

[6] R. A. Pucel, " Design Considerations for Monolithic Microwave Circuits, " *IEEE Trans. of Microwave Theory and Techniques*, Vol. 29, 513-534, June 1981.

[7] R. Simons, "Propagation Characteristics of Some Novel Coplanar Waveguide Transmission Lines on GaAs at MM-Wave Frequencies, " *1986 Conference on Millimeter Wave/Microwave Measurements and standards for Miniaturized Systems*, Alabama, 1986.

[8] M. Muraguchi, *et al*, "Uniplanar MMIC's and Their Applications, " *IEEE Trans. on Microwave Theory and Techniques*, pp. 1896-1900, Dec. 1988.

[9] T. Hirota, Y. Tarusawa, and H. Ogawa, " Uniplanar MMIC Hybrids-A Proposed New MMIC Structure ", *IEEE Trans. on Microwave Theory and Techniques*, pp. 576-581, June 1987.

[10] M. Riaziat, E. Par, G. Zdasiuk, S. Bandy and M. Glenn, "Monolithic Millimeter Wave CPW Circuits, " *1989 IEEE MTT-S International Microwave Symposium Digest*, Long Beach, CA, pp. 525-528.

[11] D. Leistner, W. Schmid and G. Eggers, " Application of Coplanar Waveguide Microwave Integrated Circuits at C- and Ku-Band Frequencies, " *Proc. of 20th European Microwave Conference* , pp. 1021-1026, Sep. 1990.

[12] L. P. B. Katehi, "Novel Transmission Lines for the Submillimeter-Wave Region, " to appear in the *IEEE Proceedings*, Nov. 1992.

[13] W. P. Harokopus, B. Cormanyos, L. P. B. Katehi and G. M. Rebeiz, "Theoretical and Experimental Study of Lens-Supported Aperture Antennas, " submitted for publication to the *IEEE Trans. on Antennas and Propagation*.

[14] X. Yang and W. Zhang, "CPW Antenna Arrays for MIC/MMIC at Millimeter Wave Frequencies, " *Electronics Letters*, Vol. 26, No. 18, pp. 1464-1465, Aug. 1990.

[15] R. E. Stegens, "Coplanar Waveguide FET Amplifiers for Satellite Communications Systems,"*Comsat Technical Review* , Vol. 9, pp. 255-267, spring 1979.

[16] J. Bellantoni, R. Compton and H. Levy, "A New W-Band Coplanar Waveguide Test Fixture, " *1989 IEEE MTT-S International Microwave Symposium Digest*, Long Beach, CA, pp. 1203-1204.

[17] R. Bitzer, "Wideband Balanced Frequency Doublers - A Proposed Novel Planar MIC Structure, " *Proc. of 21st European Microwave Conference* , pp. 333-338, Sep. 1991.

[18] R. Majidi-Ahy, *et al*, "100 GHz High-Gain InP MMIC Cascode Amplifier, " *IEEE J. of Solid State Circuits*, pp. 1370-1378, Oct. 1991.

[19] W. Chew, *et al*, "High-T$_c$ Superconductor CPW Filter, " *IEEE Electron Device Letters*, pp. 197-199, May 1991.

[20] M. Abdo and I. Wolff, "Novel 36 GHz GaAs Frequency Doublers Using (M)MIC Coplanar Technology, " *1992 IEEE MTT-S International Microwave Symposium Digest*, New Mexico, pp. 1167-1170.

[21] N. Koster, *et al*, " Investigation of Air Bridges Used for MMICs in CPW Technique, " *Proc. of 19th European Microwave Conference* , pp. 666-671, Sep. 1989.

[22] M. Houdart and C. Aury, "Various Excitations of Coplanar Waveguide, " *1979 IEEE MTT-S International Microwave Symposium Digest*, pp. 116-119.

[23] R. W. Jackson, " Considerations in the Use of Coplanar Waveguide for Millimeter Wave Integrated Circuits, " *IEEE Trans. on Microwave Theory and Techniques*, Vol. 34, 1450-1456, December 1986.

[24] W. Haydl, *et al*, "Attenuation of Millimeter Wave Coplanar Lines on GaAS and InP Over the Range 1-60 GHz, " *1992 IEEE MTT-S International Microwave Symposium Digest*, New Mexico, pp. 349-352.

[25] M. Zhang, C. Wu, K. Wu and J. Litva, "Losses in GaAS Microstrip and Coplanar Waveguide, " in *1992 IEEE MTT-S International Microwave Symposium Digest*, New Mexico, pp. 971-974.

[26] M. Davis, E. Williams and A. Celestini, "Finite-Boundary Corrections to the Coplanar Waveguide Analysis, " *IEEE Trans. on Microwave Theory and Techniques*, pp. 594-596, Sep. 1973.

[27] G. Ghione and C. Naldi, "Coplanar Waveguides for MMIC applications: Effect of Upper Shielding, Conductor Backing, Finite-Extent Ground Planes, and Line-to-Line Coupling, " *IEEE Trans. on Microwave Theory and Techniques*, Vol. 35, pp. 260-267, March 1987.

[28] J. Chang and W. Wang, "Characteristics of Asymmetrical Conductor-Backed Coplanar Waveguides, " *Int. J. of Electronics*, pp. 641-650, April 1992.

[29] G. Ghione and C. Naldi, "Parameters of Coplanar Waveguides with lower Ground Plane, " *Electronics Letters*, Vol. 19, pp. 734-735, 1983.

[30] Y. Wang and J. Okoro, "Impedance Calculations for Modified Coplanar Waveguides, " *International J. of Electronics*, pp. 861-875, May 1990.

[31] S. Bedair and I. Wolff, "Fast and Accurate Analytic Formulas for Calculating the Parameters of a General Broadside-Coupled CPW for (M)MIC Applications, " *IEEE Trans. on Microwave Theory and Techniques*, pp. 843-850, May 1989.

[32] I. Kneppo and J. Gotzman, "Basic Parameters of Nonsymmetrical Coplanar Line, " *IEEE Trans. on Microwave Theory and Techniques*, p. 718, Aug. 1977.

[33] J. Chang and W. Wang, "A Novel Approximation Method for Asymmetrical Coplanar Lines, " *Microwave and Optical Tech. Letters*, pp. 398-401, Vol. 4, No. 10, Sep. 1991.

[34] I. Wolff, D. Kiefer and S. Bedair, "Considering Some Undesired Effects Due to Dense Packing in Supported CPW MMICs by Using Combined Methods, " *1989 IEEE MTT-S International Microwave Symposium Digest*, pp. 657-660.

[35] C. Veyres and V. Fouad Hanna, "Extension of the Application of Conformal Mapping Techniques to Coplanar Lines with Finite Dimensions, " *International J. of Electronics*, pp. 47-56, Jan. 1980.

[36] D. Rowe and B. Lao, "Numerical Analysis of Shielded Coplanar Waveguides, " *IEEE Trans. on Microwave Theory and Techniques*, pp. 911-915, Nov. 1983.

[37] D. Marcuse, "Electrostatic Field of Coplanar Lines Computed with the Point Matching Method, " *IEEE J. of Quantum Electronics*, pp. 939-947, May 1989.

[38] T. Hatsuda, "Computation of Coplanar-Type Strip-Line Characteristics by Relaxation Method and Its Application to Microwave Circuits, " *IEEE Trans. on Microwave Theory and Techniques*, pp. 795-802, Oct. 1975.

[39] F. Alessandri, U. Goebel, F. Melai and R. Sorrentino, "Theoretical and Experimental Characterization of Nonsymmetrically Shielded Coplanar Waveguides for Millimeter-Wave Circuits, " *IEEE Trans. on Microwave Theory and Techniques*, pp. 2020-2026, Dec. 1989.

[40] C. N. Chen, Y. Wong and C. H. Chen, "Hybrid Quasistatic Analysis for Multi-layer Coplanar Lines, " *IEE Proceedings-H*, pp. 307-312, Aug. 1991.

[41] J. Knorr and K. Kuchler, "Analysis of Coupled Slots and Coplanar Strips on Dielectric Substrate, " *IEEE Trans. on Microwave Theory and Techniques*, pp. 541-548, July 1975.

[42] Y. Fujiki, *et al*, "Higher Order Modes in Coplanar-Type Transmission Lines, " *Electronics and Communications in Japan*, No. 2, pp. 74-81, 1975.

[43] J. Davies and D. Mirshekar-Syahkal, "Spectral Domain Solution of Arbitrary Coplanar Transmission Line with Multilayer Substrate, " *IEEE Trans. on Microwave Theory and Techniques*, pp. 143-146, Feb. 1977.

[44] Y. Shih and T. Itoh, "Analysis of Conductor-Backed CPW, " *Electronics Letters*, Vol. 18, No. 12, pp. 538-540, June 1982.

[45] G. Hasnain, A. Dienes and J. Whinnery, "Dispersion of Picosecond Pulses in Coplanar Transmission Lines, " *IEEE Trans. on Microwave Theory and Techniques*, pp. 738-741, June 1986.

[46] P. Saha, "Dispersion in Shielded Planar Transmission Lines on Two-Layer Composite Substrate, " *IEEE Trans. on Microwave Theory and Techniques*, pp. 907-911, Nov. 1977.

[47] T. Kitazawa, Y. Hayashi and M. Suzuki, "A Coplanar Waveguide with Thick Metal-Coating, " *IEEE Trans. on Microwave Theory and Techniques*, pp. 604-608, Sep. 1976.

[48] G. Liang, Y. Liu and K. Mei, "Analysis of Coplanar Waveguide by the Time-Domain Finite-Difference Method, " *1989 IEEE MTT-S International Microwave Symposium Digest*, pp. 1005-1008.

[49] K. Wu and R. Vahldieck, "The Influence of a Lossy backmetallization on the Transmission Properties in CPW, " *Proc. of 21st European Microwave Conference*, pp. 716-721, Sep. 1991.

[50] C. P. Wen, "Coplanar-Waveguide Directional Couplers, " *IEEE Trans. on Microwave Theory and Techniques*, pp. 318-322, June 1970.

[51] M. Iskander and C. Durney, "An Electromagnetic Energy Coupler for Medical Applications, " *Proceedings of the IEEE*, pp. 1463-1465, Oct. 1979.

[52] M. Iskander and C. Durney, "Electromagnetic Techniques for Medical Diagnosis: A Review, " *Proceedings of the IEEE*, pp. 126-132, Jan. 1980.

[53] M. Iskander and C. Durney, "Microwave Methods of Measuring Changes in Lung Water, " *J. of Microwave Power*, Vol. 18, No. 3, pp. 265-275, 1983.

[54] M. Iskander and T. Lind, "Electromagnetic Coupling of Coplanar Waveguides and Microstrip Lines to Highly Lossy Dielectric Media, " *IEEE Trans. on Microwave Theory and Techniques*, pp. 1910-1917, Dec. 1989.

[55] Y. Wang, "Coplanar Waveguide Short-Gap Resonator for Medical Applications, " *IEEE Trans. on Microwave Theory and Techniques*, pp. 1310-1312, Dec. 1985.

[56] M. Aikawa and H. Ogawa, "A New MIC Magic-T Using Coupled Slot Lines, " *IEEE Trans. on Microwave Theory and Techniques*, pp. 523-528, June 1980.

[57] D.F. Williams and S.E. Schwarz, "Design and Performance of Coplanar Waveguide Band-Pass Filters," *IEEE Trans. on Microwave Theory and Techniques*, Vol. MTT-31, pp. 558-566, July 1983.

[58] M. Riaziat, I. Zubeck, S. Bandy and G. Zdasiuk,, "Coplanar Waveguides Used in 2-18 GHz Distributed Amplifiers, " *1986 IEEE MTT-S International Microwave Symposium Digest*, pp. 337-338

[59] G. E. Ponchak and R. N. Simons, " Channelized Coplanar Waveguide PIN-Diode Switches, " *19th European Microwave Symposium Digest*, London, pp. 489-494, Sep. 1989.

[60] R. Simons and R. Lee, "Coplanar Waveguide/Microstrip Probe Coupler and Applications to Antennas, " *Electronics Letters*, Vol. 26, No. 24, pp. 1998-2000, Nov. 1990.

[61] A. Nesic, "Integrated Uniplanar Antenna Mixer and Local Oscillator, " *Electronics Letters*, Vol. 27, No. 1, pp. 56-58, Jan. 1991.

[62] M. Aksun, S. Chuang and Y. Lo, "Coplanar Waveguide-Fed Microstrip Antennas, " *Microwave and Optical Tech. Letters*, Vol. 4, No. 8, pp.292-295, July 1991.

[63] R. Simons and R. Lee, "Coplanar Waveguide Aperture Coupled Patch Antennas With Ground Plane/Substrate of Finite Extent, " *Electronics Letters*, Vol. 28, No. 1, pp. 75-76, Jan. 1992.

[64] R. H. Jansen, " Hybrid Mode Analysis of End Effects of Planar Microwave and Millimetrewave Transmission Lines, " *IEE Proc.*, Vol. 128, Pt. H, No. 2, pp. 77-86, April 1981.

[65] M. Naghed and I. Wolff, "Equivalent Capacitances of Coplanar Waveguide Discontinuities and Interdigitated Capacitors Using a Three Dimensional Finite Difference Method, " *IEEE Trans. on Microwave Theory and Techniques*, Vol. MTT-38, pp. 1808-1815, Dec. 1990.

[66] R. W. Jackson, " Mode Conversion at Discontinuities in Finite-Width Conductor-Backed Coplanar Waveguide, " *IEEE Trans. on Microwave Theory and Techniques*, Vol. MTT-37, pp. 1582-1589, Oct. 1989.

[67] M. Drissi, V. Fouad Hanna and J. Citerne, "Analysis of Coplanar Waveguide Radiating End Effects Using the Integral Equation Technique, " *IEEE Trans. on Microwave Theory and Techniques*, Vol. 39, pp. 112-116, Jan. 1991.

[68] J. McLean, A. Wieck, K. Ploog and T. Itoh, " Fullwave Analysis of Open-End Discontinuities in Coplanar Stripline and Finite Ground Plane coplanar Waveguide in Open Environments Using a Deterministic Spectral Domain Approach, " *Proc. of 21st European Microwave Conference*, pp. 1004-1007, Sep. 1991.

[69] N.I. Dib and P.B. Katehi, "Modeling of Shielded CPW Discontinuities Using the Space Domain Integral Equation Method (SDIE)," *Journal of Electromagnetic Waves and Applications*, Vol. 5, No. 4/5, pp. 503-523, 1991.

[70] N. Dib and P. Katehi, "The Effect of Mitering on CPW Discontinuities, " *Proc. of 21st European Microwave Conference*, pp. 223-228, Sep. 1991.

[71] J. MacLean and T. Itoh, "Fullwave Analysis of the Radiative Properties of Short-Circuit Discontinuities in Modified Coplanar Stripline, " *1992 IEEE MTT-S International Microwave Symposium Digest*, pp. 203-206.

[72] R. Bromme and R. Jansen, "Systematic Investigation of CPW MIC/MMIC Structures Using Strip/Slot 3D Electromagnetic Simulator, " *1991 IEEE MTT-S International Microwave Symposium Digest*, Boston, pp. 1081-1084.

[73] A. Tran and T. Itoh, "Full Wave Analysis of Short-Circuit Discontinuities in Open CPW with Finite Conductor Thickness, " *in 1992 IEEE AP-S International Microwave Symposium Digest*, pp. 1492-1495.

[74] U. Mueller, M. Rittweger and A. Beyer, " Coplanar Short Considered by the TLM-Method with Symmetrical Condensed Nodes, " *Proc. of 21st European Microwave Conference*, pp. 999-1003, Sep. 1991.

[75] W. Menzel and W. Grabherr, "Coplanar Waveguide Short Circuit with Finite Metallization Thickness, " *Proc. of 21st European Microwave Conference*, pp. 1187-1192, Sep. 1991.

[76] G. Bartolucci, "Full-Wave Analysis of Shieleded CPW Short-end, " *Electronics Letters*, Vol. 26, No. 19, pp. 1615-1616, Sep. 1990.

[77] K. Beilenhoff, W. Heinrich and H. Hartnagel, "Finite Difference Analysis of Open and Short Circuits in Coplanar MMIC's Including Finite Metallization Thickness Mode Conversion, " *1992 IEEE MTT-S International Microwave Symposium Digest*, pp. 103-106.

[78] T. Itoh, editor, *Numerical Techniques for Microwave and Millimeter-Wave Passive Structures*, John Wiley, 1989.

[79] C. W. Kuo and T. Itoh, " Characterization of the Coplanar Waveguide Step Discontinuity Using the Transverse Resonance Method, " *Proc. of 19th European Microwave Conference*, pp. 662-665, Sep. 1989.

[80] C. W. Kuo and T. Itoh, "Characterization of Shielded Coplanar Type Transmission Line Junction Discontinuities Incorporating the Finite Metallization Thickness Effect, " *IEEE Trans. on Microwave Theory and Techniques*, Vol. 40, pp. 73-80, Jan. 1992.

[81] C. W. Kuo, T. Kitazawa and T. Itoh, "Analysis of Shielded Coplanar Waveguide Step Discontinuity Considering the Finite Metallization Thickness Effect, " *1991 IEEE MTT-S International Microwave Symposium Digest*, pp. 473-475.

[82] G. Bartolucci, F. Giannini and C. Paoloni, " Analysis of End-Coupled Coplanar Lines, " *Proc. of Progress In Electromagnetics Research Symposium (PIERS)*, 1989, pp. 500-501.

[83] N. Dib, P. Katehi, G. Ponchak, and R. Simons, "Coplanar Waveguide Discontinuities for P-i-n Diode Switches and Filter Applications," *1990 IEEE MTT-S International Microwave Symposium Digest*, pp. 399-402.

[84] N. Dib, P. Katehi, G. Ponchak, and R. Simons, "Theoretical and Experimental Characterization of Coplanar Waveguide Discontinuities for Filter Applications, " *IEEE Trans. on Microwave Theory and Techniques*, pp. 873-882, May 1991.

[85] N. Dib, W. Harokopus, G. Ponchak and L. P. Katehi, " A Comparative Study Between Shielded and Open Coplanar Waveguide Discontinuities, " *International Journal of Microwave and MM-Wave Computer-Aided Engineering*, Vol. 2, No. 4, pp. 331-341, Oct. 1992.

[86] W. Harokopus and P. Katehi, " Radiation Loss from Open CPW Discontinuities, " *1991 IEEE MTT-S International Microwave Symposium Digest*, Boston, pp. 743-746.

[87] A. Omar and Y. Chow, "Complex Image Green's Functions for Coplanar Waveguides, " *1992 IEEE AP-S International Microwave Symposium Digest*, pp. 1496-1499.

[88] A. Omar and Y. chow, "Effect of Upper and Lower Shielding on the Elimination of the Slot-Line Mode in CPWs, " *1992 IEEE AP-S International Microwave Symposium Digest*, pp. 1508-1511.

[89] M. Rittweger, M. Abdo and I. Wolff, " Full-Wave analysis of Coplanar Discontinuities Considering Three-Dimensional Bond Wires, " *1991 IEEE MTT-S International Microwave Symposium Digest*, Boston, pp. 465-468.

[90] M. Rittweger, N. Koster, S. Koblowski, R. Bertenburg, S. Heinen and I. Wolff, "Full-Wave Analysis of a Modified Coplanar Air Bridge T-Junction, " *Proc. of 21st European Microwave Conference* , pp. 993-998, Sep. 1991.

[91] K. Beilenhoff, W. Heinrich and H. Hartnagel, " The Scattering behavior of Air Bridges in Coplanar MMIC's, " *Proc. of 21st European Microwave Conference* , pp. 1131-1135, Sep. 1991.

[92] H. Jin and R. Vahldieck, "Calculation of Frequency-Dependent S-Parameters of CPW Air-Bridges Considering Finite Metallization Thickness and Conductivity, " *1992 IEEE MTT-S International Microwave Symposium Digest*, pp. 207-210.

[93] N. Dib, G. Ponchak and L. P. Katehi, "A Theoretical and Experimental Study of CPW Shunt Stubs, " to appear in the *IEEE Trans. on Microwave Theory and Techniques*, Jan. 1993.

[94] N. Dib, P. Katehi and G. Ponchak, "Analysis of Shielded CPW Discontinuities with Air Bridges, " *1991 IEEE MTT-S International Microwave Symposium Digest*, Boston, pp. 469-472.

[95] N. Dib, G. Ponchak and L. P. Katehi, "A Comprehensive Theoretical and Experimental Study of CPW Shunt Stubs, " *1992 IEEE MTT-S International Microwave Symposium Digest*, pp. 947-950.

[96] N. Dib and L. Katehi, "Characterization of Non-Symmetric CPW Discontinuities, " *1992 IEEE MTT-S International Microwave Symposium Digest*, pp. 99-102.

[97] N. Dib, M. Gupta, G. Ponchak and L. Katehi, "Characterization of Asymmetric CPW Discontinuities, " submitted to the *IEEE Trans. on Microwave Theory and Techniques*, Sep. 1992.

[98] R. N. Simons and G. E. Ponchak, " Modeling of Some Coplanar Waveguide Discontinuities, " *IEEE Trans. on Microwave Theory and Techniques*, Vol. 36, pp. 1796-1803, Dec. 1988.

[99] A. K. Sharma and H. Wang, "Experimental Models of Series and Shunt elements in Coplanar MMICs, " *1992 IEEE MTT-S International Microwave Symposium Digest*, pp. 1349-1352.

[100] R. F. Harrington, *Time-Harmonic Electromagnetic Fields*, New York: McGraw Hill, 1961.

[101] C. A. Balanis, *Advanced Engineering Electromagnetics*, John Wiley, 1989.

[102] N. L. VandenBerg, *Full-Wave Analysis of Microstrip-Fed Slot Antennas and Couplers*, Ph. D. Thesis, University of Michigan, 1991.

[103] T. E. van Deventer, P. B. Katehi and A. C. Canggellaris, " An Integral Equation Method for the Evaluation of Conductor and Dielectric Losses in High Frequency Interconnects, " *IEEE Trans. on Microwave Theory and Techniques*, pp. 1964-1971, Dec. 1989.

[104] R. F. Harrington, *Field Computation By Moment Methods*, Macmillan, N. Y., 1968.

[105] A. W. Glisson and D. R. Wilton, "Simple and Efficient Numerical Methods for Problems of Electromagnetic Radiation and Scattering from Surfaces, " *IEEE Trans on Antennas and Propagation*, pp. 593-603, Sept. 1980.

[106] M. F. Catedra, J. G. Cuevas and L. Nuno, "A Scheme to Analyze Conducting Plates of Resonant Size Using the Conjugate Gradient Method and the Fast Fourier Transform, " *IEEE Trans on Antennas and Propagation*, pp. 1744-1752, Dec. 1988,

[107] A. Hill, *Quasi-TEM and Full Wave Numerical Methods for the Characterization of Microstrip Discontinuities*, Ph. D. Thesis, Oregon State University, 1989.

[108] J. C. Rautio, *A Time-Harmonic Electromagnetic Analysis of Shielded Microstrip Circuits*, Ph. D. Thesis, Syracuse University, 1986.

[109] I. Wolff, "From Static Approximations to Full-Wave Analysis: The Analysis of Planar Line Discontinuities, " *Int. J. of Microwave and Millimeter-Wave Computer-Aided Engineering*, Vol. 1, No. 2, pp. 117-142, 1991.

[110] W. Wertgen and R. Jansen, "Efficient Direct and Iterative Electrodynamic Analysis of Geometrically Complex MIC and MMIC Structures, " *Int. J. of Numerical Modeling : Electronic Networks, Devices and Filters*, Vol. 2, pp. 153-186, 1989.

[111] L. P. Dunleavy, *Discontinuity Characterization in Shielded Microstrip: A Theoretical and Experimental Study*, Ph. D. Thesis, University of Michigan, 1988.

[112] W.P. Harokopus and P.B. Katehi, "Characterization of Microstrip Discontinuities on Multilayer Dielectric Substrates Including Radiation Losses," *IEEE Trans. on Microwave Theory and Techniques*, Vol. 37, pp. 2058-2065, Dec. 1989.

[113] J. B. Knorr and J. Saenz, " End Effect in Shorted Slot, " *IEEE Trans. on Microwave Theory and Techniques*, Vol. 21, pp. 579-580, September 1973.

[114] W. P. Harokopus, *High Frequency Characterization of Open Microstrip Discontinuities*, Ph. D. Thesis, University of Michigan, 1991.

[115] M. davidovitz and Y. Lo, "Rigorous Analysis of a Circular Patch Antenna Excited by a Microstrip Transmission Line, " *IEEE Trans. on Antennas and Propagation*, pp. 949-958, Aug. 1989.

[116] S. Couture, J. Beal and Y. Antar, "The Cubic Spline Interpolation of a Standing Wave Envelope, " *1992 IEEE AP-S Symposium Digest*, pp. 196-199.

[117] R. Burden, J. Faires and A. Reynolds, *Numerical Analysis*, PWS Pub., 1981.

[118] P. B. Katehi, "A Generalized Method for the Evaluation of Mutual Coupling in Microstrip Arrays," *IEEE Trans. on Antennas and Propagation*, Vol. 35, pp. 125-133, Feb. 1987.

[119] R. Majidi-Ahy, K. Weingarten, M. Riaziat, D. Bloom and B. Auld, "Electrooptic Sampling Measurement of Dispersion Characteristics of Slot line and Coplanar Waveguide (Coupled Slot Line) Even and Odd Modes, " *1988 IEEE MTT-S International Microwave Symposium Digest*, pp. 301-304.

[120] T. Itoh, "Spectral Domain Immitance Approach for Dispersion Characteristics of Generalized Printed Transmission Lines," *IEEE Trans. on Microwave Theory and Techniques*, Vol. 28, pp. 733-736, July 1980.

[121] N. Dib, *Spectral Domain Analysis of Finlines with Composite Ferrite and Dielectric Substrate,* MS Thesis, Kuwait University, 1987.

[122] J. Chrameic, "Reactances of Slotline Short and Open Circuits on Alumina Substrate," *IEEE Trans. on Microwave Theory and Techniques*, pp. 1638-1641, Oct. 1989.

[123] C. Sinclair and S. Nightingale, "An Equivalent Circuit Model for the CPW step Discontinuity," *1992 IEEE MTT-S International Microwave Symposium Digest*, pp. 1461-1464.

[124] *em* is a registered trademark of Sonnet Software, Inc.

[125] G. Kibuuka, R. Bertenburg, M. Naghed and I. Wolff, " Coplanar Lumped Elements and their Application in Filters on Ceramic and Gallium Arsenide Substrates," *Proc. of 19th European Microwave Conference*, pp. 656-661, Sep. 1989.

[126] M. Naghed and I. Wolff, "Multiple Coupled Asymmetrical Coplanar Waveguides and their Application in Interdegitated Filters," *Proc. of 20th European Microwave Conference*, pp. 913-918, 1990.

[127] M. Frankel, S. Gupta, J. Valdmanis and G. Mourou, "Picosecond Pulse Formation by Transmission Line Discontinuities," *Electronics Letters*, Vol. 25, No. 20, pp. 1363-1365, Sep. 1989.

[128] W. C. Johnson, *Transmission Lines and Networks*, McGraw-Hill, 1950.

[129] W. Getsinger, "Circuit Duals on Planar Transmission Media," *1983 IEEE MTT-S International Microwave Symposium Digest*, pp. 154-156.

[130] *Universal Coaxial Microwave Test Fixture*, Design Technique Notes.

[131] T. Shibata, "Circuit Simulations Combined with Electromagnetic Field Analysis," *Workshop on CAD of Nonlinear Microwave Circuits Using Field Theoretical Methods*, 1992 IEEE MTT-S.

[132] G. Ponchak, personal communication.

[133] Sonnet Software User's Manual, Release 2.2, Nov. 1991.

[134] U. Rohde, "Improved Noise Modeling of GaAs FETs, Part 1: Using an Enhanced Equivalent Circuit Technique," *Microwave Journal*, pp. 87-101, Nov. 1991.

[135] K. Koshiji, E. Shu and S. Miki, "An Analysis of Coplanar Waveguide with Finite Conductor Thickness - Computation and Measurement of Characteristic Impedance," *Electronics and Communications in Japan*, Vol. 64-B, No. 8, pp. 69-78, 1981.

[136] T. Weller, personal communication.

[137] T. Becks and I. Wolff, " Calculation of Three-Dimensional Passive Structures including Bond-Wires, Via-Holes and Air-Bridges Using the Spectral Domain Analysis Method," *Proc. of 21st European Microwave Conference* , pp. 571-576, Sep. 1991.

[138] *CAD Oriented Numerical Techniques for the Analysis of Microwave and MM-Wave Transmission-Line Discontinuities and Junctions,* International Workshop of the German IEEE MTT/AP Chapter, Stuttgart, Sept. 13, 1991.

[139] S. Marple Jr., *Digital Spectral Analysis with Applications,* Prentice-Hall, 1987.

[140] R. Simons, "Suspended Coupled Slotline Using Double Layer Dielectric, " *IEEE Trans. on Microwave Theory and Techniques,* Vol. MTT-29, pp. 162-165, Feb. 1981.

[141] R. Lagerlof, "Ridged Waveguide for Planar Microwave Circuits, " *IEEE Trans. on Microwave Theory and Techniques,* Vol. 21, pp. 499-501, July 1973.

[142] F. Alessandri, U. Goebel, F. Melai and R. Sorrentino, "Theoretical and Experimental Characterization of Nonsymmetrically Shielded Coplanar Waveguides for Millimeter-Wave Circuits, " *IEEE Trans. on Microwave Theory and Techniques,* Vol. 37, pp. 2020-2027, Dec. 1989.

[143] K. Kawasaki and T. Itoh, "Analysis of Stitch Line for Monolithic Microwave Integrated Circuits, " *1991 IEEE MTT-S International Microwave Symposium Digest,* Boston, pp. 781-784.

[144] K. Goossen *et al,* "Nearly Dispersionless Microstrip for 100 GHz Pulses Utilizing a Buried Silicide Groundplane, " *1991 IEEE MTT-S International Microwave Symposium Digest,* Boston, pp. 1053-1056.

[145] H. Ogawa, T. Hasegawa, S. Banba and H. Nakamoto, " MMIC Transmission Lines for Multi-Layered MMICs, " *1991 IEEE MTT-S International Microwave Symposium Digest,* Boston, pp. 1067-1070.

[146] T. Rozzi, G. Gerini, A. Morini and M. De santis, "Multilayer Buried Microstrip Inset Guide, " *Proceedings of the 21st European Microwave Conference,* pp. 673-678, Sep. 1991.

[147] A. Engel and L. P. Katehi, "Low-Loss Monolithic Transmission Lines for Sub-millimeter and Terahertz Frequency Applications, " *IEEE Trans. on Microwave Theory and Techniques,* pp. 1847-1854, Nov. 1991.

[148] N. Dib, W. Harokopus, P. Katehi, C. Ling and G. rebiez, "Study of a Novel Planar Transmission Line, " *1991 IEEE MTT-S International Microwave Symposium Digest,* Boston, pp. 623-626.

[149] L. P. Katehi, N. Dib and R. Drayton, " Theoretical and Experimental Characterization of Microshield Circuits, " *International Symposium on Signals, Systems and Electronics Proceedings*, Paris, pp. 77-80, Sep. 1992.

[150] N. Dib and L. Katehi, "Impedance Calculation for the Microshield Line, " *IEEE Microwave and Guided Wave Letters*, pp. 406-408, Oct. 1992.

[151] N. Dib, R. Drayton and L. Katehi, "A Theoretical and Experimental Study of Microshield Circuits, " submitted to the *Microwave and Optical Technology Letters*, special issue on Millimeter-Wave monolithic Integrated Circuits and their System Applications.

[152] L. Rexberg, N. Dib and P. Katehi, "A Microshield Line Loop Antenna for Sub-mm Wavelength applications, " *1992 IEEE Antennas and Propagation Symposium Digest*, Chicago, pp. 1890-1893, July 1992.

[153] G. M. Rebeiz, D. P. Kasilingam, Y. Guo, P. A. Stimson and D. B. Rutledge, " Monolithic Millimeter-Wave Two-Dimensional Horn Imaging Arrays, " *IEEE Trans. on Antennas and Propagation*, Vol. 38, pp. 1473-1482, Sep. 1990.

[154] S. Gearhart, C. Ling, G. Rebeiz, H. Davee and G. Chin, "Integrated 119 μm Linear Corner-Cube Array, " *IEEE Microwave and Guided Wave Letters*, pp. 155-157, July 1991.

[155] M. Abramowitz and I. A. Stegun, *Handbook of Mathematical Functions*, Dover Pub., 1970, p. 590.

[156] W. Press, B. Flannery, S. Teukolsky and W. Vetterling, *Numerical Recipes, The Art of Scientific Computing*, Cambridge University Press, 1986, p. 188.

[157] G. F. Carrier, M. Krook and C. E. Pearson, *Functions of a Complex Variable, Theory and Technique*, Hod Books, 1983, p. 138.

[158] R. N. Simons and G. E. Ponchak, " Channelized Coplanar Waveguide: Discontinuities, Junctions and Propagation Characteristics, " *in IEEE MTT-S International Microwave Symposium Digest*, Long Beach, California, 915-918, June 1989.